APPLIED COMPUTATIONAL ELECTROMAGNETICS SOCIETY JOURNAL

September 2015
Vol. 30 No. 9
ISSN 1054-4887

The ACES Journal is abstracted in INSPEC, in Engineering Index, DTIC, Science Citation Index Expanded, the Research Alert, and to Current Contents/Engineering, Computing & Technology.

The illustrations on the front cover have been obtained from the research groups at the Department of Electrical Engineering, The University of Mississippi.

THE APPLIED COMPUTATIONAL ELECTROMAGNETICS SOCIETY

JOURNAL

Vol. 30 No. 9 September 2015

TABLE OF CONTENTS

SAR Induced by Low and High Directivity Antenna Apertures at Distances Greater than 25 mm from the Body

Md. Anas B. Mazady [1], G. Schmid [2], R. Uberbacher [2], and M. Ali [1]

[1] Department of Electrical Engineering
University of South Carolina, Columbia, SC 29208, USA
anas.eee@gmail.com, alimo@cec.sc.edu

[2] Seibersdorf Labor GmbH
Seibersdorf, Austria
Gernot.Schmid@seibersdorf-laboratories.at, Richard.Uberbacher@seibersdorf-laboratories.at

Abstract **—** A comprehensive SAR study of low and high directivity antennas operated at distances greater than 25 mm but less than 200 mm from a large homogeneous elliptical phantom is presented. The study considers antennas, such as dipoles, monopoles, planar inverted-F antennas (PIFAs), IFAs, patches, patch arrays, and dipole arrays. SAR estimation methods for low directivity antennas for both near and far field conditions are proposed and elucidated. For directive antennas and arrays radiating directly towards the phantom interesting phenomena are observed that require more detailed investigation.

Index Terms **—** Antennas, arrays, directive, RF exposure, small antennas, specific absorption rate (SAR).

I. INTRODUCTION

Electromagnetic exposures from wireless transmitters are regulated by respective regulatory bodies that restrict such exposure both for the general public and occupational professionals. The respective exposure limits (specific absorption rate – SAR) for the general public are identified as 1.6 W/Kg averaged over 1-g of tissue as established by the Federal Communications Commission (FCC) [1], and 2.0 W/Kg averaged over 10-g of tissue as established by the European Committee for Electrotechnical Standardization (CENELEC), which refers to exposure limits recommended in [2]. SAR induced in homogeneous and heterogeneous head and body phantoms has been studied for decades leading to new knowledge and standards set forth by respective standards bodies, such as the IEEE [3-4] and ICNIRP [5]. SAR studies have been conducted considering different types and sizes of antennas, various wireless device models, head models, head shapes, and sizes [6-18]. Traditionally from a compliance point of view, wireless device manufacturers have to measure SAR except for devices that are inherently compliant because of their very low transmit power; for example 1 mW for the FCC and 20 mW for CENELEC.

Given the presence of myriad wireless devices with variety of output power specifications, device geometry and size variations, and antenna geometry and size variations, it is quite overwhelming to fully grasp and quantify SAR as function of simple metrics, such as operating frequency, power, distance from device, and some simple easy to measure antenna characteristics. A simple method of estimation has two benefits, one, it leads to clear understanding by the antenna designer whether the device is in the ballpark to meet the requirements and whether for low power transmitters the device may be automatically exempt from SAR testing given such tests are costly, man-power intensive, and time consuming. With these outcomes in mind our research groups undertook SAR studies of a variety of antenna sizes and geometries when they were operated next to a flat phantom at distances less than 25 mm. The results of the first phase of our research were published in [19-21]. Subsequently, a more extensive study was undertaken to explore any empirical relationships between antenna performance metrics and SAR [22-25]. Based on that comprehensive study SAR estimation formulas were developed for devices that operate at distances 25 mm or less from the body within the frequency range of 300 MHz to 6 GHz [25]. These formulas can be used to estimate the threshold power levels that satisfy both the 1.6 W/Kg and the 2.0 W/Kg SAR limits. These formulas were developed as function of frequency, antenna to body separation, and *antenna free-space bandwidth (BW)*. Later on the results of this study were adopted into an IEC Standard [26].

The reason for choosing the antenna free-space BW for the rationale lies in the fact that BW is the

Submitted On: October 6, 2013
Accepted On: June 17, 2015

1054-4887

reciprocal of antenna quality factor (Q), and Q is expressed as the ratio of the stored and radiated energies of the antenna. Since SAR is strongly dependent on the stored near-fields of wireless device antennas (within 5-25 mm from the user's body), an empirical relationship between SAR or threshold power and BW was possible. As mentioned, the empirical formulas were developed considering SAR data of dipole antennas against a flat phantom.

Although that study covered the frequency range of 300-6000 MHz, the antenna to body distances over which the study focused on was less than 25 mm. Furthermore, the study also did not consider the SAR induced by directive antennas radiating directly towards the body. This led us to carry on a follow on further investigation that addresses these particular issues. Some preliminary results and conclusions of this work were presented earlier [27-28].

In this work we report the simulation and experimental results of SAR induced by a variety of electrically small non-resonant dipoles, resonant dipoles, resonant monopoles, planar inverted-F antennas, inverted-F antennas, microstrip patches, patch arrays and dipole arrays. The goal of this paper is to understand the SAR implications due to small low directivity antennas as well as highly directive antennas radiating directly towards the phantom when the antenna to phantom separation distance is within 40-200 mm. Since the distances are large, we considered to use a large elliptical flat phantom as defined in [29].

The details of the simulation and measurement methods are available in our earlier work [25]. Briefly, all simulations were performed using the Remcom Inc. commercial FDTD code called XFDTD. The XFDTD models containing dipole antennas were earlier validated [21] against the half-wave dipole data presented in IEEE Std. 1528-2003. The Liao absorbing boundary condition (ABC) was used to save simulation time. Before doing so, the Liao ABC usage was verified by comparing with PML (perfectly matched layers) ABC data. For impedance simulations, Gaussian pulses were used with automatic convergence at a threshold of -40 dB, while for SAR simulations, a sinusoidal waveform was used. The mesh size was generally uniform (1 mm), except for planar antennas we used graded mesh having a minimum mesh size of 0.25 mm and a maximum mesh size of 1 mm. All SAR measurements were carried out with the antennas placed next to the elliptical flat phantom ELI4 (Schmid & Partner Engineering AG, Zurich, Switzerland) containing tissue equivalent liquids for the respective frequencies. The dielectric properties of the liquids were measured prior to SAR measurements using a dielectric probe kit in combination with a vector network analyzer. All SAR measurements were conducted using the DASY3 system (Schmid & Partner Engineering AG, Zurich, Switzerland).

As it will transpire from the results and discussions, the issue of SAR at larger distances are governed by many factors including the location of the body (near-field, far field, aperture size to phantom size comparison, aperture directivity etc.).

The paper is organized as follows. First, the simulation and experimental landscape is defined that includes the frequencies, the distances, and the antennas considered in the study. Second, SAR results of low directivity antennas such as dipoles, monopoles, and PIFAs are described. Third, SAR results of directional patch antennas, patch arrays, and dipole arrays are elucidated. Fourth, a detailed comparison of the SAR data among different antenna classes is provided. And finally, an attempt is taken to suggest SAR estimation algorithms for these large distances followed by suggestion for future research works.

II. ANTENNA AND PHANTOM MODELS

The antenna types studied and their associated operating frequencies are listed in Table 1. Antenna simulation models as well as experimental prototypes were designed and developed for operation at 900, 1900, 2450, 3700, and 6000 MHz to reflect many commercial wireless applications in those frequency bands. Antennas were oriented and placed next to a large elliptical phantom at distances of 40, 100, and 200 mm for SAR calculation and measurements. Here distance, *d*, is defined as the distance from the antenna feed point to the phantom. Although data at other intermediate distances could have added more insight for the sake of saving simulation and measurement time, the above distances were considered.

Table 1: Antenna types studied and their associated frequencies. Distances from phantom were 40, 100, and 200 mm for all antennas

Antenna Type	Frequency (MHz)				
	900	1900	2450	3700	6000
Dipole	X	X	X	X	X
Monopole	X	X	X		
PIFA air	X	X			
PIFA surface			X	X	
IFA			X	X	
DB-PIFA	X	X			
DB-IFA			X		X
Patch		X	X	X	X
Patch array		X	X	X	X
Dipole array			X		

All low directivity apertures are identified in Table 2, while the directive apertures are defined in Table 3. Among directive antennas, microstrip patch antennas printed on FR substrates and then placed on the edge of a metal box (10 mm thick) were considered. Patches were designed and built for operation at 1900, 2450, 3700, and 6000 MHz. Similarly, corporate-fed four element microstrip patch array apertures were also designed and built for operation at 1900, 2450, 3700, and 6000 MHz. Collinear arrays of 3, 5, and 7 element dipoles were simulated with and without the presence of reflectors for SAR at 2450 MHz only.

Table 2: Low directivity antenna specifics; e.g., sizes and geometrical properties

Photographs	Description
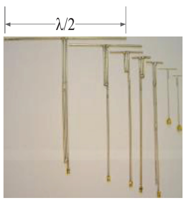 Dipoles	λ/15 (simulation only) and λ/2 wire dipoles, center fed; λ/4 balun used; wire radius=1.8 mm for frequencies up to 2450 MHz and wire radius=0.5 mm at 3700 and 6000 MHz
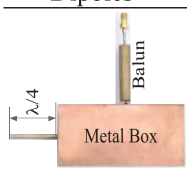 Monopoles	λ/4 long, wire radius=1.8 mm; wire on top of a metal box (box dimensions 100 mm by 40 mm by 19 mm)
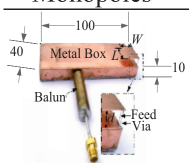 PIFA air	*L*=40 mm, *W*=31 mm by 6 mm at 900 MHz and *L*=20 mm, *W*=13.5 mm by 6 mm at 1900 MHz; feed/shorting pin using 1 mm wide strips; spacings of 2.5 and 2 mm at 900 and 1900 MHz
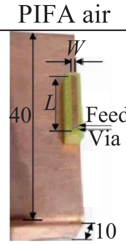 PIFA surface	*L*=16 mm, *W*=1 mm at 2450 MHz on 100 mm by 40 mm by 10 mm metal box
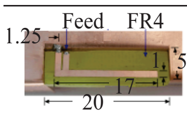 IFA	2450 MHz IFA shown
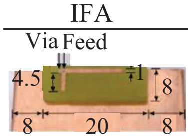 DB-PIFA	2450/6000 MHz DB-PIFA
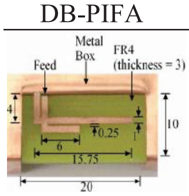 DB-IFA	2450/6000 MHz DB-IFA

Table 3: High directivity antenna/array specifics; e.g., sizes and geometrical properties

Photographs/ Diagrams	Description; Dimensions in mm			
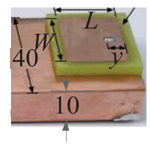 Patch	Freq. (GHz)	*L*	*W*	Feed Offset
	1.9	35.5	36.5	9.25
	2.45	27.5	36.5	6.25
	3.7	17.5	24	4.00
	6.0	11	15	1.00
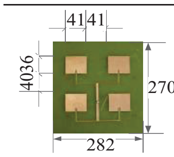 Patch array	Directivities of 10.9, 13.2, 11.6, and 11.4 dBi at 1900, 2450, 3700, and 6000 MHz respectively. Array approximately 1.5 wavelength. 1.9 GHz array photo shown.			
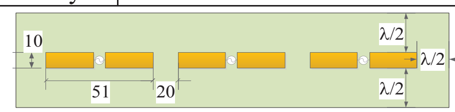 2.45 GHz linear dipole array				

Dipoles were studied at all frequencies while monopoles were studied at 900, 1900, and 2450 MHz. PIFAs on air or foam were studied at 900 and 1900 MHz to reflect mobile phone frequency bands. Surface mount PIFAs and IFAs were studied at higher frequencies to reflect their operation to support Bluetooth and WLAN type operations. Directional microstrip patches and patch arrays were investigated at 1900, 2450, 3700, and 6000 MHz. All planar antennas were studied both in the conventional (antenna element or array faces away from the body) and flipped orientations (antenna element or array faces the body) with respect to the phantom.

The geometry of the elliptical phantom used is shown in Fig. 1. The phantom consisted of a 2 mm thick shell with dielectric constant ε_r=3.7 and σ=0. The antenna to phantom distance is d. The tissue dielectric constant and conductivity values are given in Table 4. These values were obtained from [29].

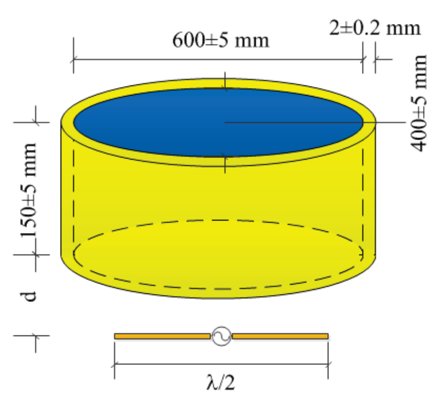

Fig. 1. Geometry of the phantom.

Table 4: Phantom tissue relative permittivity and conductivity. Tissue mass density, ρ=1000 Kg/m^3

Frequency (MHz)	900	1900	2450	3700	6000
Relative Permittivity, ε_r	41.5	40	39.2	37.7	35.1
Conductivity, σ (S/m)	0.97	1.4	1.8	3.12	5.48

III. RESULTS

A. SAR results of dipole antennas

Computed peak 1-g and 10-g averaged SAR for λ/15 and λ/2 dipoles placed at *d*=40 mm, 100 mm and 200 mm from the phantom are shown in Figs. 2 (a)-(c). All data are normalized to 1W of power. Measured 1-g and 10-g averaged SAR data for λ/2 dipoles are also shown. For all cases, the simulated and measured results are in good agreement. From Fig. 2 (a) for the case when *d*=40 mm, it is clear that the largest difference in SAR between the λ/15 and λ/2 dipoles occurs at the lowest frequency (900 MHz). At this frequency the phantom is still in the near field of the antenna. Therefore, the shorter antenna induces almost twice as much SAR than that induced by the longer antenna. As explained in [21], when the phantom is in the near field of the antenna, the shorter antenna acts almost as a point source resulting in a more localized SAR distribution. Also for *d*=40 mm, as the frequency increases (e.g., at 2450 MHz and higher) the SAR induced by the λ/15 and λ/2 dipoles are nearly identical to each other as because the aforementioned near field effect disappears.

From Figs. 2 (b) and 2 (c) (*d*=100 mm and 200 mm), it is clear that if the phantom is in the far field of the antennas, the antenna with the slightly higher directivity induces slightly higher SAR. The SAR behavior observed at around 2450 MHz can be explained from the tissue conductivity versus frequency characteristics. The non-linear conductivity increase from 900 MHz to 2450 MHz is responsible for the non-linear SAR profiles shown in Figs. 2 (a) and 2 (c).

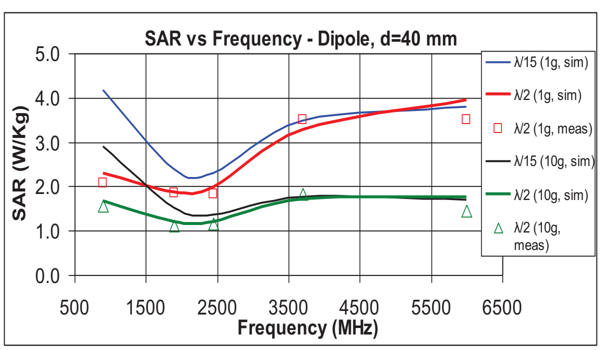

(a)

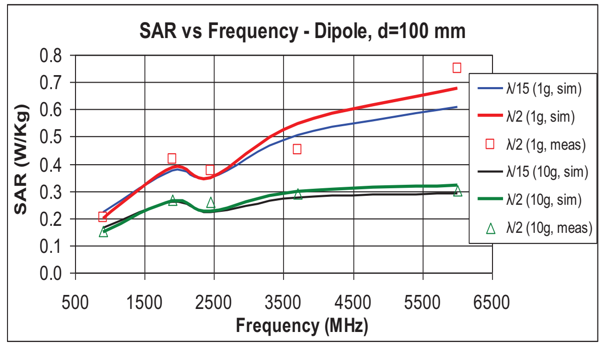

(b)

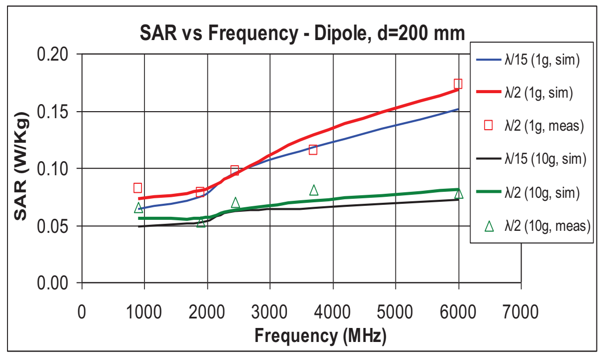

(c)

Fig. 2. SAR versus frequency of dipole antennas for *d*=40 mm, 100 and 200 mm.

B. SAR results of monopole antennas

Computed and measured peak 1-g and 10-g averaged SAR induced by quarter-wavelength long monopole antennas are compared with those induced by half-wave dipoles in Figs. 3 (a)-(c) for *d*=40, 100, and 200 mm. Note that, since the monopole box measures 19 mm in thickness for *d*=40 mm, the box is at a distance of 21 mm from the phantom.

For all three distances, the SAR due to monopole antennas are always smaller than the SAR due to dipole antennas. For *d*=40 mm, the SAR variation due to monopole antennas with frequency is monotonous (decreases almost linearly with frequency). For *d*=100 mm, the SAR versus frequency characteristics for the monopoles is similar to that of the dipoles except for the inflection point at 1900 MHz. The situation is nearly similar at *d*=200 mm. At 100 and 200 mm distances, monopole 1-g and 10-g SAR decrease till 1900 MHz and then increase with frequency. This does not occur for the dipoles because the SAR distributions for monopoles are different than dipoles. There are multiple SAR hot spots for the monopoles (caused by the current distribution along the metallic box) while there is a distinct one hot spot for the dipoles.

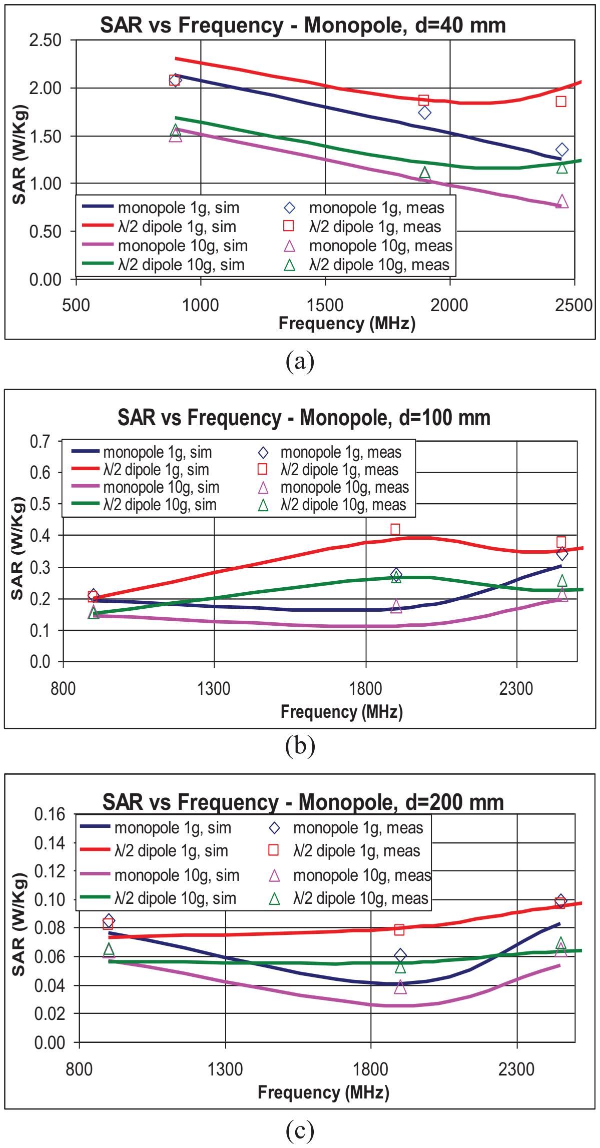

Fig. 3. SAR versus frequency of monopole antennas for d=40 mm and d=100 mm.

C. SAR results of planar inverted-F antennas (PIFAs)

SAR induced by planar inverted-F antennas (PIFAs) in the conventional orientation with respect to the phantom (here the antenna faces away from the phantom) for d=40, 100, and 200 mm are shown in Figs. 4 (a)-(c). At d=40 mm, the SAR due to PIFAs decrease with frequency monotonously like that for the monopole antennas on boxes. In almost all cases the SAR due to PIFAs is smaller than the SAR due to λ/2 dipoles except for the PIFA operating at 900 MHz and d=40 mm.

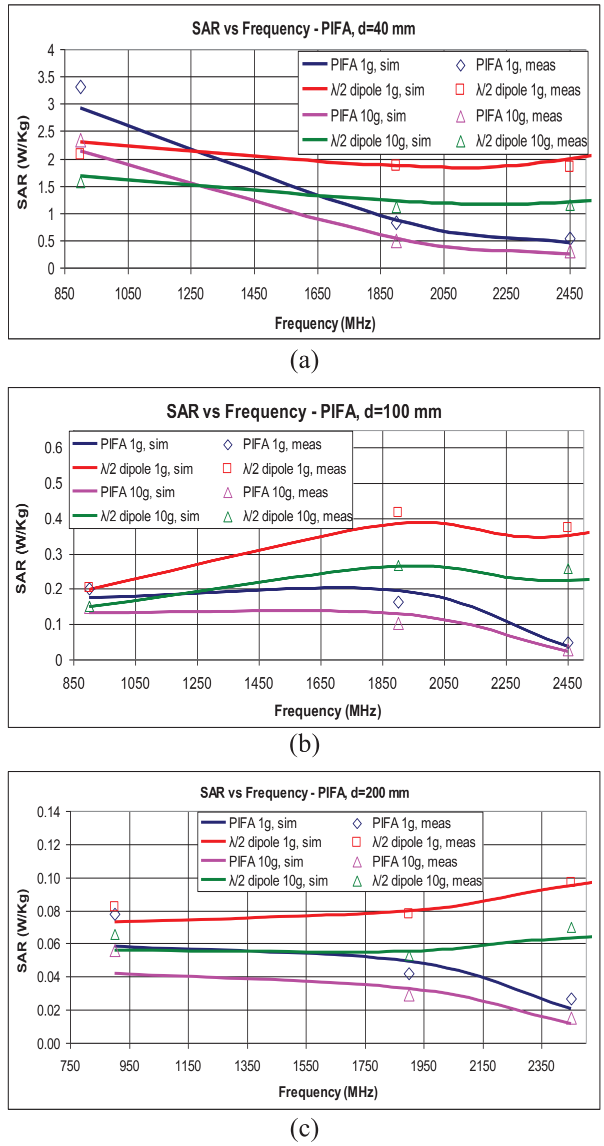

Fig. 4. SAR versus frequency of PIFAS in conventional orientation for d=40 mm, 100 mm and d=200 mm.

Nevertheless, even in this case the SAR due to a λ/15 dipole is considerably higher (4 W/kg – Fig. 2 (a)) than that due to the PIFA in question here (3 W/kg). For larger distances (e.g., d=100 and 200 mm), the rate of decrease in SAR from 1900 MHz to 2450 MHz is rapid. This occurs because the 2450 MHz PIFAs being printed on FR4 substrates are lossy (tanδ=0.02) as opposed to the 900 and 1900 MHz PIFAs which are fabricated in air. This results in decreased SAR which did not occur for the dipoles or the quarter-wave monopoles on boxes. For example, at d=200 mm and at 2450 MHz the power dissipated for a λ/2 dipole in the tissue was

0.112W out of 1W of input power. By contrast, for the same distance and at the same frequency the power lost in the FR4 substrate was 0.504W and the power dissipated in the tissue was 0.0283W.

D. Comparison

SAR induced by other antenna types, sizes were also simulated and measured. All simulation and measurement data are available in [30] and [31]. However, for the sake of clarity and brevity instead of showing SAR results for each individual antenna class separately, a comparison of the simulated peak 1-g averaged SAR induced by all low directivity antennas studied are plotted as scatter plots in Fig. 5 (i). The same for peak 10-g averaged SAR induced by all low directivity antennas studied are plotted as scatter plots in Fig. 5 (ii).

For comparison, the SAR induced by single microstrip patch antennas radiating directly towards the phantom are also shown in these figures. Microstrip patch results are available at 1900, 2450, 3700, and 6000 MHz. It is evident from Figs. 5 (i) and 5 (ii) that, patches radiating away from the phantom (ground plane facing the phantom) induce very low SAR.

Comparing the peak 1-g SAR data at all three distances it is clear that:

- Except for the microstrip patch antennas that are radiating directly towards the phantom, the SAR induced by dipole antennas are the highest compared to all antennas in this study. This observation is consistent with our earlier work [25].

When comparing the SAR due to dipoles and patches flipped, it is clear that:

- At 1900 MHz, the SAR due to patches at all three distances are smaller than the SAR due to dipoles or about the same.
- At 2450 MHz, the SAR due to patches is only slightly higher than the SAR due to dipoles.
- At 3700 MHz and higher, the SAR due to patches are consistently higher than the SAR due to dipoles. Specifically at 6000 MHz and at d=200 mm, the SAR due to a flipped patch is about 3 times the SAR due to a dipole.

To put these results in perspective, the near-field and radiating near-field boundaries of different antenna apertures are plotted in Fig. 6. For antennas smaller than 0.5λ, this boundary was evaluated as λ/2π. At 900 MHz, this boundary starts at a radius of 50 mm from the antenna. As the frequency increases the radius of this boundary decreases and vice versa. This is exactly what we see from the 1-g SAR data of the flipped patches. When the frequency is sufficiently high, e.g., 6 GHz the phantom is indeed in the far field of the antenna and thus the 1-g SAR induced is the SAR due to a small dipole (at that frequency and distance) times the linear gain of the patch antenna over the dipole.

However, if the phantom is not sufficiently in the far field, then estimating SAR by multiplying dipole SAR with the linear gain of the directive antenna will result in an over estimation of the SAR. Now for low directivity antennas that are strictly in the near field, we examine in the following if our earlier developed formulas that were reported in [25] can still be used at other distances than they were originally developed for (antenna to phantom separation, s<25 mm).

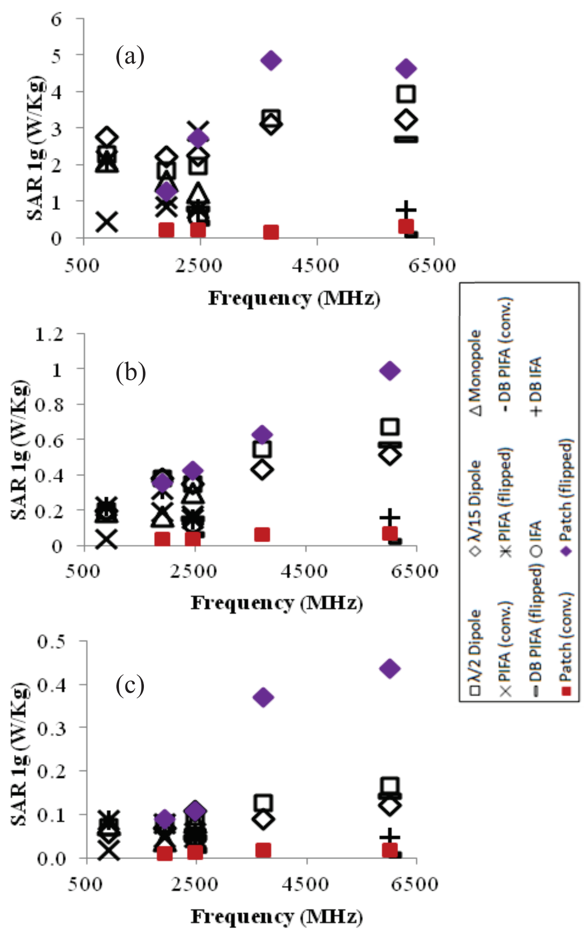

Fig. 5 (i). Peak 1-g averaged SAR comparison of all antennas at 40, 100, and 200 mm distances.

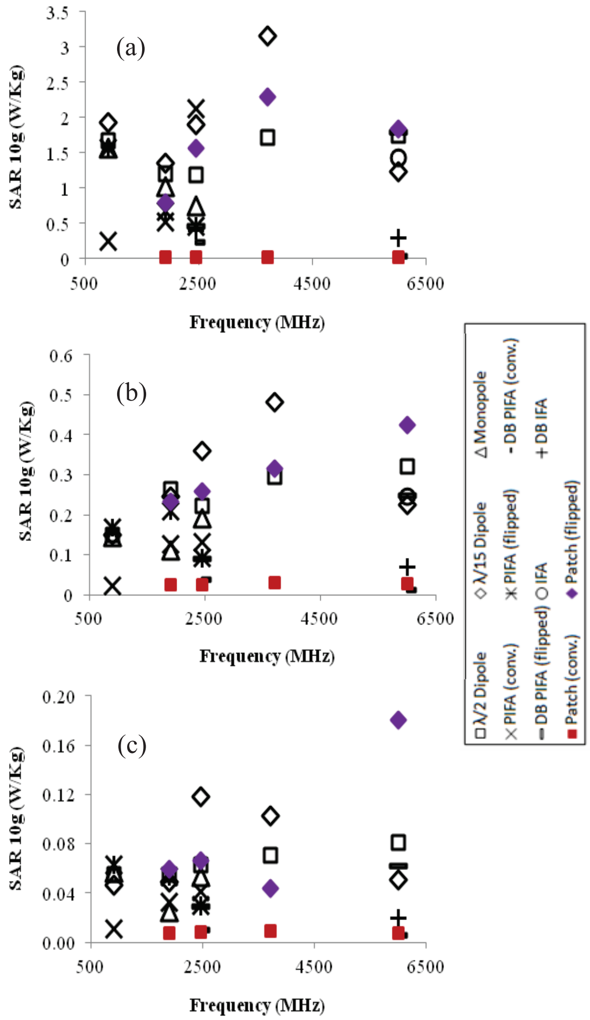

Fig. 5 (ii). Peak 10-g averaged SAR comparison of all antennas at 40, 100, and 200 mm distances.

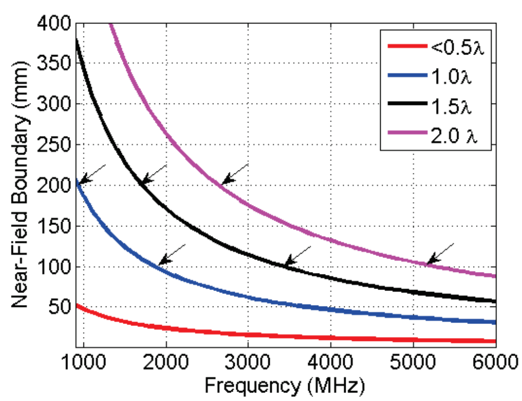

Fig. 6. Near-field boundary distances of different apertures.

In contrast, peak 10-g averaged SAR data plotted in Fig. 5 (ii) clearly shows that the only frequency at which the SAR due to the flipped patch is higher than the dipoles is only 6 GHz. This can be explained by the fact that, under far field conditions, the patch in flipped orientation causes a more focused SAR hot spot on the phantom when compared to the dipoles. This is not the case when the phantom is in the near field of the antennas. The general trend of lower average SAR values for larger averaging volumes is therefore increasingly more enhanced for the patch antenna when the distance between patch antenna and phantom approaches or exceeds the near-field/far field boundary distance. In [25], we developed a rationale to estimate the threshold power that corresponded to the 1-g and 10-g averaged SAR based on the operating frequency, f, antenna to phantom separation, s, and the antenna half power free-space bandwidth, BW. This equation is given below:

$$P_{\max,m} = \exp\left(As + Bs^2 + C\ln(BW) + D\right). \qquad (1)$$

Both 1-g and 10-g averaged SAR can be calculated from (2) if $P_{max,m}$ is known from (1) and considered as a best fit underestimate for $P_{th,m}$:

$$SAR_m = P_t \frac{SAR_{\text{limit},m}}{P_{th,m}}. \qquad (2)$$

This led to the following solution for SAR_{1g}=1.6 W/kg:

$$A = (-0.4922f^3 + 4.831f^2 - 6.620f + 8.312)/100, \qquad (3a)$$
$$B = (0.1191f^3 - 1.470f^2 + 3.656f - 1.697)/1000, \qquad (3b)$$
$$C = (-0.4228f^3 + 13.24f^2 - 108.1f + 339.4)/1000, \qquad (3c)$$
$$D = -0.02440f^3 + 0.4075f^2 - 2.330f + 4.730. \qquad (3d)$$

For SAR_{10g}=2 W/kg, the following solution was obtained:

$$A = (-0.4588f^3 + 4.407f^2 - 6.112f + 2.497)/100, \qquad (4a)$$
$$B = (0.1160f^3 - 1.402f^2 + 3.504f - 0.4367)/1000, \qquad (4b)$$
$$C = (-0.1333f^3 + 11.89f^2 - 110.8f + 301.4)/1000, \qquad (4c)$$
$$D = -0.03540f^3 + 0.5023f^2 - 2.297f + 6.104. \qquad (4d)$$

In (3) and (4), f is expressed in GHz. The free-space BW (assuming antennas are perfectly matched at their operating frequencies using lossless components) of dipole antennas are listed in Table 5.

Table 5: Dipole antenna half power free-space bandwidth. Wire radius 1.8 mm for f<3.7 GHz and wire radius=0.5 mm for f>=3.7 GHz

f (GHz)	0.9	1.9	2.45	3.7	6
λ/15	0.22	0.32	0.41	0.50	0.96
λ/2	22.2	28.2	29.6	45.5	60.2

The objective of equations (1)-(4) is to provide a conservative estimate of $P_{max,m}$ or SAR_m for $s<25$ mm for small low directivity apertures, such as dipoles, monopoles, PIFAs IFAs etc. However, applying s=38 mm (which is d=40 mm in Fig. 1) in equations (1)-(4) and using the BW data for the λ/15 dipole in Table 5, results in 1-g SAR values of 6.44, 3.17, 2.38, 2.12, and 33.8 W/kg at 0.9, 1.9, 2.45, 3.7, and 6 GHz. Comparing these data with the actual simulated data shown in Fig. 2 (a), it is clear that the data agrees well for frequencies of up to 2.45 GHz. The corresponding estimated 10-g SAR values of 2.74, 1.26, 0.90, 0.69, and 8.8 W/kg at 0.9, 1.9, 2.45, 3.7, and 6 GHz agree reasonably well for frequencies of up to 1.9 GHz when compared with the actual simulated data shown in Fig. 2 (a).

To be conservative, if we observe the near-field boundary defined by Fig. 6 at 40 mm distance, only the SAR for $f<1.9$ GHz could be estimated with reasonable accuracy. Thus, the data at higher frequencies cannot be estimated using equations (1)-(4). Therefore, to apply equations (1)-(4) for $s>25$ mm, the frequency that corresponds to $s=\lambda/2\pi$ should be first determined and then $P_{max,m}$ or SAR_m should be estimated at frequencies below that.

Note that, for frequencies of 300, 400, and 500 MHz the cutoff distances are 159, 119, and 95 mm respectively. Therefore, it is plausible that at frequencies such as 300, and 400 MHz the range over which equations (1)-(4) can be used may be extended pending further numerical and experimental validation.

E. SAR results of antenna arrays

Computed and measured peak 1-g and 10-g SAR results for the patch arrays in the flipped orientation are plotted in Figs. 7 (a)-(c). For comparison, the simulated SAR of λ/15 dipoles are also shown. It is clear that for d=40 mm the patch flipped arrays only induce higher SAR compared to a λ/15 dipole at frequencies above 3700 MHz. For d=100 MHz, this occurs at 2450 MHz, and for d=200 mm at 1900 MHz.

Thus, at higher frequencies and larger distances the SAR induced by antenna arrays are substantially higher. The phenomena of lower SAR at shorter distances and lower frequencies and higher SAR at longer distances and higher frequencies will be explained in details in section V. Simulated peak 1-g and 10-g averaged SAR data of linear 3, 5, and 7 element dipole arrays at 2450 MHz and 200 mm from the phantom are shown in Table 6. For comparison, the SAR data of a single λ/2 dipole, a single flipped patch and a 4 element patch array are also shown. Interestingly, the N=3 element array with reflector induces roughly the same SAR as the 4-element patch array. Note that, the directivities of these two arrays are very close.

Increasing the number of elements for the dipole array does not increase the SAR linearly as expected, because with increasing array size two things occur: (1) a larger array for the fixed distance means that the phantom moves more and more to the near/radiating near field, and (2) the array size becomes an appreciable fraction of the phantom size.

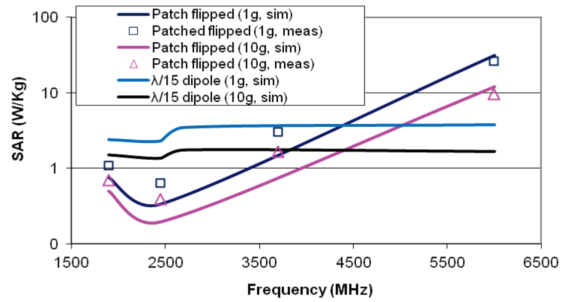

(a)

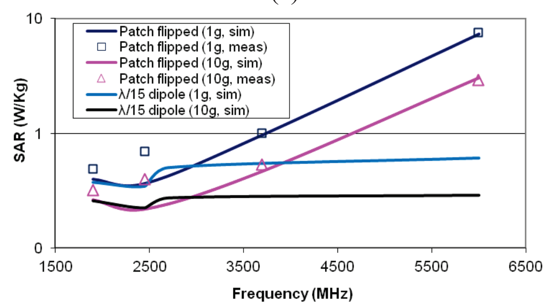

(b)

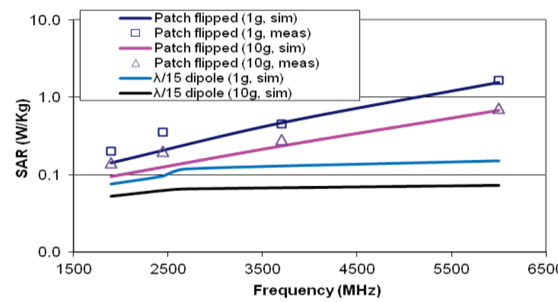

(c)

Fig. 7. SAR vs. frequency of patch antenna arrays at 40, 100, and 200 mm distance (flipped orientation).

Table 6: Comparison of SAR induced by linear dipole arrays with other antennas. Linear dipole arrays with 3, 5, 7 elements with and without reflector at 2450 MHz and 200 mm from the phantom

Antenna Type	D_0 (linear)	SAR 1g (W/Kg)	SAR 10g (W/Kg)	Dim. (mm)
λ/2 dipole	1.75	0.0949	0.0633	51
3 dipole array	4.24	0.1779	0.1087	196
3 dipole array & reflector	18.3	0.4816	0.2943	352
5 dipole array	6.77	0.108	0.0573	335
5 dipole array & reflector	28.18	0.2529	0.1554	488
7 dipole array & reflector	38.85	0.1699	0.1045	627
4 patch array	20.89	0.45	0.28	
1 patch	2.28	0.1088	0.0677	

IV. ANALYSES

From [8], the SAR induced in an infinite lossy plane considering plane wave analysis is given by:

$$SAR = \frac{\sigma}{\rho}\frac{\mu\omega}{\rho\sqrt{\sigma^2+\varepsilon^2\omega^2}}\left(1+c_{corr}\gamma_{pw}\right)^2 H_{tinc}^2 \qquad (5)$$

where ε is the tissue permittivity, $\mu = \mu_0 = 4\pi\times10^{-7}$ H/m is the tissue permeability, σ is the tissue conductivity, ρ is the tissue mass density, H_{tinc} is the rms value of the incident magnetic field intensity, and γ_{pw} is the plane wave reflection coefficient for the H_{tinc} field. Also note that,

$$\varepsilon' = \varepsilon - \sigma / j\omega \qquad (6)$$

and

$$\gamma_{pw} = \frac{2\left|\sqrt{\varepsilon'}\right|}{\left|\sqrt{\varepsilon'}+\sqrt{\varepsilon_0}\right|} - 1 \qquad (7)$$

where $\varepsilon_0 = 8.854\times10^{-12}$ F/m is the free-space permittivity.

Considering 1 W transmit power, the power density caused by an isotropic antenna at a distance of r from the antenna is $P_D = 1/(4\pi r^2)$. Considering a $\lambda/2$ dipole antenna with directivity of 1.64 the $P_D = 1.64/(4\pi r^2)$, which results in $H_{tinc} = P_D / 377$.

Considering the permittivity, conductivity, and mass density values of the homogeneous phantom given in Table 4, the above equations were used to calculate SAR as function of frequency on the surface of an infinite lossy media. After that, SAR was calculated at depths of up to 23 mm of the lossy surface at 1 mm intervals using the skin depth formula below. From these table of SAR values the 1-g and 10-g averaged SAR data were calculated:

$$\delta = \frac{1}{\omega}\left[\left(\frac{\mu_0\varepsilon_r\varepsilon_0}{2}\right)\left(\sqrt{1+\left(\frac{\sigma}{\omega\varepsilon_0\varepsilon_r}\right)^2}-1\right)\right]^{-1/2} \qquad (8)$$

Calculated SAR data using this method are compared with direct simulation and measurement data for dipoles and monopoles at 40, 100, and 200 mm distance in Fig. 8.

For antennas smaller than half-wavelength, the near field boundary is 50 mm at 900 MHz. This agrees with the results shown in Fig. 8. As seen at 40 mm distance, the only frequency at which the plane wave approximation for both 1-g and 10-g SAR deviates is 900 MHz. Thus, SAR caused by dipoles and monopoles for frequencies below 900 MHz should be estimated using our earlier proposed free-space bandwidth based approximation method. For distances greater than 50 mm, the phantom is in the far field of the small low directivity antennas. Thus, SAR can be estimated using the plane wave approximation.

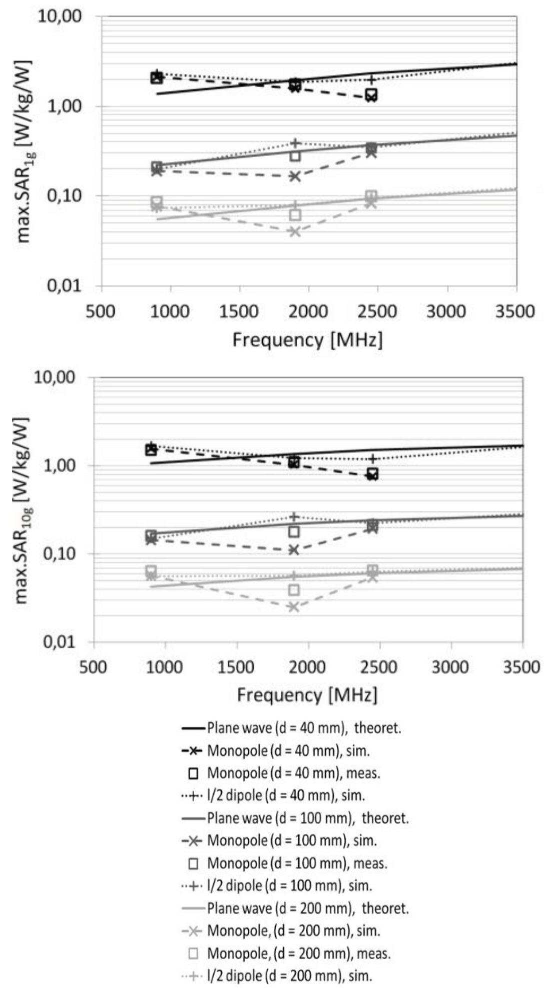

Fig. 8. Comparison of plane wave calculated SAR (dipole fed with 1 W) and SAR results obtained from direct simulations.

For large aperture directive antennas that radiate directly towards the phantom SAR estimation is not so simple. One may consider the EIRP (effective isotropically radiated power) instead of the power to estimate the SAR. Thus, if the transmit power is P_t and the antenna gain is G_t, then the EIRP should be P_tG_t. Thus, if the antenna gain is 10 times the gain of a small dipole antenna, the SAR should be multiplied by 10. However, this will only satisfy if the aperture is sufficiently far from the phantom or body such that the aperture far field radiation beam has formed. It is difficult to pin-point the exact far field distance because it will depend on the aperture electrical size and the frequency of operation. From Table 7, it is clear that for a fixed antenna to phantom separation the smaller the aperture the lower is the frequency where the near-field boundary transition takes place. Conversely for a fixed aperture, say 1.5λ, if the antenna to phantom distance increases, the reactive near-field to radiating near-field boundary occurs at a lower frequency. Thus, it is clear that for a fixed aperture size and fixed antenna to phantom separation the higher the frequency the more the likelihood that the aperture far-field beam will have formed. Thus, for similar directivity apertures (meaning apertures with similar dimensions) the SAR is likely to be much higher at higher frequencies simply because the directive beam has formed.

Table 7: Aperture size and near-field boundary for directive apertures

	Aperture Size		
Aperture to phantom distance	1λ	1.5λ	2λ
100 mm	1900 MHz	3500 MHz	5200 MHz
200 mm	900 MHz	1800 MHz	2800 MHz

V. DISCUSSIONS

Figures 9 (a) and 9 (b) illustrate the SAR factors (SF) of patch arrays over λ/15 dipole antennas for various frequencies at various distances from the phantom. Peak 1-g average SAR factors of planar patch arrays over a λ/15 dipole antenna show that at 40 mm distance only the 6000 MHz array has an SAR factor larger than 1. At 100 mm most patch arrays have an SAR factor >1 but <2 except the 6 GHz patch array which has an SAR factor >10. At 200 mm all patch arrays have an SAR factor >1 and the 6 GHz patch array has an SAR factor >10. Two factors in play are array size with respect to phantom and array electrical distance from phantom. It must be noted that all results presented here are based on SAR analysis in homogeneous phantoms as used for compliance testing according to IEC 62209-2 [29]. As reported in [32] and [33], 1-g and 10-g averaged SAR results obtained in homogeneous phantoms according to [29] can underestimate the corresponding SAR in anatomical body models when the body or phantom is no longer in the reactive near field of the antenna. The reasons for this phenomenon are standing wave effects in low conductivity tissue layers which may appear in worst case tissue layer compositions. According to [32] and [33], the extent of the possible underestimation depends on frequency and distance to the antenna and lies in the range of 2.2 to 4.7 dB. In order to stay conservative, all estimated SAR values based on the results presented in the present paper should be correspondingly scaled taking into account the results reported in [32] and [33].

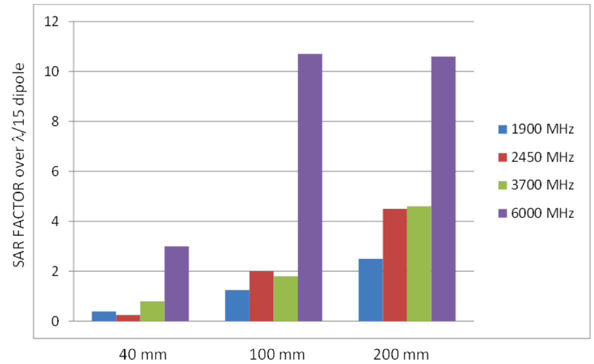

(a) 1-g average SF

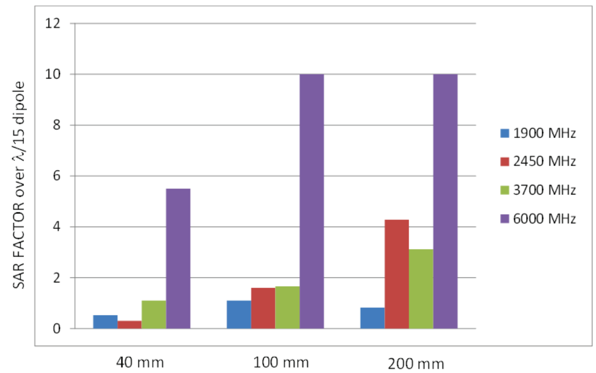

(b) 10-g average SF

Fig. 9. SAR factors (SF) of patch arrays over λ/15 dipole antennas.

VI. CONCLUSIONS

The SAR induced in a large 600 mm by 400 mm by 150 mm elliptical flat phantom by a large class of small low directivity antennas and directive patch antennas and arrays at distances of 40, 100, and 200 mm are studied and analyzed. The frequency range within which the study is conducted is from 900-6000 MHz. Both simulation and measurement results are presented which illustrate a number of significant findings. It is observed that for small low directivity antennas, the SAR may be estimated using our earlier reported antenna free-space bandwidth based formulas when the phantom is still within the near field boundary of the antenna. Conversely, if the phantom is clearly in the far field, SAR can be estimated using plane wave approximation methods by multiplying with the proper linear antenna gain. For directive antennas and arrays radiating directly towards the phantom, the plane wave approximation for SAR and multiplying by the linear gain allows a good estimate as long as the phantom is clearly in the far field of the aperture. For phantoms in the near field or radiating near field, estimating the SAR using this method will result in an overestimation due to the fact that the radiation beam has not formed yet and that the aperture could be physically larger than the phantom resulting in multiple diffused distributions. The presented results do not consider the standing wave effects in a layered tissue structure.

ACKNOWLEDGMENT

This work was supported in part by the Mobile Manufacturers Forum (MMF), Brussels, Belgium.

REFERENCES

[1] Federal Communications Commission Office of Engineering and Technology Supplement C (ed. 01-01) to OET Bulletin 65 (ed. 97-01), *Evaluating Compliance With FCC Guidelines for Human Exposure to Radiofrequency Electromagnetic Fields, Additional Information for Evaluating Compliance of Mobile and Portable Devices with FCC Limits for Human Exposure to Radiofrequency Emissions*, Washington, DC, Jun. 2001.

[2] Council of the Eurpoean Union, *Council Recommendation of July 12, 1999 on the Limitation of Exposure of the General Public to Electromagnetic Fields (0 Hz - 300 GHz)*, Document 1999/519/EC, Official Journal of the European Communities, pp. L199/59-L199/70, Jul. 30, 1999.

[3] IEEE Stand. for Safety Levels with Respect to Human Exposure to Radio Frequency Electromagnetic Fields, 3 kHz to 300 GHz, IEEE Stand. C95.1-1991.

[4] IEEE Stand. for Safety Levels with Respect to Human Exposure to Radio Frequency Electromagnetic Fields, 3 kHz to 300 GHz, IEEE Stand. C95.1-2005.

[5] ICNIRP, "International commission on non-ionizing radiation protection guidelines for limiting exposure to time-varying electric, magnetic and electromagnetic fields (up to 300 GHz)," *Health Physics*, vol. 74, no. 4, pp. 494-522, 1998.

[6] Q. Balzano, O. Garay, and T. J. Manning, "Electromagnetic energy exposure of simulated users of portable cellular telephones," *IEEE Trans. Veh. Technol.*, vol. 44, no. 3, pp. 390-403, Aug. 1995.

[7] T. Schmid, O. Egger, and N. Kuster, "Automated E-field scanning system for dosimetric assessments," *IEEE Transactions on Microwave Theory and Techniques*, vol. 44, no. 1, pp. 105-113, Jan. 1996.

[8] N. Kuster and Q. Balzano, "Energy absorption mechanism by biological bodies in the near field of dipole antennas," *IEEE Trans. Veh. Technol.*, vol. 41, no. 1, pp. 17-23, Feb. 1992.

[9] M. A. Jensen and Y. Rahmat-Samii, "EM interaction of handset antennas and a human in personal communications," in *Proc. IEEE*, vol. 83, no. 1, pp. 7-17, Jan. 1995.

[10] M. Okoniewski and M. A. Stuchly, "A study of the handset antenna and human body interaction," *IEEE Trans. Microwave Theory Tech*., vol. 44, no. 10, pp. 1855-1864, Oct. 1996.

[11] V. Hombach, K. Meier, M. Burkhardt, E. Kühn, and N. Kuster, "The dependence of EM energy absorption upon human head modeling at 900 MHz," *IEEE Trans. Microwave Theory Tech.*, vol. 44, pp. 1865-1873, Oct. 1996.

[12] K. Meier, V. Hombach, R. Kästle, R. Y-S. Tay, and N. Kuster, "The dependence of electromagnetic energy absorption upon human-head modeling at 1800 MHz," *IEEE Trans. Microwave Theory Tech.*, vol. 45, pp. 2058-2062, Nov. 1997.

[13] S. Watanabe, M. Taki, T. Nojima, and O. Fujiwara, "Characteristics of the SAR distributions in a head exposed to electromagnetic fields radiated by a hand-held portable radio," *IEEE Trans. Microw. Theory Tech.*, vol. 44, no. 10, pp. 1874-1883, Oct. 1996.

[14] O. P. Gandhi, G. Lazzi, and C. Furse, "Electromagnetic absorption in the human head and neck for mobile telephones at 835 and 1900 MHz,'' *IEEE Trans. Microwave Theory Tech*., vol. 44, no. 10, pp. 1884-1897, Oct. 1996.

[15] Q. Balzano, M. Y. Kanda, and C. C. Davis, "Specific absorption rates in a flat phantom in the near-field of dipole antennas," *IEEE Trans. Electromagn. Compat*., vol. 48, no. 3, pp. 563-568, Aug. 2006.

[16] C. C. Davis, B. B. Beard, A. Tillman, J. Rzasa, E. Merideth, and Q. Balzano, "International intercomparison of specific absorption rates in a flat absorbing phantom in the near-field of dipole antennas," *IEEE Trans. Electromagn. Compat.*, vol. 48, no. 3, pp. 579-588, Aug. 2006.

[17] G. Lazzi and O. P. Gandhi, "On modeling and personal dosimetry of cellular telephone helical antennas with the FDTD code," *IEEE Trans. Antennas Propagat*., vol. 46, pp. 525-530, Apr. 1998.

[18] P. Bernardi, M. Cavagnaro, S. Pisa, and E. Piuzzi, "Power absorption and temperature elevations induced in the human head by a dual-band monopole-helix antenna phone," *IEEE Trans. Microw. Theory Tech.*, vol. 49, no. 12, pp. 2539-2546, Dec. 2001.

[19] M. Ali, M. G. Douglas, A. Faraone, and C-K. Chou, "Upper bounds of SAR for dipole antennas

in the 300-3000 MHz frequency range," Proceedings of the *Bioelectromagnetics Society Conference*, Dublin, Ireland, Jun. 19-24, 2005.
[20] A. T. M. Sayem, M. Ali, G. Schmid, and N. Haas, "Bandwidth, efficiency, and SAR of canonical antennas," Proceedings of the *Bioelectromagnetics Society Conference*, Cancun, Mexico, Jun. 2006.
[21] M. Ali, M. G. Douglas, A. T. M. Sayem, A. Faraone, and C-K. Chou, "Threshold power of canonical antennas for inducing SAR at compliance limits in the 300-3000 MHz frequency range," *IEEE Transactions on Electromagnetic Compatibility*, vol. 49, pp. 143-152, Jan. 2007.
[22] A. T. M. Sayem, G. Schmid, B. Petric, M. G. Douglas, and M. Ali, "SAR induced by monopole and planar antennas to determine threshold power levels of wireless devices," *29th Annual Meeting of the Bioelectromagnetic Society*, Abstract book, pp. 210-214, Kanazawa, Japan, Jun. 2007.
[23] A. T. M. Sayem, G. Schmid, N. Haas, B. Petric, M. G. Douglas, and M. Ali, "Correlating bandwidth and efficiency with SAR of monopole antennas in the 300-6000 MHz band," *European Bioelectromagnetics Conference*, Bordeaux, France, Apr. 2007.
[24] A. T. M. Sayem, G. Schmid, M. G. Douglas, and M. Ali, "Comparing the SAR induced by wire and planar antennas in a flat phantom," *30th Annual Meeting of the Bioelectromagnetic Society*, Abstract book, pp. 290-292, San Diego, CA, 2008.
[25] A. T. M. Sayem, M. Ali, G. Schmid, B. Petric, and M. G. Douglas, "Correlating threshold power with free-space bandwidth for low directivity antennas," *IEEE Transactions on Electromagnetic Compatibility*, pp. 25-37, Feb. 2009.
[26] IEC Stand. 62479, *Assessment of the Compliance of Low Power Electronic and Electrical Equipment with the Basic Restrictions Related to Human Exposure to Electromagnetic Fields (10 MHz - 300 GHz)*, ed. 1, Jun. 2010.
[27] Md. A. B. Mazady, G. Schmid, R. Überbacher, M. G. Douglas, and M. Ali, "SAR induced by dipole antennas to determine low power thresholds for wireless transmitters at distances of 25-200 mm from the user," *Bioelectromagentics Society Conference*, Davos, Switzerland, Jun. 2009.
[28] Md. A. B. Mazady, G. Schmid, R. Überbacher, G. Bit-Babik, and M. Ali, "SAR induced by resonant antennas at distances of 40 and 200 mm from an elliptical phantom," *Bioelectromagentics Society Conference*, Seoul, Korea, Jun. 2010.
[29] IEC Stand. 62209-2, *Human Exposure to Radio Frequency Fields from Handheld and Body-Mounted wireless Communication Devices - Human Models, Instrumentation and Procedures - Part 2: Procedure to Determine the Specific Absorption Rate SAR for Wireless Communication Devices Used in Close Proximity to the Human Body (Frequency Range 30 MHz - 6 GHz)*, ed. 1, Mar. 2010.
[30] Md. A. B. Mazady, *Electromagnetic Exposure in a Phantom in the Near and Far Fields of Wire and Planar Antennas*, M.S. Thesis, University of South Carolina, 2010.
[31] *Quarterly Reports (Eight Reports) on Work Package 3 - Low Power Exemption Rationale for Wireless Transmitters at Distances of 25 mm or Greater from the User*, Mobile Manufacturers Forum, 2008-2010.
[32] A. Christ, A. Klingenböck, T. Samaras, C. Goiceanu, and N. Kuster, "The dependence of electromagnetic far-field absorption on body tissue composition in the frequency range from 300 MHz to 6 GHz," *IEEE Trans. Microwave Theory Tech.*, vol. 54, pp. 2188-2195, May 2006.
[33] A. Christ, T. Samaras, A. Klingenböck, and N. Kuster, "Characterization of the electromagnetic near-field absorption in layered biological tissue in the frequency range 30 MHz to 6000 MHz," *Phys. Med. Biol.*, 51, pp. 4951-4965, 2006.

Design of Shaped-Beam Parabolic Reflector Antenna for Peninsular Malaysia Beam Coverage and its Overlapping Feed Issues

Nurul H. Abd Rahman [1], Mohammad T. Islam [2], Yoshihide Yamada [3], and Naobumi Michishita [4]

[1] Antenna Research Group, Microwave Technology Centre, Faculty of Electrical Engineering
Universiti Teknologi MARA, Shah Alam, 40450, Selangor, Malaysia
nurulhuda0340@salam.uitm.edu.my

[2] Department of Electrical, Electronic and Systems Engineering, Faculty of Engineering and Built Environment
Universiti Kebangsaan Malaysia, UKM Bangi, 43600, Selangor, Malaysia
titareq@yahoo.com

[3] Malaysia Japan International Institute of Technology
Universiti Teknologi Malaysia Kuala Lumpur, Jalan Semarak, 54100 Kuala Lumpur, Malaysia
ndayamada@yahoo.co.jp

[4] National Defense Academy
1-10-20 Hashirhimizu, Yokosuka, Japan
naobumi@nda.ac.jp

Abstract **─** Design and performance of a shaped beam 12.2 GHz array-fed reflector antenna for broadcasting satellite is presented in this paper. Initial design, employing a cluster of feed horns illuminating a parabolic reflector is initially proposed for multi beam antenna (MBA) system to produce a contoured beam for Peninsular Malaysia. The precise feed positions are determined through a newly developed ray tracing program. Due to the small size of the coverage area, an issue with regards to physical constructability of the feed horns is raised. The MBA is modified by utilizing 18-element microstrip array as the feed, where each element positions are calculated by using the same caustic model. In this case, the preceding issue is solved, and high gain shaped beam coverage with uniform aperture is generated. This paper shows the results of the contoured beam antenna that have been achieved for beam scanned over a coverage size of approximately 0.9° long and 0.5° wide. Small variation of radiation level, which is less than 3dB within the edge of coverage (EOC), is also demonstrated in the performance analysis.

Index Terms **─** Antenna feeds, arrays, caustic model, ray tracing, reflector, satellite antenna.

I. INTRODUCTION

Reflector technologies have experienced many significant developments in the recent years. However, as satellite requirements become more stringent, the needs for shaped or contoured beam have rapidly increased. Contoured beam antennas have been used for various applications, such as high-speed internet access, broadcasting and military communication. In broadcasting satellite scenario, the needs for more compact and economical earth stations on user terminals have increased the power and bandwidth requirements of satellite [1]. Due to the demands for high quality of services, antennas with narrow beamwidth are requested. Narrow-beam antenna becomes desirable due to its ability to support high data rates while maintaining low satellite power. However, one spot beam can only support small coverage area on the earth [2]; thus, an approach to generate larger satellite footprint is requested. To guarantee constant high-gain signal availability to the coverage area, fine contoured beams shall be accurately designed.

Designing contoured beams involves reflector shaping and combination of multiple beams [3]. Reflector shaping technique can be performed by designing correct reflector curvature. Meanwhile, in the case of MBA, an array of feeds can be arranged to simultaneously generate multiple beams to form the desired contours. Through multi beams technique, higher gain and wider coverage are achieved at the same time. This MBA concept has been widely used by spacecraft manufacturers and researchers [3-9].

Submitted On: November 4, 2014
Accepted On: July 14, 2015

1054-4887

Many studies have been conducted to determine the optimum feed positions of the reflector. One of them is through optimization of radiation pattern in physical optic (PO)-based tool [10]. However, in that case, the relation of feed locations and beam direction was not clarified. Some researchers have introduced the theoretical concept of caustics on parabolic surfaces. As a fundamental research, caustic surface equations at focal region for plane waves were derived in two planes [11]. In that literature, the equal-path-length model was demonstrated to express the rays. The focusing ability was defined based on the physical extent of the focal spots. The concept of determining focal surfaces based on caustic data has been employed in [12]. Here, an analytical program was developed to determine the best focal spot. In the program, all incoming rays to a reflector surface, scanned in elevation (EL) and azimuth (AZ) plane were observed. As a result, the best focal spots were shown in two-dimensional; however the important feed position data such as the caustic dependency on focal-length-to-diameter ratio (*F/D*) and the locus equation were not clarified.

Recently, a parametric study on obtaining the best focal point based on minimizing phase aberrations has been carried out [13]. For that particular study, a program is developed to analyze the phase errors when the beam is scanned to different target points. Comparisons with previous approaches have been made. However, the observations were for limited cases of *F/D*. Furthermore, similarly, the significant changes of caustic with respect to *F/D* were not explained by locus equations or curves. Optimum feed position is represented by maximum scan-gain contour in [14]. It was concluded that small *F/D* values tend to have a maximum scan-gain contour closer to Petzval surface. However, this study was performed for small *F/D* only, and not for *F/D*>1, which is more preferable for satellite MBA. In reflector antenna, the *F/D* is a crucial parameter [15]. Due to its importance, authors have developed a ray tracing program in MATLAB to calculate the optimum feed position of a parabolic for various *F/D* [16,17]. In the tool, a precise caustic model with an accurate caustic locus equation has been developed. The locus equation allows fast calculation of feed positioning, and is used to design a contoured beam for Peninsular Malaysia.

In this paper, two reflector feed designs are proposed. The initial design consists of a cluster of feed horns. However, due to some issues, an 18-element microstrip array is designed as a replacement. The design procedures are presented and discussed in detail in the next segment.

II. CONTOURED BEAM FOR PENINSULAR MALAYSIA COVERAGE

Figure 1 demonstrates the Malaysia region as viewed from satellite, which consists of two beams, B_1 and B_2 representing west and east part of the country respectively. In this paper, only the case of the west region, known as Peninsular Malaysia (B_1) is observed. To produce precise beam shape, B_1 shall consist of multiple smaller beams. In preliminary design, two spot beams denoted as B_{11} and B_{12} are used to construct B_1.

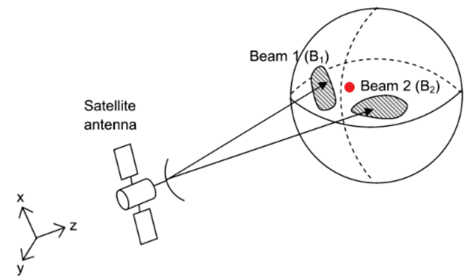

Fig. 1. Illustration of Malaysia beam from satellite point-of-view.

A. MBA concept

In designing the antenna system for B_1, several conditions are assumed. Figure 2 shows the application of multi beam technique to produce contoured beam for B_1, as viewed from 91.5°E orbital slot. The antenna field of view is centred at O. As Peninsular Malaysia is considered as geographically small, thus B_1 is designed to only comprise of two spot beams B_{11} and B_{12}, each having a narrow beamwidth, θ_{3dB}=0.5°.

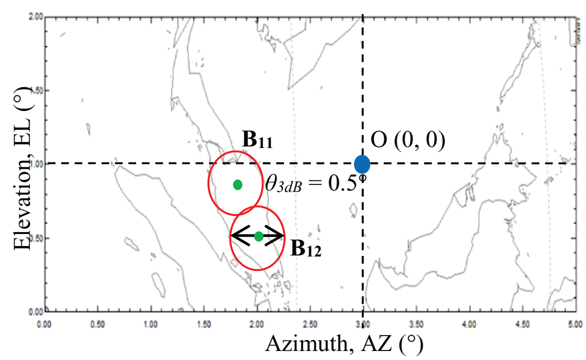

Fig. 2. Application of multi-beam technique for Peninsular Malaysia region by utilizing cluster feeds.

B. MBA design parameters

This section describes various parameters that influence the performance of the parabolic antenna.

Antenna diameter, *D*

D is chosen based on the θ_{3dB} and sidelobe level (SLL) requirements. In practice, trade-off between antenna directivity and θ_{3dB} to the SLL is a major consideration to antenna designers to yield high aperture efficiency [18]. Thus, characteristics of tapered distribution shall be taken into account. *D* is estimated as follows [19]:

$$D = (1.2 \pm 0.2 rads)\frac{\lambda}{\theta_{3dB}(rads)}. \quad (1)$$

The constant value reflects the aperture distribution, where 1 represents a uniform aperture with unity efficiency and high directivity. To reduce the SLL and by taking into account the trade-off, the value of 1.1 rads is chosen, and the D is calculated as 126λ or 3 m.

Focal-length-to-diameter ratio, *F/D*

F/D is a crucial parameter because it has strong effect on the achievable aperture and spillover efficiency. In designing satellite MBA, large *F/D* usually gives better scan performance [15]. For small F/D, especially in the case of *F/D*<0.5, the scan performance deteriorates and the caustic data used to determine feed position are less accurate. The behavior of caustic and its focusing ability for various *F/D* values have been studied in [17]. In this paper, the parameter *F/*D is set to 1.5 for better scanning performance, especially in the satellite application [8,10].

Design of radiating elements

Due to its good performance and simplicity, pyramidal horns are chosen as the feeds. Based on the single feed per beam concept, two feed horns of similar dimensions are employed to produce B_{11} and B_{12} simultaneously. The horn aperture size depends on the *F/D*. The data of how the increase of *F/D* relates to the raise in optimum horn dimension is shown in [15]. To estimate the horn size, the tilt angle between the horn to the reflector rim, θ_m is given as follows [18]:

$$\theta_m = 2\tan^{-1}\left(\frac{D}{4F}\right). \quad (2)$$

For *F/D* = 1.5, the θ_m is approximately 19°. The main concern in the horn design is to obtain radiation of at least -10 dB down at the reflector rim. This is to allow efficient illumination of reflector surface. After few adjustments and verifications using EM tool, the full dimensions of the feed horn, as illustrated in Fig. 3 is obtained as follows: *hh* = 54 mm, *hw* = 70 mm, *hl* = 63 mm, *wh* = 12 mm and *ww* = 37 mm.

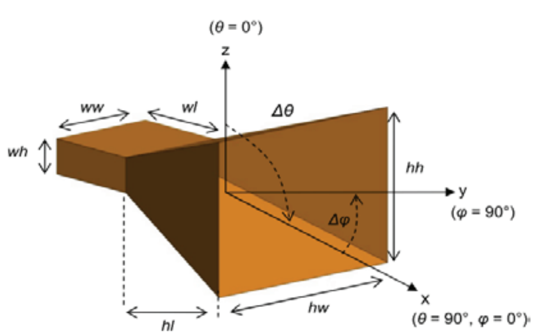

Fig. 3. Dimension of feed horn.

III. DETERMINATTION OF FEED POSITIONS

Beam deviation factor (BDF) concept has been widely used to demonstrate the dependency of feed position on *F/D* [20]. This model is very convenient to determine the optimum feed position based on the aperture-phase aberration for antennas with arbitral *F/D* value. However, there are some constraints. Due to the study model of deriving the expression, this method demonstrates the shifted beam θ_{B1} for one-dimensional lateral feed displacement F_1 only, as shown in Fig. 4. In designing MBA for B_1, the ray tracing program, together with a derived caustic locus is used.

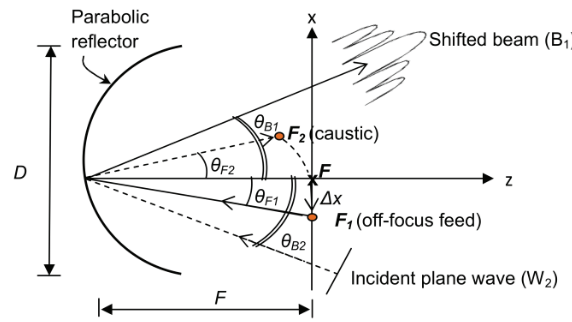

Fig. 4. Relationship of feed positions (F_1, F_2) and angles of radiated beams (θ_{B1}, θ_{B2}).

In the ray tracing model, the caustic point F_2 formed by the incoming wave from θ_{B2} is measured. The caustic movement in x and z component for various values of incident wave directions, $-\theta_{in}$ = 0° to 15° is demonstrated as shown in Fig. 5. Large θ_{in} are chosen at this stage to analyze the common behavior of the caustics and to observe the trajectory. D of 3 m is used and by considering the broadcasting satellite application, f = 12.2 GHz is selected. The results are compared to the approximate equation of caustic locus below, where $S(x, z)$ indicates the distance from the centre of reflector to the caustic point:

$$S(x,z) = F\cos\theta_{in}. \quad (3)$$

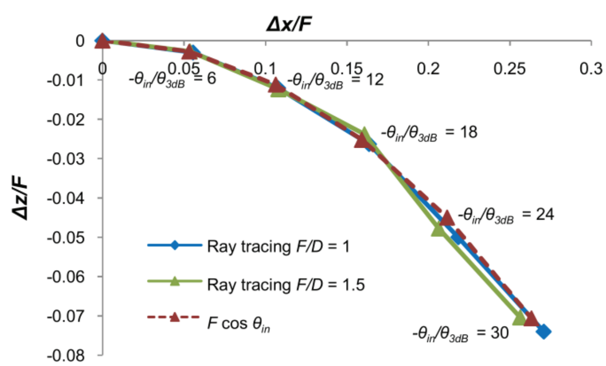

Fig. 5. Two-dimensional caustic positions.

From the good agreements of all curves, it is clarified that the optimum feed positions can be determined by equation (3). The feed positions of the MBA system can thus be calculated by using this method. It seems that higher accuracy is obtained at lower θ_{in}; thus, the application of ray tracing technique for designing contoured beam of Peninsular Malaysia is appropriate.

IV. EM COMPUTATIONS AND RADIATION CHARACTERISTICS OF MBA

The arrangement of the MBA in FEKO is shown in Fig. 6. The optimum positions for the feed horn of B_{11} and B_{12} are determined from equation (3). In the calculation, the incident beam directions θ_{in} are associated with the AZ (θ) and EL (φ) components. For B_{11} beam, the θ_{in} is (-1°, -0.6°), meanwhile for the B_{12} beam, the θ_{in} is (-1.16°, -0.17°). Both beams are very small in size; thus, the calculated caustics are very close to each other. This scenario has caused the horn apertures to be overlapped.

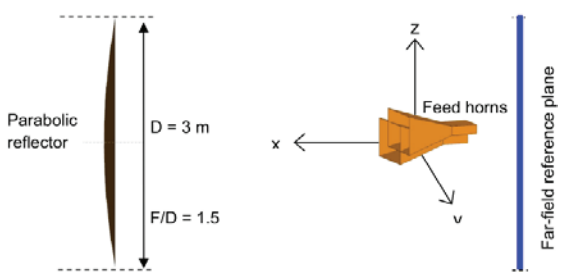

Fig. 6. A parabolic and two overlapped feed horns.

V. MICROSTRIP ARRAY FEED FOR CONTOURED BEAM OF PENINSULAR MALAYSIA

Due to the non-constructible structure, the overlapped feed horns shall be replaced with a physically realizable solution. One of the solutions is to use a microstrip array antenna. The first step is to compute the beam size of the whole B_1 region, denoted as θ_W and θ_L respectively in Fig. 7. Point 1 to 4 represents the min-max reference point.

Prior to designing the array feed, an on-focus square patch is first designed on a substrate having ε_r = 2.6, thickness h = 1.2 mm and tan δ = 0.0018. The single element size is 0.3λ in both sides. After a few adjustments, -11 dB return loss with almost 50 Ω impedance and a very good gain performance of 5.5 dBi is obtained at 12.2 GHz. The single patch element has wide beamwidth of θ_{3dB} = 100° for both E-plane and H-plane. In the case of array feed, the beamwidth of a single element patch does not play an important role, as the actual θ_{3dB} is determined through total number of elements on the array structure radiating on a single parabolic reflector. Thus, the single element design is then be duplicated to represent all four beam points on the required area. The positions of each feed elements are computed via ray tracing and translated into FEKO.

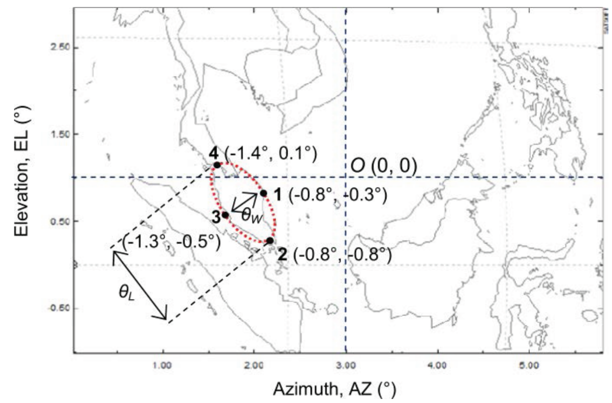

Fig. 7. Illustration showing the beam coverage for B_1 region with the -3 dB EOC points.

The calculated positions of all 4 beam points and the associated feeds, arranged together with 14 additional elements within the desired boundary are illustrated in Fig. 8. The figure also illustrates the overlapped horn areas that have been replaced by array elements. The randomly-distributed extra elements are added to ensure a good performance of the array system, particularly to achieve the desired beamwidth with uniform radiation gain (-3 dB) across the EOC.

All elements are assigned to various amplitude excitations A_i values from 0.3 to 1V to get uniform contour throughout EOC. Far-field simulation is performed based on the MoM-PO method, which is the integration of two techniques; method of moment (MoM) for microstrip array structure and physical optic (PO) for parabolic reflector. In this case, the dimension of the parabolic reflector is considered as electrically large, which is about 122λ; therefore, simulation of the parabolic reflector alone by using MoM involves a lot of memory usage and computation time. The simulation parameters are shown in Table 1.

Figure 9 shows the normalized contoured beam coverage for B_1, with four test points representing the maximum extent of the beam area, having -3 dB deviations from G_{max}. To ensure the correct beam size, the coordinates of all test points are compared with the actual peninsular beam. Table 2 presents the expected and the measured data taken at EOC. All measured EOC points match with the required test points, with the maximum deviation is around 0.05° only. Therefore, from these sets of results it can be concluded that a uniform contoured beam can be designed by the ray tracing method, regardless through the usage of horn arrays or multi-element microstrip as the feeds.

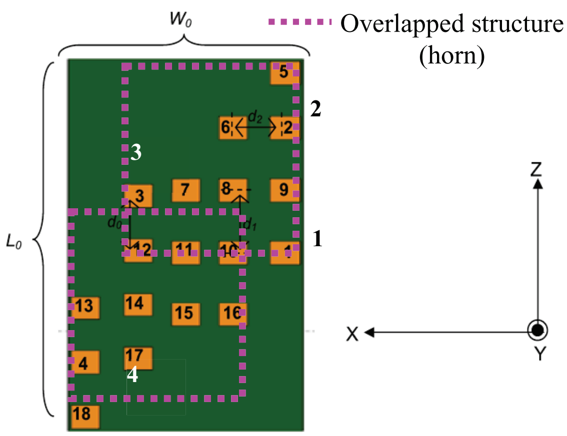

Fig. 8. Design concept of the microstrip array feed for Peninsular Malaysia and illustration of overlapped horn structure with the corresponding beam points.

Table 1: Simulation parameters

Items	Parameters	Details
Computer	Memory (RAM) Clock time	96 GB 1.8 GHz
Reflector	Mesh size	λ/2 (12.3 mm)
Array feed	Mesh size	λ/20 (1.23 mm)
Calculation process	Simulation memory Simulation time	59.43 GB 73.53 hours

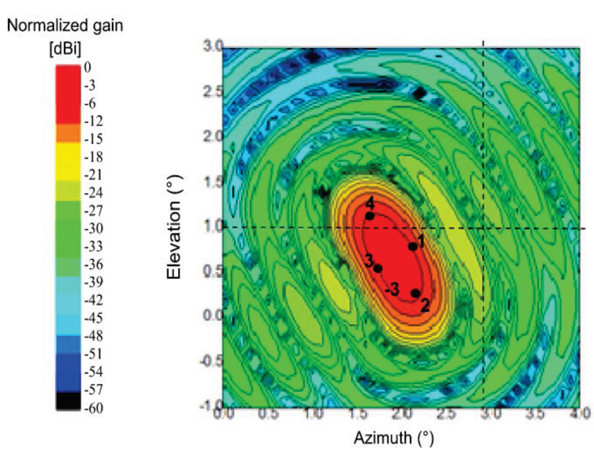

Fig. 9. Two-dimensional contoured beam for Peninsular Malaysia.

Table 2: Comparison of EOC data between calculated and obtained results

Beam Points	Required (°)	Obtained (°)
1	-0.80, -0.30	-0.81, -0.25
2	-0.80, -0.80	-0.81, -0.82
3	-1.3, -0.50	-1.3, -0.53
4	-1.4, 0.1	-1.4, 0.12

VI. EXCITATION COEFFICIENTS OF FEEDS

The displacement of feed from the focal plane introduces non-linear phase variation called phase error, which can cause gain loss, beamwidth changes and pattern distortion [15]. In designing contoured beam, the estimation of amplitude excitation A_i at the feeds is important in obtaining uniform amplitude distribution at the reflector beam. By controlling the A_i, the gain can be adjusted so that the associated power will be transmitted without any interruption. In the array feed for B_1, as shown in Fig. 10, all elements located at the edges of the structure are assigned at 1V. Meanwhile, to achieve broader beam and to reduce gain variation along EOC, the middle and adjacent elements are excited at 0.3V and 0.8V. This arrangement results in almost uniform amplitude distribution over the region.

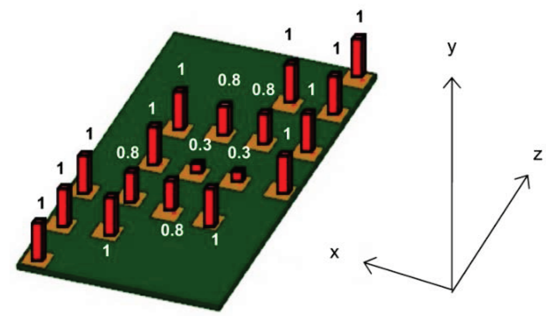

Fig. 10. Arrangement of radiating elements with the corresponding input A_i for B_1 beam.

Figure 11 demonstrates the distributions of magnetic field density for the antenna, which is useful to examine the behavior of induced currents at each element. Figure 12 shows the numerical data of the output H-field intensity. Theoretically, the induced current at each element is proportional to the input A_i. Based on the comparison between these two data, the correct relation is achieved.

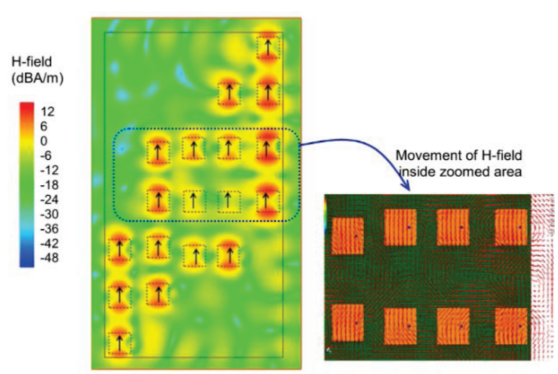

Fig. 11. Magnetic field distributions on the microstrip surface for B_1 beam.

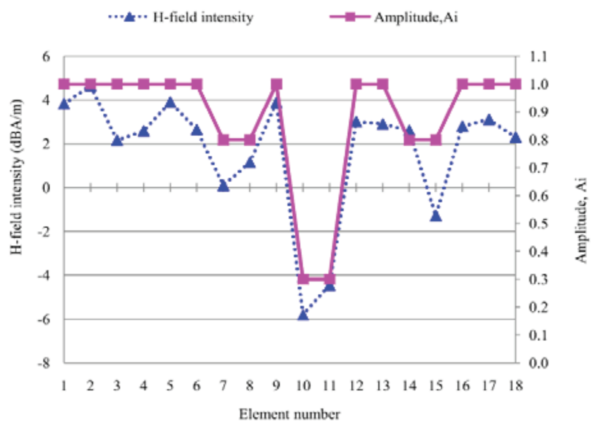

Fig. 12. Comparison between H-field intensity and input A_i for B_1 beam.

VII. CONCLUSION

A Ku-band satellite-mount antenna system to produce contoured beam coverage for Peninsular Malaysia is designed. Justifications and design equations of antenna parameters are shown. A design issue with regards to physical configuration of the initial feed horn design is discussed and an alternative solution is presented. Final antenna system, which consists of a single parabolic reflector, and a radiating feed that comprises of 18-element microstrip patch array are simulated and analyzed. The accuracy of the ray tracing method, developed to determine the precise positions of the feed elements are clarified in this paper through 3D EM solver. Uniform aperture distribution with less than -3 dB EOC gain variation and accurate beam shape with maximum angular deviation of 0.05° over the Peninsular Malaysia is obtained.

ACKNOWLEDGMENT

Authors would like to thank Ministry of Education Malaysia and Universiti Teknologi MARA for continuous support towards this research project.

REFERENCES

[1] Malaysian Communications and Multimedia Commission, Satellite Industry Developments, Cyberjaya, 2008.

[2] J. R. Wertz and W. J. Larson, *Space Mission Analysis and Design*, 3rd edition, Microcosm, California, 1992.

[3] C. C. Chen and C. F. Franklin, "Ku-band multiple-beam antenna," *NASA Contract Report 154364*, NASA Langley Research Center, 1980.

[4] E. R. Boudriau, "Multiple-beam antennas for military satellite communications systems," *DREO Technical Note 95-1*, Defense Research Establishment, Ottawa, 1995.

[5] M. Naderi and S. Campanella, "NASA's advanced communications technology satellite (ACTS) - An overview of the satellite, the network, and the underlying technologies," *AAIA 12th International Communication Satellite Systems Conference*, pp. 204-224, 1988.

[6] A. Howell and D. Greenwood, "Antennas for Inmarsat III and beyond," *IEE Colloquium on Satellite Antenna Technology in the 21st Century*, pp. 4/1-4/6, 1991.

[7] R. Jorgensen, P. Balling, and W. J. English, "Dual offset reflector multibeam antenna for international communications satellite applications," *IEEE Transactions on Antennas and Propag*ation, vol. AP-33, no. 12, pp. 1304-1312, 1985.

[8] M. Schneider, C. Hartwanger, and H. Wolf, "Antennas for multiple spot beam satellites," *CEAS Space Journal*, vol. 2, no. 1-4, pp. 59-66, 2011.

[9] N. J. G. Fonseca and J. Sombrin, "Multi-beam reflector antenna system combining beam hopping and size reduction of effectively used spots," *IEEE Antennas and Propagation Magazine*, vol. 54, no. 2, pp. 88-99, 2012.

[10] M. Mahajan, R. Jyoti, K. Sood, and S. B. Sharma, "A method of generating simultaneous contoured and pencil beams from single shaped reflector antenna," *IEEE Transactions on Antennas and Propagation*, vol. 61, no. 10, pp. 5297-5301, 2013.

[11] R. E. Collin and F. J. Zucker, *Antenna Theory: Part 2*, McGraw-Hill, New York, 1969.

[12] C. J. Sletten, *Reflector and Lens Antennas*, Artech House, Massachusetts, 1988.

[13] A. Garcia-Pino, N. Llombart, B. Gonzalez-Valdes, and O. Rubinos-Lopez, "A bifocal ellipsoidal Gregorian reflector system for THz imaging applications," *IEEE Transactions on Antennas and Propagation*, vol. 60, no. 9, pp. 4119-4129, 2012.

[14] W. V. T. Rusch and A. C. Ludwig, "Determination of the maximum scan-gain contours of a beam-scanning paraboloid and their relation to the Petzval surface," *IEEE Transactions on Antennas and Propagation*, vol. AP-21, no. 2, pp. 141-147, 1973.

[15] C. A. Balanis, *Antenna Theory: Analysis and Design*, 3rd edition, John Wiley & Sons Inc., New Jersey, 2005.

[16] N. H. Abd Rahman, M. T. Islam, N. Misran, Y. Yamada, and N. Michishita, "Design of a satellite antenna for Malaysia beams by ray tracing method," *International Symposium on Antennas and Propagation*, pp. 1385-1388, 2012.

[17] N. H. Abd Rahman, M. T. Islam, N. Misran, Y. Yamada, and N. Michishita, "Evaluation of caustics for parabolic reflector antennas through focal region ray tracings," *International Conference*

on Signal Processing and Communication Systems, pp. 1-4, 2013.
[18] W. L. Stutzman and G. A. Thiele, *Antenna Theory and Design*, 2nd edition, John Wiley & Sons, New York, 1988.
[19] S. Silver, *Microwave Antenna Theory and Design*, McGraw-Hill, New York, 1986.
[20] Y. T. Lo, "On the beam deviation factor of a parabolic reflector," *IRE Transactions on Antennas and Propagation*, vol. 8, no. 3, pp. 347-349, 1960.

Nurul Huda Abd Rahman received her M. Eng. in Electronic from the University of Surrey, United Kingdom in 2008 and a Ph.D. in Electric, Electronic and Systems Engineering from the Universiti Kebangsaan Malaysia in 2014. In August 2008, she joined Astronautic Technology (M) Sdn. Bhd. (known as ATSB®) as a Radio Frequency Engineer. At ATSB®, she was involved in various small-class satellite development projects and R&D for satellite X-band transmission system. She also was involved in a mission definition study for national communication satellite project. She has wide experiences in designing RF and communication modules. In 2014, she was appointed as a Lecturer in Universiti Teknologi MARA Malaysia (UiTM). Her current research interests include antennas for space and terrestrial applications, array antennas, reflector and lens antennas, RF and microwave design and electromagnetic analysis.

Mohammad Tariqul Islam is a Professor at the Department of Electrical, Electronic and Systems Engineering of the Universiti Kebangsaan Malaysia (UKM). He is also the Group Leader of Radio Astronomy Informatics Group at UKM. Prior to joining UKM, he was a Lecturer in Multimedia University, Malaysia. He is a Senior Member of the IEEE, regular Member of Applied Computational Electromagnetic Society (ACES) and serving as the Editor-in-Chief of the International Journal of Electronics & Informatics (IJEI). Tariqul has been very promising as a researcher, with the achievement of several International Gold Medal awards. Over the years, he has carried out research in the areas of antenna design, radio astronomy antennas, satellite antennas, and electromagnetic analysis. His publications include over 160 research journal papers, nearly 150 conference papers, and few book chapters on various topics related to antennas, microwaves and electromagnetic analysis with 8 inventory patents filed. So far, his publications have been cited 1578 times, and the H-index is 24 (Source: Scopus). For his contributions, he has been awarded "Best Researcher Award" in 2010 and 2011 at UKM. He is now managing many research projects from the Ministry of Science, Technology and Innovation, Ministry of Education Malaysia and some International research grants from Japan.

Yoshihide Yamada graduated from the Nagoya Institute of Technology and received the B.S. and M.S. degrees in Electronics in 1971 and 1973, respectively. He received the D.E. degree from the Tokyo Institute of Technology in 1989. In 1973, he joined the Electrical Communication Laboratories of the Nippon Telegraph and Telephone Corporation (NTT). Until 1984, he was engaged in research and development related to reflector antennas for terrestrial and satellite communications. Beginning in 1985, he engaged in R&D for base station antennas for mobile radio systems. In 1993, he moved to the NTT Mobile Communications Network Inc. (NTT DoCoMo). In 1995, he was temporarily transferred to the YRP Mobile Telecommunications Key Technology Research Laboratories Co., Ltd. At the same time, he was a Guest Professor at the Cooperative Research Centre of Niigata University, and a Lecturer at the Science University of Tokyo, both in 1996 to 1997. In 1998, he took a position as a Professor at the National Defense Academy. In 2014, he starts working as a Professor at Malaysia-Japan International Institute of Technology (MJIIT) of Universiti Teknologi Malaysia Kuala Lumpur. He is interested in very small RFID antennas, shaped dielectric lens antennas, and electromagnetic simulations of large objects. He is a Member of the IEICE and JSST of Japan and an IEEE Society Member of AP, VT, and COMM.

Naobumi Michishita received the B.E., M.E., and D.E. degrees in Electrical and Computer Engineering from Yokohama National University in 1999, 2001, and 2004, respectively. He joined the Department of Electrical and Electronic Engineering, National Defense Academy, as a Research Associate in 2004 and in 2014 holds the Associate Professor title. He was a Visiting Scholar at the University of California, Los Angeles from 2006 to 2007. He received the Young Engineer Award from the IEEE AP-S Japan Chapter and IEICE in 2004 and 2005, respectively. His current research interests include metamaterial antennas and electromagnetic analysis. He is a member of IEEE.

Enhancement of Scan Angle Using a Rotman Lens Feeding Network for a Conformal Array Antenna Configuration

A. Mahmoodi and A. Pirhadi

Faculty of Electrical and Computer Engineering
University of Shahid Beheshti G.C. (SBU), Tehran, +98, Iran
ami.mahmoodi@mail.sbu.ac.ir, a_pirhadi@sbu.ac.ir

Abstract **─** An antenna with a wide scan angle in a wide frequency band is obtained by feeding a conformal arc array with a modified formulation of Rotman lens design. In this paper, two kinds of Rotman lenses are designed to feed a linear array and a conformal array and their scan angles are compared in a specified frequency band. The phase distributions of the linear array elements are linear in all scan angles, but these phase distributions are nonlinear in the conformal array. Therefore in order to design a Rotman lens for conformal arrays, the conventional Rotman lens design formulations must be modified. For this purpose, first the phase distributions of conformal array elements were obtained using the particle swarm optimization (PSO) process. Then by modifying the conventional Rotman Lens design formulations used for linear arrays, appropriate formulations for conformal arrays are obtained. In the end, by selecting two specified linear and conformal arrays with equal number of elements, their maximum scan angles in a specified frequency band are studied. It is shown that in the same frequency band the maximum scan angle increases about 20% in the Rotman Lens fed conformal array antenna.

Index Term **─** Conformal array, PSO, Rotman lens.

I. INTRODUCTION

Using an appropriate beam forming network that can feed array antennas has several applications in radar and satellite communication systems. The main problem of usual beam forming networks is their small bandwidth which causes the locations of radiation beams of the array to vary with frequency. Rotman lens [1] is a wideband feed network that relies on path lengths and is designed based on a true time delay (TTD) response. Using the TTD scheme to feed array antennas prevents the dependence of scanning angles on frequency [2]. To have different scan angles, the Rotman lens should provide linear phase distributions with different slopes, along equi-spaced linear array antenna elements which are independent from frequency. Up to now, many types of Rotman lenses have been designed, constructed and modified with various applications in microwave and millimeter-wave frequency bands [1,3]. Also, various works in Rotman lens design have been done with the goals of low phase error [4] and low insertion loss [5].

There is an increasing demand for conformal arrays in modern systems and that is due to their ability in being mounted on surfaces with different shapes. This causes the aerodynamic drag to reduce considerably and the structures get less visible to the human eye. Another important advantage of conformal arrays which is of vital importance in radar applications is their wide angle coverage. Other benefits include space saving, potential increase in the available aperture, reduction of radar cross-section (RCS), elimination of radome-included bore-sight error, etc. [6].

In this study, an increase in the maximum scan angle is obtained from a conformal array that is fed by a Rotman lens. To this purpose, in the first step, the design formulations of a trifocal Rotman lens [7] which is used to feed linear arrays are modified to feed the conformal array. Next, in order to compare the maximum scan angles, two linear and conformal arrays fed by their corresponding Rotman lenses are examined. Also, to obtain the phase distribution of the conformal array antenna at different scan angles, the PSO procedure has been used.

In Section II, the modified formulations of Rotman lens for conformal array antennas are presented. In Section III, the optimum phase distributions for the modified Rotman lens formulations are obtained based on the PSO method. Finally in Section IV, the designed Rotman lenses are simulated with the EM full wave-simulation software (HFSS) and the simulation results of the linear and conformal arrays are compared. It must be noticed in the mentioned procedures the modified formulations of input and output curvatures of Rotman lens are obtained by suitable code in Matlab software. Then the obtained shapes are imported to the EM full wave simulator HFSS to simulate electromagnetic characteristics of Rotman lens.

Submitted On: October 14, 2014
Accepted On: July 12, 2015

II. ROTMAN LENS FORMULATIONS BASED ON ARRAY ANTENNA CONFIGURATIONS

Different design methods have been reported for Rotman lenses used for linear arrays [1,4,8]. These methods include the trifocal method, quadrufocal method and non-focal method of which the trifocal method is the most frequently used one. Based on the conventional trifocal lens principles, some trifocal Rotman lens formulations have been developed to obtain the desired phase distributions for linear array antennas [7,9,10]. In this section, these formulations are developed such that they can be used for conformal array antennas.

A. Modified Rotman lens formulations for feeding conformal array antennas

Figure 1 represents a general structure of a Rotman lens to feed a conformal array. Curve E represents the desired configuration of the conformal array antenna.

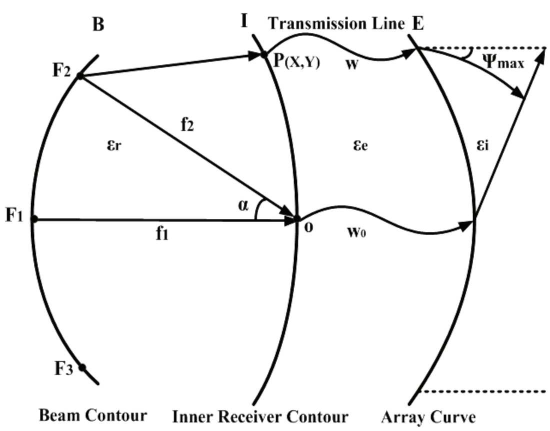

Fig. 1. Trifocal Rotman lens structure for conformal arrays.

The conventional trifocal Rotman lens for linear arrays produces linear phase distributions for linear array elements. For conformal array antennas, Rotman lens formulations must be modified to produce suitable phase distributions which depend on the configuration of the array antenna. An important point that must be noticed in the new design formulations is determining the required phase distributions to create a set of three design equations. This is done by using a procedure similar to the one used in [1]. Based on the design procedure in [1], the modified formulations for Rotman lens design are presented in Eqs. (1a-c). In these equations, $l\varphi_0$ produces the required phase distribution of the conformal array for zero scan angle and similarly $l\varphi_0 \pm l\varphi_1$ create the suitable phase distributions of conformal array to produce the radiation pattern with maximum scan angles, $\pm\Psi_\alpha$, respectively. The optimization procedure to determine these phase distributions are presented in the next section;

$$F_2P\sqrt{\epsilon_r} + W\sqrt{\epsilon_e} + (l\varphi_0 + l\varphi_1) = f_2\sqrt{\epsilon_r} + W_0\sqrt{\epsilon_e}, \quad (1a)$$

$$F_3P\sqrt{\epsilon_r} + W\sqrt{\epsilon_e} + (l\varphi_0 - l\varphi_1) = f_2\sqrt{\epsilon_r} + W_0\sqrt{\epsilon_e}, \quad (1b)$$

$$F_1P\sqrt{\epsilon_r} + W\sqrt{\epsilon_e} + l\varphi_0 = f_1\sqrt{\epsilon_r} + W_0\sqrt{\epsilon_e}, \quad (1c)$$

where F_iP is the physical distance between points F_i and P. Also, $l\varphi_{0,1} = \varphi_{0,1} \times (\lambda_g/2\pi)$ and λ_g is the wavelength.

Normalizing Eqs. (1a-c) by the electrical length of the central focal length, $\sqrt{\epsilon_r} f_1$, results in:

$$\frac{F_2P}{f_1} = \beta - \omega - a - b, \quad (2a)$$

$$\frac{F_3P}{f_1} = \beta - \omega + a - b, \quad (2b)$$

$$\frac{F_1P}{f_1} = 1 - \omega - b, \quad (2c)$$

where

$$\beta = \frac{f_2}{f_1},\ a = \frac{\varphi_1}{f_1},\ b = \frac{\varphi_0}{f_1} \text{ and } \omega = \frac{W - W_0}{f_1}.$$

Based on the geometrical configuration of Rotman lens (Fig. 1),

$$F_2P^2 = (-f_2\cos\alpha - X)^2 + (-f_2\sin\alpha + Y)^2 = f_2^2 + X^2 + Y^2 + 2f_2X\cos\alpha - 2f_2Y\sin\alpha, \quad (3a)$$

$$F_3P^2 = (-f_2\cos\alpha - X)^2 + (-f_2\sin\alpha - Y)^2 = f_2^2 + X^2 + Y^2 + 2f_2X\cos\alpha + 2f_2Y\sin\alpha, \quad (3b)$$

$$F_1P^2 = (f_1 + X)^2 + Y^2. \quad (3c)$$

After normalizing Eqs. (3a), (3b) and (3c) by f_1^2 and equating them with the square of Eqs. (2a), (2b) and (2c) respectively, the set of three goal equations is obtained. By solving these three equations, the positions of the X and Y coordinates of the phase centers of array ports and transmission line lengths (W_i) are obtained. This method can be used for any practical array curves including linear arrays. For conventional linear array configurations the expressions $l\varphi_0$ and $l\varphi_0 + l\varphi_1$ are replaced by zero and $\pm Y_3\sqrt{\epsilon_i}\sin(\psi_a)$ respectively, in which Ψ_α is the maximum scan angle of the array. But in this paper, we use the modified phase distributions for both linear and conformal arrays. In the next section, the optimization procedures to obtain the phase distributions for a linear array and a specified conformal array are explained.

III. OPTIMUM PHASE AND AMPLITUDE DISTRIBUTIONS OF THE CONFORMAL AND LINEAR ARRAYS

To obtain the required phase distributions of φ_1 and φ_0 in Rotman lens design formulations, at first the configuration of the conformal array and its radiating elements, must be determined. Therefore, antenna elements and array configurations are discussed in the following sections.

A. Conformal and linear array configurations and their radiation elements

Because of the wide operating frequency band in this study (10-14 GHz), double ridged horn antennas are used as the radiating elements of the array antennas. As shown in the Fig. 2, radiation characteristics of this antenna are almost constant and VSWR<2 in the operating frequency band.

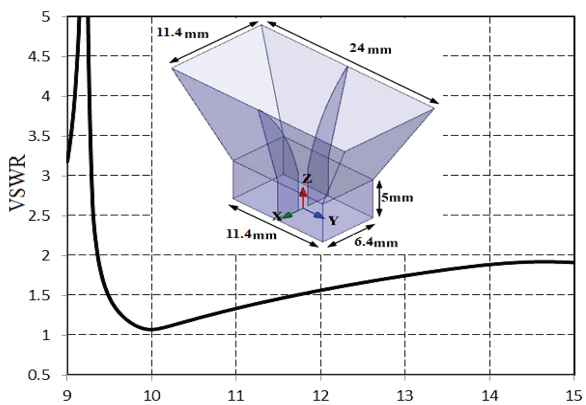

(a)

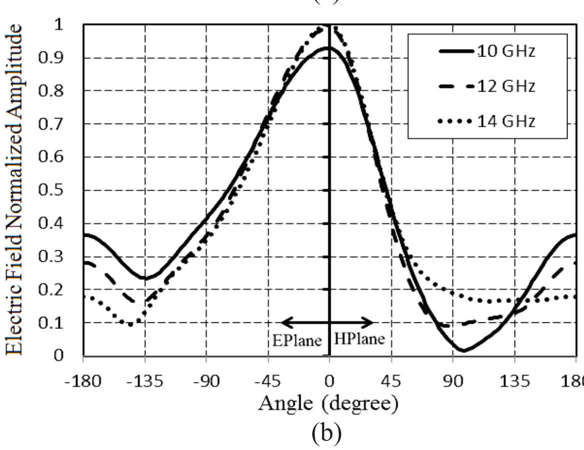

(b)

Fig. 2. Radiation characteristics of double ridged horn antenna: (a) VSWR, (b) normalized amplitude of electric field radiation patterns, E and H-plane.

Two configurations of array antennas including the linear array and the conformal arc array are synthesized in this study. To have a precise comparison of the radiation patterns of the synthesized arrays, we use equal number of elements with equal element spacing for both of these arrays. The main problem of the array designs with wide scan angles is the existence of grating lobes, so the array elements are placed as close as possible to each other. Figure 3 (a) shows a linear array of 16 double ridged horn antennas. The conformal array can be formed on any desired curves. Without loss of generality in this paper, the conformal array elements stand on a quarter of a circle. Figure 3 (b) shows the conformal array configuration ($\gamma=45^0$).

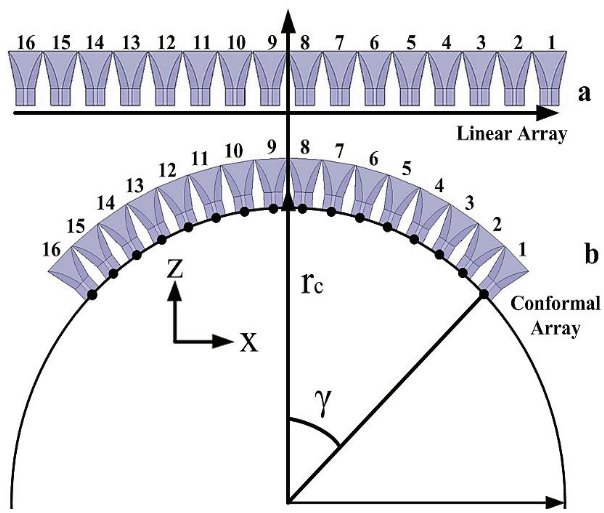

Fig. 3. Array antenna configurations of double ridged horn antennas: (a) linear array, (b) arc curve conformal array ($\gamma=45^0$).

Since one of the most important parameters in a finite array is the coupling between array elements, in the next section active element radiation patterns [11] of the arrays are used in the synthesis process of the array antennas.

B. Synthesis of linear and conformal arrays using the PSO algorithm

In this section, the PSO algorithm is used to obtain the optimum phase and amplitude distributions for linear and conformal array elements. The phase distributions are used to construct the Rotman lens design formulations and the amplitude distributions are used to design of the Rotman lens ports. To this end, the phases and amplitudes of the array elements are used to produce the particles of the PSO algorithm. The particles move in a multidimensional search space so that every particle adjusts its position with respect to its adjacent particles while considering their prior experience. In general, the velocity and position of each particle, p_k, is expressed as follows [12]:

$$\bar{v}_k(t) = \bar{v}_k(t-1) + c_1 r_1[\bar{P}_k(t-1) - \bar{x}(t-1)] + c_2 r_2[\bar{G}_k(t-1) - \bar{x}(t-1)] \quad (4)$$
$$\bar{x}(t) = \bar{x}(t-1) + \bar{v}_k(t).$$

In Eq. (4), $\bar{x}$ and $\bar{v}$ represent the position and the velocity of particles respectively. The positive constants c_1 and c_2 are usually equal, $c_1 = c_2 = 2$. r_1 and r_2 are two random values in the range (0,1). The best previous position of k_{th} particle (coefficient) is presented as $\bar{P}_k(t-1)$ and $\bar{G}_k(t-1)$ denotes the best k_{th} particle in the population. Equation (4) is used to update the velocity and position of the coefficients as a function of their previous velocity and positions, then the coefficients move towards a new position. In each update the phases and amplitudes of the array elements are replaced with new ones and the obtained radiation pattern is compared with the desired radiation pattern. To this purpose, the error function or the fitness function is defined as the absolute difference between the target and calculated patterns of the array.

The optimization process is continued until the error function converges to the acceptable value. Figure 4 shows the desired radiation patterns in broadside and the maximum scan angle of -65^0. The fitness function used in the PSO procedure is defined as:

$$\text{Fitness function} = \sum_{i=1}^{5} W_i \sum_{\theta=\theta_{i-1}}^{\theta_i} |F_o - F_d|,$$

F_d is the desired goal radiation pattern and F_N is the normalized calculated complex array factor. Also, $F_N(\theta, \varphi) = \sum_{n=1}^{N} A_n e^{j\varphi_n} E_n(\theta, \varphi)$, in which $E_n(\theta, \varphi)$ is an embedded complex number that represents active radiation fields for the n^{th} element and must be multiplied by the amplitude and phase vector $A_n e^{j\varphi_n}$. Weighting coefficients depicted in the desired patterns are defined in each part of the patterns to scale the error of that part in the optimization procedure.

C. Phase and amplitude distributions for linear and conformal array Rotman lens designs

Considering the modified formulations in Eq. (1), knowing the phase distributions of φ_0 and φ_1 is necessary in the Rotman lens design. Also, because the Rotman lens operates based on the TTD properties, it is possible to use the radiation pattern of the array elements at an arbitrary frequency in the operating frequency band (10-14 GHz) for the PSO procedure. Therefore, in this paper we use the active element radiation patterns at center frequency to synthesize the conformal array antenna.

The PSO algorithm has been run with the use of 800 particles and 500 iterations to obtain the optimized amplitude and phase distributions of the arrays. Figure 4 (a) shows the optimized radiation pattern for zero scan angle and Fig. 4 (b) shows the optimized radiation pattern for -65^0 scan angle for the linear and conformal arrays.

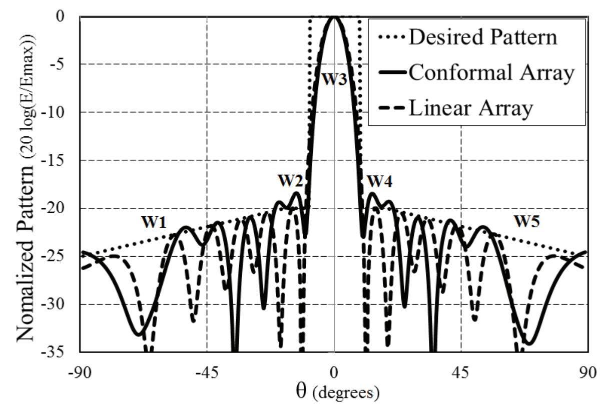

(a)

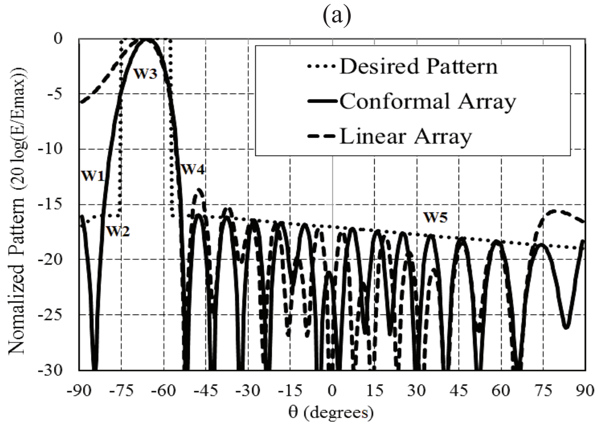

(b)

Fig. 4. Optimized radiation patterns: (a) zero scan angle ($w_1=w_5=0.4$, $w_2=w_4=2.2$ and $w_3=1.8$), (b) -65^0 scan angle ($w_1=0.8$, $w_2=1.8$, $w_3=3.4$, $w_4=2.8$ and $w_5=1.6$).

Figure 4 (b) shows the fitted pattern for -65^0 scan angle. It is shown that the linear array could not make a good fitted pattern. Figures 5 and 6 show the phase and amplitude distributions of array elements for zero and -65^0 scan angles.

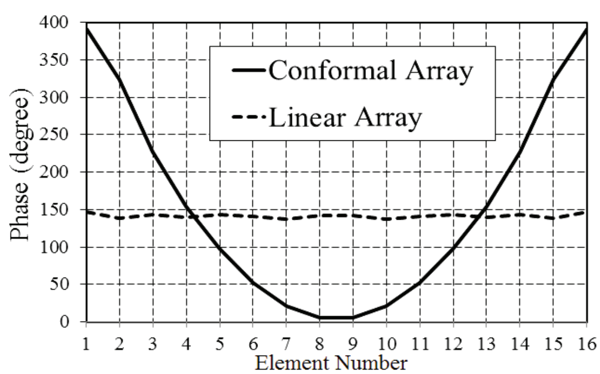

(a)

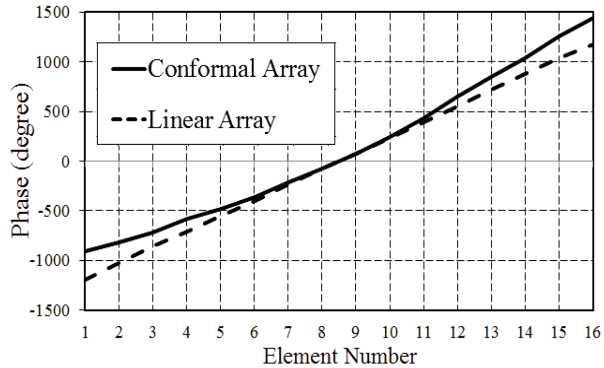

(b)

Fig. 5. Phase distributions of array elements: (a) zero scan angle, (b) -65^0 scan angle.

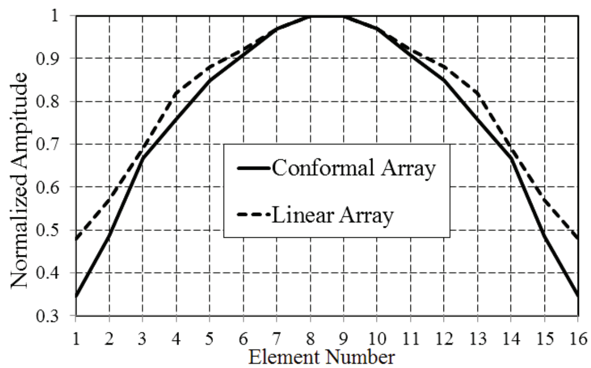

(a)

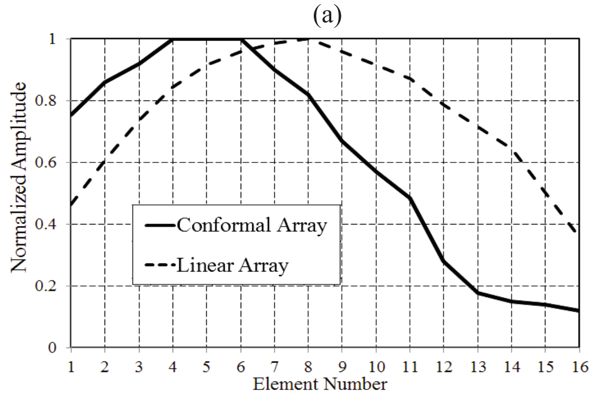

(b)

Fig. 6. Amplitude distributions of array elements: (a) zero scan angle, (b) -65^0 scan angle.

In the conformal array antenna, unlike the linear array antenna, the phase distributions for zero and -65^{o} scan angles, represent the nonlinear behavior of the phase distributions. Also, the amplitude distribution for -65^{o} scan angle shows that the elements which point to the -65^{o} scan angle have greater amplitudes. Difference between the amplitude distributions in conformal and linear arrays is due from the different orientation of array ports and radiating elements. Unlike the linear array, in the conformal array the radiating elements are oriented in different directions based on the array curvature. Therefore, the radiation patterns of conformal array elements are different. In the Rotman lens design the amplitude distributions for different scan angles are realized by suitable design of the beam ports corresponding to each scan angle in the radiation pattern. This principle is studied in the next section.

IV. DESIGN OF THE ROTMAN LENSES

As mentioned earlier, to design the Rotman lenses to feed the linear and conformal array antennas, it is necessary to have the phase distributions φ_0 and φ_1. Beside the phase distributions, the amplitude distributions of array elements for these scan angles must be produced by the Rotman lenses. To design the Rotman lens for the arc-shaped array, two points must be made clear. First, the phase distributions of the array elements and second the amplitude distributions of the array elements for different scan angles. By obtaining the optimized phase distributions and applying them to the modified Rotman lens equations, the lens can realize the desired phase distributions. To create the desired amplitude distributions, especially for maximum scan angles, the input ports must be designed and directed correctly. These amplitude distributions depend on beam ports widths, the shape of the inner receiver curve and the angle of input ports orientations. The widths of the beam ports and shape of the inner receiver curve can be realized by controlling the trifocal lens parameters. Table 1 shows the parameters used for designing the proposed Rotman lenses.

Table 1: Rotman lens design parameters

f_1	Center focal length	262 mm
f_2	Off focal length	249.5 mm
NB	Number of beam ports	11
NA	Number of array ports	16
α	Focal angle	24º
ε_r	Cavity permittivity	2.2
w_0	Center transmission line length	194 mm
f_0	Center frequency	12 GHz

The optimization results for amplitude distribution of -65^{o} scan angle shows that the elements which correspond to this scan angle have higher amplitudes. This amplitude distribution has an important role in controlling the side lobes of the radiation pattern. To have this amplitude distribution on antenna elements, beam ports have to be oriented towards the desired angle. Figure 7 shows the designed Rotman lenses with 11 beam ports and 16 array ports for linear and conformal arrays respectively. Because of amplitude tapering for the linear array in Fig. 6, each beam port is directed towards the center of the array port contour, like in [13].

Figure 7 (b) shows that the orientation of beam port 1 for the conformal array Rotman lens is not towards the center of the array port contour. In fact, the orientation of beam port 1 is shifted by Γ degrees from the center of the array curve, as shown in Fig. 7 (b). This is done based on the obtained optimized amplitude distributions for the conformal array (as shown by the solid lines in Fig. 6) and causes certain array elements to have higher amplitudes.

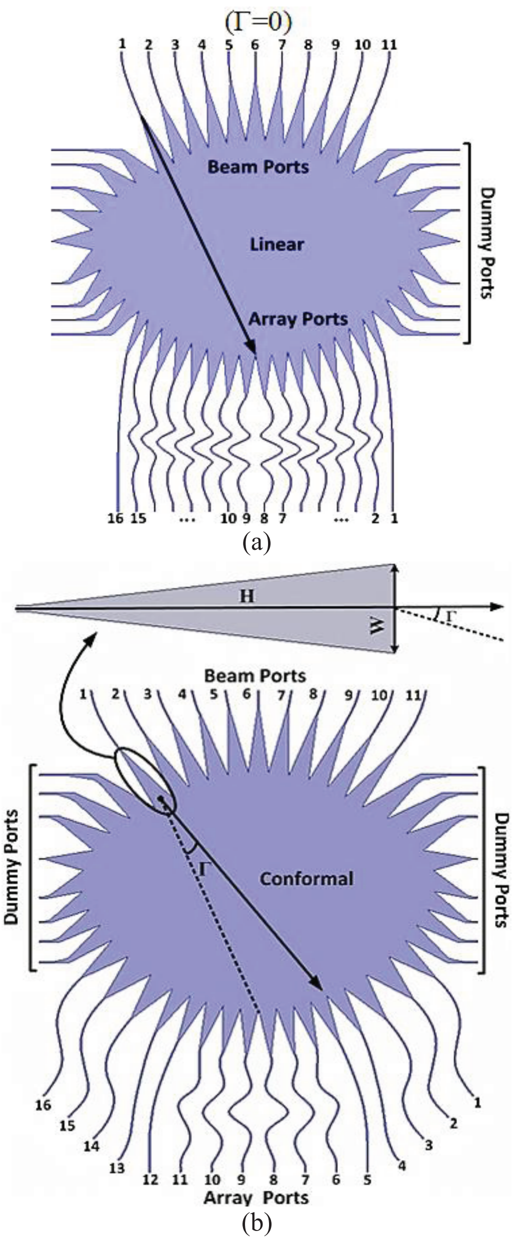

Fig. 7. Modified Rotman lens structures: (a) linear array, (b) conformal array.

The purpose of the dummy ports is to minimize the multipath interference [14]. The substrate of the microstrip structure is *Rogers RT/duroid 5880(tm) with* $\varepsilon_r = 2.2$, $tan\delta = 0.0009$. Figure 8 shows two amplitude distributions across array ports for the two Rotman lens designs shown in Fig. 7, when beam port 1 is excited.

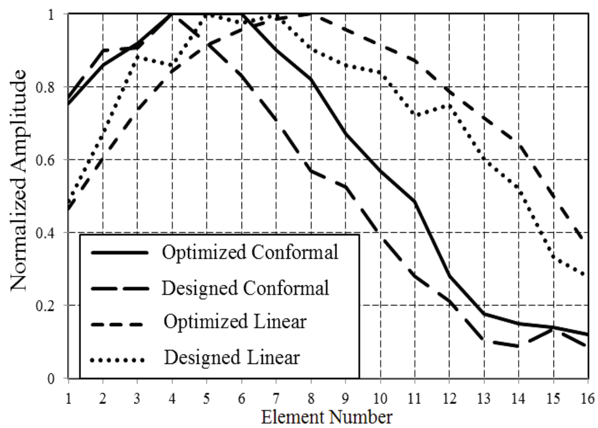

Fig. 8. Amplitude distribution across array ports when port 1 is excited.

V. SIMULATION RESULTS OF THE PROPOSED ROTMAN LENSES

Figure 9 shows the radiation patterns of the linear array of Fig. 3 (a) fed by the modified Rotman lens of Fig. 7 (a) at the frequencies of 10, 12 and 14 GHz. To better clarify the grating lobes, the radiation patterns of 7-11 beam ports are not shown.

Figures 9 (a) and 9 (b) show that the gain of the array antenna at the maximum scan angle decreases considerably at the frequencies of 10 and 12 GHz, and Fig. 9 (c) shows that not only the gain decreases, but also the grating lobes increase considerably at 14 GHz. At the maximum scan angle the decrease in the gain is 3.45 dB and 5.3 dB at the frequencies of 12 and 14 GHz respectively, compared to the gain at the zero scan angle.

Figures 10 (a-c) show the radiation patterns of the conformal array of Fig. 3 (b) fed by the modified Rotman lens of Fig. 7 (b) at the frequencies of 10, 12 and 14 GHz. These figures show that the maximum gain reduction of the conformal array at different frequencies is acceptable up to the -65^0scan angle and the grating lobes do not increase at these frequencies.

To better compare the maximum scan angle of linear and conformal arrays, the acceptable radiation patterns for the maximum available scan angles are depicted for both of the array configurations in Fig. 11. The acceptable maximum scan angles for the conformal array and the linear array are -65^0 and -55^0 respectively.

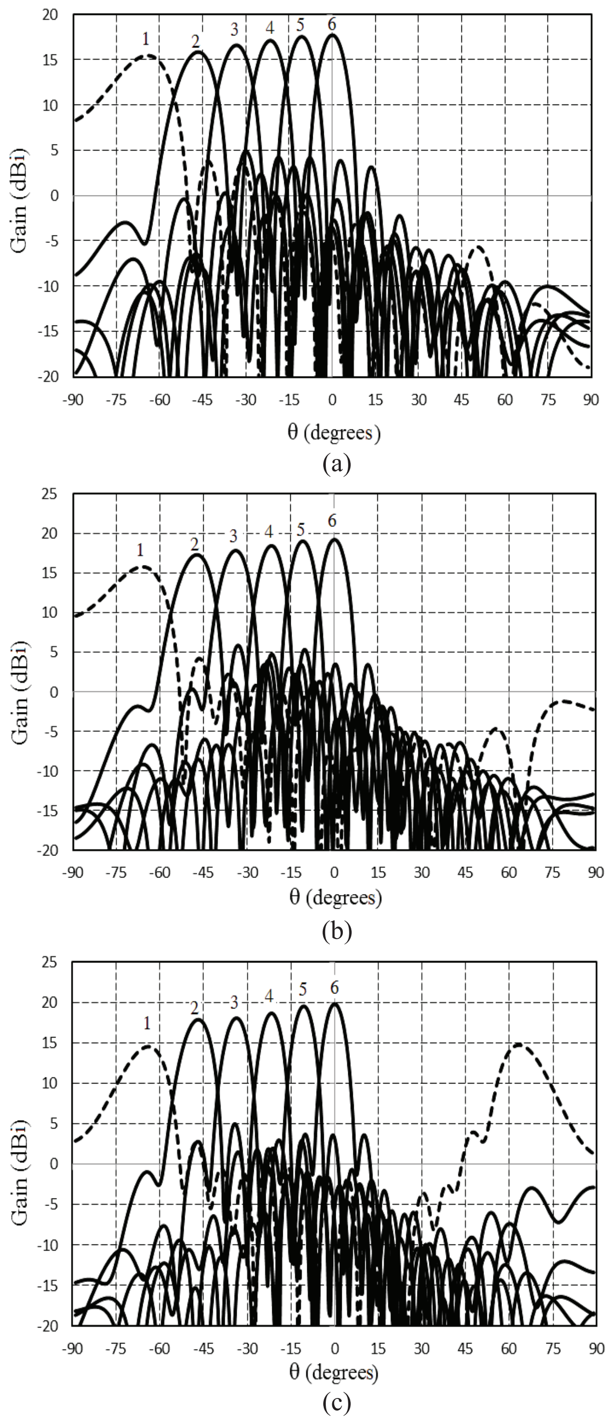

Fig. 9. Radiation pattern of the linear array of double ridged horn antennas fed by modified Rotman lens: (a) 10 GHz, (b) 12 GHz, and (c) 14 GHz.

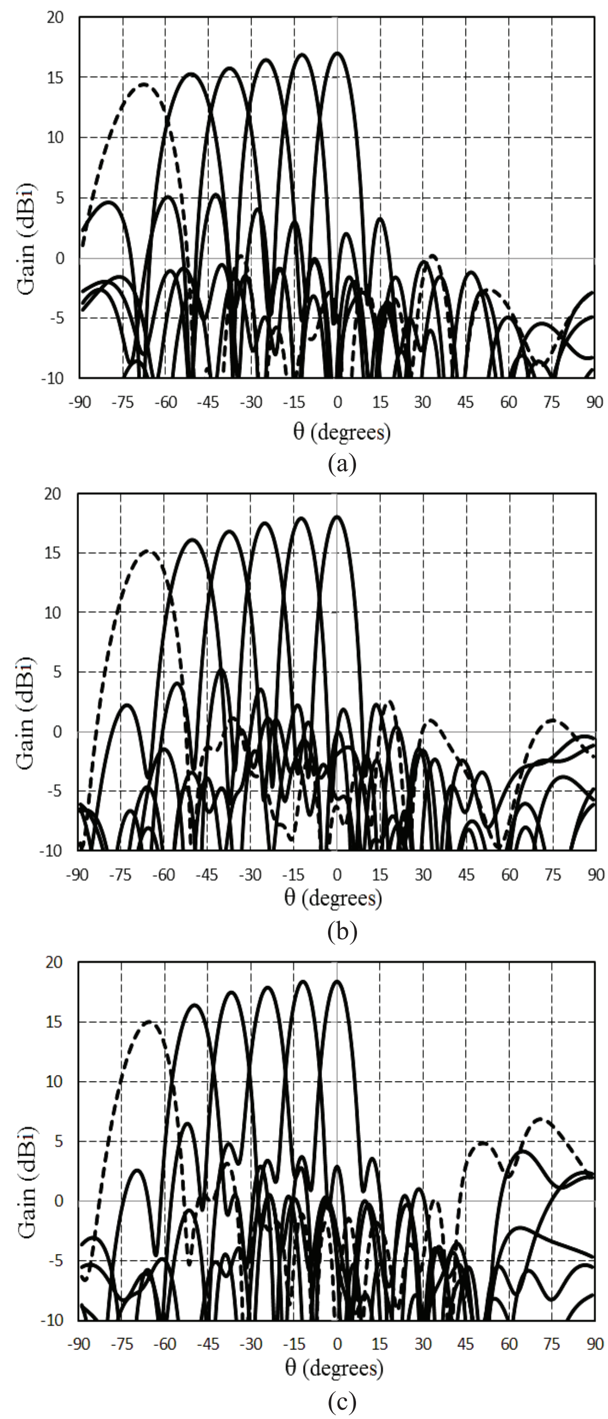

Fig. 10. Radiation pattern of the conformal array of double ridged horn antennas fed by the modified Rotman lens: (a) 10 GHz, (b) 12 GHz, and (c) 14 GHz.

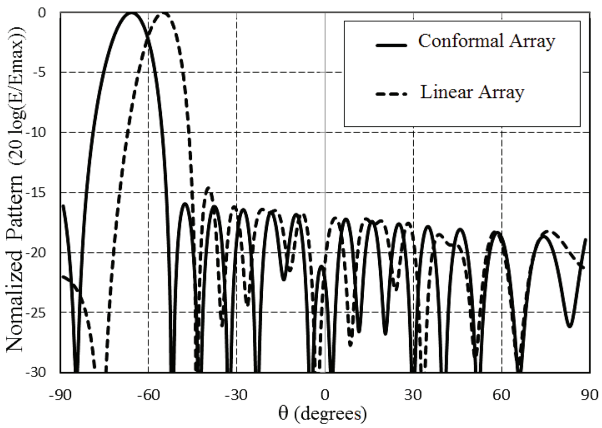

Fig. 11. Optimized radiation patterns for -65^0 and -55^o scan angles for conformal and linear arrays.

VI. CONCLUSION

An improvement in the scan angle of a wide band array antenna is obtained through feeding a conformal array antenna with a modified design of the Rotman lens. The proposed Rotman lens structure is based on the trifocal design method with new phase distributions in zero and maximum scan angles. The effect of amplitude distributions across array elements are fully considered in the design process. These phase and amplitude distributions are obtained by synthesizing the conformal array using the PSO algorithm. The radiation patterns of the linear and conformal arrays with equal numbers of elements are compared and the enhancement in the scan angle of the conformal array antenna is clearly observed.

REFERENCES

[1] R. Turner and W. Rotman, "Wide-angle microwave lens for line source," *IEEE Transactions on Antennas and Propagation*, pp. 623-632, 1963.

[2] Y. T. Lo and S. W. Lee, *Antenna Handbook: Volume III Applications*, Springer, 1993.

[3] C. S. Cho, F. Barnes, and J. Kim, "Dielectric slab Rotman lens for microwave/millimeter-wave applications," *Microwave Theory and Techniques, IEEE Transactions on*, vol. 53, pp. 2622-2627, 2005.

[4] J. Dong, A. L. Zaghloul, and R. Rotman, "Phase-error performance of multi-focal and non-focal two-dimensional Rotman lens designs," *IET Microw. Antennas Propag.*, vol. 4, no. 12, pp. 2097-2103, 2010.

[5] L. Schulwitz and A. Mortazawi, "A new low loss Rotman lens design using a graded dielectric substrate," *IEEE Transactions on Microwave Theory and Technique*, vol. 56, Dec. 2008.

[6] W. Bu-hong and G. Ying, "Frequency-invariant and low cross-polarization pattern synthesis for conformal array antenna," *in Radar Conference, 2008, RADAR'08, IEEE*, pp. 1-6, 2008.

[7] T. Katagi, "An improved design method of Rotman lens antennas," *IEEE Trans. Antennas Propag.*, vol. 32, no. 5, pp. 524-527, May 1984.

[8] J. Rao, "Multifocal three-dimensional bootlace lenses," *IEEE Transactions on Antennas and Propagation*, vol. 30, pp. 1050-1056, 1982.

[9] R. C. Hansen, "Design trades for Rotman lenses," *IEEE Trans. Antennas Propag.*, vol. 39, pp. 464-472, 1991.

[10] M. S. Smith, "Design considerations for Ruze and Rotman lenses," *Radio Electron. Eng.*, vol. 52, pp. 181-187, 1982.

[11] A. K. Bhattacharyya, *Phased Array Antennas*, A John Wiley & Sons, Inc., 2006.

[12] Y. Eberhart and R. C. Shi, "Empirical study of particle swarm optimization," in *Proc. 1999 Congress on Evolutionary Computation*, pp. 1945-1950, 1999.

[13] M. S. Smith and A. K. S. Fong, "Amplitude performance of Ruze and Rotman lenses," pp. 329-336, 1983.

[14] L. Musa and M. S. Smith, "Microstrip port design and sidewall absorption for printed Rotman lens," *Microwaves, Antennas and Propagation, IEEE Proceeding*, vol. 136, issue 1, pp. 53-58, Feb. 1989.

Amin Mahmoodi received his B.S. and M.S. in Electrical Engineering from the Shahid Beheshti University (SBU) in 2012 and 2014 respectively. His interests involve phased arrays, beam forming networks, antenna and passive microwave devices.

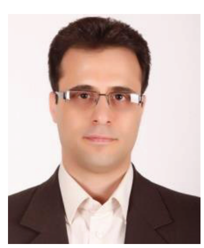

Abbas Pirhadi received his B.S. degree in Electrical Engineering from the Isfahan University of Technology, Isfahan, Iran in 2000, and M.S. and Ph.D. degree in Communication Engineering from Tarbiat Modares University (TMU), Tehran, Iran in 2002 and 2007, respectively. From 2002 to 2006, he joined the Antenna and Propagation Group of the Iran Telecommunication Research Center (ITRC) as a Researcher. Also, in 2008 he joined the Shahid Beheshti University (SBU), where he is the Assistant Professor at the faculty of Electrical and Computer Engineering. His research interests include microwave antennas, theoretical and computational electromagnetic with applications to antenna theory and design.

Reflectarray Nano-Dielectric Resonator Antenna Using Different Metals

Hend A. Malhat, Nermeen A. Eltresy, Saber H. Zainud-Deen, and Kamal H. Awadalla

Department of Electrical Engineering
Faculty of Electronic Eng., Menoufia University, 32952, Egypt
er_honida1@yahoo.com, anssaber@yahoo.com

Abstract **─** Nano-antennas have been introduced with wide bandwidth for faster data communications. The material properties of good conducting metals introduce plasmonic behavior at THz frequencies. The material property of good conducting metals using the Durde Lorentz model have been investigated. The radiation characteristics of nano-dielectric resonator antenna NDRA reflectarray at 633 nm have been investigated. A parametric study for the NDRA unit-cell dimensions and material has been introduced. Different types of metals are used as a supporting plane of the NDRA unit-cell. A NDRA with silver, copper, and aluminum supporting plane have been designed and analyzed for reflectarray antennas. A nano-reflectarray unit-cells with supporting plane having different metals have been introduced. Comparisons between the radiation characteristics of reflectarrays with different supporting plane metals have been illustrated. A compromise between the size, maximum gain, and operating bandwidth of the nano-reflectarray is investigated for terahertz applications. The finite integral technique is used to carry a full wave analysis to design a NDRA reflectarray.

Index Terms **─** DRA, nano-antenna, reflectarray.

I. INTRODUCTION

The radiation characteristics of a conventional radio-frequency RF antenna have been presented in detail [1]. Nano-antenna is a resonant device, which converts the EM wave into a localized energy at terahertz frequencies [2]. Recently, wide bandwidth nano-antennas have been introduced for faster information exchange. Nano-antennas have many applications including solar cells, on-chip wireless optical communication and biological imaging. Different forms of the microwave antennas such as dipole, monopole, Yagi-Uda, and bow-tie antenna have been investigated at the terahertz frequencies [3-6] which focus on resonant metallic nanostructures. The materials of nano-antennas are generally good conducting metals such as gold and silver [7]. The resonant structures of good conducting metals show electromagnetic resonances, when being excited by an incident light, this is called surface plasmon polariton resonances SPPRs. The optical properties of these metals are described by the Drude-Lorentz model, which considers both the free electrons contributions and harmonic oscillator SPPRs contributions [8]. However, only the high ohmic losses of metals at THz frequencies affect the radiation efficiency of nano-antennas [2]. The nano-antenna resonance length is not determined by the free space wavelength, but by the SPP wavelength in the metal [2]. The current distribution on the nano-antenna has a standing wave pattern similar to that of the RF antennas, but with non-uniform spacing between subsequent current lobes. Nano-antenna arrays introduce a superior directivity, field confinement, absorption cross-section and flexibility in beam shaping compared with single nano-antennas. Dielectric resonator antennas DRAs have many attractive features and applications at microwave frequencies [9]. The DRAs have different shapes such as a hemisphere, cylinder, or rectangular and are typically mounted on a metal layer regarded as perfect electric conductor. The DRAs are generally constructed from low-loss high-permittivity dielectric materials up to ε_r=100. To increase the efficiency of resonant nano-antennas, the low-loss high-permittivity dielectric materials available at THz frequencies are used. At THz frequencies, the wave penetrates the metals due to the plasmonic effect and the antenna scaling property is not valid. The radiation characteristics of the DRA at 633 nm have been investigated in [10]. High-gain microwave antennas have been employed in many applications such as radar and satellite communications. The parabolic reflector and phased array antenna have high gain, narrow main lobe and high power capacity, but suffer some disadvantages as high cost, large volume, and lossy feed networks. Reflectarray antenna combines the advantages of parabolic reflector and phased array and overcomes their disadvantages [11]. The reflectarray antenna consists of a primary source illuminating a planar surface composed of an array of unit-cells. The phase shift of each unit-cell is adjusted to collimate the reflected wave in the desired direction. Reflectarray suffers from feeder blocking effect, so it requires an offset feed to avoid blockage losses, which

Submitted On: March 10, 2015
Accepted On: June 1, 2015

leads to destroying the symmetry of the antenna aperture and increases the angle of incidence to some individual elements [12-14]. The detailed analysis of the radiation characteristics of NDRA element and NDRA reflectarray at 633 nm investigated in [10].

In this paper, the optical material properties of different conducting metals at THz frequencies have been investigated. A parametric study of the NDRA unit-cell for reflectarray at 633 nm has been introduced. The effect of changing the type of the metal material properties on the performance of the NDRA unit-cell is investigated. A 21×21 unit-cell elements NDRA reflectarray has been designed and analyzed using the finite integral technique based on the commercial software CST Microwave Studio [15,16]. Reflectarray with different metal supporting plane have been introduced. A comparison between the radiation characteristics of reflectarray with silver, copper and aluminum supporting plane has been presented.

II. MATERIAL PROPERTIES AT TERAHERTZ RANGE

At THz frequencies, the behavior of conventional metals properties behaves in a different way compared to the microwave frequencies [7]. In microwave frequency range the electric field inside the conductors is zero, which leads to perfect reflection from the surface of the metal, as the conductivity of metal is very high. However, at THz frequencies, the assumption of perfect conductor metals is not valid and the losses cannot be neglected [8]. The material properties in the THz range can be described by a free electron gas moving through a lattice of positive ions. The frequency dependent complex permittivity and the electrical conductivity of metal in the THz frequency range are described using Durde Lorentz model [8]:

$$\varepsilon_r = \varepsilon_1 + j\varepsilon_2 = [1 - \frac{\omega_p^2}{\omega\omega - j\vartheta_p}], \tag{1}$$

$$\sigma = \sigma_1 + j\sigma_2 = \varepsilon_o \frac{\omega_p^2}{j\omega + \vartheta_p}, \tag{2}$$

where ε_1 is the real part of permittivity and is a measure of how much energy from an external field is stored in a material. ε_2 is the imaginary part of permittivity loss factor. It is a measure of how dissipative or lossy a material is to an external field, ε_o is the dielectric constant of vacuum, ω is the angular frequency of the electromagnetic wave, ϑ_p is the angular collision frequency, and ω_p is the electron plasma angular frequency [8]:

$$\omega_p = \sqrt{n_e q^2/\varepsilon_o m_e} = 56.40\sqrt{n_e}, \tag{3}$$

where n_e is the free electron density, m_e is the electron mass, and q is the charge of the electron. Figure 1 shows the variation of electric permittivity ε, and the conductivity σ, versus frequency in the THz range of gold, copper, silver and aluminum. The electrical permittivity and conductivity of all metals take an exponential variation with frequency. ε_1 *and* σ_2 are increased by increasing frequency negative with reduced magnitude with higher frequency while ε_2 and σ_1 are decreased in magnitude by increasing frequency. The skin depth is representing how deep the electromagnetic wave can penetrate the material surface [8]:

$$\delta(\omega) = \frac{2c\sqrt{\frac{\varepsilon_1}{2} + \frac{1}{2}\sqrt{\varepsilon_1^2 + \varepsilon_2^2}}}{\omega\varepsilon_2}, \tag{4}$$

where c is the speed of light. The variations of skin-depth versus frequency for different types of metals are shown in Fig. 2. At 474 THz, the skin depth is 32 nm for gold, 28 nm for copper, 24.5 nm for silver and 17 nm for aluminum.

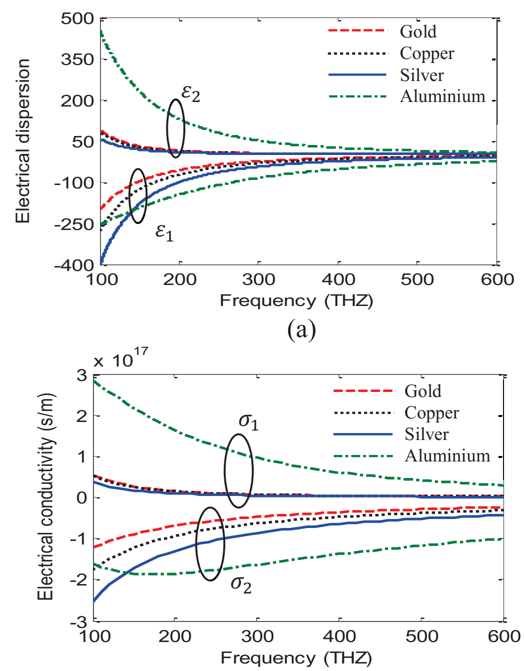

(a)

(b)

Fig. 1. The variations of complex permittivity and electrical conductivity versus frequency for different types of metals: (a) electrical dispersion, and (b) electrical conductivity.

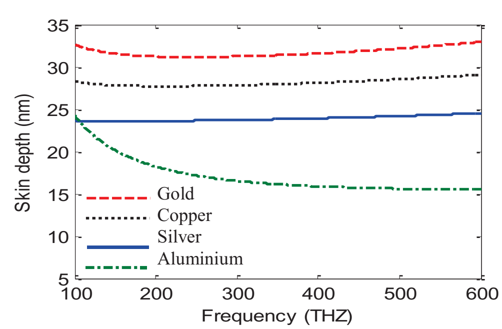

Fig. 2. The skin depth variation versus frequency.

III. THEORY OF REFLECTARRAY ANTENNA

The reflectarray operation can be seen as a phased array with spatial feed located at (x_f, y_f, z_f) from the array aperture. For the reflectarray located in x-y plane, the wave is reflected from each unit-cell at direction $(\theta_0,\emptyset_o)$ suffer from additional phase shift due to the position of the element in the array (x_{ci}, y_{ci}) and spacing between the cell element and the feeding horn d_{ij}, as shown in Fig. 3. To collimate the reflected wave at direction $(\theta_0,\emptyset_o)$ each unit-cell require a compensation phase:

$$\varphi_{ij}(x_{ci}, y_{ci}) = k_o d_{ij} + \emptyset_{cij}, \tag{5}$$

where $k_o = 2\pi/\lambda_o$ is the wave number, d_{ij} is given by [12]:

$$d_{ij} = \sqrt{\; x_{ci} - x_f{}^2 + \left(y_{ci} - y_f\right)^2 + z_f{}^2}\,, \tag{6}$$

and $\emptyset_{cij}$ is the phase shift due to the location of the unit-cell in the array:

$$\varphi_{cij} = -x_{ci} sin\theta_0 cos\emptyset_o - y_{ci}\, sin\theta_0\, sin\emptyset_o. \tag{7}$$

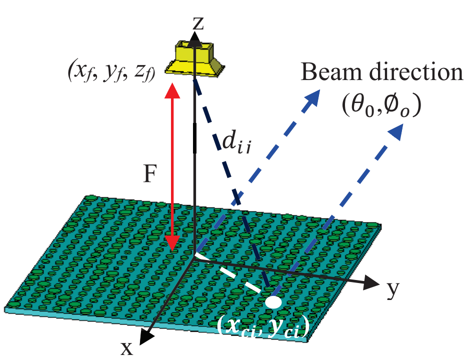

Fig. 3. The detailed structure of the reflectarray configuration.

IV. DESIGN OF NDRA REFLECTARRAY WITH SILVER SUPPORTING PLANE

The unit-cell of nano dielectric resonator reflectarray consists of a NDRA made of titanium dioxide TiO_2, with anisotropic frequency independent dielectric permittivity of 8.29 in x- and y-axis directions and 6.71 in z-axis direction. The estimated loss tangent is 0.001 [10]. The NDRA has a cylindrical shape with radius R and height h_d placed on a square ground plane with side length L and thickness h as shown in Fig. 4 (a). To calculate the required reflection coefficient phase compensation in each unit-cell, the unit-cell is put in a waveguide simulator [13]. The perfect electric and magnetic wall boundary conditions are posted onto the sides of the surrounding waveguide, and result in an infinite array. A linearly polarized plane wave was applied as the far-field excitation of the unit-cells inside the waveguide simulator and only normal incidence angle is considered. There are several limitations to the infinite array approach. First, all elements of the reflectarray/transmitarray are identical; this is not the case in the real reflectarray/transmitarray in which the diameters of the NDR in each cell element must vary according to the required phase compensation. Secondly, the reflectarray/transmitarray itself is not infinite in extent. Finally, only normal incidence is considered. However, the plane wave has an oblique angle on the real array element, but the phase variation is nearly the same for incidence angles up to 30º [14]. Different types of metals are used for ground plane as silver, gold, copper, and aluminium. The properties of the ground plane metals are determined using Eq. (1) at 474 THz and are listed in Table 1. The required compensation phase of the reflection coefficient for each unit-cell is achieved by varying the NDRA radius R. Figure 5 shows the variation of the reflection coefficient magnitude and phase versus the NDRA radius at 474 THz for different types of ground plane metals. The gold ground plane has the worst reflection coefficient variation from -30.4 to -2.9, while the silver ground plane gives the best reflection coefficient magnitude varies from -5.8 to -1.7 dB for the NDRA radius varying from 85 nm to 170 nm. This is because the conductivity of the aluminum material is higher than that of the silver material at 474 THz as appeared in Fig. 1 (b), and the penetration depth in aluminum ground plate is higher than that of silver as shown in Fig. 2. The phase of the reflection coefficient span of variation is 360º for the silver, 19º for gold, 215º for the copper, and 136º for the aluminum ground plate. The silver material has the best performance for the reflectarray unit-cell with reflection coefficient magnitude variation from -5.8 to -1.7 dB, and phase variation from 0 to 360 degrees.

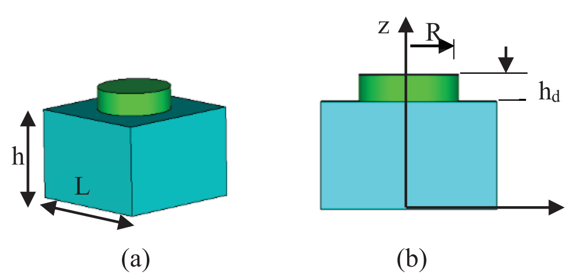

Fig. 4. The detailed structure of the NDRA reflectarray unit-cell: (a) 3-D view, and (b) side view.

Table 1: The optical properties of the different types of metals at 474 THz [17]

Metal	ω_p (rad/sec)	υ_p (rad/sec)	δ (nm)
Silver	1.28×10^{16}	9.19×10^{13}	24.5
Gold	0.98×10^{16}	2.8×10^{14}	32
Copper	1.13×10^{16}	3.2×10^{14}	28
Aluminum	2.3×10^{16}	1.04×10^{15}	17

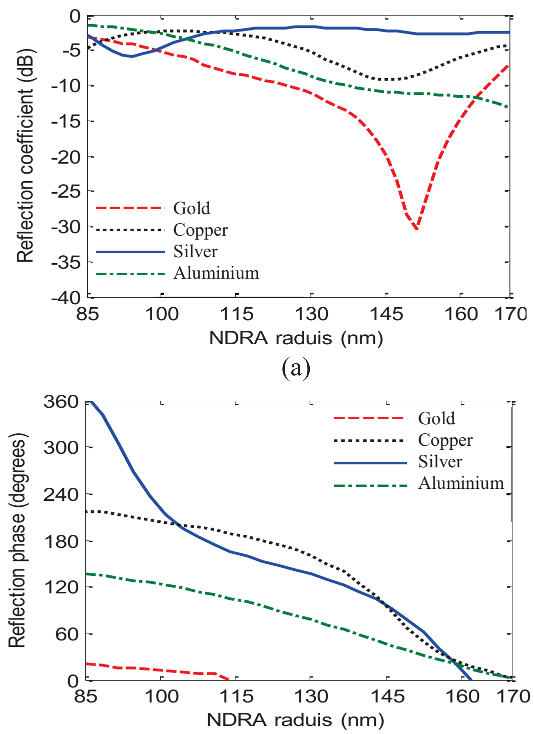

Fig. 5. The variation of the reflection coefficient magnitude and phase versus the NDRA radius at 474 THz: (a) reflection coefficient magnitude, and (b) reflection coefficient phase magnitude.

Figure 6 shows the effect of changing the silver ground plane thickness of the unit-cell on the variation of the reflection coefficient magnitude and phase. By increasing the ground plane thickness, the reflection coefficient magnitude is decreased and the reflection coefficient phase variation is increased to achieve 360 degrees. A compromise between the magnitude and phase of the reflection coefficient has been made. A ground plane thickness of 200 nm has been chosen for reflection coefficient magnitude variation from -1.7 to -5.8 and 360 degrees phase variations. The electric field distribution on the unit-cell of the NDRA reflectarray with silver supporting plane h=200 nm, h_d=50 nm, and R=130 nm is shown in Fig. 7. The incident plane wave penetrate the silver supporting plane at a distance equal to the skin depth at this frequency 24.5 nm and reflects back to the source direction. The reflection occurs because the thickness of the silver supporting plane is much bigger than the silver skin depth about 8.16 δ.

A 21×21 unit-cell elements NDRA reflectarray is constructed using silver plane with L=350 nm, h=200 nm, and h_d=50 nm as shown in Fig. 8. The array has total dimensions of 7.35×7.35 μm^2. A linearly polarized pyramidal nano-horn antenna is used to feed the NDRA reflectarray located at 8.133 μm from the array aperture. The nano-horn antenna is constructed from gold with L_h=487.5 nm, and aperture size $a \times b$ of 810 nm × 1275 nm. The nano-horn antenna has a maximum gain of 11.1 dBi at 474 THz. The E- and H-plane radiation patterns at 474 THz of the nano-horn and the NDRA reflectarray with different plane thickness h=30, 70 and 200 nm are shown in Fig. 9. The maximum gain of the NDRA reflectarray is increased by increasing the plane thickness and the SLL is decreased. For h=200 nm, the first SLLs are -17.9 dB and -15.1 dB in E- and H-plane respectively. The HPBW of the NDRA reflectarray is 4.5 degrees in E-plane and 4.7 degrees in H-plane compared to 40.3 degrees in E-plane and 41.3 degrees in H-plane for the nano-horn antenna.

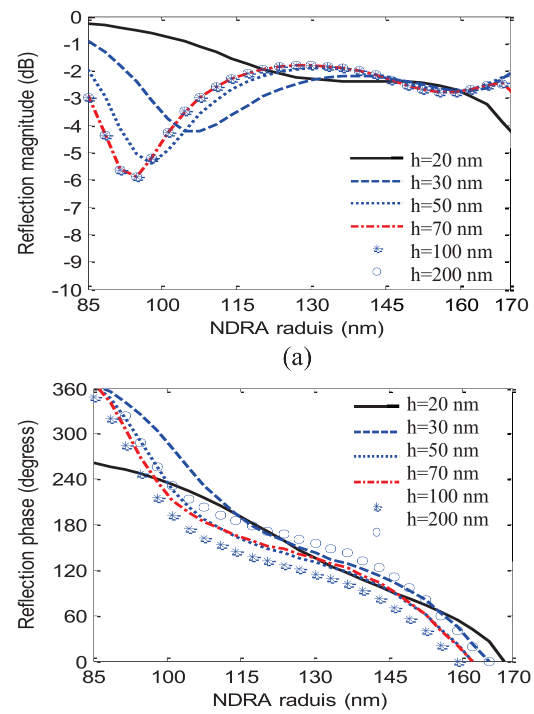

Fig. 6. The variations of the reflection coefficient magnitude and phase versus the NDRA radius: (a) reflection coefficient magnitude, and (b) reflection coefficient phase magnitude.

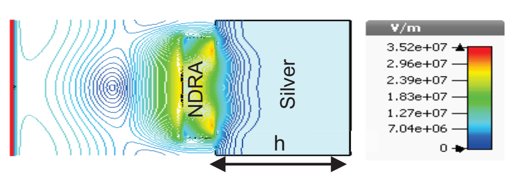

Fig. 7. The electric field distribution on the unit-cell with silver supporting plane, h=200 nm, L=350 nm, h_d =50 nm and R=130 nm.

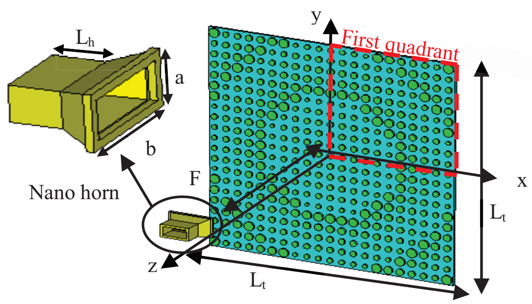

Fig. 8. The 21×21 unit-cell elements NDRA reflectarray with silver supporting plane.

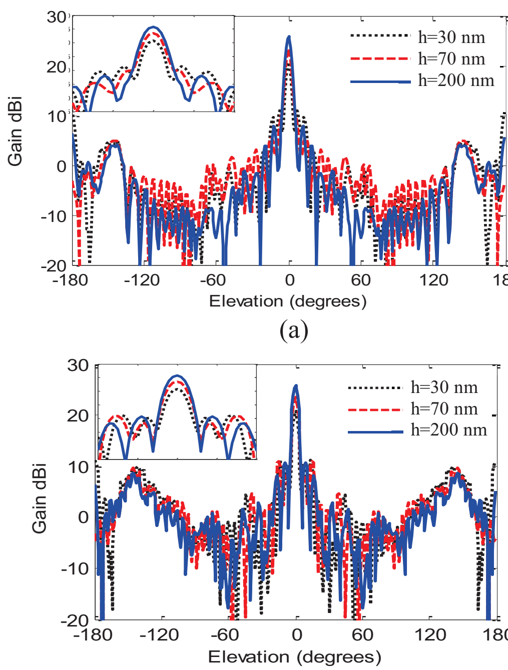

(a)

(b)

Fig. 9. The gain patterns plot for a 21×21 NDRA reflectarray with silver supporting plane for variable ground plane thickness.

V. DESIGN OF NDRA REFLECTARRAY WITH COPPER SUPPORTING PLANE

The NDRA unit-cell with copper supporting plane has the same construction as shown in Fig. 4. The supporting plane is replaced by copper material. The dimensions of the NDRA unit-cell with copper supporting plane is designed and optimized to operate at 474 THz. The unit-cell dimensions are h_d =105 nm placed on a square copper ground plane with side length L=350 nm, thickness h=200 nm and variable values for NDRA radius R. The incident wave penetrate the copper supporting plane down to the skin depth and reflects back to the source. The variations of the reflection coefficient magnitude and phase for the unit-cell with copper supporting plane are shown in Fig. 10. A 300^o phase shift of the reflection coefficient unit-cell is achieved by varying the NDRA radius R from 75 to 175 nm. While the reflection coefficient magnitude is changed from -1.8 to -5.6 dB at 474 THz. A 21×21 unit-cell elements NDRA reflectarray with copper supporting plane of thickness h=200 nm, length of 7.35 µm and NDRA height of 105 nm is constructed. The NDRA reflectarray has maximum gain of 27.2 dBi with front to back ratio of 21 dB. The gain variation versus frequency for the NDRA reflectarray with copper supporting plane and the nano-horn are shown in Fig. 11. The 1-dB gain bandwidth is 35 dB.

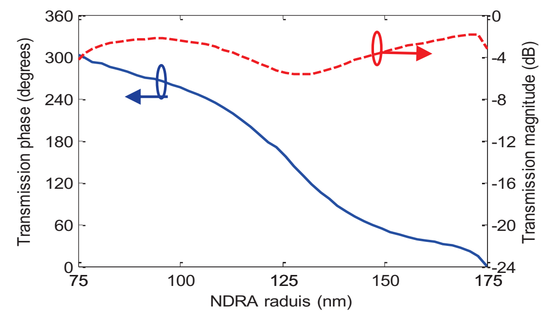

Fig. 10. The variation of the reflection coefficient phase and magnitude versus the NDRA radius at 474 THz.

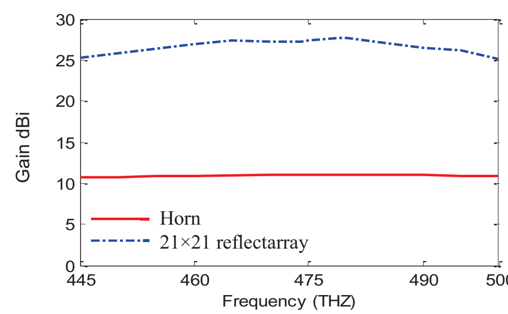

Fig. 11. The gain variation versus frequency for a 21×21 NDRA reflectarray with copper supporting plane at L=350 nm, h=200 nm, and h_d=105 nm.

VI. DESIGN OF NDRA REFLECTARRAY WITH ALUMINUM SUPPORTING PLANE

A NDRA reflectarray unit-cell with aluminum supporting plane with side length L=350 nm, thickness h=200 nm, and hd=170 nm operated at 474 THz is investigated. Figure 12 (a) shows the electric field distribution on NDRA reflectarray unit-cell with aluminum supporting plane at 474 THz with h=200 nm, hd=170 nm and R=130 nm. The reflection coefficient magnitude and phase variations versus the NDRA radius are shown in Fig. 12 (b). A 360^o phase variation and reflection coefficient magnitude variation from -4.7 to -5.4 dB are achieved. The gain variation versus frequency for the NDRA reflectarray with aluminum supporting plane is shown in Fig. 13.

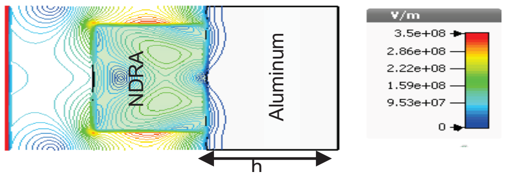

(a)

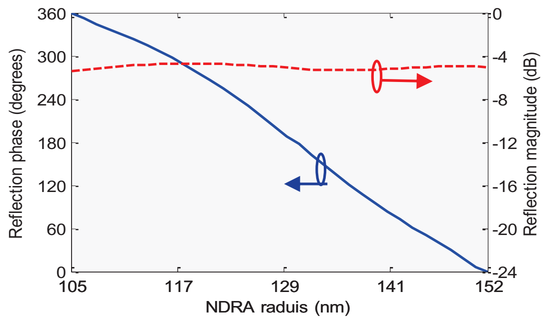

(b)

Fig. 12. (a) The electric field distribution on the NDRA reflectarray unit-cell with aluminum supporting plane, and (b) the reflection coefficient phase and magnitude versus the NDRA radius at 474 THz.

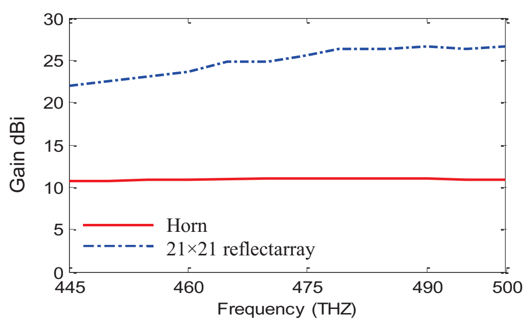

Fig. 13. The gain variation versus frequency for a 21×21 NDRA reflectarray with aluminum supporting plane.

VII. COMPARISON BETWEEN NDRA REFLECTARRAYS WITH DIFFERENT METAL SUPPORTING PLANES

The E-and H-plane gain patterns for 21×21 NDRA reflectarrays with silver, copper, and aluminum supporting planes are shown in Fig. 14. The reflectarray with copper supporting plane has the maximum gain of 27.8 dBi with lower HPBW of 4.4^{o} due to the higher reflection coefficient magnitude relative to the other metals. The reflectarray with aluminum supporting plane has the lower gain and the higher bandwidth, due to the increase in the NDRA height with variation of its relative permittivity in the z-direction. Table 2 lists a comparison between the radiation characteristics of the reflectarrays with different metals supporting plane. A compromise between gain, 1-dB bandwidth, SLL, and HPBW has been applied for choosing the appropriate reflectarray for THz applications.

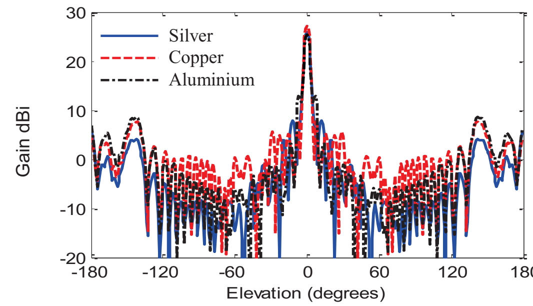

(a) x-z plane

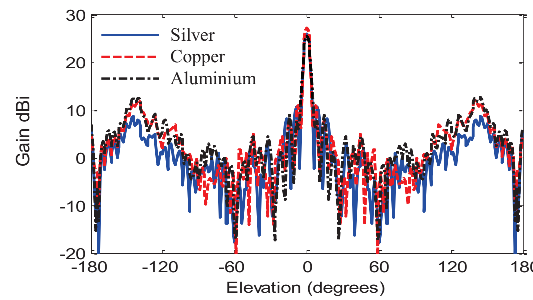

(b) y-z plane

Fig. 14. The gain radiation patterns plot for a 21×21 NDRA reflectarray with different supporting plane nano metals.

Table 2: Comparison between the radiation characteristics of NDRA reflectarrays with different metals supporting planes

Material	Silver	Copper	Aluminum
Gain dBi	25.8	27.2	25.4
1-dB BW	30 THz	35 THz	40 THz
SLL (dB)	-17.9	-19.4	-12.51
HPBW (degrees)	4.5	4.5	4.3

VIII. CONCLUSION

The use of NDRA in the design of nano-reflectarray for terahertz application at 633 nm is introduced. The reflectarray unit-cell consists of a cylindrical NDR on a square ground plane of a good conductor. A parametric study for the unit-cell dimensions has been introduced. The gold ground plane has got the worst reflection coefficient, while the silver ground plane gives the best reflection coefficient magnitude. A compromise between the magnitude and phase of the reflection coefficient has been made. A silver ground plane thickness of 200 nm has been chosen for reflection coefficient magnitude variation from -1.7 to -5.8 dB and 360 degrees phase variation. A 21×21 unit-cell elements NDRA reflectarray is constructed using silver supporting plane with L=350 nm, h=200 nm, and hd=50 nm. The maximum gain of the NDRA reflectarray is increased by increasing the plane thickness and the SLL is decreased.

REFERENCES

[1] A. C. Balanis, *Antenna Theory Analysis and Design*, 3rd edition, John Wiley & Sons, USA, 2012.

[2] M. Agio, "Optical antennas as nanoscale resonators," *Nanoscale Journal*, vol. 3, pp. 692-706, 2011.

[3] P. Muhlschlegel, H. J. Eisler, O. J. F. Martin, B. Hecht, and D. W. Pohl, "Resonant optical antennas," *Science Magazine*, vol. 308, pp. 1607-1609, Jun. 2005.

[4] T. H. Taminiau, F. B. Segerink, R. J. Moerland, L. Kuipers, and N. F. Hulst, "Near-field driving of a optical monopole antenna," *Journal of Optics A: Pure and Applied Optics*, vol. 9, pp. 315-321, Aug. 2007.

[5] I. S. Maksymov, A. E. Miroshnichenko, Y. S. Kivshar, "Actively tunable optical Yagi-Uda nanoantenna with bistable emission characteristics," *Optics Express*, vol. 8, pp. 8929-8938, Feb. 2012.

[6] H. Fischer and O. J. Martin, "Engineering the optical response of plasmonic nanoantennas," *Optics Express*, vol. 16, no. 12, pp. 9144-9154, Jun. 2008.

[7] R. Vajtai, *Hand Book of Nanomaterials*, Springer Handbooks, New York, USA, 2013.

[8] N. Kumar, "Spontaneous emission rate enhancement using optical antennas," *Ph.D. Thesis*, University of California, Berkeley, USA, 2013.

[9] K. M. Luk, K. W. Leung, and J. R. James, *Dielectric Resonator Antennas*, Research Studies Press, Hertfordshire, England, 2002.

[10] L. Zou, "Dielectric resonator antennas from multifunction microwave devices to optical nano-antennas," *Ph.D. Thesis*, School of Electrical and Electronic Engineering, University of Adelaid, Australia, Mar. 2013.

[11] S. H. Zainud-Deen, H. A. Malhat, S. M. Gaber, M. Ibrahim, and K. H. Awadalla, "Plasma reflectarray," *Plasmonics*, vol. 8, no. 3, pp. 1469-1475, Sept. 2013.

[12] J. Huang and J. A. Encinar, *Reflectarray Antennas*, John Wiley and Sons, Inc., New Jersy, USA, 2007.

[13] S. H. Zainud-Deen, H. A. Malhat, S. M. Gaber, and K. H. Awadalla, "Perforated nanoantenna reflectarray," *Progress in Electromagnetics Research M, PIER M*, vol. 29, pp. 253-265, 2013.

[14] H. A. Malhat, S. H. Zainud-Deen, and S. M. Gaber, "Circularly polarized graphene based transmitarray for terahertz applications," *Progress in Electromagnetics Research M, PIER M*, vol. 36, pp. 185-191, 2014.

[15] R. Schumann, T. Weiland, W. H. Schilders, E. J. Maten, and S. H. Houben, "Recent advances in finite integration technique for high frequency applications," *Scientific Computing in Electrical Engineering*, vol. 4, pp. 46-57, 2004.

[16] CST Microwave Studio, http://www.cst.com/.

[17] M. A. Ordal, L. L. Long, R. J. Bell, S. E. Bell, R. R. Bell, R. W. Alexander, Jr., and C. A. Ward, "Optical properties of the metals Al, Co, Cu, Au, Fe, Pb, Ni, Pd, Pt, Ag, Ti, and W in the infrared and far infrared," *Applied Optics*, vol. 22, no. 7, pp. 1099-11201, Apr. 1983.

Hend Abd El-Azem Malhat was born in Menouf, Egypt, on December 12, 1982. She received the B.Sc. and M.Sc. degrees from Menoufia University in 2004 and 2007, respectively. She received her Ph.D. degree in Antenna Engineering from Menoufia University, Egypt in 2011. She is currently an Associat Professor in the Department of Electrical and Electronic Engineering in the Faculty of Electronic Engineering, Menoufia University, Egypt. Her research interest at present include graphene antennas, plasma antennas, wavelets technique, transmitarray, reflectarray and RFID.

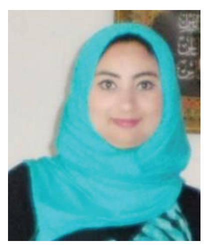

Nermeen A. Elteresy was born in Menouf, Egypt, on Sebtemer 29, 1990. She received the B.Sc. degree from Menoufia University in 2012. She is currently working toward her M.Sc. degree in Antenna Engineering from Menoufia University. Her research interest at present include nano-antennas, DRA, transmitarray, and reflectarray.

Saber Helmy Zauind-Deen was born in Menouf, Egypt, on November 15, 1955. He received the B.Sc. and M.Sc. degrees from Menoufia University in 1973 and 1982, respectively, and the Ph.D. degree in Antenna Engineering from Menoufia University, Egypt in 1988. He is currently a Professor in the Department of Electrical and Electronic Engineering in the Faculty of Electronic Engineering, Menoufia University, Egypt. His research interest at present include microstrip and leaky wave antennas, DRA, RFID, optimization techniques, FDFD and FDTD, scattering problems and breast cancer detection.

Kamal H. Awadalla was born in El-Santa - Gharbiya - Egypt, on February 1, 1943. He received the B.Sc. and M.Sc. from the Faculty of Engineering, Cairo University, Egypt, in 1694 and 1972, respectively, and the Ph.D. degree from the University of Birmingham, UK. in 1978. He is currently a Professor Emeritus in the Dept. of Electrical and Electronic Engineering in the Faculty of Electronic Engineering, Menoufia University, Egypt. His research interest at present include microstrip and leaky wave antennas, DRA, RFID, optimization techniques.

Compact Triple-Band S-Shaped Monopole Diversity Antenna for MIMO Applications

Jalil Mazloum [1], Seyed Ali Ghorashi [2], Mohammad Ojaroudi [3], and Nasser Ojaroudi [3]

[1] Electrical Engineering Department
Shahid Sattari Aeronautical University of Science and Technology, Tehran, Iran
jalil9898@yahoo.com

[2] Cognitive Telecommunication Research Group, Faculty of Electrical & Computer Engineering
Shahid Beheshti University, G. C., 1983693113, Tehran, Iran
a_ghorashi@sbu.ac.ir

[3] Young Researchers and Elite Club
Ardabil Branch, Islamic Azad University, Ardabil, Iran
m.ojaroudi@iauardabil.ac.ir, n.ojaroudi@yahoo.com

Abstract **─** In this paper, a novel WLAN frequency range monopole antenna is designed and manufactured for MIMO applications. The proposed antenna consists of two L-shaped slots in the S-shaped radiating patch. In this structure, the S-shaped monopole antenna can create dual resonances within the WLAN frequency range. The placement of two L-shaped slots within the S-shaped monopole antenna creates an extra resonance and the desired resonant frequencies are obtained by adjusting the dimension of the S-shaped monopole and the L-shaped slots. The operating frequencies of the proposed antenna are 2.4/5.2/5.8 GHz, which covers WLAN systems. Also, the two elements array configuration of this S-shaped monopole antenna which can be used in MIMO with a very high isolation over three operational bands is studied. The prototypes of the proposed antenna have been constructed and studied experimentally. Good diversity performance, return loss and radiation pattern characteristics are obtained in the frequency band of interest. Simulated and measured results are presented to validate the usefulness of this small proposed antenna structure for MIMO applications.

Index Terms **─** Diversity antenna, Multi-Output Multi-Input (MIMO) applications, triple-band S-shaped monopole.

I. INTRODUCTION

In wireless systems, signals may combine destructively at a receiver, causing fading to occur. With the rapid growth of wireless communication, it is important to attain sufficient channel capacity and combat multi-path fading and co-channel interferences [1]. In order to improve the quality of wireless downlink signal, more than one antenna is necessary for the terminal side. In this kind of mobile terminal, two or more antenna elements are envisaged and the restricted space available for antenna is an open issue [2]-[3]. Antenna diversity is a well-known technique to enhance the performance of wireless communication systems by reducing the short term fading and co-channel interference effects of the channel [1]. The reliability of the system can be improved with the use of diversity technology, which is achieved by using the information from the different branches available to the receiver so as to increase the signal-to-noise ratio (SNR) at the decoding stage.

In the last few years, there have been rapid developments in wireless local area networks (WLAN). The 2.4/5.2/5.8 GHz (2.4-2.84 GHz/5.15-5.35 GHz/ 5.725-5.825 GHz) bands are demanded in practical WLAN applications. During the last years, there are various antenna designs, which enable antennas with low-profile, lightweight, flush mounted and WLAN devices. These antennas include the planar inverted-F antennas [4], and the slot antennas [5]. Planar monopoles are extremely attractive to be used in WLAN applications, and growing research activities are being focused on them in MIMO application systems, because of its advantages, such as simple structure, small size and low cost. Consequently, a number of planar monopoles with different geometries have been experimentally characterized [6]-[9].

In this paper, we propose a printed omni-directional antenna using S-shaped radiating patch. An S-shaped radiating patch with a pair of L-shaped slots which are printed on a dielectric substrate to generate triple-band operation at 2.4, 5.2, and 5.8 GHz is reported. This

Submitted On: May 13, 2013
Accepted On: May 25, 2015

structure is suitable particularly for WLAN applications. Two-element arrays of such antennas for MIMO applications are analyzed and the results of the pair that provides the lowest mutual coupling and better omni-directional radiation pattern are given. The proposed structure is designed based on the antenna presented in [10], but with a lower mutual coupling and higher isolation. In this paper we present a structure for the MIMO antenna elements, in which the identical two antenna elements are orthogonally placed. Then the two antenna elements have orthogonal polarization which can reduce the mutual coupling between the two antennas. The proposed antenna shows advantages of small size, low cost and good omni-directional radiation characteristics. The presented monopole antenna has a small size of 12×18 mm^2.

II. ANTENNA DESIGN

The presented small monopole antenna fed by a microstrip line is shown in Fig. 1, which is printed on an FR4 substrate of thickness 0.8 mm, permittivity 4.4, and loss tangent 0.018. The basic monopole antenna structure consists of a square patch, a feed line, and a ground plane. The square patch has a width of W. The patch is connected to a feed line with the width of W_f and the length of L_f+L_{gnd}. On the other side of the substrate, a conducting ground plane is placed. The proposed antenna is connected to a 50-Ω SMA connector for signal transmission.

In this study, two L-shaped slots in the S-shaped radiating patch is used to perturb an additional resonance at higher frequencies of WLAN frequency range. In other words, in this structure two L-shaped slots are playing an important role in the triple-band characteristics of this antenna. The final dimensions of the designed antenna are specified in Table 1.

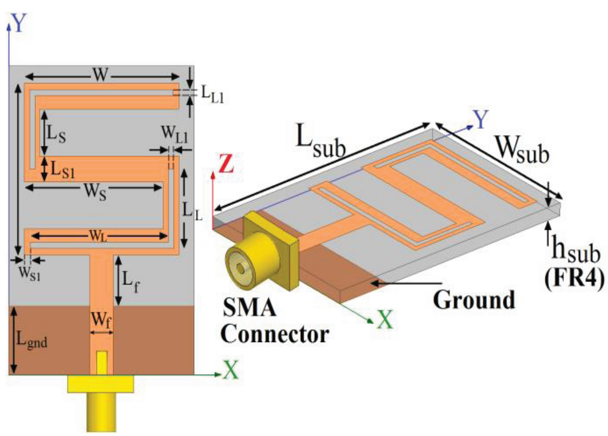

(a) (b)

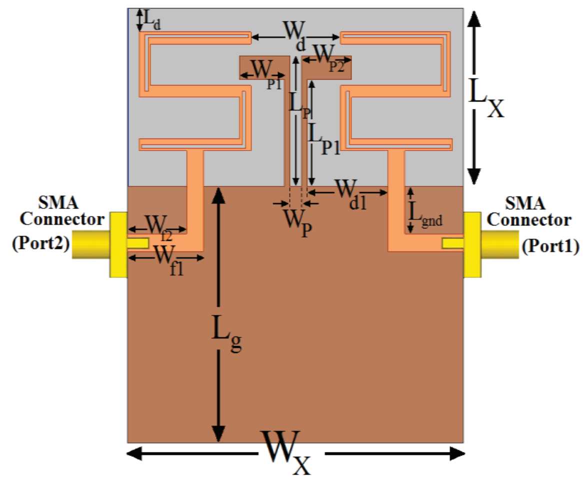

(c)

Fig. 1. Geometry of the proposed S-shaped monopole antenna with a pair of L-shaped slots on the radiating patch: (a) top view, (b) side view, and (c) geometry of the proposed diversity antenna.

Table 1: The final dimensions of the designed antenna

Param.	mm	Param.	mm	Param.	mm
W_{Sub}	12	L_{Sub}	18	W_f	1.5
L_f	3	W	10	L_{gnd}	4
W_S	9.25	L_S	3.5	W_{S1}	0.25
L_{S1}	1	W_L	9.5	L_L	4.75
W_{L1}	0.25	L_{L1}	0.25	L_X	15
W_X	30	L_g	25	W_d	8
L_d	2	W_{d1}	7	L_P	11
W_P	1	W_{P1}	4	L_{P1}	9
W_{P2}	4.5	W_{f1}	7	W_{f2}	5

III. RESULTS AND DISCUSSIONS

A. Monopole antenna for WLAN applications

The proposed microstrip monopole antenna with various design parameters as constructed, and the numerical and experimental results of the input impedance and radiation characteristics are presented and discussed. The parameters of this proposed antenna are studied by changing one parameter at a time and fixing the others. Ansoft HFSS simulations are used to optimize the design and agreement between the simulation and measurement is obtained [11].

Return loss characteristics for ordinary square patch antenna with a rectangular slit (Fig. 2 (a)), S-shaped monopole antenna (Fig. 2 (b)), and the proposed antenna (Fig. 2 (c)) are compared in Fig. 3. As shown in Fig. 3, in order to generate dual-band characteristics (2.4/5.2 GHz), we use S-shaped radiating patch. By adding two

L-shaped slots in the S-shaped radiating patch, a triple-band is achieved that covers all the 2.4/5.2/5.8 GHz WLAN.

In order to understand the phenomenon behind this additional resonance performance, the simulated current distributions on the radiating patch for the ordinary square antenna with a rectangular slit and the S-shaped radiating patch at 2.4 GHz and 5.2 GHz are presented in Figs. 4 (a) and (b), respectively. It is found that by using this S-shaped radiating patch, the second resonance at 5.2 GHz can be achieved. Other important design parameters of this structure are L-shaped slots on the S-shaped radiating patch. Figures 5 (a) and (b) present the simulated current distributions on the radiating patch of the proposed antenna at the second resonance (5.2 GHz), and the third resonance (5.8 GHz), respectively. As shown in Figs. 5 (a) and (b), at the second and third resonances, the current flows are more dominant around of the L-shaped slots [12].

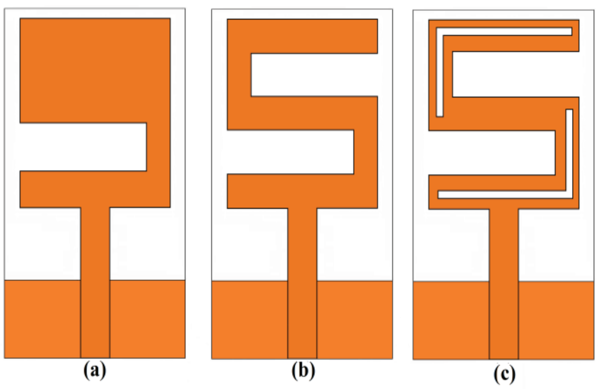

Fig. 2. (a) Ordinary square monopole antenna with a rectangular slit, (b) ordinary S-shaped monopole antenna, and (c) the proposed antenna.

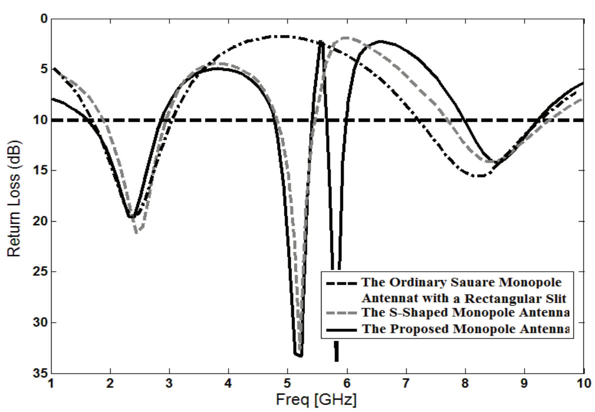

Fig. 3. Simulated return loss characteristics for the various square monopole antenna structures shown in Fig. 2.

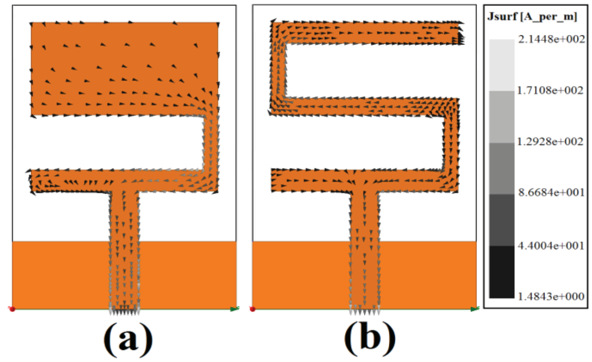

Fig. 4. Simulated surface current distributions on radiating patch for the proposed antenna without L-shaped slots: (a) at the first resonance frequency (2.4 GHz), (b) at the second resonance (5.2 GHz).

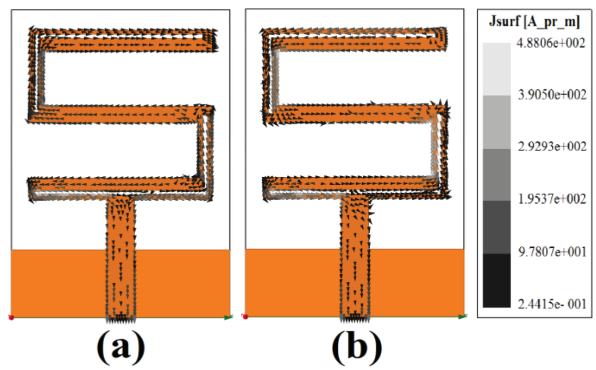

Fig. 5. Simulated surface current distributions on radiating patch for the proposed antenna: (a) at second resonance frequency (5.2 GHz), (b) at third resonance frequency (5.8 GHz).

B. Monopole antenna array structures for MIMO applications

This antenna element can be arrayed for MIMO applications. The performance of an antenna array suitable for MIMO applications is based on various parameters such as mutual coupling, and radiation pattern. As shown in Fig. 1 (c), two such monopole antennas can be arranged back to back with symmetric configuration and is printed on a printed circuit board (PCB). As shown in Fig. 1 (c), in order to increase the isolation and reduce the mutual coupling between the two monopoles, the L-shaped sleeves are introduced in the ground plane of this design. These sleeves on ground plane act as parasitic elements which help to adjust the resonant frequency and improve bandwidth [4]. Each antenna is directly fed by a 50 Ω microstrip line with 1.5 mm in width.

The antenna configuration with detailed dimensions and the effects of some important parameters of the proposed antenna have been fabricated as shown in Fig. 6, and discussed to show how this diversity antenna works. The measured and simulated return loss and mutual coupling characteristic of the proposed antenna were shown in Figs. 7 and 8, respectively. The operating frequencies of the proposed antenna are 2.4/5.2/5.8 GHz, which covers WLAN system. Figure 8, in which the antenna elements are orthogonal, show lower mutual coupling than those structures in which the elements are parallel. For such orthogonal elements, the pattern of each element lies on a plane. As shown in Figs. 7 and 8, there exists a discrepancy between measured data and the simulated results. This discrepancy is mostly due to a number of parameters such as the fabricated antenna dimensions as well as the thickness and dielectric constant of the substrate on which the antenna is fabricated, the wide range of simulation frequencies and also the effect of SMA. In order to confirm the accurate return loss characteristics for the designed antenna, it is recommended that the manufacturing and measurement process need to be performed carefully, besides, SMA soldering accuracy and FR4 substrate quality needs to be taken into consideration [13].

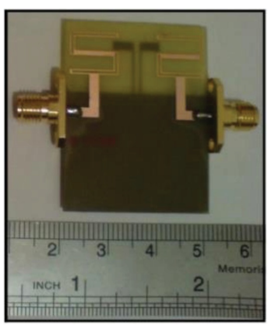

Fig. 6. Photograph of the realized diversity antenna.

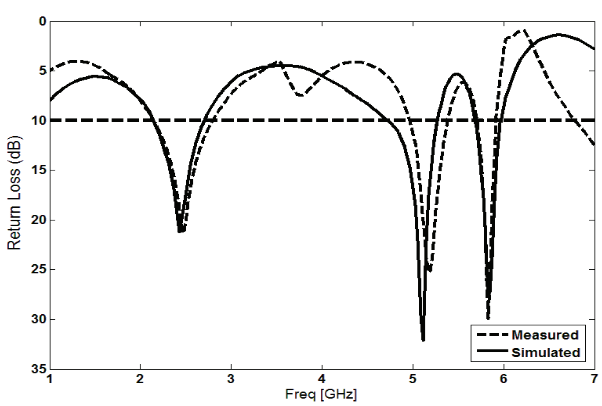

Fig. 7. Measured and simulated return loss of the MIMO configured proposed antenna for arrangement of two elements beside.

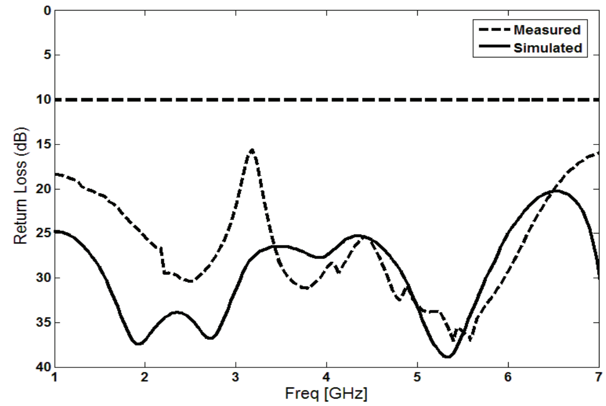

Fig. 8. Measured and simulated insertion loss (mutual coupling) of the MIMO configured proposed antenna for arrangement of two elements beside.

Figures 9, 10 and 11 illustrate the measured radiation patterns at resonance frequencies, including the co-polarization and cross-polarization, in the H-plane (x-z plane) and E-plane (y-z plane) of the two antenna elements. It can be seen that the two antenna elements have orthogonal polarizations, and also the radiation patterns in *x-z* plane are nearly omni-directional for the three frequencies.

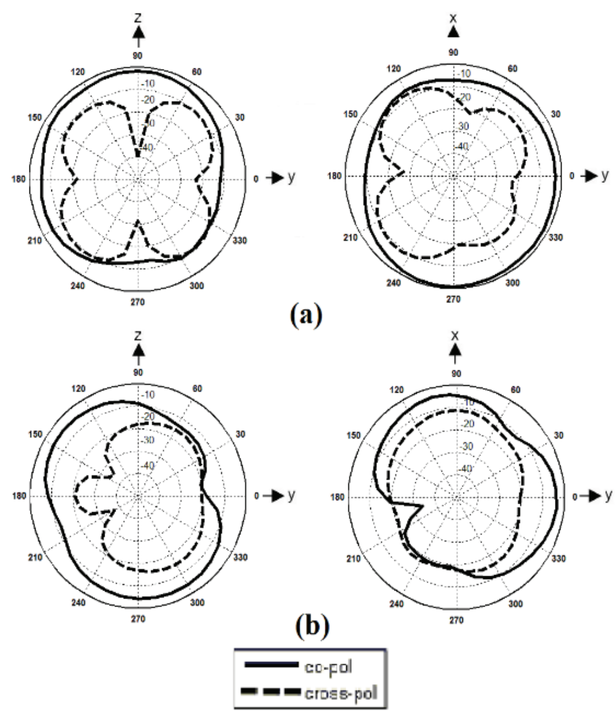

Fig. 9. Measured radiation patterns for monopole 1 (left) and monopole 2 (right) excitations at 2.4 GHz (first resonance frequency).

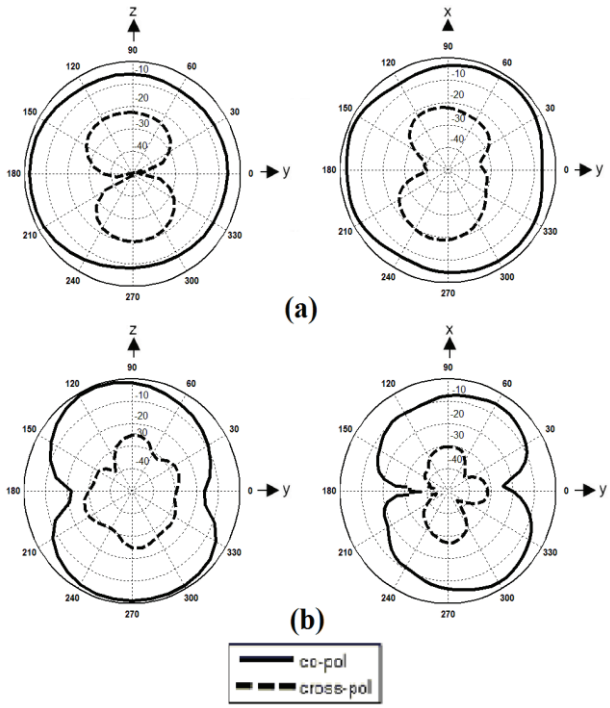

Fig. 10. Measured radiation patterns for monopole 1 (left) and monopole 2 (right) excitations at 5.2 GHz (second resonance frequency).

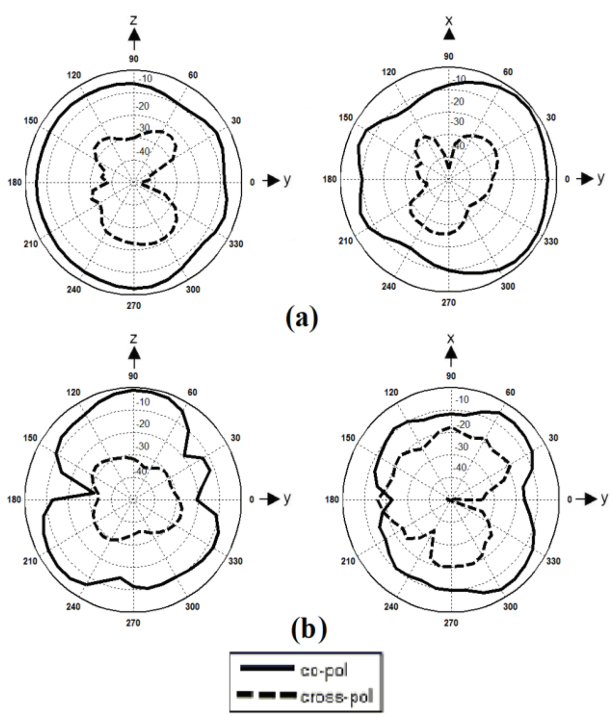

Fig. 11. Measured radiation patterns for monopole 1 (left) and monopole 2 (right) excitations at 5.8 GHz (third resonance frequency).

The envelope correlation can be computed from the S-parameters using the following formula [14]:

$$\rho_e = \frac{\left|S_{11}^* S_{12} + S_{21}^* S_{22}\right|^2}{\left(1-\left|S_{11}\right|^2-\left|S_{12}\right|^2\right)\left(1-\left|S_{22}\right|^2-\left|S_{21}\right|^2\right)}.$$

Figure 12 shows the simulated envelope correlation of the array structure of Fig. 1 (c). For the antenna diversity, the practically acceptable envelope correlation is less than 0.5. The calculated envelope correlation of the proposed antenna array structure of Fig. 1 (c) can be shown to be less than 0.002. The evaluation of results shows that the antenna is a good candidate for diversity system for MIMO application.

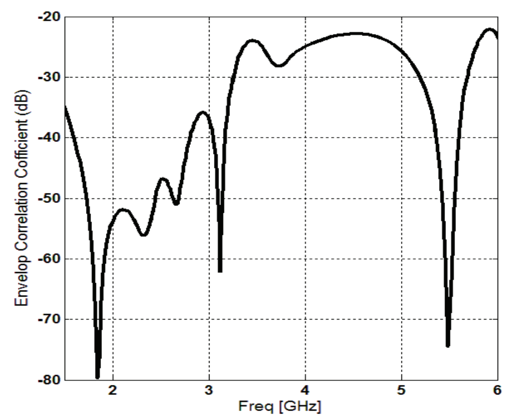

Fig. 12. Simulated envelope correlation coefficient against frequency using HFSS.

IV. CONCLUSION

A new triple-band diversity small printed monopole antenna (PMA) with triple-band performance for WLAN applications, presented in this paper. The operating frequencies of the proposed antenna are 2.4/5.2/5.8 GHz which covers WLAN system. In order to generate a triple-band performance, we insert two L-shaped slots in the S-shaped radiating patch. Also two-element arrays of such antennas in MIMO applications are analyzed. To evaluate the diversity performance, the envelope correlation coefficient of the antenna elements from measured results is calculated. It is proved that the proposed antenna can provide pattern diversity to mitigate multi-path fading problem for WLAN operations. The designed antenna has a small size of 12×18 mm^2. Simulated and experimental results show that the proposed antenna could be a good candidate for MIMO applications.

REFERENCES

[1] R. G. Vaghan and J. B. Andersen, "Antenna diversity in mobile communications," *IEEE Trans. on Veh. Techn.*, vol. 36, no. 4, pp. 149 172, Nov.

1987.

[2] Y. S. Li, W. Li, and W. Yu, "A multi-band/UWB MIMO/diversity antenna with an enhanced isolation using radial stub loaded resonator," Applied Computational Electromagnetics Society (ACES) Journal, vol. 28, no. 1, pp. 8-20, Jan. 2013.

[3] H. Oraizi and B. Rezaei, "Application of inductive loadings for the dual and broad banding of CPW-fed ring antennas," Applied Computational Electromagnetics Society (ACES) Journal, vol. 27, no. 7, pp. 587-595, July 2012.

[4] P. Wang, G. J. Wen, and Y. Huang, "Compact CPW-fed planar monopole antenna with triple-band operation for WLAN/WiMAX applications," Applied Computational Electromagnetics Society (ACES) Journal, vol. 27, no. 8, pp. 691-696, Aug. 2012.

[5] R. Rouhi, Ch. Ghobadi, J. Nourinia, and M. Ojaroudi, "Ultra-wideband small square monopole antenna with band notched function," *Microwave and Optical Tech. Letters*, vol. 52, no. 8, Aug. 2010.

[6] G. Chi, B. Li, and D. Qi, "Dual-band printed diversity antenna for 2.4/5.2 GHz WLAN application," *Microw. Opt. Technol. Lett*., vol. 45, no. 6, pp. 561-563, June 2005.

[7] S. A. Mohammad Nezhad and H. R. Hassani, "A novel triband E-shaped printed monopole antenna for MIMO application," *IEEE Antennas and Wireless Propagation Letters*, vol. 9, pp. 576-579, 2010.

[8] M. Ojaroudi, H. Ebrahimian, Ch. Ghobadi, and J. Nourinia, "Small microstrip-fed monopole printed monopole antenna for UWB applications," *Microwave and Optical Tech. Letters*, vol. 52, no. 8, Aug. 2010.

[9] M. P. Karaboikis, V. C. Papamichael, G. F. Tsachtsiris, C. F. Soras, and V. T. Makios, "Integrating compact printed antennas onto small diversity/MIMO terminals," *IEEE Trans. Antennas Propag*., vol. 52, no. 7, pp. 2067-2078, July 2008.

[10] M. Ojaroudi, S. A. Ghorashi, and N. Ojaroudi, "Design of triple-band S-shaped monopole antenna with a pair of L-shaped slots for MIMO applications," *GeMic*, 2012.

[11] Ansoft High Frequency Structure Simulation (HFSS), ver. 13, Ansoft Corporation, 2010.

[12] M. Ojaroudi, Sh. Yzdanifard, N. Ojaroudi, and M. Nasser-Moghaddasi, "Small square monopole antenna with enhanced by using inverted T-shaped slot and conductor-backed plane," *IEEE Transactions on Antenna and Propagation*, vol. 59, no. 2, pp. 670-674, Feb. 2011.

[13] A. Ghazi, M. N. Azarmanesh, and M. Ojaroudi, "Muti-resonance square monopole antenna for ultra-wideband applications," *Progress In Electromagnetics Research C*, vol. 14, pp. 103-113, 2010.

[14] T. Y. Wu, S. T. Fang, and K. L. Wong, "A printed diversity dual-band monopole antenna for WLAN operation in the 2.4 and 5.2 GHz bands," *Microwave Opt. Technol. Lett*., vol. 36, no. 25, pp. 436-439, Apr. 2003.

Study on Band Gaps of the Photonic Crystal in THz Frequency Range Based on the Periodic WCS-PSTD Method

Juan Chen, Anxue Zhang, and Jianjun Li

[1] The Key Laboratory for Physical Electronics and Devices of the Ministry of Education
Xi'an Jiaotong University, Xi'an, 710049, China
chen.juan.0201@mail.xjtu.edu.cn

Abstract **─** In this paper, a periodic weakly conditionally stable -pseudospectral time domain (WCS-PSTD) method is presented to simulate photonic crystal in Terahertz frequency range. The time step size in this method is only determined by the mesh length Δz and the spatial discretization along the z direction only needs two cells per minimum wavelength. The 3D formulas of the method are presented and the time stability condition of the method is demonstrated. Numerical results show that this method is more efficient than the periodic finite difference time domain (FDTD) method in terms of computer memory and computation time.

Index Terms **─** Finite difference time domain, pseudospectral method, time stability condition, weakly conditionally stable.

I. INTRODUCTION

Terahertz (THz) wave has significant transmission loss in free space, so the design and fabrication of controlling device for THz frequency radiation are imperative. Photonic crystal as a novel artificial material has photonic band gaps characteristic [1, 2]. It can be used to control the transmission of THz wave. Therefore, study on the photonic crystal has important effect on the development of Terahertz technique.

The finite-difference time-domain (FDTD) method is one of the most effective tools for the analysis of the photonic crystal [3, 4]. However, because the cross-section of the photonic crystal is circular, staircase approximation is used to model the curved surface. To decrease the approximation error, the cells' size must be very small compared with the wavelength. These fine cells reduce the time step size in the FDTD method, and hence, the FDTD method is computationally expensive. In addition, in the THz frequency region, the longitudinal direction of the photonic crystal is electrically large structure in most cases. Applying the FDTD method to simulate electrically large object, to decrease the dispersion error, a large number of cells (typically 10-20 cells per wavelength) are required. This stringent requirement severely limits the length of the photonic crystal solvable and increases the computation time inevitably.

Recently, a new weakly conditionally stable-pseudospectral time domain (WCS-PSTD) method [5] which is based on the hybrid implicit explicit difference technique [6-9] and the pseudospectral scheme [10-12] is presented. In this method, the time step size is not confined by fine cells and is extremely useful for problems with very fine structures along one or two directions. Meanwhile, this method allows a coarse spatial discretization that only needs two cells per minimum wavelength. Thus, for the simulation of the object which has fine and electrically large structures simultaneously, the WCS-PSTD algorithm is more efficient than the FDTD method in terms of computer memory and computation time. However, for the simulation of the photonic crystal which has periodic structures, the WCS-PSTD method needs to cope with the periodic boundary.

To solve this problem, this paper presents a periodic WCS-PSTD method which introduces the periodic boundary in the conventional WCS-PSTD method [5]. It also combines the hybrid implicit explicit difference technique with the pseudospectral scheme. The time step size in this method is not confined by fine cells and the space discretization along electrically large direction only needs two cells per minimum wavelength. The 3D formulas of the periodic WCS-PSTD method are presented, and final updating equations are given. The time stability condition and space discretization limitation of the method are discussed. When this method is applied to simulate photonic crystal, high computational efficiency is obtained and less computer memory is required, which is demonstrated through numerical examples by comparing with the periodic FDTD method.

By using the periodic WCS-PSTD method to simulate the photonic crystal, some useful conclusions are obtained. The simulation result shows that the photonic crystal has obvious band gap characteristic. The frequency and bandwidth of the band gap have relation with the permittivity of the photonic crystal. As the

Submitted On: June 19, 2014
Accepted On: June 11, 2015

increase of the permittivity, the frequency of the band gap decreases and the relative bandwidth of the band gap becomes wider. Besides, the smaller the radius and period length of the photonic crystal are, the higher the frequency range of the band gap. The relative bandwidth of the band gap reaches maximum value when the ratio between the diameter of the photonic crystal and the period length is 0.6.

II. FORMULATIONS

Figure 1 shows a schematic view of the photonic crystal under study. The cross-section of the photonic crystal is circular and needs to use very small cells to staircase approximation, as shown in Fig. 2. The length (L) of the photonic crystal is much larger than the wavelength in the THz frequency region. Typically, it is 20-30 times the wavelength. So, the photonic crystal is a complicated structure which has fine size (along the x and y direction) and electrically large size (along the z direction) simultaneously.

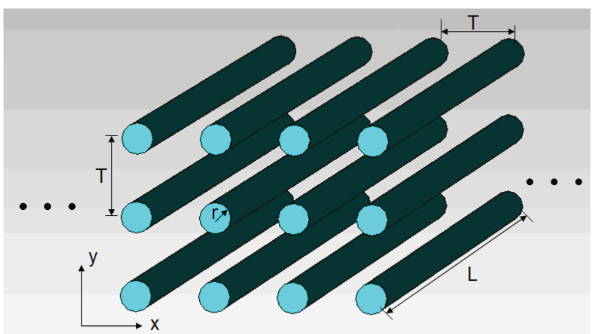

Fig. 1. Schematic view of photonic crystal.

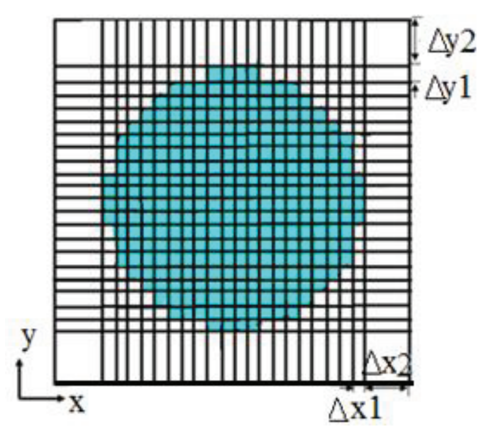

Fig. 2. The staircase approximation of the photonic crystal's cross-section.

In the FDTD method, the small cell sizes $\Delta x1$ and $\Delta y1$ will confine the time step size Δt and result in a large number of computation time. To remove the confine of the fine space increment on the time step size, the periodic WCS-PSTD method uses a hybrid implicit explicit difference technique to replace the explicit difference along the x and y directions. The 3D formulas for the periodic WCS-PSTD method are as follows:

<First procedure>

$$\varepsilon \frac{E_x^{n+1/2} - E_x^n}{\Delta t} = \frac{\partial\left(H_z^{n+1/2} + H_z^n\right)}{2\partial y} - \frac{\partial H_y^n}{\partial z}, \tag{1.1}$$

$$E_y^{n+1/2} = E_y^n, \tag{1.2}$$

$$\varepsilon \frac{E_z^{n+1/2} - E_z^n}{\Delta t} = \frac{\partial\left(H_y^{n+1/2} + H_y^n\right)}{2\partial x}, \tag{1.3}$$

$$H_x^{n+1/2} = H_x^n, \tag{1.4}$$

$$\mu \frac{H_y^{n+1/2} - H_y^n}{\Delta t} = \frac{\partial\left(E_z^{n+1/2} + E_z^n\right)}{2\partial x} - \frac{\partial E_x^{n+1/2}}{\partial z}, \tag{1.5}$$

$$\mu \frac{H_z^{n+1/2} - H_z^n}{\Delta t} = \frac{\partial\left(E_x^{n+1/2} + E_x^n\right)}{2\partial y}. \tag{1.6}$$

<Second procedure>

$$E_x^{n+1} = E_x^{n+1/2}, \tag{2.1}$$

$$\varepsilon \frac{E_y^{n+1} - E_y^{n+1/2}}{\Delta t} = \frac{\partial H_x^{n+1/2}}{\partial z} - \frac{\partial\left(H_z^{n+1/2} + H_z^{n+1}\right)}{2\partial x}, \tag{2.2}$$

$$\varepsilon \frac{E_z^{n+1} - E_z^{n+1/2}}{\Delta t} = -\frac{\partial\left(H_x^{n+1/2} + H_x^{n+1}\right)}{2\partial y}, \tag{2.3}$$

$$\mu \frac{H_x^{n+1} - H_x^{n+1/2}}{\Delta t} = \frac{\partial E_y^{n+1}}{\partial z} - \frac{\partial\left(E_z^{n+1/2} + E_z^{n+1}\right)}{2\partial y}, \tag{2.4}$$

$$H_y^{n+1} = H_y^{n+1/2}, \tag{2.5}$$

$$\mu \frac{H_z^{n+1} - H_z^{n+1/2}}{\Delta t} = -\frac{\partial\left(E_y^{n+1/2} + E_y^{n+1}\right)}{2\partial x}, \tag{2.6}$$

where n and Δt are the index and size of time step.

The calculation for one discrete time step is performed using two procedures in the periodic WCS-PSTD method. The first procedure is based on Eqs. (1.1)-(1.6), and the second procedure is based on Eqs. (2.1)-(2.6). It can be seen from these equations that for the spatial derivatives ∂x and ∂y, a hybrid implicit explicit difference technique is used; thus, the equations (1.1), (1.3), (1.5), (1.6), (2.2)-(2.4) and (2.6) can't be calculated directly, because they all include the unknown components defined at the same time step. For example, updating of $E_x^{n+1/2}$ component, as shown in Eq. (1.1), needs the unknown $H_z^{n+1/2}$ components at the same time step; thus the $E_x^{n+1/2}$ component has to be updated implicitly. By substituting Eq. (1.6) into Eq. (1.1), the equation for $E_x^{n+1/2}$ component is given as:

$$\left(1-\frac{\Delta t^2}{4\varepsilon\mu}\frac{\partial^2}{\partial^2 y}\right)E_x^{n+1/2} = \left(1+\frac{\Delta t^2}{4\varepsilon\mu}\frac{\partial^2}{\partial^2 y}\right)E_x^n - \frac{\Delta t}{\varepsilon}\frac{\partial H_y^n}{\partial z} + \frac{\Delta t}{\varepsilon}\frac{\partial H_z^n}{\partial y}. \tag{3}$$

Because the periodic WCS-PSTD method applies the hybrid implicit explicit difference technique to the derivatives ∂x and ∂y, its time step size will have no relation with the spatial increments Δx and Δy. This will be demonstrated in the next section.

In the FDTD method, to decrease the dispersion error resulted from the spatial finite difference, spatial discretization should satisfy the condition that 10-20 cells per wavelength are required. This stringent requirement causes a large number of cells along the z direction in the simulation of the photonic crystal, because the longitudinal direction of the photonic crystal is often larger than the wavelength. It not only severely increases the memory requirement, but also increases the computation time.

To overcome the limit of the wavelength on the space discretization Δz, the periodic WCS-PSTD method uses a Fourier transform algorithm instead of finite difference to represent the spatial derivative ∂z. This allows a coarse spatial discretization along z direction that only two nodes per minimum wavelength are required (the demonstration will be shown in the next section). For other spatial derivatives ∂x and ∂y, it also applies centered second-order finite differences as that in the standard FDTD method. Thus, the equation for $E_x^{n+1/2}$ component can be obtained as follows:

$$\begin{aligned}
&\left(1+2\tau_1\right)E_x^{n+1/2}\left(i+1/2,j,k\right)-\tau_1E_x^{n+1/2}\left(i+1/2,j+1,k\right)\\
&-\tau_1E_x^{n+1/2}\left(i+1/2,j-1,k\right)\\
&=\left(1-2\tau_1\right)E_x^{n}\left(i+1/2,j,k\right)+\tau_1E_x^{n}\left(i+1/2,j+1,k\right)\\
&+\tau_1E_x^{n}\left(i+1/2,j-1,k\right)\\
&+\frac{\Delta t}{\varepsilon\Delta y}\left[H_z^n\left(i+1/2,j+1/2,k\right)-H_z^n\left(i+1/2,j-1/2,k\right)\right]\\
&-\frac{\Delta t}{\varepsilon}\Im^{-1}\left\{\hat{j}k_z\Im\left[H_y^n\left(i+1/2,j,k\right)\right]\right\},
\end{aligned} \tag{4}$$

where, $\hat{j}=\sqrt{-1}$, $\tau_1=\Delta t^2/4\varepsilon\mu\Delta y^2$, Δy is the spatial increment along y direction; *i*, *j*, and *k* denote the indices of spatial increments respectively along x, y, and z directions; $\Im$ and $\Im^{-1}$ represent the Fourier transforms and inverse Fourier transforms which were described in detail in references [13].

After $E_x^{n+1/2}$ component is obtained by using equation (4), component $H_z^{n+1/2}$ is explicitly updated straightforward as follows:

$$\begin{aligned}
&H_z^{n+1/2}\left(i+1/2,j+1/2,k\right)=H_z^{n}\left(i+1/2,j+1/2,k\right)\\
&+\frac{\Delta t}{2\mu\Delta y}\begin{bmatrix}E_x^{n+1/2}\left(i+1/2,j+1,k\right)-E_x^{n+1/2}\left(i+1/2,j,k\right)\\ +E_x^{n}\left(i+1/2,j+1,k\right)-E_x^{n}\left(i+1/2,j,k\right)\end{bmatrix}.
\end{aligned} \tag{5}$$

By following the same procedure, the equation for $E_z^{n+1/2}$ component can be obtained as follows:

$$\begin{aligned}
&\left(1+2\tau_2\right)E_z^{n+1/2}\left(i,j,k+1/2\right)-\tau_2E_z^{n+1/2}\left(i+1,j,k+1/2\right)\\
&-\tau_2E_z^{n+1/2}\left(i-1,j,k+1/2\right)\\
&=\left(1-2\tau_2\right)E_z^{n}\left(i,j,k+1/2\right)+\tau_2E_z^{n}\left(i+1,j,k+1/2\right)\\
&+\tau_2E_z^{n}\left(i-1,j,k+1/2\right)\\
&+\frac{\Delta t}{\varepsilon\Delta x}\left[H_y^n\left(i+1/2,j,k\right)-H_y^n\left(i-1/2,j,k\right)\right]\\
&-\frac{\Delta t^2}{2\varepsilon\mu\Delta x}\Im^{-1}\left\{\hat{j}k_z\Im\left[E_x^{n+1/2}\left(i+1/2,j,k\right)\right]\right\}\\
&+\frac{\Delta t^2}{2\varepsilon\mu\Delta x}\Im^{-1}\left\{\hat{j}k_z\Im\left[E_x^{n+1/2}\left(i-1/2,j,k\right)\right]\right\},
\end{aligned} \tag{6}$$

where, $\tau_2=\Delta t^2/4\varepsilon\mu\Delta x^2$, Δx is the spatial increment along x direction.

Because the photonic crystal has periodic structure along the x direction, the computation of $E_z^{n+1/2}$ component at the periodic boundary needs to be modified as follows:

$$\begin{aligned}
&E_z^{n+1/2}\left(i,j,k+1/2\right)\\
&-\tau_2\left[E_z^{n+1/2}\left(2,j,k+1/2\right)-E_z^{n+1/2}\left(1,j,k+1/2\right)\right]\\
&+\tau_2\left[E_z^{n+1/2}\left(I,j,k+1/2\right)-E_z^{n+1/2}\left(I-1,j,k+1/2\right)\right]\\
&=E_z^{n}\left(i,j,k+1/2\right)\\
&+\tau_2\left[E_z^{n}\left(2,j,k+1/2\right)-E_z^{n}\left(1,j,k+1/2\right)\right]\\
&-\tau_2\left[E_z^{n}\left(I,j,k+1/2\right)-E_z^{n}\left(I-1,j,k+1/2\right)\right]\\
&+\frac{\Delta t}{\varepsilon\Delta x}\left[H_y^n\left(1+1/2,j,k\right)-H_y^n\left(I-1/2,j,k\right)\right]\\
&-\frac{\Delta t^2}{2\varepsilon\mu\Delta x}\Im^{-1}\left\{\hat{j}k_z\Im\left[E_x^{n+1/2}\left(1+1/2,j,k\right)\right]\right\}\\
&+\frac{\Delta t^2}{2\varepsilon\mu\Delta x}\Im^{-1}\left\{\hat{j}k_z\Im\left[E_x^{n+1/2}\left(I-1/2,j,k\right)\right]\right\},
\end{aligned} \tag{7}$$

here, $i=1$ and I denote the meshes at the periodic boundary respectively.

The computations for other components $H_y^{n+1/2}$, E_y^{n+1}, E_z^{n+1}, H_x^{n+1} and H_z^{n+1} can be obtained by following the same procedure and will not be discussed in detail.

It should be noted that, in contrast to the standard Yee's algorithm, the periodic WCS-PSTD method does not require a spatially staggered grid along the z direction, because Fourier transforms operation is global. It means that the field components E_x and H_y, E_y and H_x are located at the same nodes in the periodic WCS-PSTD method, as shown in Fig. 3.

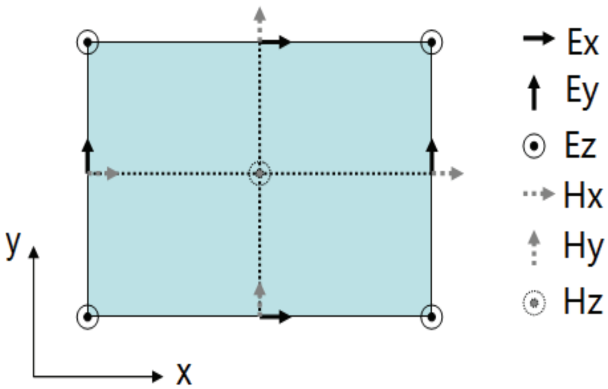

Fig. 3. Spatial grid of the field components in the periodic WCS-PSTD method.

III. STABILITY AND NUMERICAL DISPERSION ANALYSIS

The relations between field components of Eqs. (1) and (2) can be represented in a matrix form as follows:

$$[E]U^{n+1/2} = [F]U^{n}, \tag{8}$$

$$[C]U^{n+1} = [D]U^{n+1/2}, \tag{9}$$

where,

$$[E] = \begin{bmatrix} 1 & 0 & 0 & 0 & 0 & -aD_y/2 \\ 0 & 1 & 0 & 0 & 0 & 0 \\ 0 & 0 & 1 & 0 & -aD_x/2 & 0 \\ 0 & 0 & 0 & 1 & 0 & 0 \\ bD_z & 0 & -bD_x/2 & 0 & 1 & 0 \\ -bD_y/2 & 0 & 0 & 0 & 0 & 1 \end{bmatrix},$$

$$[F] = \begin{bmatrix} 1 & 0 & 0 & 0 & -aD_z & aD_y/2 \\ 0 & 1 & 0 & 0 & 0 & 0 \\ 0 & 0 & 1 & 0 & aD_x/2 & 0 \\ 0 & 0 & 0 & 1 & 0 & 0 \\ 0 & 0 & bD_x/2 & 0 & 1 & 0 \\ bD_y/2 & 0 & 0 & 0 & 0 & 1 \end{bmatrix},$$

$$[C] = \begin{bmatrix} 1 & 0 & 0 & 0 & 0 & 0 \\ 0 & 1 & 0 & 0 & 0 & aD_x/2 \\ 0 & 0 & 1 & aD_y/2 & 0 & 0 \\ 0 & -bD_z & bD_y/2 & 1 & 0 & 0 \\ 0 & 0 & 0 & 0 & 1 & 0 \\ 0 & bD_x/2 & 0 & 0 & 0 & 1 \end{bmatrix},$$

$$[D] = \begin{bmatrix} 1 & 0 & 0 & 0 & 0 & 0 \\ 0 & 1 & 0 & aD_z & 0 & -aD_x/2 \\ 0 & 0 & 1 & -aD_y/2 & 0 & 0 \\ 0 & 0 & -bD_y/2 & 1 & 0 & 0 \\ 0 & 0 & 0 & 0 & 1 & 0 \\ 0 & -bD_x/2 & 0 & 0 & 0 & 1 \end{bmatrix},$$

$U^n = \begin{bmatrix} E_x^n & E_y^n & E_z^n & H_x^n & H_y^n & H_z^n \end{bmatrix}'$, $a = \Delta t/\varepsilon$, $b = \Delta t/\mu$, $D_m = \partial/\partial m$ ($m = x, y, z$) represents the first derivative operator with respect to m.

By substituting Eq. (9) into Eq. (8), it obtains:

$$\left([E][C]\zeta - [E][D][E]^{-1}[F]\right)U^n = 0, \tag{10}$$

ζ indicates growth factor. By applying the forward Fourier transforms to both sides of equation (10), it obtains equation (11), where, $X = \dfrac{abD_x^2}{4}$, $Z = \dfrac{ab(jk_z)^2}{4}$, $Y = \dfrac{abD_y^2}{4}$, $S = (1-X)(1-Y)$, $T = \dfrac{abD_xD_y}{4}$:

$$\begin{bmatrix} \zeta-1 & -T(\zeta+1) & 0 & 0 & aD_z & -\dfrac{aD_y}{2}(\zeta+1) \\ \dfrac{2T}{(1-Y)} & \zeta-1 & 0 & -aD_z & \dfrac{-aD_zT}{(1-Y)} & \dfrac{aD_x}{2}\left(\zeta+\dfrac{1+Y}{1-Y}\right) \\ 0 & 0 & \zeta-1 & \dfrac{aD_y}{2}(\zeta+1) & \dfrac{-aD_x(\zeta+1)}{2} & 0 \\ \dfrac{-bD_zT(1+Y)}{S} & -b\zeta D_z & \dfrac{bD_y}{2}\left(\zeta+\dfrac{(1+X)}{(1-X)}\right) & \zeta-1 & \dfrac{2T(1-Y+2Z)}{S} & \dfrac{-abD_xD_zY}{S} \\ b\zeta D_z & 0 & \dfrac{-bD_x}{2}(\zeta+1) & -T(\zeta+1) & \zeta-1 & 0 \\ \dfrac{-bD_y}{2}(\zeta+1) & \dfrac{bD_x}{2}(\zeta+1) & 0 & 0 & 0 & \zeta-1 \end{bmatrix} U^n = 0. \tag{11}$$

For a nontrivial solution of (11), the determinant of the coefficient matrix in (11) should be zero. It can be obtained:

$$\left(\zeta-1\right)^2\begin{pmatrix}\left(\zeta-1\right)^2-4Z\zeta-Y\left(\zeta+1\right)^2\\ -X\left(\zeta+1\right)^2+XY\left(\zeta+1\right)^2\end{pmatrix}^2=0. \quad (12)$$

By solving equation (12), the growth factor ζ is obtained:

$$\zeta_1=1, \quad (13)$$

$$\zeta_{2,3}=\frac{N\pm\sqrt{N^2-R^2}}{R}, \quad (14)$$

where, $R=1-X-Y+XY$, $N=1+X+Y+2Z-XY$. According to the stability condition during field advancement, the module of growth factor ζ cannot be larger than 1. In equation (14), the relation $\left|\zeta_{2,3}=1\right|$ can be obtained when the condition $R^2\geq N^2$ is satisfied. D_x and D_y represent the first derivative operator with respect to x and y. They are approximated by centered second-order finite differences. So it has the relations $D_x=2j\sin\left(k_x\Delta x/2\right)/\Delta x$ and $D_y=2j\sin\left(k_y\Delta y/2\right)/\Delta y$ [6],

$$R^2\geq N^2\Rightarrow 1+Z\geq 0. \quad (15)$$

Because the maximum value of k_z is $\frac{2\pi}{2\Delta z}$, it has:

$$ab\left(\frac{2\pi}{2\Delta z}\right)^2\leq 4\Rightarrow\Delta t\leq\frac{2\Delta z}{c\pi}, \quad (16)$$

where, $c=1/\sqrt{\varepsilon\mu}$ is the speed of light in the medium.

It can be seen from Eq. (16) that the maximum time step size in the periodic WCS-PSTD method is only determined by the cell size Δz. This is very useful when the object of analysis has fine scale dimensions along the x and y directions.

By substituting the expression $\zeta=e^{j\omega\Delta t}$ into equation (12), the dispersion relation for the periodic WCS-PSTD method can be obtained as follows:

$$\sin^2\left(\frac{\omega\Delta t}{2}\right)=\frac{r_y^2+r_x^2+r_z^2+r_x^2r_y^2}{1+r_x^2+r_y^2+r_x^2r_y^2}, \quad (17)$$

where, $r_z=\left(c\Delta tk_z/2\right)^2$, $r_x=\left(c\Delta t\sin\left(k_x\Delta x/2\right)/\Delta x\right)^2$, $r_y=\left(c\Delta t\sin\left(k_y\Delta y/2\right)/\Delta y\right)^2$. It can be seen from equation (17) that the numerical dispersion error of the periodic WCS-PSTD method has no relation with the spatial cell size Δz. It is only decided by the cell sizes Δx, Δy, and the time step size Δt. As a result, the spatial cell size Δz is not confined by the wavelength. It only needs to satisfy the Nyquist sampling theorem that only two nodes per minimum wavelength are required along the z direction.

It concludes from above analysis that in the periodic WCS-PSTD method, the time step size Δt is only determined by the spatial increment Δz, and spatial increment Δz only needs to satisfy with the condition: $\Delta z\leq\lambda_{\text{minimum}}/2$. This will be very useful in the simulation of the photonic crystal, because the photonic crystal has very fine scale along x and y directions and is electrically large along z direction. For solving this problem the periodic WCS-PSTD method is more efficient than the periodic FDTD method in terms of computer memory and computation time, which will be demonstrated in next section.

IV. SIMULATION AND ANALYSIS

To demonstrate the accuracy and efficiency of the periodic WCS-PSTD method, the photonic crystal shown in Fig. 1 is simulated. The radius (r) and length (L) of the photonic crystal are 20 um and 3000 um, respectively. The period length of the photonic crystal is T=100 um. The material of the photonic crystal is silicon with dielectric constant $\varepsilon_r=11.7$. A uniform plane wave polarized along the x direction is normally incident on the photonic crystal. The propagation direction of the wave is along the y direction. The time dependence of the excitation function is as follows:

$$E_x(t)=\exp[-\frac{4\pi(t-t_0)^2}{t_1^2}], \quad (18)$$

where, t_0 and t_1 are constants, and both equal to 1×10^{-12}s. In such a case, the highest frequency of interest is 2 THz and the minimum wavelength of the source is about 150 um.

The periodic WCS-PSTD method is used to simulate the transmitted field at the back of the photonic crystal. For comparison, the results calculated by the periodic FDTD method are also shown. Because the structure has circular cross-section, it is discretized by using staircase approximation, as shown in Fig. 2. To guarantee the computational accuracy, the circle is discretized by using 20×20 cells, so the cell sizes $\Delta x1$ and $\Delta y1$ are both equal to 2 um, corresponding to 1/75 of the minimum wavelength. In other computation domain, $\Delta x2$ and $\Delta y2$ are 3 um and 15 um, respectively. Along the z direction, for the periodic FDTD method, considering the limit of the wavelength on the space discretization, the space increment Δz is selected to be 15 um, corresponding to 1/10 of the minimum wavelength. While for the periodic WCS-PSTD method, space increment Δz can be increased to 75 um, corresponding to 1/2 of the minimum wavelength. To cut off the outer boundary, periodic boundary condition is applied along the x direction and convolutional perfectly matched layer (CPML) that are ten cells thick are applied along the y and z directions. Thus, for the periodic FDTD and periodic WCS-PSTD methods, the total mesh numbers are $40\times110\times240$ and $40\times110\times80$, respectively. The time step size in the periodic FDTD method is:

$$\Delta t = 1\Big/ c\sqrt{\left(\frac{1}{2\times10^{-6}}\right)^2+\left(\frac{1}{2\times10^{-6}}\right)^2+\left(\frac{1}{15\times10^{-6}}\right)^2} = 4.69\times10^{-3}\text{ps},$$

which is the maximum time step size to ensure the numerical stability. In the periodic WCS-PSTD method, the time step size that is only determined by cell size Δz is selected to be $\Delta t = \dfrac{2\times75\times10^{-6}}{c\pi} = 159\times10^{-3}$ ps, which is 34 times as that of the periodic FDTD method.

Figure 4 depicts the transmitted field E_x calculated by using the periodic FDTD method and the periodic WCS-PSTD method. It can be seen from this figure that the results of these two methods agree very well with each other, which shows the periodic WCS-PSTD method has high computational accuracy.

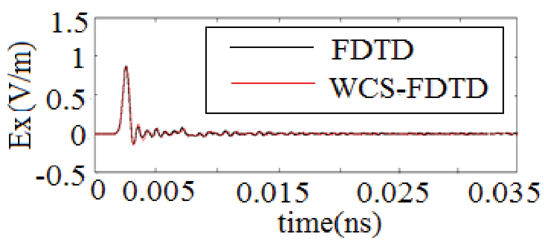

Fig. 4. The transmitted field E_x calculated by using periodic FDTD method and periodic WCS-PSTD method.

The computation time and memory requirement of the simulation above are summarized in Table 1. It can be seen from this table that both the memory requirement and computation time of the periodic WCS-PSTD method are reduced significantly compared with those of the periodic FDTD method. Because large spatial cell and large time step size are used, the memory requirement of the periodic WCS-PSTD method is reduced by 60%, and its computation time is almost 1/30 of that of the periodic FDTD method.

Table 1: Simulation time and memory requirement for the periodic FDTD method and periodic WCS-PSTD method

	Δz (um)	Δt (ps)	Time (minute)	Memory Requirement (Mb)
FDTD method	15	0.0046	320	311.73
WCS-PSTD method	75	0.159	12	115.45

The transmission coefficient (Tr) of the photonic crystal calculated by using the periodic FDTD method and the periodic WCS-PSTD method are presented in Fig. 5. The computation formula of Tr is as follows:

$$T_r = 20\log_{10}\left|E_x / E_x^{'}\right|, \tag{19}$$

here, E_x denotes the transmitted field E_x calculated by using the periodic FDTD method and the periodic WCS-PSTD method; $E_x^{'}$ is the magnitude of the incident wave.

It can be seen from Fig. 5 that in the frequency range from 1.5 THz to 1.8 THz, the transmission coefficient Tr is below to -10 dB. This is a direct evidence of that the photonic crystal has obvious band gap in this frequency range. The relative bandwidth of the band gap is 18.18%. The distribution of the electric field E_x at frequency 1.7 THz is shown in Fig. 6. From this figure, it can be seen that the incident wave is reflected completely and little wave penetrates the photonic crystal at this frequency.

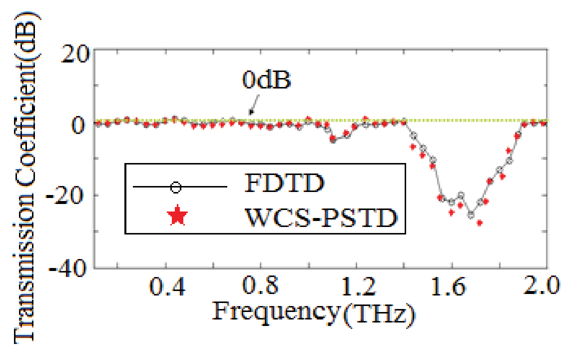

Fig. 5. The transmission coefficient of the photonic crystal calculated by using the periodic FDTD method and the periodic WCS-PSTD method.

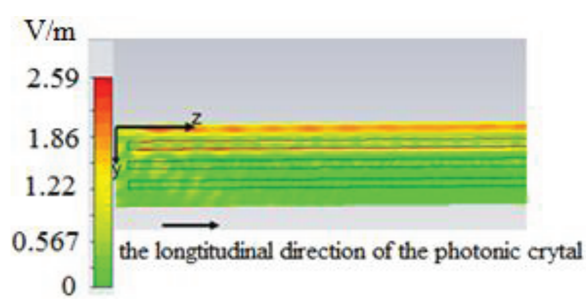

Fig. 6. The distribution of the electric field E_x at frequency 1.7 THz.

It should be noted that in Fig. 5 there is a slightly divergence between the results of the periodic FDTD method and the periodic WCS-PSTD method at 1.7 THz. The difference between these two methods in time domain is too small to be neglected, as shown in Fig. 4, but in frequency domain, it is enlarged by the resonance effect of the photonic crystal at 1.7 THz. The divergence between these two methods is brought about by the splitting-error in the periodic WCS-PSTD method. The periodic WCS-PSTD method applies the hybrid implicit explicit difference technique. This technique will bring a splitting error which is proportional to the time step size. The detailed discussion about the splitting error of the hybrid implicit explicit difference technique has been presented in [14]. So, compared with the periodic FDTD method, the accuracy of the WCS-PSTD is reduced slightly. However, this reduction of the accuracy doesn't affect the periodic WCS-PSTD method to get correct results. The periodic WCS-PSTD method can be used in the analysis which doesn't require the accuracy strictly.

Because the periodic WCS-PSTD method is more efficient than the periodic FDTD method in terms of computer memory and computational time, it is used to analyze the band gap characteristic of the photonic crystal in detail.

Firstly, the relation between the frequency range of band gap and the radius of the photonic crystal is analyzed. The length and period of the photonic crystal is 3000 um and 100 um. The radius of the photonic crystal increases from 5 um to 40 um. The variations of the frequency range of the band gap with respect to radius are shown in Table 2. In this table, Rt which is equal to $2 \times r/T$ represents the ratio between the diameter of the photonic crystal and the period length. It can be seen from this table that as the increase of the radius, the band gap of the photonic crystal moves to a lower frequency range. The relative bandwidth of the band gap has maximum value equal to 29.85% when the radius of the photonic crystal is 30 um.

Table 2: Variations of the frequency range of the band gap with respect to the radius

r (um)	Rt	Frequency Range (THz)	Relative Bandwidth
10	0.2	2.70-2.80	3.64%
15	0.3	1.97-2.06	4.47%
20	0.4	1.50-1.80	18.18%
25	0.5	1.30-1.75	29.51%
30	0.6	1.14-1.54	29.85%
35	0.7	1.03-1.33	25.42%
40	0.8	0.97-1.18	19.53%

When it keeps the radius r=20 um unchanged and increases the period length of the photonic crystal from 50 um to 200 um, the band gap of the photonic crystal also moves to a lower frequency range, as shown in Table 3. The relative bandwidth of the band gap has maximum value equal to 30.12% when period length of the photonic crystal is 66.66 um.

From Table 2 and 3, we can see that the relative bandwidth of the band gap is mainly determined by the ratio between the diameter and the period length. It reaches its maximum value when the ratio is 0.6, no matter what the radius and period length are.

Table 3: Variations of the frequency range of the band gap with respect to the period length

T (um)	Rt	Frequency Range (THz)	Relative Bandwidth
50	0.8	1.94-2.37	19.95%
60	0.7	1.78-2.32	26.34%
66.66	0.6	1.72-2.33	30.12%
80	0.5	1.62-2.19	29.92%
100	0.4	1.50-1.80	18.18%
133	0.3	1.48-1.61	4.85%
200	0.2	1.34-1.37	3.97%

In addition, the frequency range and relative bandwidth of the band gap also have relation with the dielectric constant of the photonic crystal. The variations of the frequency range and bandwidth with respect to relative dielectric constant ε_r are shown in Table 4. Here, the geometry of the photonic crystal, including the period length, radius and length, are unchanged. It can be seen from this table that as the increase of the dielectric constant, the frequency of the band gap decreases and the relative bandwidth becomes wider.

However, if the polarization of the incident wave is along the z direction, namely, the longitudinal direction of the photonic crystal, the band gap characteristic will become unobvious. The transmission coefficient of the photonic crystal impinged by a plane wave polarized along the z direction is shown in Fig. 7. In this figure, the transmission coefficient is above -10 dB in all the frequency range, which means that some incident wave passes through the photonic crystal and the band gap of the photonic crystal disappears.

Table 4: Variations of the frequency range of the band gap with respect to relative dielectric constant

ε_r	Frequency Range (THz)	Relative Bandwidth
3	2.64-2.67	1.13%
5	2.23-2.67	7.34%
7	1.94-2.16	10.73%
9	1.74-2.01	14.40%
11	1.60-1.90	17.14%
13	1.48-1.83	21.25%

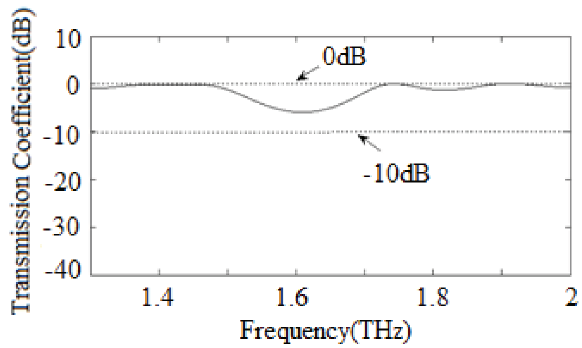

Fig. 7. The transmission coefficient of the photonic crystal impinged by a plane wave polarized along the z direction.

To validate this, the distribution of the electric field E_z at the frequency 1.7 THz is depicted in Fig. 8. It can be seen from this figure, that at this case most of the incident wave penetrate the photonic crystal obviously.

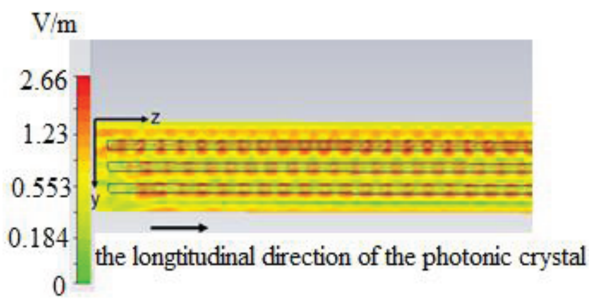

Fig. 8. The distribution of the electric field E_z at frequency 1.7 THz.

It concludes from the analysis above that when the photonic crystal is impinged by a plane wave polarized along the radial direction, the photonic crystal exhibits obvious band gap characteristic; the smaller the radius and period length of the photonic crystal are, the higher the frequency range of the band gap. The relative bandwidth of the band gap reaches maximum value when the ratio between the diameter of the photonic crystal and the period length is 0.6. Besides, the frequency and bandwidth of the band gap have relation with the permittivity. As the increase of the permittivity, the frequency of the band gap decreases and the relative bandwidth of the band gap becomes wider.

VI. CONCLUSION

This paper introduces a periodic WCS-PSTD method which is based on the hybrid implicit explicit difference technique and pseudospectral scheme to simulate the photonic crystal. The maximum time step size in this method is only determined by cell size Δz and the spatial discretization along z direction only needs two cells per wavelength. When this method is applied to simulate the photonic crystal, high computational efficiency is obtained and less computer memory is required, which is demonstrated through numerical examples by comparing with the periodic FDTD method. This method not only can be used in the simulation of photonic crystal, but also be useful in other electromagnetic problems where both fine and electrically large structures are used.

ACKNOWLEDGMENT

This work was supported by National Natural Science Foundations of China (No. 61001039 and 61231003), and also supported by the Fundamental Research Funds for the Central Universities.

REFERENCES

[1] S. Savel'ev, A. L. Rakhmanov, and F. Nori, "Using Josephson vortex lattices to control terahertz radiation: tunable transparency and terahertz photonic crystals," *Phys. Rev. Lett.*, vol. 94, no. 15, 157004, Apr. 2005.

[2] A. Bingham, Y. G. Zhao, and D. Grischkowsky, "THz parallel plate photonic waveguide," *Appl. Phys. Lett.*, vol. 87, no. 5, 051101, 2005.

[3] K. S. Yee, "Numerical solution of initial boundary value problems involving Maxwell's equations in isotropic media," *IEEE Trans. Antennas Propagat.*, vol. 14, no. 3, pp. 302-307, May 1966.

[4] A. Taflove, *Computational Electrodynamics*, Norwood, MA: Artech House, 1995.

[5] J. Chen and J. Wang, "The WCS-PSTD method for solving electromagnetic problems both with fine and electrically large structures," *IEEE Trans. Antennas Propagat.*, vol. 62, no. 5, pp. 2695-2701, May 2014.

[6] J. Chen and J. Wang, "A novel WCS-FDTD method with weakly conditional stability," *IEEE Trans. Electromagn. Compat.*, vol. 49, no. 2, pp. 419-426, Feb. 2007.

[7] J. Chen and C. M. Tian, "Using WCS-FDTD method to simulate various cylindrical metallic enclosures," *International Journal of Numerical Modelling: Electronic Networks, Devices and Fields*, vol. 24, no. 1, pp. 87-98, Jan. 2011.

[8] B. K. Huang, G. Wang, Y. S. Jiang, and W. B. Wang, "A hybrid implicit-explicit FDTD scheme with weakly conditional stability," *Microw. Opt. Tech. Letters*, vol. 39, no. 10, pp. 97-101, Oct. 2003.

[9] J. Chen and J. Wang, "A 3-D hybrid implicit-explicit FDTD scheme with weakly conditional stability," *Microwave Opt. Tech. Lett.*, vol. 48, no. 11, pp. 2291-2294, Nov. 2006.

[10] Q. H. Liu, "Large-scale simulations of electromagnetic and acoustic measurements using the pseudospectral time-domain (PSTD) algorithm," *IEEE Trans. Geoscience and Remote Sensing*, vol. 37, no. 2, pp. 917-926, Mar. 1999.
[11] Q. L. Li and Y. C. Chen, "Application of the PSTD for scattering analysis," *IEEE Trans. Antennas Propagat.*, vol. 50, no. 9, pp. 1317-1319, Sep. 2002.
[12] Z. Lin, "The optimal spatially-smoothed source patterns for the pseudospectral time-domain method," *IEEE Trans. Antennas Propagat*., vol. 58, no. 1, pp. 227-229, Jan. 2010.
[13] W. H. Press, B. P. Flannery, S. A. Teukolsky, and W. T. Vetterling, *Numerical Recipes-The Art of Scientific Computing*, Cambridge: Cambridge University Press, 1986.
[14] J. Chen and J. G. Wang, "Weakly conditionally stable and unconditionally stable FDTD schemes for 3D Maxwell's equations," *Progr. Electromagn. Res. B*, vol. 19, pp. 329-366, 2010.

Juan Chen received the Ph.D. degree in Electromagnetic Field and Microwave Techniques at the Xi'an Jiaotong University, Xi'an, China, in 2008. She now serves as an Associate Professor at Xi'an Jiaotong University. Her research interests are the numerical electromagnetic methods, antenna designs, and electromagnetic compatibility.

Reconfigurable Circular Polarization Antenna with Utilizing Active Devices for Communication Systems

Vahid Zarei [1], Hamid Boudaghi [1], Mahdi Nouri [2], and Sajjad Abazari Aghdam [3]

[1] Microelectronics Research Laboratory
Urmia University, Urmia, Iran
vahidzprp@gmail.com, st_h.boudaghi@urmia.ac.ir

[2] Department of Electrical Engineering
University of Isfahan, Isfahan, Iran
mnouri@eng.ui.ac.ir

[3] CEECS Department
Florida Atlantic University FL, USA
Sabazariaghd2012@fau.edu

Abstract **─** In this paper, the reconfigurable antenna with circular polarization diversity is proposed for wireless local area network (WLAN) communication systems. The proposed antenna consisting of two PIN diodes are appropriately positioned to achieve polarization diversity. By switching the PIN diodes ON/OFF mode, the proposed antenna enables to operate either RHCP mode or LHCP mode. A good impedance match ($S_{11} \leq$ -10 dB) of 935 MHz (1.995~2.930 GHz) at RHCP mode, an impedance bandwidth ($S_{11} \leq$ -10) of 965 MHz (1.935~2.960 GHz) at LHCP mode. The experimental result shows that the proposed antenna has a circular polarization bandwidth (AR $\leq$ 3 dB) of about 415 MHz at the center frequency of 2.4 GHz for both RHCP and LHCP mode.

Index Terms **─** Circular polarization, microstrip antenna, PIN diode, reconfigurable.

I. INTRODUCTION

Circular polarization is one of the common polarization schemes used in current wireless communication systems, such as radar and satellite systems, since it can provide better mobility and weather penetration than linear polarization. With the rapid development of wireless communication systems, such as wireless local area network (WLAN), multi-input and multi-output (MIMO) and personal communications service (PCS), radio frequency terminals with multiple functions are required to adapt to various standards and systems. Reconfigurable antennas with frequency adjustability, radiation pattern selectivity, and polarization diversity are good candidates for these applications [1,2].

In general, a polarization reconfigurable antenna can be designed to switch between different linear polarizations, two circular polarizations (right hand and left hand circular polarization) and any number of elliptical polarizations (with different axial ratios and tilt angles). In most investigations the point refers to the switch between (right hand circular polarization) RHCP and (left hand circular polarization) LHCP in a desired frequency [3,4]. In some papers, antenna could switch to linear polarization in addition of RHCP and LHCP too [5-8]. In some cases, the polarization is switched between vertical and horizontal linear polarization [9,10]. Proposed [11-14]. Adopting an electrical and mechanical method as well as active elements may provide reconfigurable antennas in terms of frequency band [15-17], polarization [18], pattern [19] and multi-application [20] in some UWB antennas these elements are used to obtain alterable notched-bands. For this purpose some designs include RF MEMS [21], PIN diodes [22], microfluidic [23] and Varactor diodes [24,25,26].

In this paper, a novel CPW-Fed microstrip antenna which uses two PIN diodes to switch between RHCP and LHCP, is introduced. This antenna is designed to work in center frequency of 2.4 GHz which is applicable in WLAN system.

This proposed CP reconfigurable antennas with concise structure are easy to be manufactured and can be used in various wireless communication systems. Section 2 demonstrates the design principle and the configurations of CP reconfigurable patch antennas with L elements on the patch and on the ground. Section 3 describes the simulated and experimental performances of the two patch antennas in details. The conclusions are

Submitted On: March 25, 2014
Accepted On: June 4, 2015

drawn in Section 4.

II. DESIGN PRINCIPLE AND ANTENNA CONFIGURATIONS

Figure 1 shows the geometry and dimensions of the proposed antenna, which consists of a rectangular ground plane with dimension of L and W and a square slot in the center of ground. Four inverted-L-shape grounded strips around the corners, and an inverse vertical T-shape strip between two upper inverted-L-shape strips are embedded in the square slot.

The proposed antenna is designed on an FR4 substrate with a loss tangent of 0.02, permittivity of 4.4, and a thickness of 1 mm. The antenna is fed by a 50-ohm CPW having a single strip of width W_{f1}=5 mm and two identical gaps of width g=0.4 mm. The single strip of the CPW is protruded into the slot by a width of W_{f1}, W_{f2}, W_{f3} and W_{f4}. Two parameters, W_{f1} and g are adjusted to produce 50 Ω impedance for feeding of the antenna. Other parameters of feeding strip such as W_{f2}, W_{f3}, W_{f4} and the width of them are embedded and adjusted for impedance matching and resonance bandwidth improvement.

The CP operation of the proposed antenna is chiefly related to the four grounded inverted-L strips inserted around the corners of the square slot.

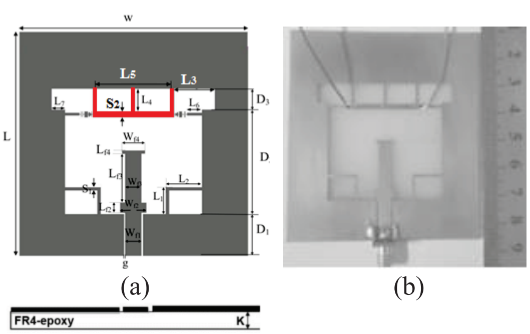

Fig. 1. (a) Geometry of the proposed antenna, (b) photograph of the fabricated antenna, and (c) dimension of proposed antenna: $\mathbf{L_1}$=9, $\mathbf{L_2}$=11, $\mathbf{L_3}$=12.5, $\mathbf{L_4}$=7.5, $\mathbf{L_5}$=23, $\mathbf{L_6}$=5.5, $\mathbf{L_7}$=4, $\mathbf{S_1}$=1, $\mathbf{S_2}$=2, $\mathbf{D_1}$=14, $\mathbf{D_2}$=35, $\mathbf{D_3}$=7, $\mathbf{W_{f1}}$=5, $\mathbf{W_{f2}}$=8, $\mathbf{W_{f3}}$=5, $\mathbf{W_{f4}}$=7, $\mathbf{L_{f2}}$=3.3, $\mathbf{L_{f3}}$=16.5, $\mathbf{L_{f4}}$=1, **g=0.4, K=1** (unit: mm).

In Fig. 1 the path of current in upper strips can be controlled by use of two PIN diodes. To feed PIN diodes by DC supply, two stubs with dimension of 1×1.5 mm are used. Each stub has one 100 pF capacitor in one side and other side is connected to PIN diode. To make diodes ON we can use these stubs for giving positive DC voltage to diodes [22].

When diode is in the OFF-state, it works like a small capacitor which can be considered as an open circuit. When diode is in ON-state it works like a small resistance. In an ideal state, this resistance can be considered as a short circuit.

PIN diodes used in the proposed antenna are BAR64-02W diodes. According to datasheet of this diode, in ON-state it has 2.1 Ω resistance and in OFF-state it equals to 0.17 pF capacitance.

III. EXPERIMENTAL RESULTS AND DISCUSSION

In each step of the design procedure, the full-wave analyses of the proposed antenna were performed using Ansoft HFSS (ver. 13). For simulation of the diodes in on state we model them by a resistance of 2.1 Ω. We also model the diodes in off state with a capacitance of 0.17 pF.

The proposed antenna with dimensions in Fig. 1 (c) has been fabricated on an FR4 substrate with a loss tangent of 0.02, permittivity of 4.4, rectangular dimensions of 75×70 mm, and thickness of 1 mm. The photograph of fabricated antenna is shown in Fig. 1 (b). In Fig. 2, the measurement and simulated results of in RHCP and LHCP state are shown. An Agilent E8363C vector network analyzer has been used to measure antenna parameters. Embedding inverted-L-shape grounded strips at the upper corner of square slots make the CP polarization possible. These strips are separated by two PIN diodes. When D1 is ON and D2 is OFF, the polarization of the antenna will be RHCP, and when D2 is ON and D1 is OFF, the polarization of the antenna will be LHCP. So by making the diodes ON or OFF different polarization will be obtained.

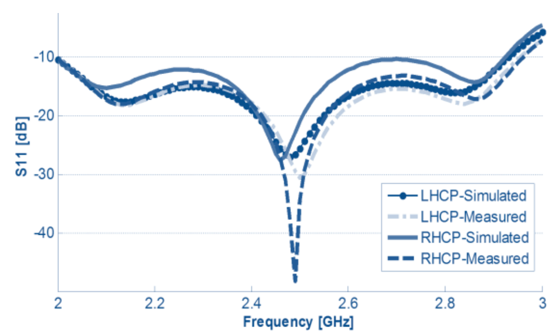

Fig. 2. Simulated and measured reflection coefficient of the antenna for RHCP and LHCP.

The simulated and measured axial ratio (AR) results in RHCP and LHCP states is shown in Fig. 3. As it is seen, the AR for RHCP and LHCP states is the same and in frequency range of 2.180~2.595, the AR is lower than 3 dB. In this bandwidth, it can be considered a circular polarization for proposed antenna.

The L-shape strips at the lower corners are for AR improvement and increasing of the antenna bandwidth. Center frequency of AR are affected by length of L6.

This length is chosen to have minimum axial ratio at frequency of 2.4 GHz. As we can see in Fig. 4, by increasing the length L6 the axial ratio bandwidth shifts to lower frequencies.

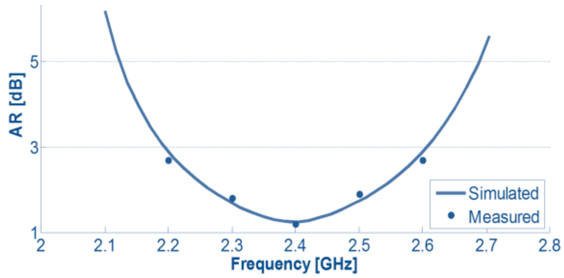

(a)

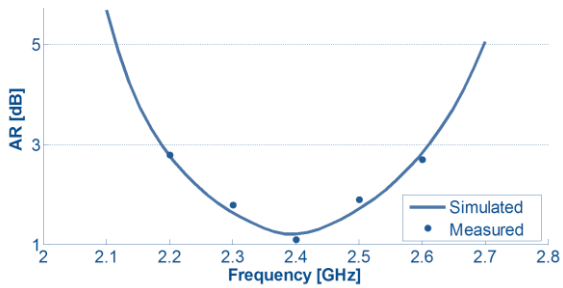

(b)

Fig. 3. Measured and simulated AR for: (a) RHCP and (b) LHCP.

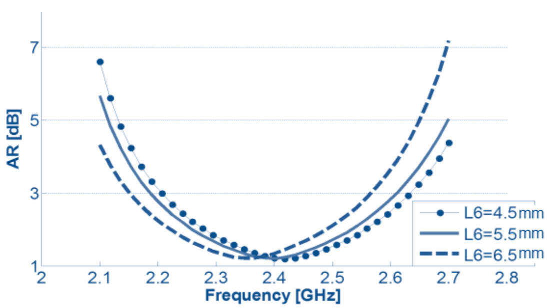

Fig. 4. Simulated AR values for different values of L6.

Current distributions on the patch antenna when it is fed from OFF/ON state of PIN diode are shown in Fig. 5, respectively. The symmetry in current distributions is mainly due to preserved symmetry in the antenna design. When diodes are ON, the current distribution is stronger and enforces the current distribution on the main patch for circular polarization.

The inversed T-shape strip embedded between upper L-shape strips will increase the gain of the antenna and make it smoother in the bandwidth. The simulated results for the gain of the proposed antenna in RHCP and LHCP state are shown in Fig. 6. In this figure, the measured results of the gain in LHCP state is shown too.

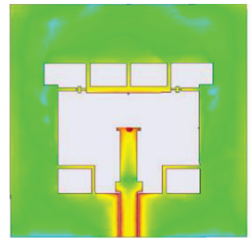

(a)

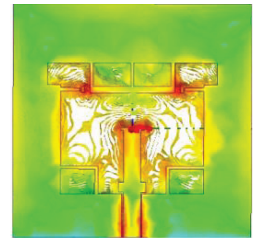

(b)

Fig. 5. Simulated current distribution on the antenna frequency 20.4 GHz: (a) PIN diode OFF and (b) PIN diode ON.

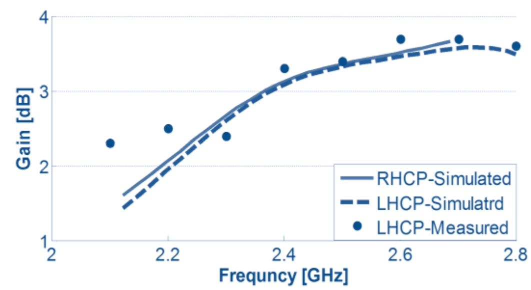

Fig. 6. Measured and simulated results for antenna gain in RHCP and LHCP.

The gain of proposed antenna is upper than 2 dB in the desired bandwidth and in center frequency 2.4 GHz it is 3.2 dB. In Fig. 6, it can be seen that as the operation frequency increases, the antenna gain is increased too. The antenna gain in the AR bandwidth in the best mood is 3.6 dB. The gain of the antenna has a direct relationship with the length of the antenna. Figure 7 shows the gain of the antenna for different values of L. Increasing the length of the antenna will increase the gain of the antenna and it has a negligible effect on the AR and return loss. The radiation pattern of the proposed antenna is demonstrated respectively in Fig. 8 (a) H-plan and Fig. 8 (b) E-plan. Also Figs. 9 (a) and (b) shows respectively comparison of radiation pattern for RHCP and LHCP.

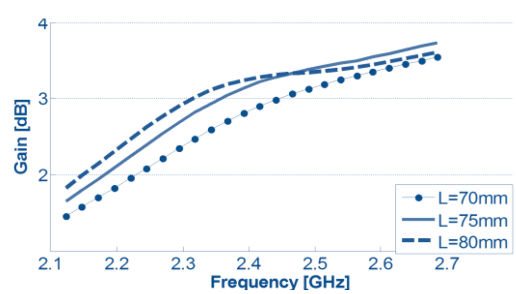

Fig. 7. Gain of the proposed antenna for various values of L.

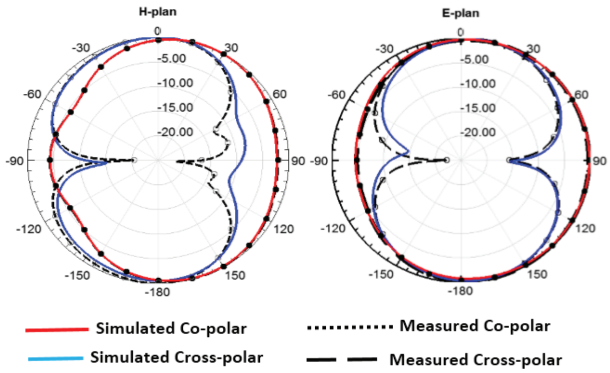

(a) (b)

Fig. 8. Radiation pattern of antenna: (a) H-plan and (b) E-plan.

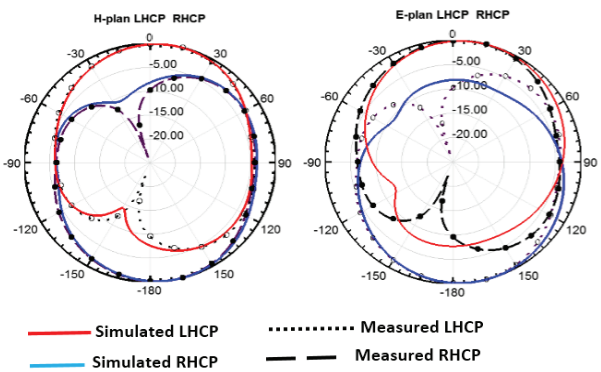

(a) (b)

Fig. 9. Radiation pattern of antenna: (a) RHCP antenna and (b) LHCP antenna.

IV. CONCLUSION

A novel polarization reconfigurable antenna has been presented. The antenna is simple to design and fabricate and exploits PIN diode switches to deliver reconfigurable capability. This antenna uses four inverted-L grounded strips for the excitation of two orthogonal resonant modes for CP radiation. Measured results have good agreement with simulated ones. The proposed antenna is suitable for Bluetooth/WLAN (2400–2484 MHz) frequencies.

REFERENCES

[1] J. T. Aberle, S-H. Oh, D. T. Auckland, and S. D. Rogers, "Reconfigurable antennas for portable wireless devices," *IEEE Antennas and Propagation Magazine*, vol. 45, no. 6, pp. 148-154, 2003.

[2] A. Kim, J. Kim, and H. Lee "Reconfigurable annular ring slot antenna with circular polarization diversity," *Proceedings of Asia-Pacific Microwave Conference, IEEE*, 2007.

[3] S. Pyo, J-W. Baik, and Y-S. Kim, "Slot-perturbed microstrip antenna for switchable circular polarization," *Electronics Letters*, vol. 47, no. 10, May 2011.

[4] Y. Kim, J. Kim, J. Kim, and H. Lee, "Reconfigurable annular ring slot antenna with circular polarization diversity," *Proceedings of Asia-Pacific Microwave Conference,* IEEE, pp. 815-818, 2007.

[5] Y. Sung, "Investigation in to the polarization of asymmetrical-feed triangular microstrip antennas and its application to reconfigurable antennas," *IEEE Trans. Antennas Propag*., vol. 58, no. 4, Apr. 2010.

[6] P-Y. Qin, A. R. Weily, Y. J. Guo, and C-H. Liang, "Polarization reconfigurable U-slot patch antenna," *IEEE Trans. Antennas Propag*., vol. 58, no. 10, pp. 3384-3388, Oct. 2010.

[7] M. S. Nishamol, V. P. Sarin, D. Tony, C. K. Aanandan, P. Mohanan, and K. Vasudevan, "An electronically reconfigurable microstrip antenna with switchable slots for polarization diversity," *IEEE Trans. Antennas Propag*., vol. 59, no. 9, pp. 3424-3427, Sep. 2011.

[8] X-X. Yang, B-C. Shao, F. Yang, A. Z. Elsherbeni, and B. Gong, "A polarization reconfigurable patch antenna with loop slots on the ground plane," *IEEE Trans. Antennas Propag*., vol. 11, pp. 69-72, 2012.

[9] Y. Li, Z. Zhang, W. Chen, and Z. Feng, "Polarization reconfigurable slot antenna with a novel compact CPW-to-slotline transition for WLAN application," *IEEE Antennas and Wireless Propag. Lett*., vol. 9, pp. 252-255, 2010.

[10] Y. Li, Z. Zhang, W. Chen, Z. Feng, and M. F. Iskander, "Dual-polarization slot antenna using a compact CPW feeding structure," *IEEE Antennas and Wireless Propag. Lett*., vol. 9, pp. 191-194, 2010.

[11] H. Mardani, S. Abazari Aghdam, and M. Mardani, "An effective approach for creating multi-notch characteristics in monopole antennas," *International Conference on Electronics Device, Systems & Applications (ICEDS)*, Apr. 1-4, 2011.

[12] H. Mardani and S. Abazari Aghdam, "A novel multi-notch compact monopole antenna for UWB applications," *IEICE Electron. Exp*., vol. 8, no. 20, 1698-1702, 2011.

[13] S. Abazari Aghdam and M. Hosseini Varkiani, "Small monopole antenna with semi-circular ground plane for UWB applications with variable band-notch structure," *Microwave Optical Technology Lett*., vol. 55, no. 1, Jan. 12-14, 2013.

[14] Y. Yousefzadeh, J. Pourahmadazar, and S. Abazari Aghdam, "Compact UWB microstrip BPF using meander line resonator," *Proc. IEEE Int. Symp. Antennas Propag. (APSURSI)*, 802-803, 2013.

[15] S. Abazari Aghdam, "A novel UWB monopole antenna with tunable notched behavior using

varactor diode," *IEEE Antennas Wireless Propag. Lett*., vol. 13, 1536-1225, 2014.
[16] S. Abazari Aghdam and J. S. Bagby, "Resonator type for the creation of a potentially reconfigurable filtering band in a UWB antenna," *Progress In Electromagnetics Research Letters*, vol. 52, 17-21, 2015.
[17] S. A. Abazari Aghdam and J. Bagby, "Monopole antenna with tunable stop-band function," *Proc. 14th Annu. IEEE Wireless Microw. Technol. Conf*., 1-3, 2013.
[18] V. Zarei, H. Bodaghi, and S. A. Aghdam, "A novel CPW-fed polarization reconfigurable microstrip antenna," *Proc. 83rd ARFTG Conf*., 1-4, 2014.
[19] M. Nouri, S. Abazari Aghdam, and V. Tabataba Vakili, "An optimal method for narrowband interference mitigation in the GPS," *International Conference on Modeling, Simulation and Applied Optimization (ICMSAO-2011)*, pp. 1-4, Apr. 2011.
[20] H. Boudaghi, J. Pourahmadazar, and S. Abazari Aghdam, "Compact UWB monopole antenna with reconfigurable band notches using PIN diode switches," *Proc. 14th Annu. IEEE Wireless Microw. Technol. Conf*., 1-4, 2013.
[21] S. Montori, F. Cacciamani, R. V. Gatti, R. Sorrentino, G. Arista, C. Tienda, José A. Encinar, and G. Toso, "A transportable reflectarray antenna for satellite Ku-band emergency communications," *IEEE Trans. Antennas Propag*., vol. 63, no. 4, Apr. 2015.
[22] H. Boudaghi, M. Azarmanesh, and M. Mehranpour, "A frequency-reconfigurable monopole antenna using switchable slotted ground structure," *IEEE Antennas and Wireless Propaga. Lett*., vol. 11, pp. 655-658, 2012.
[23] J. D. Barrera and G. H. Huff, "A fluidic loading mechanism in a polarization reconfigurable antenna with a comparison to solid state approaches," *IEEE Trans. Antennas Propag*., vol. 62, no. 8, pp. 4008-4014, Aug. 2014.
[24] S. Abazari Aghdam, "Reconfigurable antenna with a diversity filtering band feature utilizing active devices for communication systems," *IEEE Trans. Antennas Propag*., vol. 61, no. 10, pp. 5223-5228, Oct. 2013.
[25] S. Abazari Aghdam and J. Bagby, "Reconfigurable monopole antenna for filtered multi-radio wireless application," *Proc. IEEE Int. Symp. Antennas Propag. (APSURSI)*, 1746-1747, 2013.
[26] M. Nouri and S. Abazari Aghdam, "Reconfigurable UWB antenna with electrically control for triple on-demand rejection bandwidth," *Microwave and Optical Technology Lett*., vol 57, issue 8, pp. 1894-1897, Aug. 2015.

Vahid Zarei received the B.S. degree in Telecommunications Engineering from the University of Kordestan, Kordestan, Iran, in 2009, and the M.S. degree in Telecommunications Engineering from the University of Urmia, Urmia, Iran in 2013. His research interests include antenna design and microwave circuit design, applied electromagnetics, reconfigurable structures, smart antenna, wireless communication systems and also RFID.

Hamid Boudaghi received the B.S. degree in Telecommunications Engineering from the University of Tabriz, Tabriz, Iran, in 2007, and the M.S. degree in Telecommunications Engineering from the University of Urmia, Urmia, Iran in 2012. Currently he is a Transmission Expert at the Telecommunication Company of Iran (TCI). His research interests include antenna design and microwave circuit design, applied electromagnetics, reconfigurable structures, wireless communication systems and also cellular networks.

Mahdi Nouri (S'09–M'11) received the B.S. and M.S. degrees in Communication System Engineering, the M.S. degree in Communication Secure System Engineering from Iran University of Science and Technology (IUST), Tehran, in 2011. He is currently working toward the Ph.D. degree in Electronic Engineering at University of Isfahan, Isfahan, Iran. His research interests includes on radar, Antenna, security, signal processing and DSP.

Sajjad Abazari Aghdam received the B.Sc. degree in Electrical Engineering Telecommunications from the IAU, Urmia, Iran, in 2008 and the M.Sc. degree in Electrical Engineering - Telecommunications from IAU, Tehran, Iran, in 2011. He is currently working toward the Ph.D. degree in Electronic Engineering at Florida Atlantic University, Boca Raton, FL, USA. In 2012, he was a Teacher Assistant and Research Assistant at Florida Atlantic University. His current research interests include wireless communications, mobile computing, long term evolution (LTE) wireless networks, intelligent jamming, antenna and RF design, reconfigurable antennas, and numerical methods in electromagnetic, radars, digital signal processing and Cryptography.

Terahertz Dielectric Sensor Based on Novel Hexagon Meta-Atom Cluster

Nadeem Naeem [1], Alyani Ismail [1,2], Adam Reda Hassan Alhawari [1,2], and Mohd Adzir Mahdi [1,2]

[1] Faculty of Engineering
Universiti Putra Malaysia, Serdang, 43400, Malaysia
nadeemnaeem@yahoo.com

[2] Research Centre of Excellence for Wireless and Photonics Network
Universiti Putra Malaysia, Serdang, 43400, Malaysia
{Alyani, alhawari, mam}@upm.edu.my

Abstract **─** In this paper, we report meta-atom sensor based on planar hexagon split ring resonators. The sub-wavelength structure is designed to operate in terahertz frequency band. A modified version of split ring resonator geometry is simulated for sensing dielectric changes by placing thin dielectric layers as sample materials on the full frontal surface of sensor. The effective parameters are retrieved using Nicolson-Ross and Weir method. The meta-atom sensor shows significant changes in resonant frequency as a function of transmission (magnitude of S_{21} parameter) response, which was observed when the sensor is loaded with the dry layer of dielectric materials of different dielectric constants. This paper contributes new shape of meta-atom structure used as a terahertz dielectric sensor. The proposed sensor can be used in multitudinous terahertz near field sensing applications.

Index Terms **─** Dielectric sensor, meta-atom, near field, split ring resonator, terahertz.

I. INTRODUCTION

Meta-atoms or metamaterials are attractive man-made materials that can influence the light waves in astonishing manners. The structure of metamaterial is primarily constructed of subwavelength metallic resonators printed all together on dielectric substrate materials. Their electromagnetic properties are mainly consequent from the resonating metal structure rather than from atoms and or molecules as they do in conventional materials [1].

Meta-atoms can be manufactured to get a wide range of electromagnetic characteristics at desired frequencies. Such characteristics are still not founded in naturally occurring materials, which is why they named ‘meta’, which means beyond the materials. The natural materials typically occupy the positive real electric permittivity and magnetic permeability; whereas, negative values of the permittivity and permeability are possibly attainable in nature through the radiation manipulation [2]. Meta-atoms, e.g., thin metallic wires [3], can reduce and shift the fundamental frequency to a lower part of the frequency spectrum, thus resulting in a negative permittivity and permeability at lower frequencies. In nature, achieving negative values of permeability is uncommon but can be obtained from magnetic resonances in ferro-magnets at high frequencies. Meta-atoms, such as split-ring resonators (SRR) [4] and cut-wire pairs [5], can exhibit magnetic dipoles and negative permeability in response to magnetic waves up to the optical regime [6]. Achieving negative values of electromagnetic responses in meta-atoms open ways to realize double-negative characteristics, in which the permittivity and permeability are less than zero at the same frequencies resulting in negative-index material. Such types of sophisticated materials have never been occurred in the nature [7].

In their initial stages, the meta-atoms were tested in combination with the transmission wires to exhibit effective parameters of negative permittivity and permeability [8]. Negative index materials have incited a very wide interest in meta-atoms due to their strange behavior, and became the hub of metamaterial research and extend its operation in visible frequency spectrum [9].

Meta-atoms offered volume of opportunities in order to improve functional abilities of existing microwave and optical components and devices with exploring unexampled applications. Current research explored so far super lenses [10], biosensors based on meta-atoms, which are sensitive to small changes in the amount and response of a sample [11] and invisibility cloaks for the camouflage of an object from being detected [12]. Terahertz metamaterial research is newly emerged technology; that is why fundamental studies,

Submitted On: August 31, 2014
Accepted On: May 20, 2015

novel designs and advanced metamaterial applications are yet to be sufficiently explored. It is conceived that this novel research field will have great impact on science and engineering.

The split ring resonators have been used as fundamental circuits in numerous meta-atom applications. Because of their fascinating properties, they are still at the top of all their counterparts. They proved their effectiveness in high frequency applications where the other circuits do not. The artificial structures exhibit negative resonances at negative refractive index regions, which is impossible for any natural material. Meta-atom resonators find useful applications in detection of gas leakage and defects [13] infrared and thermal emission detectors [14] and in imaging [15,16].

Split ring resonators of different geometries are used as a basic unit cell for sensor clusters because of their unique characteristics of having negative permeability, permittivity and refractive index, which is numerically proved in open literature. Initially, meta-atoms were proposed for microwave frequency band and later they were introduced in terahertz and infrared frequency. In recent years, meta-atoms have proved their worth in terahertz nondestructive sensing applications because of the non-ionizing characteristics. There are many analytical models of split ring resonators are reported up to now.

Split ring resonator based meta-atom sensor is a circuit that can provide specific quantitative analytical information. Split ring resonators are arranged in circular and rectangular geometries for various scientific applications. The effect of substrate material cannot be ignored at very high frequencies; also metal strips offer very high loss [17]. The loss can be minimized by utilizing very thin and low permittivity substrate material [18]. Considering high loss situation, low permittivity substrate is utilized in this report.

There are a number of geometrical shapes reported in the literature demonstrating the usage of SSR. S-shape resonators [19], omega resonators [20], various shapes of hexagons [21,22,23,24,25] and v-shape resonators [26] and other geometries are reported for left-handed meta-atoms applications. Meta-atoms with double negative index have attracted the interest of the scientists, especially in the terahertz regime [27].

Meta-atoms exhibit concentrated electromagnetic field, which is necessary to get the improved selectivity of sensors for detection of quite minute amount of analytes [28]. Such detection ability opens minds for new applications to be explored through the use of meta-atoms. For example, meta-atoms have replaced the use of metallic conductors in many applications where surface plasmons were employed [29]. The sub wavelength sized meta-atoms are capable to be used as sensing devices at high frequencies [30]. Resonant modes of two dimensional sub wavelength resonators are suitable for sensing applications [31]. The non-destructive property of meta-atoms makes them highly suitable candidate for label free sensing of biochemical substances. Meta-atoms are also proposed for sensing of dielectrics by using electric permittivity near-zero narrow waveguide channels [32]. A meta-atom based microwave nondestructive evaluation sensor to detect materials with smaller imperfections compared to a wavelength was reported in [33]. It is revealed through studies that the sensitivity and resolution of ordinary sensors can be significantly enhanced by incorporation of meta-atoms.

Split ring resonators with different shapes are used for the sensors and microelectronic devices. Split ring resonator based biosensor with a small electrical size to detect the occurrence of bio molecular binding was experimentally demonstrated [34]. The structure of that biosensor was consisted of two pairs of SRR and a planar microwave transmission line.

So far, meta-atom based thin dielectric layer sensing structures have proved their effectiveness in the field of sensing. These electrically small devices are potential candidates for future scientific applications.

II. MATERIAL AND METHODS

The meta-atoms are periodically arranged in the form of cluster, which is illustrated in Fig. 1. Meta-atoms are of particular interest in the terahertz regime because of high spectral resolution, where most natural materials exhibit only weak electric and magnetic responses, and hence, cannot be utilized for sensing of minute samples. The introduction of terahertz meta-atom is believed to be an important step that can further advance terahertz research and development. Simulation results demonstrate the responses and their effective parameters like the real parts of negative permeability and electric permittivity.

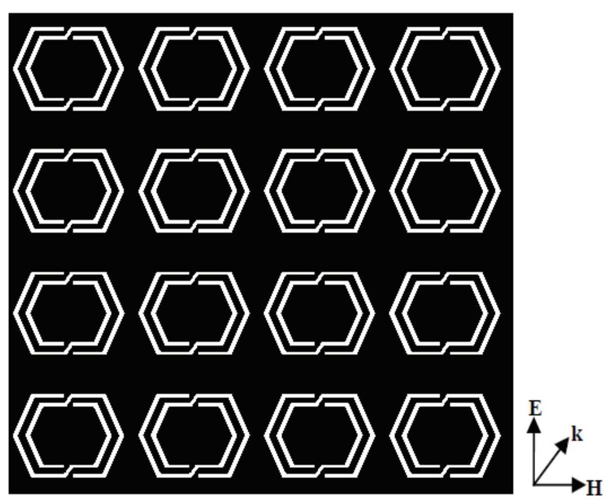

Fig. 1. 4 by 4 novel meta-atom cluster.

The increase in the number of split rings will increase the number of split gaps and metallization on the substrate; thus, an increase in the surface electric field will be observed on the split gap areas and overall surface of the metamaterial unit cell. The increasing values of overall capacitance, which includes gap and surface capacitance, will reduce the operating frequency as they are inversely proportional to each other. A simple inductor and capacitor (*LC*) tank circuit can represent the analogy of split ring resonator. The split rings form the magnetic inductance and can be considered as inductors. The capacitance is mainly formed in and around split gap areas.

The split ring resonator exhibit electromagnetic resonance when the electric energy stored in capacitor; i.e., gap is in balance with the magnetic energy stored in the inductors, i.e., split rings. The changes in capacitance, *C* and inductance, *L* due to dielectric loading from bio-molecule leads to a considerable shift in the frequency of resonance [35] as shown in equation (1):

$$f_C = \frac{1}{2\pi\sqrt{LC}}. \tag{1}$$

The unit cell of the dielectric sensor is designed with new shape of hexagonal split ring resonators (HSRR). Two HSRR are aligned face to face with modified gaps at the top and bottom spaced with 1.5 µm to each other on a thin dielectric substrate. Figure 2 shows the geometric dimensions of the HSRR. The proposed meta-atom cluster is simulated using Computer Simulation Technology (CST) studio suite 2014 to compute the complex scattering constitutive parameters. The simulated scattering parameters are obtained for the retrieval of effective parameters.

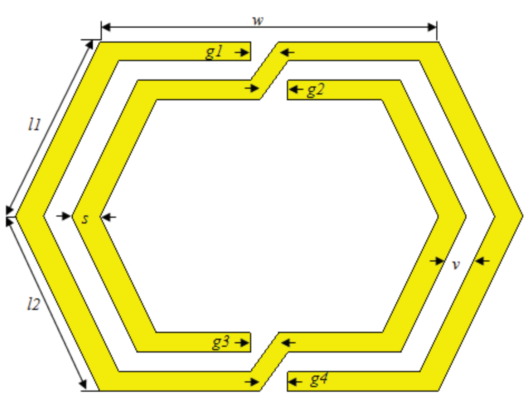

Fig. 2. Meta-atom unit cell design structure.

The effective parameters of hexagon split ring resonators are extracted using Nicolson-Ross and Weir method [36,37]. The Kramers-Kronig relationship [38] is further applied in order to get improved results. The unit cell dimensions are 30µm×30µm×0.5µm=450µm^3. The width of inner and outer gap area is made 1.5 µm. The split ring is made of gold strips with the permittivity ε_r=11.9.

The gold strips are printed on the substrate. Selection of the material strip is based on the fact that electrical conductivity of gold and annealed copper is 5.8×10^7 Siemens per meter. The strip thickness is 0.017 µm. The use of low permittivity materials causes deeper resonances at terahertz frequency [39]. Due to this reason, RT5880LZ with relative permittivity (ε_r) of 1.96 and permeability (μ_r) of 1 is used as a substrate material to achieve smaller unit to wavelength ratio. The cell dimensions are summarized in Table 1.

Table 1: Meta-atom unit cell dimensions

Parameters	Dimensions (µm)
Gap (*g1*, *g2*, *g3*, *g4*)	1.5
Strip width (*s*)	1
Strip spacing (*v*)	1
Strip length (*l1*, *l2*)	10.062
Horizontal width (*w*)	20
Substrate thickness	0.5

The effective parameters like permittivity and permeability are calculated using equations (2) and (3) as:

$$\mu_r = \frac{2}{jk_0 d} \times \frac{1-\upsilon_2}{1+\upsilon_2}, \tag{2}$$

$$\varepsilon_r = \frac{2}{jk_0 d} \times \frac{1-\upsilon_1}{1+\upsilon_1}. \tag{3}$$

In above equations, 'k_0' is the wave number and 'd' is the substrate thickness.

The scattering parameters are represented as the sum and difference terms as given in equations (4) and (5):

$$\upsilon_1 = S_{21} + S_{11}, \tag{4}$$

$$\upsilon_2 = S_{21} - S_{11}. \tag{5}$$

A. Quality factor of the resonant meta-atom cluster

Quality factor or Q factor is an important figure of merit that needs to be considered when describing the sensitivity of the meta-atom cluster based dielectric sensors. The Q factor of a resonance peak or dip can be calculated from the resonant frequency (f_0) and the frequency bandwidth (Δf) of the resonant peak at -3 dB power point [40], as shown in equation (6). Quality factors in the microwave portion of terahertz frequency operated meta-atoms are observed approximately 10 [41]. Unloaded Q factor of reported meta-atom cluster is calculated using -3 dB bandwidth formula and the result is summarized in Table 2.

$$Q = f_0 / \Delta f. \tag{6}$$

Table 2: Unloaded Q factor at resonant frequency

Resonant Frequency	Quality Factor
3.9 THz	95

The value of Q factor is proportional to the location of resonant frequency. This value is also dependent on the sharpness of the transmission. The deeper and narrower transmission dip with near to zero reflection results in higher value of Q factor.

III. RESULTS AND DISCUSSION

The sensor is constituted by hexagon split ring resonators, which are periodically arranged on a thin dielectric substrate material. Perpendicular incidence external field is applied in order to get strong electric and magnetic field response from meta-atom sensor. The direction of incidence is such that it is perpendicular to the metamaterial surface plane to observe the transmission spectra of the metamaterial unit cell. The electric and magnetic field is polarized in parallel to the long edges of the sensor along y-axis and z-axis respectively. The perpendicular incident waves can induce electric response when the electric field polarization is parallel to the long edges of the structure, and the parallel incident waves are easy to infuse the magnetic response when there is a loop in the metamaterial split ring resonator structure. The strong *LC* resonance can also be observed by the surface electric field distribution, and that the electric field is mainly focused on the upper and lower capacitive gap area as shown in Fig. 3.

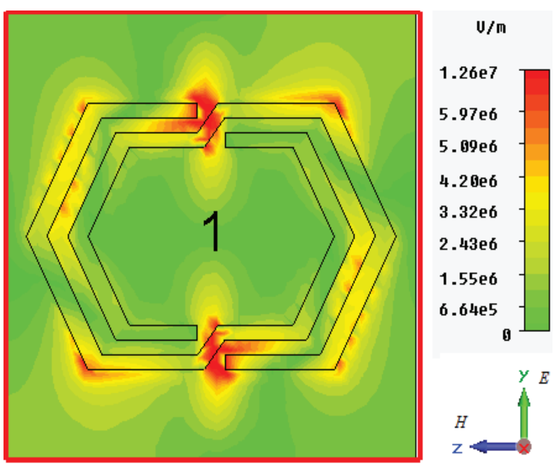

Fig. 3. Surface electric field distribution localized in the split gaps of hexagonal meta-atom unit cell.

The localization of surface electric field distribution is concentrated on the small gap areas because of increased capacitance. The overall surface electric field of sensor is not attributed only to the field at the split gaps.

The effective complex permeability of proposed meta-atom sensor at resonant frequency is shown in Fig. 4. According to that, the real value of complex permeability is negative at the frequency at the resonant frequency. There is only one instance where the real part of effective permittivity goes negative, and that is the region of resonance. The effective permittivity graph is shown in Fig. 5. The real part of electric permittivity and magnetic permeability exhibit a sharp negative value around the fundamental resonant frequency and remains negative in the frequency region from 3.9 to 4.1 THz.

Split ring resonators are asymmetric structures and mainly used in microwave and terahertz applications because of the presence of loop structure in their structural geometry. At the electric resonant frequency, the current flows parallel to the polarization direction, which indicates that the meta-atom split ring resonator acts like an electric dipole. The flowing surface current in the long metallic wires generates magnetic response, which is why, the retrieved permeability goes negative around the resonant frequency. In comparison to the magnetic response, the electric response is stronger, which can be observed in negative value of electric and magnetic response of the retrieved permittivity and permeability.

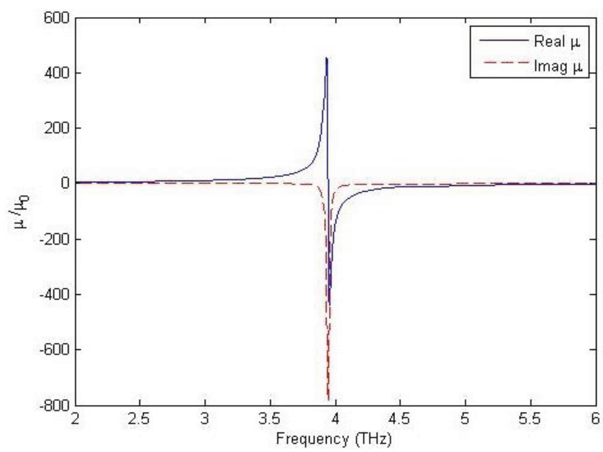

Fig. 4. Effective permeability.

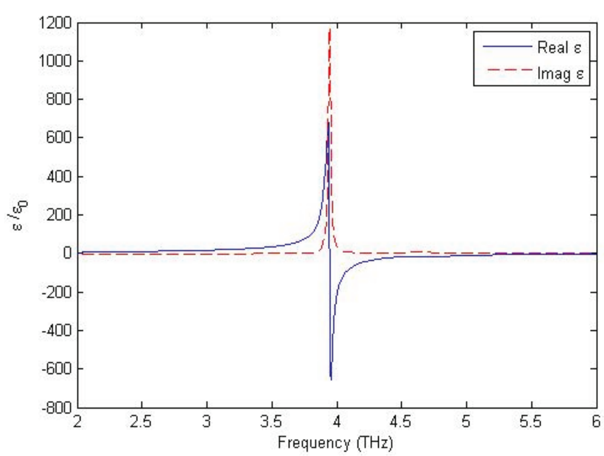

Fig. 5. Effective permittivity.

The reason of this response is the perpendicular incidence and parallel polarization of electric field component. When flowing current on the two corners of split ring resonator goes in phase causes less induction in the metallic wires and magnetic field becomes weaker at resonant frequency.

A stop band is observed at the resonant frequency under unloading condition or when the sample layer is not loaded on the surface of sensor. At the same instant, the real part of the effective permittivity goes sharp to the negative value. The real part of the retrieved permeability also becomes negative around the resonant frequency. Simultaneous negative values of permittivity and permeability can cause refractive index to exhibit negative value. The imaginary value of effective complex permittivity is appeared to be positive, which somehow satisfies the conditions for passivity and causality keeping in view of limitations related to Nicholson-Ross and Weir method [42], in which the meta-atom cluster behaves as a power source with no power dissipation. The dielectric constant and thickness of substrate is kept constant in all experimental simulations along with the sample thickness, which is maintained to 100 nanometer. Scaling down the sensor size to the suitable values will result in sensing the presence of thinner sample layers. There is a shift in the transmission observed when the meta-atom cluster based sensor was loaded with three different dielectric materials of different dielectric constants, as shown in Fig. 6.

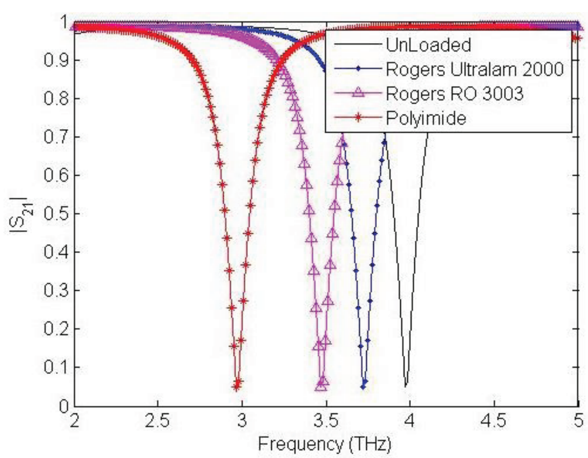

Fig. 6. Transmission spectra of meta-atom cluster under unloading and loading conditions.

Changing electric field causes the change in refractive index that yields the shift in transmission on frequency domain when the structure is loaded with dielectric materials of different permittivity. These materials were simulated for different loading conditions and are tabulated in Table 3.

Table 3: Dielectric materials used for sample loadings

Material	Relative Permittivity	Relative Permeability	Shift $\Delta f/f$
Rogers Ultralam 2000	2.5	1	0.2 THz
Rogers RO 3003	3	1	0.5 THz
Polyimide	3.5	1	1.1 THz

Unloaded transmission (S_{21} magnitude) is observed at the resonant frequency when the surface of the sensor was not exposed to the sample material. Transmission shift was observed when the cluster was loaded consecutively with Rogers Ultralam 2000, Rogers RO 3003 and Polyimide.

IV. CONCLUSION

The planar hexagon meta-atom cluster based dielectric sensor reported in this paper exhibits left handed characteristics at THz frequency band. The presence of the thin dry dielectric layers on the surface of the sensor was observed as the transmission (S_{21} parameter magnitude) is shifted towards lower frequency values. Significant changes were observed under loading samples with higher dielectric constants. Fabrication and dielectric characterization of such meta-atom cluster based sensor is the future extension of this research work.

REFERENCES

[1] J. B. Pendry, “Metamaterials in the sunshine,” *Nat. Mater.*, vol. 5, no. 8, pp. 599-600, Aug. 2006.

[2] J. Li and Y. Huang, *Time-Domain Finite Element Methods for Maxwell’s Equations in Metamaterials*, Springer Series in Computational Mathematics 43, Springer-Verlag Berlin Heidelberg, 2013.

[3] J. B. Pendry, A. J. Holden, W. J. Stewart, and I. Youngs, “Extremely low frequency plasmons in metallic mesostructures,” *Phys. Rev. Lett.*, vol. 76, no. 25, pp. 4773-4776, June 1996.

[4] J. B. Pendry, A. J. Holden, D. J. Robbins, and W. J. Stewart, “Magnetism from conductors and enhanced nonlinearphenomena,” *IEEE Trans. Microw. Theory Tech.*, vol. 47, no. 11, pp. 2075-2084, Nov. 1999.

[5] D. A. Powell, I. V. Shadrivov, and Y. S. Kivshar, “Cut-wire-pair structures as two-dimensional magnetic metamaterials,” *Opt. Lett.*, vol. 16, no. 19, pp. 15 185-15 190, Sep. 2008.

[6] G. Dolling, C. Enkrich, M. Wegener, J. F. Zhou, C. M. Soukoulis, and S. Linden, “Cut-wire pairs and plate pairs as magnetic atoms for optical metamaterials,” *Opt. Lett.*, vol. 30, no. 23, pp. 3198-3200, Dec. 2005.

[7] J. B. Pendry and D. R. Smith, "Reversing light with negative refraction," *Phys. Today*, vol. 57, no. 6, pp. 37-43, June 2004.
[8] D. R. Smith, W. J. Padilla, D. C. Vier, S. C. Nemat-Nasser, and S. Schultz, "Composite medium with simultaneously negative permeability and permittivity," *Phys. Rev. Lett*., vol. 84, no. 18, pp. 4184-4187, May 2000.
[9] G. Dolling, M. Wegener, C. M. Soukoulis, and S. Linden, "Negative-index metamaterial at 780 nm wavelength," *Opt. Lett*., vol. 32, no. 1, pp. 53-55, Jan. 2007.
[10] X. Zhang and Z. Liu, "Super lenses to overcome the diffraction limit," *Nat. Mater*., vol. 7, no. 6, pp. 435-441, 2008.
[11] C. Debus and P. H. Bolivar, "Frequency selective surfaces for high sensitivity terahertz sensing," *Appl. Phys. Lett*., vol. 91, no. 18, pp. 184 102-1–184 102-3, Oct. 2007.
[12] R. Liu, C. Ji, J. J. Mock, J. Y. Chin, T. J. Cui, and D. R. Smith, "Broadband ground-plane cloak," *Science*, vol. 323, no. 5912, pp. 366-369, Jan. 2009.
[13] M. Evangelidis, L. Ma, and M. Soleimani, "High definition electrical capacitance tomography for pipeline inspection," *Progress in Electromagnetics Research*, vol. 141, 1-15, 2013.
[14] S. D. Campbell and R. W. Ziolkowski, "Infrared core-shell-based metamaterials to control thermal emissions," 7th *European Conference on Antennas and Propagation (EuCAP)*, Apr. 8-12, 2013.
[15] D. S. Wilbert, M. P. Hokmabadi, J. Martinez, P. Kung, and S. M. Kim, "Terahertz metamaterials perfect absorbers for sensing and imaging," *Proceeding of Terahertz and Ultrashort Electromagnetic Pulses for Biomedical Applications*, San Francisco, California, USA, Feb. 02, 2013.
[16] B. S. Rodriguez, S. Rafique, R. Yan, M. Zhu, V. Protasenko, D. Jena, L. Liu, and H. G. Xing, "Terahertz imaging employing graphene modulator arrays," *Optics Express*, vol. 21, no. 2, pp. 2324-2330, Jan. 28, 2013.
[17] P. Drude, *Zur Elektronentheorie der Metalle; II. Teil. Galvanomagnetische und thermomagnetische Effecte*, Annalen der Physik, 308 (11): 369, 1900.
[18] J. F. O'Hara, R. Singh, I. Brener, E. Smirnova, J. Han, A. J. Taylor, and W. Zhang, "Thin-film sensing with planar terahertz metamaterials: sensitivity and limitations," *Optics Express*, vol. 16, no. 3, 2008.
[19] H. Chen, L. Ran, J. Huangfu, X. Zhang, and K. Chen, "Left-handed materials composed of only S-shaped resonators," *Phys. Rev. E*, vol. 70, 057605 (1)-(4), 2004.
[20] B. I. Wu, W. Wang, J. Pacheco, X. Chen, T. Grzegorczyk, and J. A. Kong, "A study of using metamaterials as antenna substrate to enhance gain," *PIER 51*, pp. 295-328, 2005.
[21] S. Bose, M. Ramraj, and S. Raghavan, "Design, analysis and verification of hexagon split ring resonator based negative index metamaterial," *Annual IEEE India Conference (INDICON)*, pp. 1009-1013, 2012.
[22] F. H. Wee, F. Malek, A. U. Al-Amani, and F. Ghani, "Effect of two different superstrate layers on Bismuth Titanate (BiT) array antennas," *Scientific Reports 4*, 2014.
[23] H. Benosman and N. B. Hacene, "Multi-band meta-material structures based on hexagonal shaped magnetic resonators," *24th International IEEE Conference on Microelectronics (ICM)*, pp. 1-4, 2012.
[24] A. Singh and S. K. Sharma, "Calculation of resonant frequency of hexagonal split ring resonator using ANN," *International Journal of Research in Engineering and Technology*, vol. 3, pp. 144-147, June 2014.
[25] S. Bose, M. Ramaraj, S. Raghavan, and S. Kumar, "Mathematical modeling, equivalent circuit analysis and genetic algorithm optimization of an N-sided regular polygon split ring resonator (NRPSRR)," *Procedia Technology*, 6, pp. 763-770, 2012.
[26] E. Ekmekci and G. Turhan-Sayan, "Investigation of permittivity and permeability for a novel V-shaped metamaterial using simulated S-parameters," *Proceedings of 5th International Conference on Electrical and Electronics Engineering*, Bursa, Turkey, Dec. 2007.
[27] Y. Yuan, C. Bingham, T. Tyler, S. Palit, T. H. Hand, W. J. Padilla, D. R. Smith, N. M. Jokerst, and S. A. Cummer, "Dual-band planar electric metamaterial in the terahertz regime," *Opt. Express*, vol. 16, no. 13, pp. 9746-9752, 2008.
[28] Z. Jakšić, S. Vuković, J. Matovic, and D. Tanasković, "Negative refractive index metasurfaces for enhanced biosensing," *Materials*, 4, pp. 1-36, 2011.
[29] A. Ishimaru, S. Jaruwatanadilok, and Y. Kuga, "Generalized surface plasmon resonance sensors using metamaterials and negative index materials," *Progress in Electromagnetic Research*, 51, pp. 139-152, 2005.
[30] M. Shamonin, O. Radkovskaya, C. J. Stevents, G. Faulkner, D. J. Edwards, O. Sydoruk, O. Zhuromskyy, E. Shamonina, and L. Solymar, "Waveguide and sensor systems comprising metamaterial element," *Proc. DPG-Spring Cond. Matter*, Dresden, Germany, pp. 114-118, Mar. 2006.

[31] T. Chen, S. Li, and H. Sun, "Metamaterials application in sensing," *Sensors*, no. 3, pp. 2742-2765, 2012.

[32] A. Alù and N. Engheta, "Dielectric sensing in ε-near-zero narrow waveguide channels," *Phys. Rev. B*, 78, pp. 045102:1-045102:5, 2008.

[33] D. Shreiber, M. Gupta, and R. Cravey, "Comparative study of 1-D and 2-D metamaterial lens for microwave nondestructive evaluation of dielectric materials," *Sensor Actuator A: Phys*., 165, pp. 256-260, 2011.

[34] H. J. Lee and J. G. Yook, "Biosensing using split-ring resonator at microwave regime," *Appl. Phys. Lett*., 92, pp. 254103:1-254103:3, 2008.

[35] I. M. Rusni, A. Ismail, A. R. H. Alhawari, M. N. Hamidon, and N. A. Yusof, "An aligned-gap and centered-gap rectangular multiple split ring resonator for dielectric sensing applications," *Sensors*, 14, no. 7, pp. 13134-13148, 2014.

[36] A. M. Nicolson and G. F. Ross, "Measurement of the intrinsic properties of materials by time-domain techniques," *IEEE Transactions on Instrumentation and Measurement*, vol. IM-19, no. 4, Nov. 1970.

[37] W. B. Weir, "Automatic measurement of complex dielectric constant and permeability at microwave frequencies," *Proceedings of the IEEE*, 62, no. 1, pp. 33-36, 1974.

[38] Z. Szabo, G. H. Park, R. Hedge, and E. P. Li, "A unique extraction of metamaterial parameters based on Kramers-Kronig relationship," *IEEE Transactions on Microwave Theory and Techniques*, 58, no. 10, pp. 2646-2653, 2010.

[39] C. Sabah and H. G. Roskos, "Terahertz sensing application by using planar split-ring-resonator structures," *Microsystem Technologies*, 18, no. 12, pp. 2071-2076, 2012.

[40] X. J. He, L. Qiu, Y. Wang, Z. X. Geng, J. M. Wang, and T. L. Gui, "A compact thin-film sensor based on nested split-ring-resonator (SRR) metamaterials for microwave applications," *J. Infrared Millim. Terahertz Waves*, 32, pp. 902-913, 2011.

[41] W. Cao, R. Singh, I. A. Al-Naib, M. He, A. J. Taylor, and W. Zhang, "Low-loss ultra-high-*Q* dark mode plasmonic Fano metamaterials," *Optical Letters*, vol. 37, no. 16, Aug. 15, 2012.

[42] F. Monticone and A. Alù, "Fundamental passivity and causality bounds on metamaterial cloaking," *Radio Science Meeting (USNC-URSI NRSM), US National Committee of URSI National*, pp. 1,1, Jan. 9-12, 2013.

Nadeem Naeem received his B.E. in Electronic Engineering and his M.E. in Telecommunication and Control Engineering from Mehran University of Engineering and Technology, Jamshoro, Pakistan in 2006 and 2009. Currently, he is a Ph.D. student in Electronic Engineering from Universiti Putra Malaysia. His area of interest is electromagnetic devices and microwaves applications. He is working as Assistant Professor in Quaid-e-Awam University of Eng. Sci. & Tech., Pakistan.

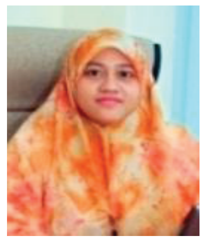

Alyani Ismail received her B.E. in Communication, Computer and Human Centered Systems from University of Huddersfield United Kingdom, her M.Sc. and Ph.D. degrees in Electronic Engineering from University of Birmingham, United Kingdom. She joined as a Lecturer in Universiti Putra Malaysia in 2006 and is presently working as Associate Professor in same university. Her field of specialization is design of microwave waveguides and filters for micromachining.

Adam Reda Hassan Alhawari received his M.Sc and Ph.D. from Universiti Putra Malaysia, his area of interest is Microwave Devices, Microwave Absorbers, Metamaterial Antennas, Metamaterial Sensors and Applications, RFID, Terahertz Science and Technology. He is currently working as a Lecturer in the Computer and Communication Systems Department, Universiti Putra Malaysia.

Mohd Adzir Mahdi received his B.E. in Electrical Engineering from Universiti Kebangsaan Malaysia (UKM), his M.Sc. and Ph.D. degree from University of Malaya. He is a Professor of Photonics in Universiti Putra Malaysia. He specializes in Optical Fiber Amplifiers and Lasers-Optical Fiber Communications - Bio-photonics.

Using MATLAB to Model Inhomogeneous Media in Commercial Computational Electromagnetics Software

A. Farahbakhsh, D. Zarifi, and A. Abdolali

[1] Department of Electrical Engineering
Iran University of Science and Technology, Tehran, Iran
farahbakhsh@ib-eco.com, zarifi@iust.ac.ir, abdolali@iust.ac.ir

Abstract **─** This paper presents a new method to model inhomogeneous media in commercial electromagnetics software, especially FEKO. In this method, the inhomogeneous medium is fragmented to some homogeneous pieces. If the size of these pieces is chosen correctly, then the electromagnetic behaviors of them and inhomogeneous medium are the same. Since creating these homogeneous pieces in FEKO manually is very difficult and time consuming, MATLAB is employed to create these pieces in FEKO.

Index Terms **─** FEKO, inhomogeneous media, MATLAB.

I. INTRODUCTION

These days, the computational electromagnetic software products, like FEKO [1], become essential tools for any electromagnetic design procedure. These products can simulate a various type of electromagnetic media and devices such as antennas, waveguides, filters, couplers, radomes and so on. So, many designers use them to verify their designs. But most of them cannot model the inhomogeneous media in a user-friendly way.

On the other hand, the usage of inhomogeneous media is quickly increasing due to their enormous applications. For example, the inhomogeneous media are used as antenna radome, substrate of microstrip devices and device coating [2-4]. And also, they are used to design microwave filters [5] and frequency selective surfaces [6].

This paper presents new toolboxes to model inhomogeneous media in computational electromagnetics software. These toolboxes are based on MATLAB [7] which is a powerful numerical computing environment and is widely used for research, academic and industrial purposes. A toolbox that is based on MATLAB has some advantages, e.g., the user can utilize the general-purpose functions of MATLAB to customize it.

In this paper, modeling of inhomogeneous medium in FEKO is presented, but the proposed method can be easily applied to other commercial computational electromagnetics software, such as CST [8], HFSS [9].

II. DESIGN PROCEDURE

In the presented method, the inhomogeneous medium is fragmented to N homogeneous pieces and the inhomogeneous medium is estimated by these homogeneous pieces. If the dimensions of pieces are very smaller than wavelength or the inhomogeneous medium parameters are about constant in each piece, then the electromagnetic behavior of fragmented medium is similar to the one for inhomogeneous medium. In other words, the inhomogeneous medium is modeled by some homogeneous pieces, which their sizes are depended on the simulation frequency and inhomogeneous medium parameters.

In this method, a large number of homogeneous media should be created in FEKO to model inhomogeneous media. But creation of these pieces in FEKO manually is very difficult, time consuming and almost impossible and it is necessary to automate it.

To solve this problem, FEKO is controlled by using MATLAB [8] and a toolbox is created in MATLAB in which inhomogeneous medium is estimated to some homogeneous small pieces and create these pieces in FEKO. The output of this toolbox is a FEKO file that contains modeled inhomogeneous medium.

A. Using MATLAB to create media in FEKO

FEKO in addition to having a CAD environment for modeling various types of media and geometries, has a scripting interface for advanced users which is named Edit FEKO. In Edit FEKO environment, user can utilize all the capabilities of FEKO by using known and defined commands.

Considering this particular capability of FEKO, any structure can be created in FEKO by using MATLAB. To do this, MATLAB must write all necessary Edit FEKO commands to an ASCII file that its suffix is PRE. This file could be opened in Edit

Submitted On: September 13, 2014
Accepted On: June 4, 2015

FEKO and any other commands can be added to it depending on user needs. After simulation by FEKO, the modeled structure and its results are available in POST FEKO.

B. Inhomogeneous media modeling

There is two ways in FEKO to model a homogeneous medium in Cartesian coordinate. The first is to use QU command to create cubical dielectric elements. This is the simplest way to model a dielectric or magnetic cube in Edit FEKO, but periodic boundary conditions cannot be applied to the media which are created by this command. Hence, this way is useful to model finite inhomogeneous media.

Another way is to use BP and ME commands. The BP command creates a flat parallelogram which its type is determined by using ME command. So, dielectric media can be created by combining these two commands. Periodic boundary condition can be applied to the media which are created by the second method. So, this method is useful to model infinite inhomogeneous media. Two toolboxes are presented in this paper. The first toolbox can be modeled infinite inhomogeneous media and the second one is used to model finite inhomogeneous media.

C. Infinite structures

To model and simulate infinite inhomogeneous structures in two dimensions, as discussed above, the inhomogeneous medium is fragmented to several homogeneous media using MATLAB as shown in Fig. 1.

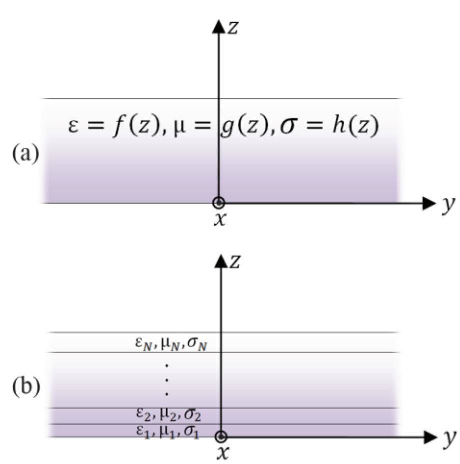

Fig. 1. (a) A typical infinite inhomogeneous medium, and (b) its estimation by some homogeneous media.

The medium parameters of each homogeneous piece are estimated by the average weights of inhomogeneous parameters as given in equations 1, 2 and 3:

$$\varepsilon_n = \frac{1}{\alpha_n - \alpha_{n-1}} \int_{\alpha_{n-1}}^{\alpha_n} f(\alpha)d\alpha, \quad n = 1,2,\ldots,N \tag{1}$$

$$\mu_n = \frac{1}{\alpha_n - \alpha_{n-1}} \int_{\alpha_{n-1}}^{\alpha_n} g(\alpha)d\alpha, \quad n = 1,2,\ldots,N \tag{2}$$

$$\sigma_n = \frac{1}{\alpha_n - \alpha_{n-1}} \int_{\alpha_{n-1}}^{\alpha_n} h(\alpha)d\alpha. \quad n = 1,2,\ldots,N \tag{3}$$

In these equations, ε_n, μ_n and σ_n are medium parameters of n^{th} piece and α_{n-1} and α_n are its start and end position, respectively.

It is remarkable that in this toolbox, while the variations of inhomogeneous medium parameters are more severe, more fragmentation is done and vice versa. So, it needs shorter time to simulate.

Figure 2 shows the toolbox for infinite media. Inputs of this toolbox are ε_r, μ_r and σ of inhomogeneous medium, the direction of homogeneity and its range, minimum fragmentation size, variation tolerance and the address of output file.

More fragmentation is generated if minimum fragmentation size is decreased. If difference of medium parameters of two nearby pieces is less than variation tolerance value, then these two pieces will be merged together.

In the right side of toolbox window, the fragmented media and parameters of each section are shown.

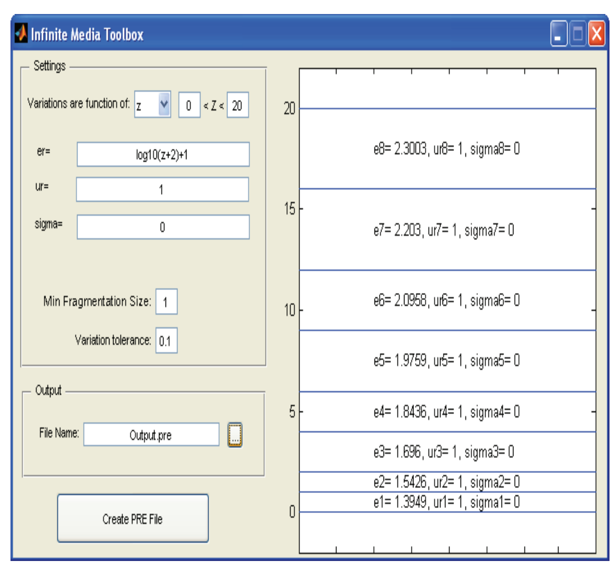

Fig. 2. Presented toolbox to model infinite inhomogeneous media.

In order to verify the proposed method, an infinite inhomogeneous medium is modeled in FEKO by presented toolbox. The parameters of the modeled medium are $\varepsilon_r(z)=4e^{5z}$, $\mu_r=1$, $\sigma(z)=0$ and its thickness is 20 *cm* along z axis. The medium is infinite along x and y axes.

A plane wave with TE^z polarization is illuminated to it and the angle of incidence is θ^i. The frequency of plane wave is 1 *GHz* and its electric field strength is 1 *V/m*. The reflection and transmission coefficients of this structure are obtained by simulation. Figure 3 shows this modeled structure with periodic boundary condition in FEKO.

This structure has analytical solution [9]; therefore, the results of simulation can be compared with analytical results. Figure 4 depicts the simulation and analytical results for assumed structure.

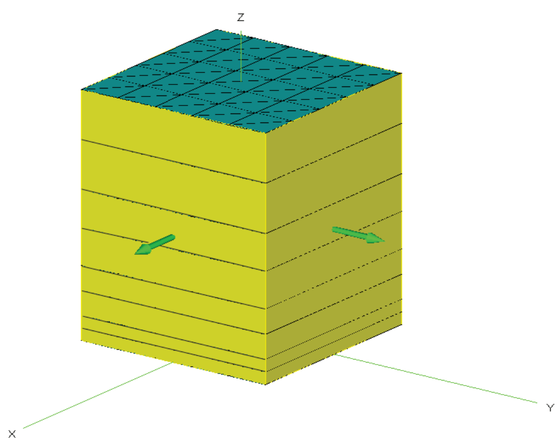

Fig. 3. The estimated model of mentioned structure in FEKO.

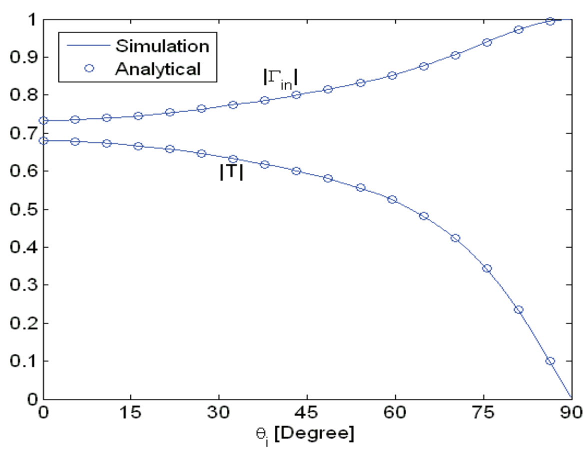

Fig. 4. The amplitute of transmition and reflection coefficient obtained from analytical solution and simulation.

As can be seen in Fig. 4, the proposed method acts as expected and its results have exact agreement with analytical results.

Another slob with constitutive parameters $\varepsilon_r(z)=4+5z/d$, $\mu_r=1$, $\sigma(z)=0$ is modeled by the proposed toolbox. The thickness of slab is 20 *cm*. A plane wave impinges normally on the slab and the reflection and transmission coefficient of the slab are simulated and the results are compared to an analytical solution [10] that is plotted in Fig. 5. As shown in this figure, the simulated and analytical results are in full compliance.

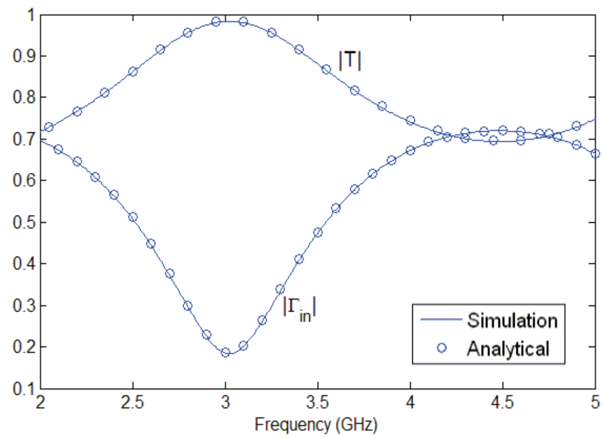

Fig. 5. The amplitute of transmition and reflection coefficient obtained from analytical solution and simulation.

D. Finite structures

To model finite inhomogeneous structures in FEKO as discussed above, the inhomogeneous medium is divided to several homogeneous cubes using MATLAB as depicted in Fig. 6.

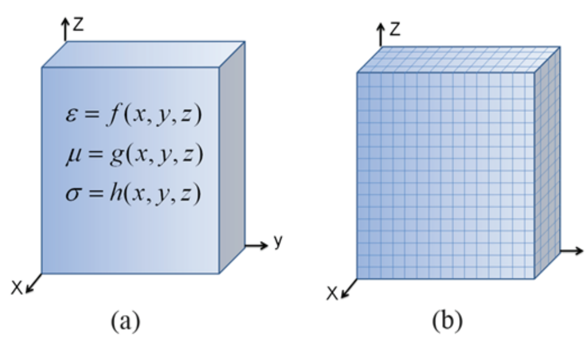

Fig. 6. (a) A typical finite inhomogeneous medium, and (b) its estimation by some homogeneous cubes.

Figure 7 shows the toolbox for finite inhomogeneous media. Its inputs are medium dimensions in x, y and z axes, ε_r, μ_r and σ functions, the size of small homogeneous cubes and the address of output file which its type is PRE file.

A finite inhomogeneous medium with $\mu_r = 1$, $\varepsilon_r = \log(x^2 + y^2 + z^2 + 1) + 1$ and $\sigma = 0$ is modeled by proposed toolbox. The dimensions of medium are equal in three axes and are equal to 20 *cm*. The modeled medium is depicted in Fig. 8.

A plane wave with TE^z polarization is illuminated to the issued structure at $\theta^i = 135^o$ and $\phi^i = -135^o$. The frequency of plane wave is 1 *GHz* and its electric field strength is 1 *V/m*.

The radar cross section (RCS) of issued structure is simulated and ploted in xy-plane as shown in Fig. 9.

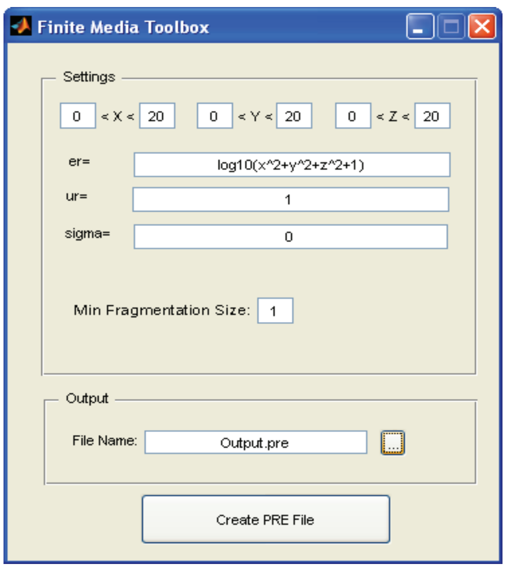

Fig. 7. Presented toolbox to model finite inhomogeneous meida.

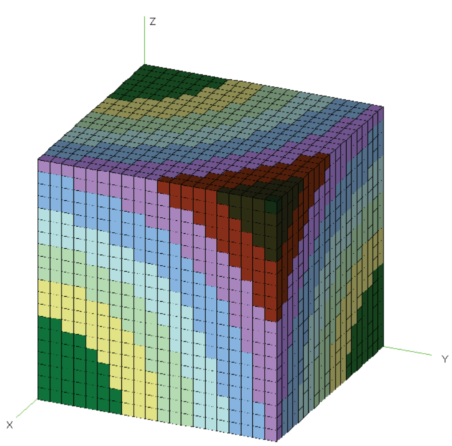

Fig. 8. The estimated model of mentioned structure in FEKO.

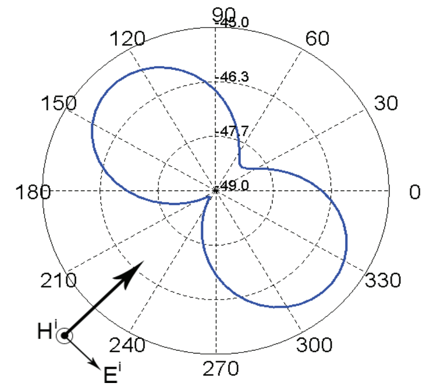

Fig. 9. Radar cross section of proposed finite structure.

III. CONCLUSION

In this paper, a new method is presented in which inhomogeneous media are modeled in FEKO by using MATLAB. In this method, inhomogeneous medium is fragmented to some homogeneous pieces and these pieces are created in FEKO by MATLAB. Two toolboxes are presented in this paper to implement this method for finite and infinite inhomogeneous media. To verify the proposed method, a structure which has analytical solution is modeled by this method. The simulation results and analytical solutions have exact agreement.

REFERENCES

[1] FEKO 5.4, EM Software & Systems-S.A. (Pty) Ltd., Copyright 2005-2008.

[2] R. Barrar and R. Redheffer, "On nonuniform dielectric media," *IRE Transactions on Antennas and Propagation*, vol. 3, no. 3, pp. 101-107, Jul. 1955.

[3] R. Stovall and K. Mei, "Application of a unimoment technique to a biconical antenna with inhomogeneous dielectric loading," *IEEE Transactions on Antennas and Propagation*, vol. 23, no. 3, pp. 335-342, 1975.

[4] K. P. Gaikovich and P. K. Gaikovich, "Inverse problem of scattering for inhomogeneous layered media," *10th Anniversary International Conference on Transparent Optical Networks, ICTON 2008*, Jun. 2008.

[5] P. Bilotti, A. Toscano, and L. Vegni, "New efficient design of microwave inhomogeneous media filters," *2000 IEEE MTT-S International Microwave Symposium Digest.*, vol. 2, pp. 1081-1084, 2000.

[6] M. Choubani, F. Choubani, A. Gharsallah, J. David, and N. E. Mastorakis, "Analysis and design of antireflection and frequency selective surfaces with stratified and inhomogeneous media," *ICECS '06 13th IEEE International*

Conference on Electronics, Circuits and Systems, 2006, Dec. 2006.

[7] Matlab the Language of Technical Computing, The Mathworks Inc. (www.mathworks.com), Copyright 1984-2008.

[8] R. L. Haupt, "Using MATLAB to control commercial computational electromagnetics software," *Applied Computational Electromagnetics Society Journal*, vol. 23, no. 1, Mar. 2008.

[9] M. Khalaj-Amirhosseini, "Analysis of lossy inhomogeneous planar layers using fourier series expansion," *IEEE Transactions on Antennas and Propagation*, vol. 55, no. 2, pp. 489-493, 2007.

[10] D. Zarifi, M. Soleimani, and A. Abdolali, "State transition matrix of inhomogeneous planar layers," *IET Microwaves, Antennas & Propagation*, vol. 9, no. 4, pp. 301-306, 2014.

Ali Farahbakhsh was born in Kerman, Iran in 1984. He received the B.Sc. degree from Kerman Bahonar University, Kerman, Iran and the M.Sc. degree from Sistan and Baluchestan University, Zahedan, Iran, both in Electrical Engineering, in 2007 and 2010 respectively. Currently, he is pursuing his Ph.D. degree in Electrical Engineering at Iran University of Science and Technology. His research interests are electromagnetic waves propagation and scattering, electromagnetic compatibility, antenna design and measurement.

Davoud Zarifi was born in Kashan, Iran, in 1987. He received the B.Sc. degree from the University of Kashan, Kashan, Iran, in 2009 and the M.Sc. degree from the Iran University of Science and Technology (IUST), Tehran, Iran, in 2011, where he is currently working toward the Ph.D. degree, all in Electrical Engineering. His research interests are electromagnetic waves in complex media, numerical techniques for electromagnetics, inverse problems in electromagnetic, and applications of ordinary and chiral metamaterials.

Ali Abdolali was born in Tehran, Iran, in 1974. He received the B.Sc. degree from the University of Tehran, the M.Sc. degree from the University of Tarbiat Modares, Tehran, and the Ph.D. degree from the Iran University of Science and Technology (IUST), Tehran, Iran, all in Electrical Engineering in 1998, 2000, and 2010, respectively. In 2010, he joined the Department of Electrical Engineering, Iran University of Science and Technology, Tehran, Iran, where he is an Assistant Professor of Electromagnetic Engineering. His research interests include electromagnetic wave scattering, radar cross section (RCS), radar absorbing materials (RAM), EM waves controlling, cloaking, metamaterials, EM waves in complex media (anisotropic, inhomogeneous, dispersive media, metamaterials), frequency selective surfaces (FSS), and bioelectromagnetism (BEM). He has authored or co-authored over 50 articles in international journals and conferences.

Influence of the Simulation Parameters on the Normalized Impedance Derived by the Random Coupling Model Simulation

Xin Li [1], Cui Meng [1], Yinong Liu [1], and Edl Schamiloglu [2]

[1] Key Laboratory of Particle & Radiation Imaging, Ministry of Education
Department of Engineering Physics, Tsinghua University, Beijing, 100084, China
lixin20060817@gmail.com, mengcui@mail.tsinghua.edu.cn, liuyinong@mail.tsinghua.edu.cn

[2] Department of Electrical and Computer Engineering
University of New Mexico, Albuquerque, MSC01 1100, USA
edls@unm.edu

Abstract **–** The random coupling model (RCM, introduced by the "chaos group" in the University of Maryland, is found of great use in making statistical predictions of the induced voltages and currents on objects or components within complicated (wave-chaotic) cavities when excited by external high power microwave (HPM) radiation. A key point to applying the RCM to a real system is to generate the normalized cavity impedance, which can be described by the random matrix theory (RMT), from the cavity loss parameter by using random matrix Monte Carlo simulation. The influences of the simulation parameters on the statistics of the generated normalized impedance are presented and discussed in this paper. It's found that the statistics of the normalized impedance only depends on the loss parameter, α, which agrees with the theory. When α increases, the variances of the eigenvalues, the diagonal elements and the off-diagonal elements of the normalized impedance are exponentially damped with different damping factor, which are experimentally verified in the paper.

Index Terms **–** Cavity loss parameter, normalized impedance matrix, random coupling model.

I. INTRODUCTION

The coupling of high power electromagnetic (HPEM) waves with systems such as cars, aircraft, ships, and et. al., has drawn a lot of attention. One problem in treating these problems is the short wave length nature of the radiation. When the wavelength of the radiation becomes much smaller than the enclosure size of the target system, the coupling properties depend in great detail on the size and shape of the enclosure, the geometry of the coupling ports, and on the frequency of the radiation [1]. Furthermore, the electromagnetics quantities within the enclosure will be very sensitive to the enclosure shape, the internal object positions and orientations, the external radiation frequency, and the coupling ports geometry. At present, even with a lot of fast and powerful computers that utilize efficient 3-D numerical simulation, addressing this problem is still a great challenge because of numerous computational time and CPU resources.

To deal with this problem, the "chaos group" at the University of Maryland introduced the random coupling model, which is a statistical model that can characterize the fluctuations of the impedance and scattering matrices of wave-chaotic metallic-enclosed cavity coupled with one port [2] and multiple ports [3]. This model has been extended to make statistical predictions of the induced voltages and currents on components within the enclosure when excited by external short wave-length EM radiation [4].

Considering the short trajectories effects, Hart et. al., show that the statistics of the impedance matrix, $\boldsymbol{Z}_{\text{cav}}$, of a wave-chaotic cavity coupled with N ports, can be divided into two parts that describe the universal and system-specific properties of the cavity as, [5,6]:

$$\boldsymbol{Z} = j\Im[\boldsymbol{Z}_{\text{ave}}] + (\Re[\boldsymbol{Z}_{\text{ave}}])^{1/2}\boldsymbol{z}(\Re[\boldsymbol{Z}_{\text{ave}}])^{1/2}. \tag{1}$$

The matrix, $\boldsymbol{Z}_{\text{cav}}$, is the ensemble average of cavity impedance which describes the system-specific details of the cavity.

The normalized impedance matrix, $\boldsymbol{z}$, can be derived from the random matrix theory and the random plane wave hypothesis [2,3]. The $N\times N$ normalized impedance matrix for the time reversal symmetry (TRS) electromagnetic-wave systems within which the medium is characterized by real, symmetric permittivity and permeability tensors, is shown as:

$$\boldsymbol{z}_N = \frac{1}{j\pi}\sum_{n=1}^{M}\frac{\boldsymbol{w}_N\boldsymbol{w}_N^T}{\left(k^2-k_n^2\right)/\Delta k_n^2 - j\alpha}, \tag{2}$$

where $\boldsymbol{w}_{\text{N}}$ is N dimensional vector whose elements are Gaussian random variables with zero mean and unit

Submitted On: October 18, 2014
Accepted On: June 4, 2015

1054-4887

variance, α is the cavity loss parameter, k is the wave number corresponding to the incoming frequency, k_n is the wavenumber of cavity eigenvalues, Δk_n^2 is the mean spacing of the adjacent eigenvalues and for a 3D cavity $\Delta k_n^2=2\pi^2/(kV)$ (V is the cavity volume).

For the TRS system, the probability density function (PDF) of the normalized nearest neighbor eigenfrequency spacing ε, defined as equation (3), follows a certain universal curves which is the well-known Wigner distribution as shown in equation (4), [7]:

$$\varepsilon = \frac{k_{n+1}^2 - k_n^2}{\Delta k_n^2}, \tag{3}$$

$$P(\varepsilon) = \frac{\pi}{2}\varepsilon Exp\left(-\frac{\pi\varepsilon^2}{4}\right). \tag{4}$$

In this paper, 2×2 normalized impedance matrix $\boldsymbol{z}$ is considered. A large ensemble of $\boldsymbol{z}$ is generated based on equation (2) through random matrix Monte Carlo simulation (which will be described in Section II). In Section III and IV, the influence of the simulation parameter M and α on the statistics of $\boldsymbol{z}$ will be discussed respectively. According to the simulation results, the statistics of $\boldsymbol{z}$ only depends on α and the relation between them is experimentally verified in Section V.

II. RANDOM MATRIX MONTE CARLO SIMULATION

According to equation (2), the point to generate the normalized impedance $\boldsymbol{z}$ is to produce M independent normalized eigenvalues $k_n^2/\Delta k_n^2$ with the PDF of nearest spacing ε following the Wigner distribution. An alternative approach given in [7] is to generate an $M\times M$ real symmetric random matrix corresponding to the Gaussian orthogonal ensemble (GOE) in which the diagonal elements are independent Gaussian-distributed with zero mean and unit variance, and the off-diagonal elements have the same distribution with the diagonal elements except for the variance equaling to 0.5.

The distribution of the eigenvalues, λ_M, of the random matrix is shown in Fig. 1 (a), for M=6000 and it's not uniform. By introducing a mapping function $\varsigma(\lambda_M, M)$ (as shown in equation (5)), each λ_M is converted into a new variable λ'_M which is uniformly-distributed in ($-M/2$, $M/2$), as shown in Fig. 1 (b). The PDF of the normalized spacing of λ'_M is plotted in Fig. 2, which agrees well with the Wigner distribution:

$$\lambda_M' = \frac{M}{2\pi}\left[\pi + 2sin^{-1}\left(\frac{\lambda_M}{\sqrt{2M}}\right) + 2\frac{\lambda_M}{\sqrt{2M}}\frac{\sqrt{2M-\lambda_M^2}}{\sqrt{2M}}\right] - \frac{M}{2}. \tag{5}$$

Based on the above approach, it seems that two simulation parameters, M and α, may have influence on the statistical properties of the generated normalized impedance matrix $\boldsymbol{z}$. In this paper, with each given (M, α), 100,000 normalized matrix, $\boldsymbol{z}$, are generated and the eigenvalues, λ_z, of all the $\boldsymbol{z}$ are grouped into one set that contains 200,000 elements. The values of M and α are chosen and shown in Table 1.

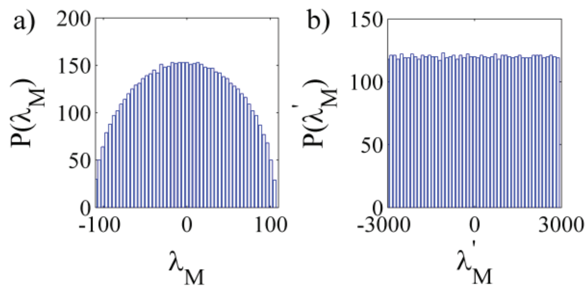

Fig. 1. (a) Distribution of the eigenvalues, λ_M, of 6000×6000 sized random matrix corresponding to GOE, and (b) distribution of the mapped eigenvalue, λ'_M, converted from λ_M shown in (a) through equation (5).

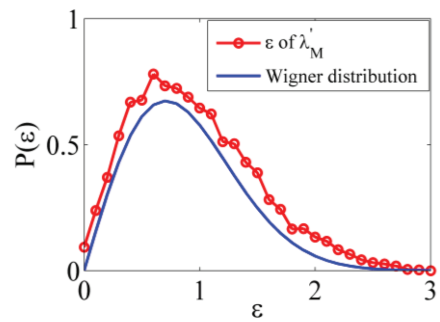

Fig. 2. The PDF of the normalized nearest neighbor eigenfrequency spacing for the mapped eigenvalues λ'_M which agrees with the Wigner distribution.

Table 1: Selections of simulation parameters

M	α
500	0.1-15 in a step of 0.1
1000	0.1-15 in a step of 0.1
6000	1-100 a step of 1

III. VARIATION OF THE STATISTICS OF λ_z FOR DIFFERENT VALUES OF M

Figures 3 to 5 show the PDFs of the real part, Re[λ_z], and the imaginary part, Im[λ_z], of the eigenvalues of the normalized impedance matrix with different M for α equaling to 0.1, 6 and 15 respectively. It can be seen that the value of M doesn't have significant effect on the statistics of the normalized impedance with a given α while α<15. In consideration of the simulation time which consumed most in calculating the eigenvalues of random matrices with high order, M can be chose to 1000.

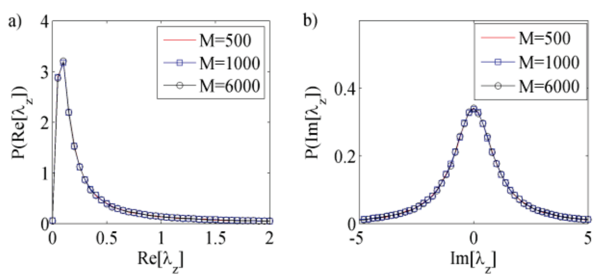

Fig. 3. (a) PDFs of the real part, and (b) the imaginary part of λ_z with different values of M when α equals to 0.1.

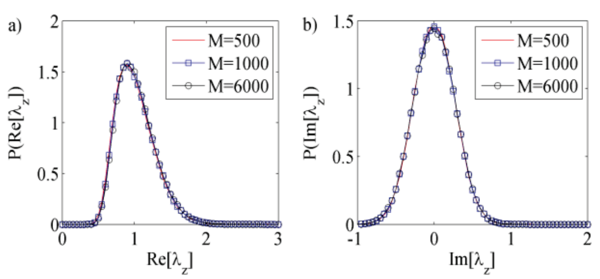

Fig. 4. (a) PDFs of the real part, and (b) the imaginary part of λ_z with different values of M when α equals to 6.

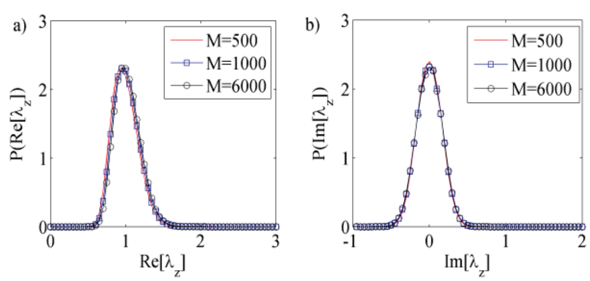

Fig. 5. (a) PDFs of the real part, and (b) the imaginary part of λ_z with different values of M when α equals to 15.

IV. VARIATION OF THE STATISTICS OF λ_z FOR DIFFERENT VALUES OF α

When α=0, the eigenvalues of the normalized impedance matrix are purely imaginary quantities. In this limit, [3] has shown that the eigenvalues are Lorentzian distributed with zero mean and unit width. When α=∞, both the real part and the imaginary part of the eigenvalues will be Gaussian distributed with the mean value equal to 1 and 0, respectively.

The PDFs of (a) the real part and (b) the imaginary part of the grouped eigenvalues of the normalized impedance matrix with different values of α are shown in Fig. 6. It can be seen that as α increase, the PDF of Re[λ_z] evolves from being peaked between Re[λ_z]=0 and Re[λ_z]=1, into a Gaussian-type distribution that peaked at Re[λ_z]=1 for large α, and the PDF of Im[λ_z] begins to sharpen up, developing a Gaussian appearance, which is in good agreement with the description in [7].

The variances of the real part and the imaginary part of the eigenvalues of z are identical and [7] gives the relation between them and the loss parameter which is shown in equation (6):

$$\sigma^2_{\mathrm{Re}[\lambda_z]} = \sigma^2_{\mathrm{Im}[\lambda_z]} = \frac{1}{\pi\alpha}, \quad \text{for } \alpha \gg 1, \tag{6}$$

where, σ^2 is the variance, Re[λ_z] and Im[λ_z] denote the real part and the imaginary part of the eigenvalues respectively.

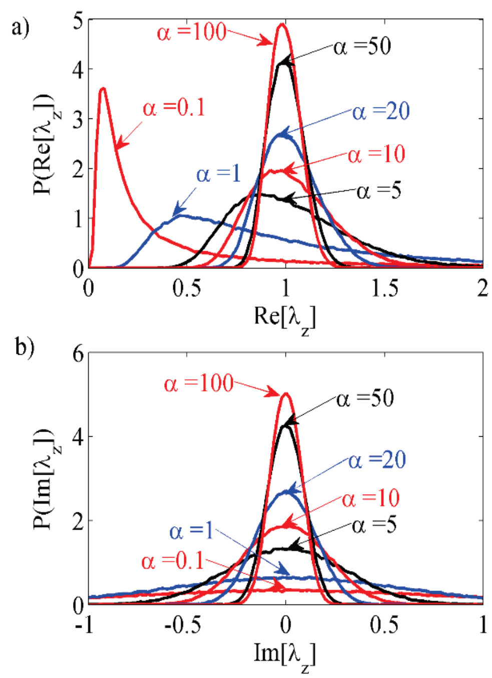

Fig. 6. (a) PDFs of the real part, and (b) the imaginary parts of λ_z with different values of α.

A more accurate result can be derived from Fig. 7, that is:

$$\sigma^2_{\mathrm{Re}[\lambda_z]} = \sigma^2_{\mathrm{Im}[\lambda_z]} = \frac{4}{3\pi\alpha}. \tag{7}$$

Based on Fig. 8, the relation between the variances of the diagonal elements of z and the loss parameter is:

$$\sigma^2_{\mathrm{Re}[z_{jj}]} = \sigma^2_{\mathrm{Im}[z_{jj}]} = \frac{1}{\pi\alpha}, \tag{8}$$

where, the z_{jj} (j=1 or 2) denotes the diagonal element of the normalized impedance matrix z.

The relation between the variances of the off-diagonal elements and the loss parameter is shown in Fig. 9 and equation (9), which is in good agreement with that given in [8]:

$$\sigma^2_{\mathrm{Re}[z_{ij}]} = \sigma^2_{\mathrm{Im}[z_{ij}]} = \frac{1}{2\pi\alpha}. \tag{9}$$

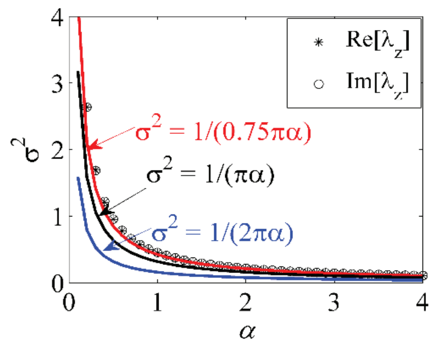

Fig. 7. The variances of real part and imaginary part of the eigenvalues of z vary with increasing α.

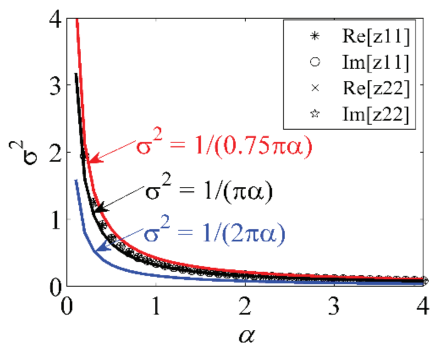

Fig. 8. The variances of real part and imaginary part of the diagonal elements of z vary with increasing α.

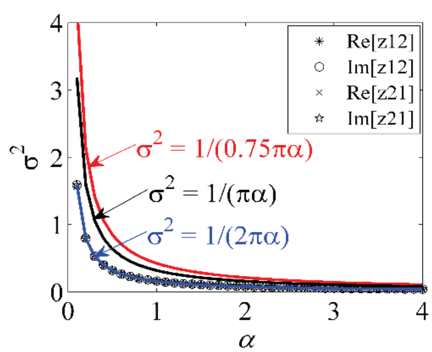

Fig. 9. The variances of real part and imaginary part of the off-diagonal elements of z vary with increasing α.

V. EXPERIMENTAL VERIFICATION

To verify the results given in part III and IV, an experiment is carried out on an empty computer case (40 cm × 40 cm × 20 cm) which is excited by two ports as shown in Fig. 9. The measurement is typically carried by measuring the scattering matrix $\boldsymbol{S}$, which will be transferred to the impedance matrix $\boldsymbol{Z}$, obtained through standard bilinear relationship:

$$\boldsymbol{Z} = \boldsymbol{Z}_0^{1/2}(\boldsymbol{I}+\boldsymbol{S})(\boldsymbol{I}-\boldsymbol{S})^{-1}\boldsymbol{Z}_0^{1/2}, \tag{10}$$

where, $\boldsymbol{Z}_0$ is a diagonal matrix of the characteristic impedance of the transmission line connected to the ports of cavities which is 50 Ω in our experiment and I is the unit matrix.

In order to realize a larger ensemble of the cavity impedance matrix for analyzing its statistics, a mode stirrer which comprises of a shaft and two metallic coated, orthogonally oriented blades is employed, as shown in Fig. 10. By rotating the mode stirrer in control of the stepper motor, the orientation of the blades is changed and each orientation corresponds to a different inner configuration. The blades are rotated for 100 different orientations in this paper.

For each configuration, the scattering parameters between two ports are measured by network analyzer from 6 GHz to 7 GHz and the number of points is set to 1000.

Then the normalized impedance matrix can be calculated from the cavity impedance matrix through equation (1). The variances of the eigenvalues, the diagonal elements and the off-diagonal elements are listed in Table 2 with the relevant loss parameters calculated by equations (7), (8) and (9) respectively. For each loss parameter, 100,000, 2×2 normalized impedance matrices are generated by doing Monte Carlo simulation with M=1000.

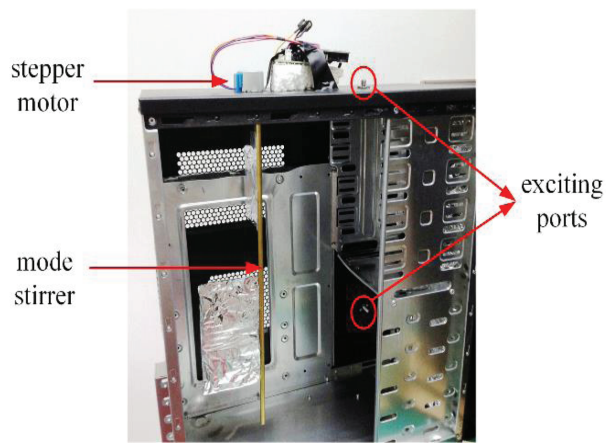

Fig. 10. Experimental setup.

To compare the statistics of these generated normalized impedance matrices with different loss parameters, the PDFs of the eigenvalues of z are chosen to be compared. The PDFs of (a) the real part, and (b) the imaginary part of the eigenvalues of z are shown in Fig. 11. It's obvious that the PDFs of the real and imaginary parts of the eigenvalues of the Monte Carlo simulated normalized impedance with the losses listed in Table 2 are almost identical, which are in good agreement with those derived from the measured data.

Table 2: The variances of the eigenvalues and elements of *z*

$\sigma^2(\times 10^{-2})$	λ_z	z_{11}	z_{22}	z_{12}	z_{21}
Re	6.67	5.66	4.71	2.65	2.49
Im	6.68	5.69	4.70	2.64	2.50
α	6.36	5.61	6.76	6.02	6.38

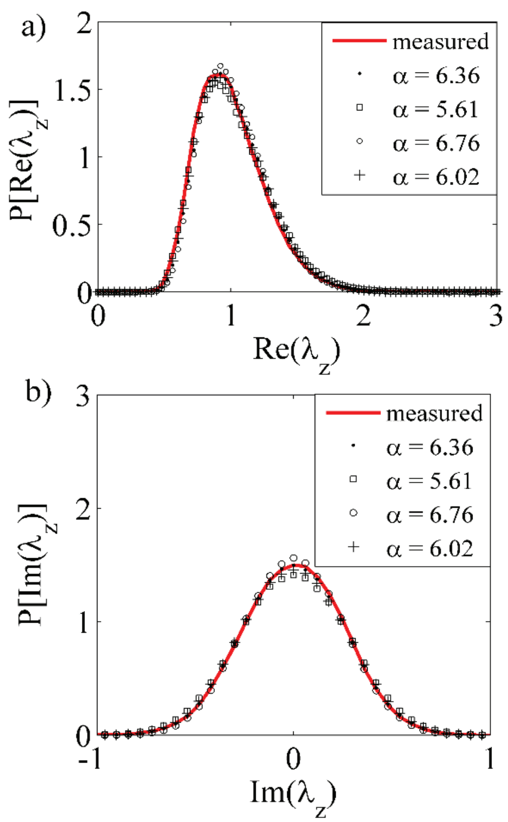

Fig. 11. PDFs of: (a) the real part, and (b) the imaginary part of the eigenvalues of the normalized impedance derived from the measured data (red curve) and those from the Monte Carlo simulated normalized impedance with different loss parameters listed in Table 2.

VI. CONCLUSIONS

It is concluded that, the statistics of the normalized impedance only depends on the cavity loss parameter α, which is in good agreement with the theoretical result. When α increases, the variances of the real part and the imaginary part of the eigenvalues, the diagonal elements and the off-diagonal elements of the normalized impedance matrix are damped as a function of α shown in equations (7), (8) and (9) respectively, which has been experimentally verified.

REFERENCES

[1] IEC 61000-5-9 Electromagnetic Compatibility (EMC) – Part 5-9: Installation and Mitigation Guidelines – System Level Susceptibility, 2009.

[2] X. Zheng, T. M. Antonsen Jr., and E. Ott, "Statistics of impedance and scattering matrices in chaotic microwave cavities: single channel case," *Electromagnetics*, vol. 26, no. 1, pp. 3-35, 2006.

[3] X. Zheng, T. M. Antonsen Jr., and E. Ott, "Statistics of impedance and scattering matrices of chaotic microwave cavities with multiple ports," *Electromagnetics*, vol. 26, no. 1, pp. 37-55, 2006.

[4] S. Hemmady, T. M. Antonsen Jr., E. Ott, and S. M. Anlage, "Statistical prediction and measurement of induced voltages on components within complicated enclosures: a wave-chaotic approach," *IEEE Trans. on EMC*, vol. 54, no. 4, pp. 758-771, 2012.

[5] J. A. Hart, T. M. Antonsen Jr., and E. Ott, "Effect of short ray trajectories on the scattering statistics of wave chaotic systems," *Physical Review E*, vol. 80, no. 4, p. 041109, 2009.

[6] J. Yeh, J. A. Hart, E. Bradshaw, T. M. Antonsen, E. Ott, and S. M Anlage, "Experimental examination of the effect of short ray trajectories in two-port wave-chaotic scattering systems," *Physical Review E*, vol. 82, no. 4, p. 041114, 2010.

[7] S. Hemmady, "A wave-chaotic approach to predicting and measuring electromagnetic field quantities in complicated enclosures, *Ph.D.*, University of Maryland, 2006.

[8] Z. B. Drikas, J. Gil Gil, S. K. Hong, J. Yeh, B. T. Taddese, and S. M. Anlage, "Application of the random coupling model to electromagnetic statistics in complex enclosures," *IEEE Trans. on EMC*, vol. 56, no. 6, pp. 1480-1487, 2014.

Xin Li received her B.S. degree in Physics Engineering from Tsinghua University, Beijing, China, in 2006 and is currently pursuing the Ph.D. degree at the Department of Engineering Physics in Tsinghua University. Her research interest include the BLT topology and statistical electromagnetics.

Cui Meng (M'08) received the bachelour's degree in 1992, and the Ph.D degree in 2003. She became an Associate Professor of the Department of Engineering Physics, Tsinghua University,in 2007. Her current research interests include numerical simulating of high power electromagneitc environment, measurement of high power transient EMP.

Yinong Liu was born in Beijing in 1963. He received the B.S. in Engineering Physics from Tsinghua University in 1985. Since 2003 he has been a Professor in Tsinghua University. His research interests include electronics and electromagnetic compatibility for experimental physics and radiation imaging.

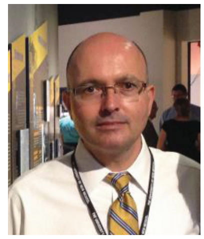

Edl Schamiloglu was born in The Bronx, NY in 1959. He received the B.S. degree in Applied Physics and Nuclear Engineering from Columbia University, NY, in 1979, the M.S. degree in Plasma Physics from Columbia University in 1981, and the Ph.D. degree in Engineering (minor in Mathematics) from Cornell University, Ithaca, NY, in 1988. He joined the University of New Mexico (UNM) as Assistant Professor in 1988 and he is currently Distinguished Professor of Electrical and Computer Engineering and directs the Pulsed Power, Beams, and Microwaves Laboratory.

Optimization of Impedance Bandwidth of a Stacked Microstrip Patch Antenna with the Shape of Parasitic Patch's Slots

Z. Manzoor [1] and G. Moradi [2]

[1] Department of Electrical Engineering
Amirkabir University of Technology, Tehran, Iran
Zahra_manzoor@yahoo.com

[2] Department of Electrical and Computer Engineering
Amirkabir University of Technology, Tehran, Iran
ghmoradi@aut.ac.ir

Abstract **─** In this paper, a novel configuration of wideband stacked microstrip antenna for X/Ku band is presented and analyzed. By cutting five narrow rectangular and one trapezoidal slot on parasitic patch with different dimensions, the impedance bandwidth and resonance frequency of the proposed antenna is adjusted. Also, the effect of incorporated parallel slots on driven patch is examined based on equivalent circuit of E-shaped microstrip antenna. Antenna characteristics are simulated by CST simulator and far-field radiation patterns of simulated and measured results of an array of the proposed antenna are compared.

Index Terms **─** Equivalent circuit, stacked microstrip antenna, X/Ku band.

I. INTRODUCTION

Low gain, narrow bandwidth and low efficiency are confined microstrip antenna's applications beside their attractive features such as low weight, small size and ease of integration with microwave integrated circuits (MIC) [1].

Suffering from very narrow bandwidth poses efforts to design wideband microstrip antennas. Different methods like cutting slots in microstrip patch antenna [2] and stacking [3] have been reported to enhance the bandwidth of microstrip antennas. Impedance mismatch is reduced by a slot which is cut in microstrip patch antenna. In that way, the bandwidth increases. Also, by using multilayered substrates in microstrip antennas, degree of freedom to optimize antenna's performance characteristics such as bandwidth and gain increases [4].

Based on these approaches, the stacked microstrip antennas have appeared. In these structures, commonly two conducting patches are used in each layer. The bottom patch as a driven patch is excited by a coaxial probe and the upper patch is a parasitic patch [5].

In many reports such as [6] and [7], E-shaped rectangular patch antenna is used as the driven patch in stacked microstrip antennas. By referring to [8], an E-shaped rectangular patch is known as a wideband antenna due to two parallel slots cut into the rectangular patch. So, this antenna can be a proper driven patch to enhance stacked microstrip bandwidth.

In this paper, the E-shaped rectangular patch antenna is chosen as a driven patch. Contrast to common stacked antennas which have a simple rectangular patch as a parasitic patch, in this paper, a rectangular patch with six slits that have different lengths and widths. Also, one trapezoidal slot is cut in parasitic patch. This kind of parasitic patch can add different poles to antennas return loss. In fact, by inserting different slots with different dimensions and shapes in parasitic patch, the bandwidth of stacked antennas can be adjusted and the resonance bandwidth of them can be shifted to expected frequencies based on equivalent circuit of proposed antennas.

According to several applications for X/Ku band such as vehicle tracking, weather forecasting radars, dimensions of driven and parasitic patches are optimized to work in X/Ku band. The proposed antenna is simulated in CST and simulated results are compared with measurement.

II. ANTENNA DESIGN AND THEORETICAL CONSIDERATIONS

The geometry of the proposed antenna is presented in Fig. 1. In the present work, the patch is fed by co-axial cable (50 ohm). As shown in Fig. 1, the E- shaped patch is printed on the lower substrate as the driven patch. Dimensions of such patch are optimized to work in X/Ku band. Based on [9], the equivalent circuit of E-shaped is illustrated in Fig. 2. It can be seen, ΔC which is added due to two parallel slots, plays the main role in changing

Submitted On: November 12, 2014
Accepted On: June 26, 2015

the input impedance according to the equation 1, 2 and 3, which is modified based on small value of ΔC.

In [9], the ΔC is given by:

$$Zin = \frac{1}{R + j\omega L_2 + \dfrac{1}{j\omega C_2}}, \tag{1}$$

$$C_2 = \frac{\Delta C . C_1}{\Delta C + C_1} \approx \Delta C, \tag{2}$$

$$\Delta C = 2l_2 \frac{\varepsilon_0}{\pi}\left[\ln\left(2\frac{1+\sqrt{k'}}{1-\sqrt{k'}}\right)\right] + \ln\coth\left(\frac{\pi w_2}{4h_2}\right) + 0.013\frac{h_2}{w_2}, \tag{3}$$

where

$$k' = \sqrt{1-k^2}, \tag{4}$$

$$k^2 = \frac{\left(\dfrac{2(2w_2 + wf)}{w_2} - 1\right)}{\left(1 + \dfrac{2w_2 + wf}{w_2}\right)\left(\dfrac{wf}{w_2}\right)}. \tag{5}$$

In equation (3), the length of etched slots along a resonance edge has the main parameter to calculate. So, by varying l_2 and w_2, the input impedance can be controlled. To determine E-shaped antenna's dimensions, at the first step based on [1], the length and width of a rectangular patch are calculated for resonation in desire frequency. The length and width of E-shaped microstrip patch antenna are chosen same as the length and width of a rectangular patch:

$$L_P = \frac{c}{2f_r\sqrt{\dfrac{\varepsilon_r + 1}{2}}}, \tag{6}$$

$$\varepsilon_{reff} = \frac{\varepsilon_r + 1}{2} + \frac{\varepsilon_r - 1}{2}\left[1 + 12\frac{h_1}{L_P}\right]^{-1/2}, \tag{7}$$

$$L_{eff} = \frac{c}{2f_r\sqrt{\varepsilon_{reff}}}, \tag{8}$$

$$\Delta L = 0.421h\frac{(\varepsilon_{reff} + 0.3)(\dfrac{L_P}{h} + 0.264)}{(\varepsilon_{reff} - 0.258)(\dfrac{L_P}{h} + 0.8)}. \tag{9}$$

In the next step, the amount of C_1 and L_1 which is shown in Fig. 2, are calculated based on [1]. ΔC should be around 100 times smaller than C_1 to satisfy the equation (2). According to this point, l_2 and w_2 are estimated. As the result of this analysis, the impedance bandwidth can be adjusted based on equation (1). To improve VSWR, two slits are etched along non resonance edges. In the next step, to enhance the impedance bandwidth, a wideband structure is chosen as the parasitic patch which is located on top layer. A rectangular patch with seven slots is selected to improve band width. According to different lengths and widths of these slots, the band width of the antenna can control and widens up to 23%. Also, different shapes of such slots have impressive effect on VSWR due to the alternation that is accrued in equivalent circuit of the stacked antenna based on [10]. Dimensions of the proposed stacked antenna are mentioned in Table 1. The thickness of lower layer (h_2) and top layer (h_1) are 1.65 mm and RO4003 is chosen as the substrate for both layers in demonstrated structure.

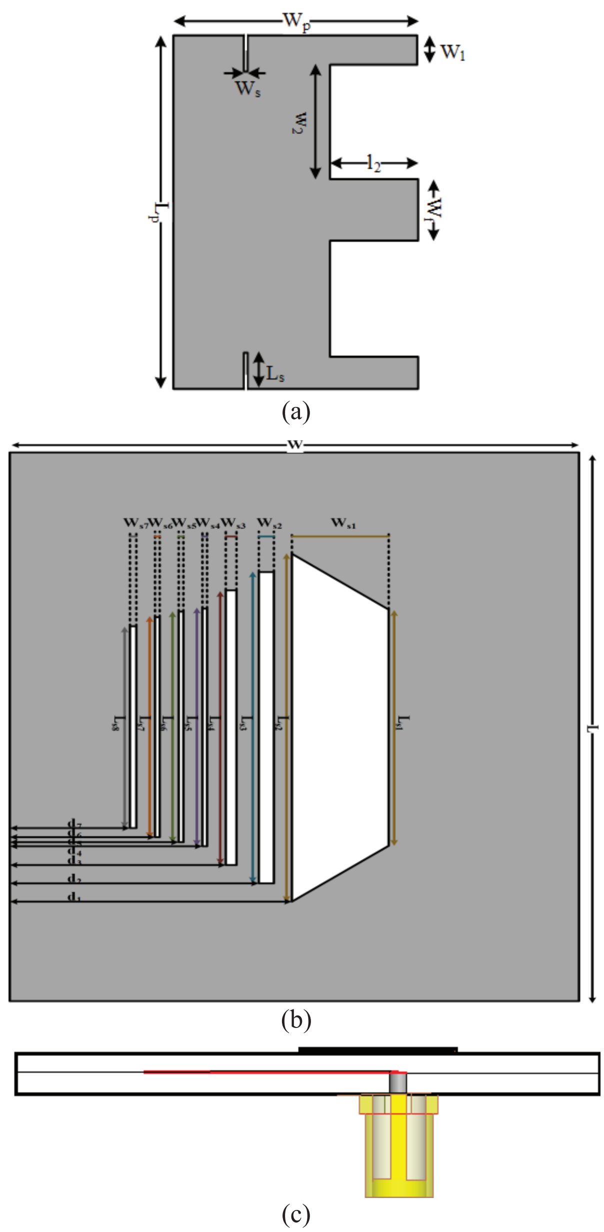

Fig. 1. (a) E-shaped microstrip antenna as the driven patch in lower layer, (b) rectangular microstrip antenna with six rectangular slits and a trapezoidal slot as the parasitic patch in the top layer, and (c) side view of the proposed stacked antenna.

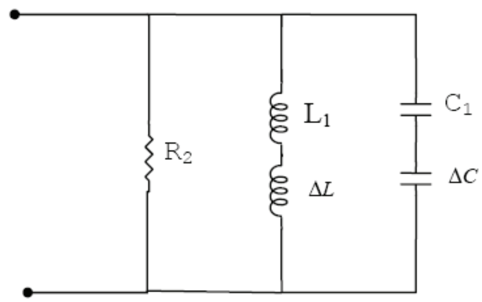

Fig. 2. Equivalent circuit of the E-shaped patch antenna.

Table 1: Dimensions of the proposed stacked microstrip antenna

Parameters	Dimensions (mm)
Wp	20
Lp	30
Ws	0.3
W_1	2.5
W_2	10
l_2	7.5
W_f	5
L_s	3
L	15
W	12
Ls1	6.5
Ls2	9.5
Ws1	2
Ls3	8.5
Ws2	0.3
Ls4	7.5
Ws3	0.2
Ls5	6.5
Ws4	0.1
Ls6	6.3
Ws5	0.1
Ls7	6
Ws6	0.1
Ws7	0.1
Ls8	5.5
d_1	6
d_2	5.3
d_3	4.6
d_4	4.1
d_5	3.6
d_6	3.1
d_7	2.6

In this paper, to design antenna which its center frequency is 12 GHz, the calculated length is 18.3 mm. This dimension causes C_1 to become around 1 pF. In that way, by choosing ΔC~0.01 pF, the dimensions of parallel slots on E-shaped antenna is calculated based on equation (3).

III. RESULTS AND DISCUSSION

Variation of S_{11} with different values of l_2 is shown in Fig. 3. As illustrated in Fig. 3, l_2 as the length of the etched slots along a resonance edge on driven patch, has the significant impact on shifting resonance frequency. By increasing l_2, the resonance frequency decreases due to increase in electrical length of slots on driven patch.

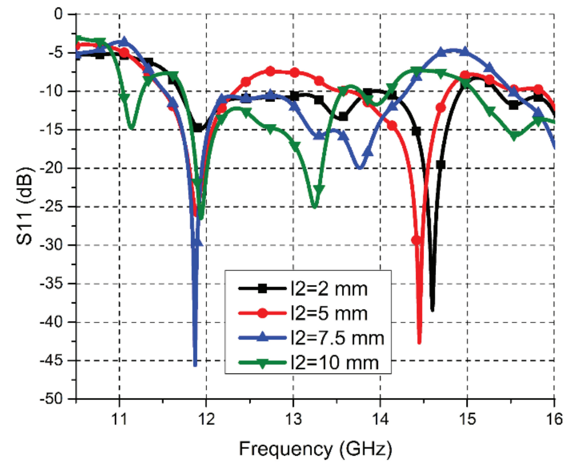

Fig. 3. Variation of S_{11} with different values of l_2.

By adding parasitic patch on E-shaped microstrip antenna, mutual capacitance is added to equivalent circuit of the proposed antenna [12]. Based on [13], this mutual capacitance's value depends on top layer thickness. Variation of reflection coefficient with upper layer thickness is simulated and shown in Fig. 4. By increasing the upper layer thickness, mismatch of the antenna decreases in wide range of frequencies. In that way, the impedance bandwidth will enhance dramatically. This extend in the impedance bandwidth, is the result of the decrease in the mutual capacitance which is created between driven and parasitic patches [11].

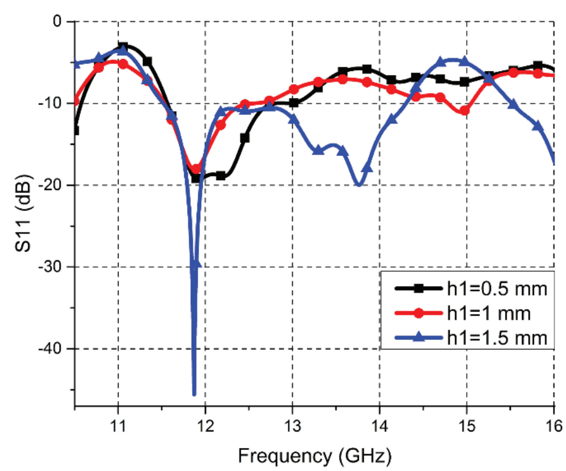

Fig. 4. Variation of S_{11} with upper layer thickness.

Finally, to improve antenna's gain, the stacked structure is used as the element of an array. To confirm this, far field pattern of single and array structures are compared in Fig. 5.

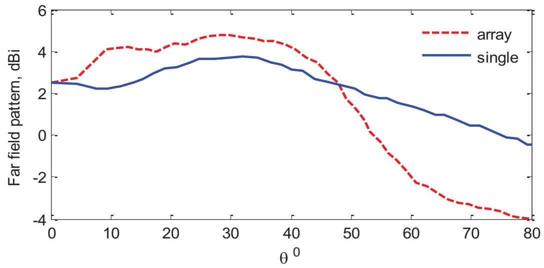

Fig. 5. Far field pattern of the proposed single and array antenna.

By considering the plane of the antenna is theta=90°, for specific application that antenna's gain should be improved between phi=0° and phi=30°, the proposed antenna has the better gain as the array structure with 29.2 mm distances between two elements.

For the fabricated array antenna which is shown in Fig. 6, array's gain of simulation and measurement of the representative structure are shown in Fig. 7. It can be seen that the simulated and the measured results are in a good agreement. As can be seen in Fig. 7, the main lobe of the proposed antenna is around φ=70° at the plane θ=90°.

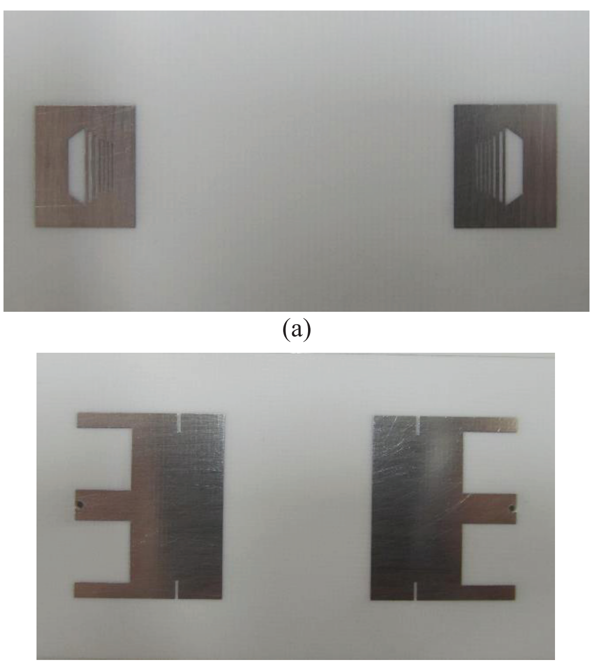

(a)

(b)

Fig. 6. (a) The parasitic patch of proposed antenna, and (b) the driven patch of proposed antenna.

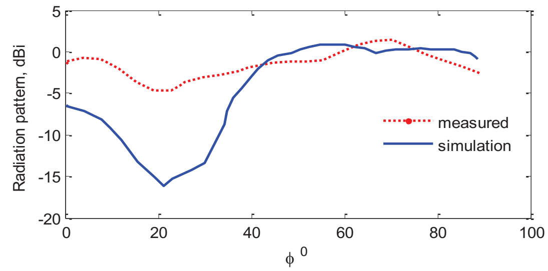

Fig. 7. Antenna far-field radiation pattern at θ=90°.

IV. CONCLUSION

A novel design of wideband stacked microstrip antenna has been constructed by cutting six different slots with different areas on parasitic patch. This modification on parasitic patch antenna shape, enhanced the bandwidth of the microstrip antenna up to 23%, which shows improvement in comparison with the recent existing data [14]. Based on the equivalent circuit of E-shaped microstrip antenna, the frequency band that antenna works is adjusted. To improve antenna gain, the proposed antenna has been used as the element of an array. The far-field radiation patterns of simulated and measured results are compared, which shows acceptable agreement.

REFERENCES

[1] R. Garg, P. Bhartia, I. Bahl, and A. Ittipiboon, *Microstrip Antenna Design Handbook*, Artech House, Norwood, MA, 2001.

[2] X. X. Zhang and F. Yang, "Study of slit cut microstrip antenna and its application," *Microwave Opti. Technol. Lett.*, vol. 18, pp. 297-300, 1998.

[3] J. A. Ansari and R. B. Ram, "Broadband stacked U-slot microstrip patch antenna," *Progress In Electromagnetic Research Letters*, vol. 4, pp. 17-24, 2008.

[4] J. T. Aberle, M. Chu, and C. R. Birtcher, "Scattering and radiation properties of varactor-tuned microstrip antennas," *IEEE Antennas Propagat. Soc. Int. Symp. Digest*, vol. 4, pp. 2229-2232, July 1992.

[5] D. K. Srivastava, J. P. Saini1, and D. S. Chauhan, "Wideband electromagnetically coupled coaxial probe fed slot loaded stacked patch antenna," *International Journal of Engineering, Science and Technology*, vol. 3, no. 3, pp. 154-159, 2011.

[6] R. Divyal and M. Priya, "Design and characterization of E-shape microstrip patch antenna for wireless communication," *ICTACT Journal on Communication Technology*, vol. 04, issue: 01, Mar. 2013.

[7] R. S. Kushwaha and D. K. Srivastava, "A compact printed extremely wideband microstrip patch antenna with stacked configuration," *International*

Journal of Advanced Research in Computer Science and Software Engineering, vol. 3, issue 12, Dec. 2013.
[8] M. T. Islam, M. N. Shakib, and N. Misran, "Broadband E-H shaped microstrip patch antenna for wireless systems," *Progress In Electromagnetics Research, PIER 98*, pp. 163-173, 2009.
[9] P. Hemendra, S. V. Pandey, and M. Sahoo, "Design of a modified E-shaped dual band patch antenna for Ku band application," *International Conference on Communication Systems and Network Technologies*, 2012.
[10] W. J. R. Hoefer, "Equivalent series inductance of a narrow transverse slit in microstrip," *IEEE Trans. Microwave Theory Tech.*, vol. MTT-25, pp. 822-824, Oct. 1977.
[11] K. R. Carver and J. W. Mink, "Microstrip antenna technology," *IEEE Trans. Antennas Propag.*, vol. 39, pp. 2-24, 1981.
[12] K. A. Pradyot, P. Reena, S. S. Pattnaik, and R. C. Saraswat, "Analysis of an electromagnetically coupled stacked cylindrical-rectangular microstrip patch antenna," *International Journal of Microwave and Optical Technology*, vol. 4, no. 1, Jan. 2009.
[13] S. S. Shivnarayan and B. R. Vishkarma, "Analysis of slot loaded rectangular microstrip patch antenna," *Indian Journal of Radio and Space Physics*, vol. 34, pp. 424-430, 2005.
[14] J. Neenansha, N. Rajesh, K. Anubhuti, and G. Puran, "Dual band E-shape microstrip patch antenna on RT Duroid 5880 substrate for pervasive wireless communication," *(IJCSIT) International Journal of Computer Science and Information Technologies*, vol. 2, no. 3, pp. 1075-1081, 2011.

Zahra Manzoor received her B.Sc. degree in Electrical Engineering from Tabriz University, Tabriz, Iran. She got her M.Sc. in Electrical Engineering from Amirkabir University of Technology (Tehran Polytechnic), Tehran, Iran in 2013. Her main research interests are microwave and passive microwave circuits and systems. She is currently working in local companies and research centers on design and fabrication of microwave planar structures.

Gholamreza Moradi was born in Shahriar, Iran in 1966. He received the Ph.D. degree in Electrical Engineering from Amirkabir University of Technology (Tehran Polytechnic), Tehran, Iran in 2002. His main research interests are numerical electromagnetics, antennas, active microwave and mm-wave circuits and systems. He is currently an Associate Professor with the Electrical Engineering Department, Amirkabir University of Technology. He has published several papers in the refereed journals and international conferences.

Design of Balanced SIW Filter with Transmission Zeroes and Linear Phase

Q. Xiao and C. X. Zhou

Ministerial Key Laboratory of JGMT
Nanjing University of Science and Technology, Nanjing, 210094, China
850127498@qq.com, zhouchx1010@gmail.com

Abstract **─** This paper provides a design method for balanced bandpass filters (BPFs) with high performance based on substrate integrated waveguide (SIW) structure. A novel balanced SIW filter with the characteristics of transmission zeroes, linear phase and wideband common-mode suppression is proposed. By analyzing the equivalent circuits of the proposed SIW filter under differential-mode (DM) and common-mode (CM) excitations, the DM transmission with CM suppression characteristic of the filter is demonstrated. The source-load coupled microstrip lines are introduced to realize the negative coupling and the design method for filters with source-load coupling is given. Good agreement is demonstrated between the simulated and the measured ones

Index Terms **─** Balanced filter, linear phase, substrate integrated waveguide (SIW), transmission zeroes.

I. INTRODUCTION

Balanced circuits have drawn much attention as they have higher immunity to environmental noise and low electromagnetic interference compared with single-ended circuits. As the key components, various balanced filters have been widely studied and demonstrated [1-7]. In the early times, the microwave differential filters were developed by microstrip line structures, such as the stretched or coupled transmission lines, the coupled stepped impedance resonators (SIR), the stepped impedance slotline multiple-mode resonators (MMR) and the double-sided parallel-strip lines (DSPSL) [1-5]. To overcome the drawbacks of high radiation loss, low power handling capability, low-factor, and maintain the benefits of low-cost, compact size and good integration, the substrate integrated waveguide (SIW) balanced filters was proposed [6,7]. In [6], the balanced bandpass filters (BPFs) are realized by the structures of half-mode substrate integrated waveguide (HMSIW) and folded HMSIW. The common-mode (CM) suppression is achieved by applying a non-coupling slot and the spectral separation of differential-mode (DM)-CM resonances in the HMSIW and folded HMSIW cases, respectively. The proposed BPFs can achieve the CM rejection level more than 40 dB over a wide frequency range. To improve the filter selectivity, a differential BPF with two transmission zeros is presented in [7] based on SIW structure. The CM suppression is realized by a new balanced SIW section on single-layer substrate technology. However, to meet stringent requirements imposed on the most recent wireless standards, a flat group delay filter response should be guaranteed to avoid signal blur besides sharp rejection.

This paper proposes a balanced SIW BPF with transmission zeroes, linear phase and wideband common-mode suppression. By analyzing the equivalent circuits of the proposed SIW filter under DM and CM excitations, the DM transmission with CM suppression characteristic of the filter is demonstrated. Another innovative point of the paper is that the source-load coupled microstrip lines are introduced and the design method for filters with source-load coupling is given. To the best of our knowledge, there is no reported work done so far on balanced BPFs with both linear phase and highly selectivity. The proposed balanced BPF is designed using the SIW scheme at 10 GHz and can achieve almost perfectly flat group delay over the central 60% of the pass band.

II. BALANCED FILTER DESIGN

The balanced filter is designed on F4B substrate, with thickness of 0.5 mm, relative permittivity of 2.65, and dielectric loss tangent of 0.001 (at 10 GHz). The geometry of the proposed balanced BPF is shown in Fig. 1 (a). The four-port circuit is ideally symmetric with respect to the vertical and horizontal symmetry plane. It is composed of six SIW cavities which are represented by R_1, R_2, R_3, R_4, R_1', and R_4', respectively.

A. Common-mode analysis

Under CM operation, the vertical symmetry plane becomes a perfect magnetic wall and the CM equivalent circuit is shown in Fig. 1 (b). R_1 and R_4 are the original resonators of the proposed balanced BPF, which operate in TE_{101} for the first resonant mode. The cavity 2(C_2) and cavity 3(C_3) are half of the original resonators R_2 and R_3 with the vertical symmetry plane being a magnetic wall

Submitted On: May 29, 2014
Accepted On: July 12, 2015

and the other three sidewalls being electric wall. In this case, the modes for R_2 and R_3 are TE_{101} for the first resonant mode. As R_1 and R_4 are designed to resonant at the operating frequencies, the resonant frequencies of C_2 and C_3 with similar size of R_1 and R_4 will not be in the operating pass-band. Thus, it performs a bandstop characteristic under CM excitations. To verify the above inference, simulated frequency responses under CM excitations are given in Fig. 2. We can see that the CM transmission is suppressed to be lower than -17 dB in a wideband.

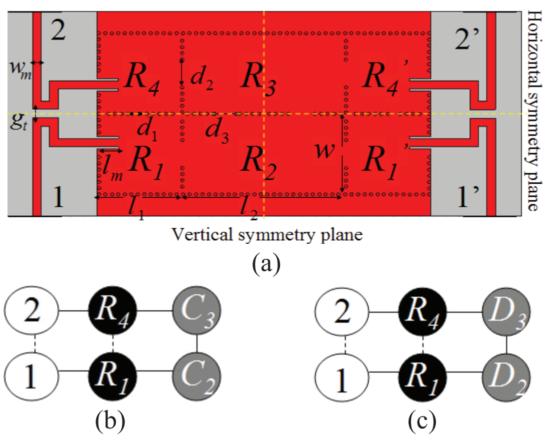

Fig. 1. Geometry and schematic topologies of the proposed balanced SIW filter: (a) geometry of the balanced BPF, (b) equivalent 2-port half bisection under CM operation, and (c) equivalent 2-port half bisection under DM operation.

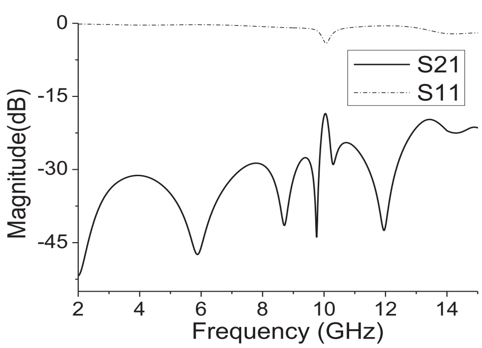

Fig. 2. Simulated results of the CM response.

B. Differential-mode analysis

While for DM operation, the vertical symmetry plane becomes a perfect electric wall, and the DM circuit can be obtained as shown in Fig. 1 (c). D_2 and D_3 are half of R_2 and R_3 with all four sidewalls being the electric wall. In this case, the modes for R_2 and R_3 are TE_{102} for the first resonant mode.

A 2-port 4-pole generalized chebyshev filter with both high selectivity and linear phase is synthesized with zeros [2.5j,-2.5j,1.4,-1.4]. Zeros [2.5j,-2.5j] in the imaginary axis are used to produce transmission zeros and zeros [1.4,-1.4] in the real axis are used to improve the phase. The synthesized S-parameters including magnitude and group delay with center frequency of f_0=10 GHz and bandwidth of BW=400 MHz are plotted as the dotted curves in Fig. 3, with the coupling matrix [8]:

$$M=\begin{array}{c c} & \begin{array}{cccccc} S & 1 & 2 & 3 & 4 & L \end{array} \\ \begin{array}{c} S\\1\\2\\3\\4\\L \end{array} & \begin{bmatrix} 0 & 1.0425 & 0 & 0 & 0 & -0.0298\\ 1.0425 & 0 & 0.9226 & 0 & 0.1471 & 0\\ 0 & 0.9226 & 0 & 0.6488 & 0 & 0\\ 0 & 0 & 0.6488 & 0 & 0.9266 & 0\\ 0 & 0.1471 & 0 & 0.9226 & 0 & 1.4025\\ -0.0298 & 0 & 0 & 0 & 1.4025 & 0 \end{bmatrix} \end{array}$$

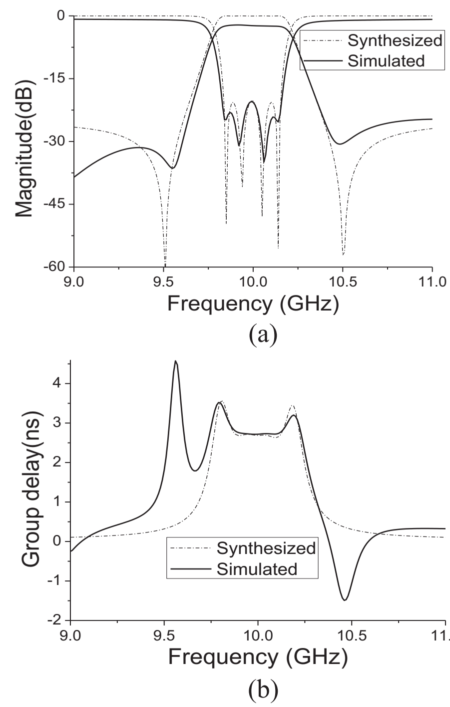

Fig. 3. Synthesized and simulated frequency responses of the equivalent 2-port half bisection under DM operation: (a) S-parameters and (b) group delay.

The dimensions of d_1, d_2, d_3 and l_m in Fig. 1 (a) for the required M_{14}, M_{12}, M_{23} and M_{S1} can be determined from Fig. 4 (a)-(c) with the method in [9] respectively.

The 50-Ω coupled microstrip lines in Fig. 1 (a) are proposed to realize the source-load coupling in this paper. While magnetic coupling (positive coupling in the coupling matrix) can be achieved with an inductive window between two adjacent SIW resonators [10], the coupled microstrip lines can achieve the electric coupling (negative coupling in the coupling matrix). Thus, both positive and negative couplings can be realized in the same plane. However, there is no relative handling with the source-load coupling M_{SL} in the existing literature. The proposed 50-Ω coupled microstrip lines to realize the source-load coupling are treated as two coupled resonators in this paper shown in Fig. 5 (a) for the first time. The relationship between the source-load coupling M_{SL} and the distance g_t between the coupled microstip lines is shown in Fig. 5 (b). Then the dimension of g_t for the required M_{SL} can be determined from Fig. 5 (b) [9].

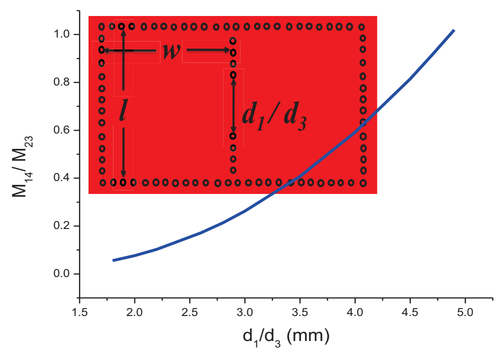

(a)

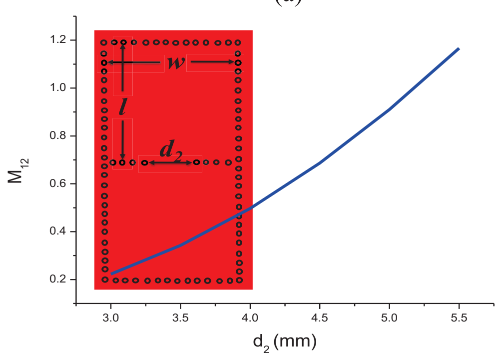

(b)

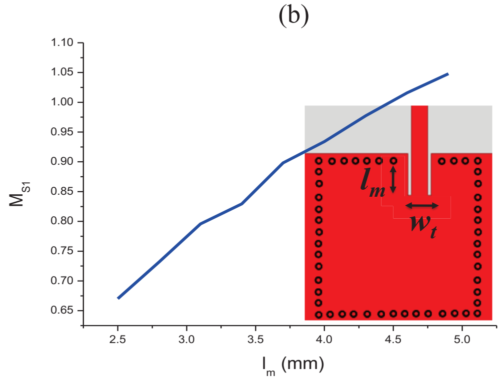

(c)

Fig. 4. Design curves for the 2-port BPF: (a) relationship between the coupling coefficient M14/M23 and the iris distance d between resonator 1 and 4 or resonator 2 and 3, (b) relationship between the coupling coefficient M12 and the iris distance d between resonator 1 and 2, and (c) relationship between the coupling coefficient MS1 and the insertion length of lm.

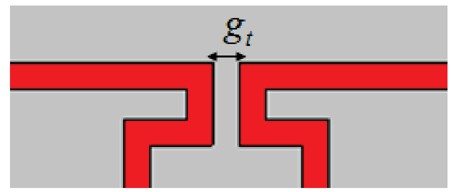

(a)

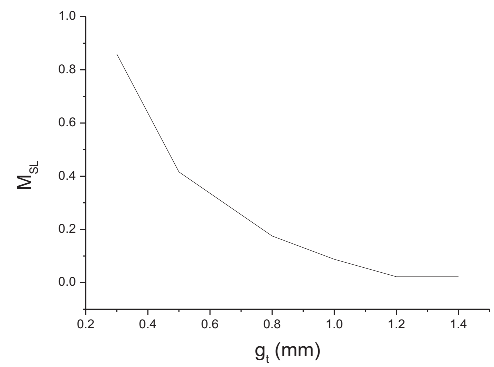

(b)

Fig. 5. Geometry of the source-load coupling and the design curve: (a) geometry of the source-load coupling and (b) relationship between the source-load coupling coefficient M_{SL} and the distance g_t between microstip lines.

After optimization, the simulated results of the 2-port BPF are plotted as the solid curves in Fig. 3. The mismatch of the group delay in the stop-band is due to the existence of the transmission zeroes. In addition to this, good agreement can be achieved between the synthesized results and the simulated ones.

C. Design of the balanced filter

The procedure for the design of the balanced SIW filter with both transmission zeros and linear phase is outlined as follows:

Step 1) **Determine the requirement of the balanced filter.** Based on the desired frequency response, center frequency, bandwidth and transmission zeros can be determined.

Step 2) **Design the 2-port filter.** The 2-port filter is synthesized according to the requirement in step 1 and the coupling matrix are calculated [8]. Then, the dimensions of the 2-port filter can be determined from the extracted design curves with the method in [9].

Step 3) **Realize the balance filter.** By duplicating the 2-port filter along the vertical symmetry plane, The balanced filter can be achieved.

Based on the above analysis of the CM and DM operations, a balanced BPF with transmission zeroes, linear phase and wideband common-mode suppression can be achieved with the main design parameters: g_t=1.4 mm, l_m=3.29 mm, l_1=12.87 mm, l_2=25.28 mm, w=13 mm, w_m=1.35 mm, d_1=1.9 mm, d_2=4.5 mm, d_3=4.08 mm. The simulated results of the balanced BPF under DM and CM operations are plotted as the dotted curves in Figs. 6 (a) and (b), respectively. The group delay responses of the balanced BPF are plotted as the dotted curves in Fig. 6 (c).

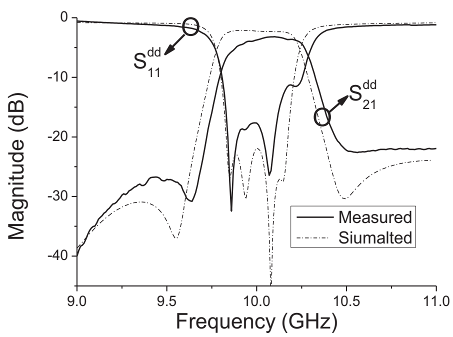

(a)

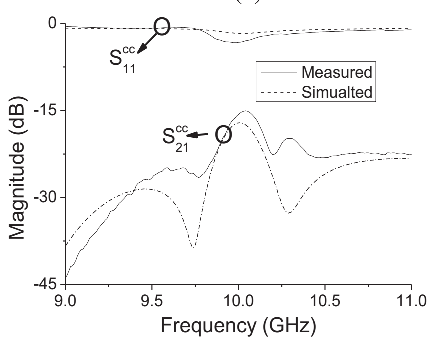

(b)

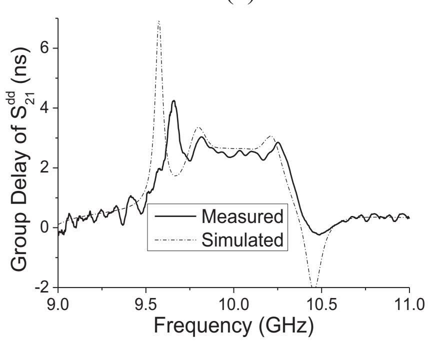

(c)

Fig. 6. Measured and simulated responses of the filter: (a) DM responses, (b) CM responses, and (c) group delay responses.

III. RESULTS AND DISCUSSION

Figure 7 shows the photograph of the fabricated filter. The simulated and measured results of the filter are plotted in Fig. 6. The measured central frequency is 10.02 GHz, and 3-dB bandwidth is 400 MHz. The in-band insertion loss and return loss are better than -3.5 dB and -12 dB, respectively. The two transmission zeroes are located at 9.55 GHz and 10.5 GHz. The group delay equalization is over 60% of the pass-band. The measured results include the influence of the limited fabrication precision and measurement errors, thus they are somewhat worse than the simulated results

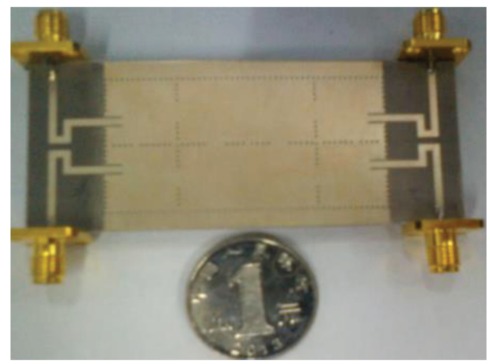

Fig. 7. Photograph of the fabricated differential filter.

IV. CONCLUSIONS

In this paper, a new balanced SIW BPF with high performances is proposed. The design of the balanced filter is simplified through designing a 2-port filter with high performance and duplicating it along the vertical symmetry plane. The source-load coupled microstrip lines are introduced and the design method for filters with source-load coupling is given. Simulated and measured results show that the presented filter has the performances of linear phase, high out-of-band rejection, and good common suppression which can be applied to the microwave system of high quality.

ACKNOWLEDGMENT

This work was supported by the National Natural Science Foundation Committee of China (61401202).

REFERENCES

[1] C-H. Lee, C-I. G. Hsu, and C-C. Hsu, "Balanced dual-band BPF with stub-loaded SIRs for common-mode suppression," *IEEE Microw. Wireless Compon. Lett*., vol. 20, no. 2, pp. 70-72, 2010.

[2] T. B. Lim and L. Zhu, "Highly selective differential-mode wideband bandpass filter for UWB application," *IEEE Microw. Wireless Compon. Lett*., vol. 21, no. 3, pp. 133-135, 2011.

[3] X-H. Wang, Q. Xue, and W-W. Choi, "A novel ultra-wideband differential filter based on double-sided parallel-strip line," *IEEE Microw. Wireless Compon. Lett.*, vol. 20, no. 8, pp. 471-473, 2010.

[4] C-H. Lee, C-I. G. Hsu, and C-J. Chen, "Band notched balanced UWB BPF with stepped-impedance slotline multi-mode resonator," *IEEE Microw. Wireless Compon. Lett.*, vol. 22, no. 4, pp. 182-184, 2012.

[5] X-H. Wu and Q-X. Chu, "Compact differential ultra-wideband bandpass filter with common-mode suppression," *IEEE Microw. Wireless Compon. Lett*., vol. 22, no. 9, pp. 456-458, 2012.

[6] M-H. Ho and C-S. Li, "Novel balanced band-pass filters using substrate integrated half-mode waveguide," *IEEE Microw. Wireless Compon. Lett*., vol. 23, no. 2, pp. 78-80, 2013.

[7] X. Xu, J-P. Wang, and L. Zhu, "A new approach to design differential-mode bandpass filters on SIW structure," *IEEE Microw. Wireless Compon. Lett*., vol. 23, no. 12, pp. 635-637, 2013.

[8] S. Amari, U. Rosenberg, and J. Bornemann, "Adaptive synthesis and design of resonator filters with source/load-multiresonator coupling," *IEEE Trans. Microw. Theory Tech*., vol. 50, no. 8, pp. 1969-1978, 2002.

[9] J. S. Hong and M. J. Lancaster, *Microstrip Filters for RF/Microwave Applications*, Wiley, New York, 2001.

[10] X-P. Chen, W. Hong, T-J. Cui, J-X. Chen, and K. Wu, "Substrate integrated waveguide (SIW) linear phase filter," *IEEE Microw. Wireless Compon. Lett*., vol. 15, no. 11, pp. 787-789, 2005.

Q. Xiao was born in Shandong Province, China, in 1990. She received the B.S. degree in Electronic Information Science and Technology from Dezhou University, Shandong, China, in 2012, and is currently working toward the master degree at Nanjing University of Science and Technology. Her research interests is RF/microwave circuit designs.

C. X. Zhou was born in Jiangsu Province, China, in 1985. She received the B.S. degree in Electronic Information Science and Technology from Nankai University, Tianjin, China, in 2007, and the Ph.D. degree at Nankai University. She has been a Lecture at Nanjing University of Science and Technology since 2012. From September 2010 to February 2012, she is a Visiting Student in the Department of Electrical and Computer Engineering, National University of Singapore, Singapore. Her research interests include RF/microwave circuit designs and integration.

Compact Dual-Wideband BPF Based on Quarter-Wavelength Open Stub Loaded Half-Wavelength Coupled-Line

Jin Xu

School of Electronics and Information,
Northwestern Polytechnical University, Xi'an, 710072, P.R. China
E-mail: xujin227@nwpu.edu.cn

Abstract **—** In this paper, a novel dual-wideband bandpass filter (BPF) is presented by using quarter-wavelength open stub loaded half-wavelength coupled-line. Equivalent voltage-current analysis method is applied to analyze this structure, which shows it has two tunable transmission zeros and dual-wideband frequency response. As an example, a dual-wideband BPF covering 1.228/1.57/6.8 GHz for GPS (Link 1 and Link 2) and RFID applications is designed, fabricated and measured. The fabricated filter has a compact size of $0.043\lambda_g \times 0.213\lambda_g$. The measured results show that the fabricated filter has the merits of low insertion loss, good return loss and high band-to-band isolation. The proposed dual-band BPF also has a very simple physical topology and quick design procedure.

Index Terms **—** Bandpass filter (BPF), coupled-line, dual-wideband, stub-loaded resonator.

I. INTRODUCTION

Modern dual-mode communication system requires a dual-band bandpass filter (BPF) to enhance the electrical performance of the radio frequency end. In recent years, many structures have been proposed to meet the above requirement. In [1], two sets of uniform-impedance half-wavelength resonators are used to design a dual-narrowband BPF for 1.8 GHz DCS and 2.4 GHz WLAN applications. A dual-passband BPF with multi-spurious suppression is realized by using asymmetrical stepped-impedance resonators in [2]. In [3], compact dual-band BPFs with controllable bandwidths are proposed by using stub loaded multiple-mode resonator. In [4], the quad-mode resonator is applied to design a compact and high-selectivity dual-mode dual-band BPF. Modified coupled-line is another effective structure to design dual-band BPF. It is widely known that coupled-line is a classical structure used in single-band BPF design, mainly due to its compact 1-D planar physical configuration and high passband selectivity. In [5,6], S. Lee and Y. Lee firstly introduce capacitive or inductive stubs in traditional coupled-line structure to achieve dual-band frequency response, and the transverse dimension of coupled-line-type BPF is decreased simultaneously. However, these two dual-band BPFs suffer from relatively large circuit size, complicated physical topology and design procedure. In the author's previous work [7,8], two stub loaded coupled-line dual-band BPFs have been proposed, and a good filter performance and compact circuit size has been achieved. Nevertheless, the insertion loss in [7] and out-of-band rejection in [8] need further improvements. In addition, the bandwidth in [7] cannot meet the requirement of modern dual high-data-rate communication system.

In this paper, a novel quarter-wavelength open stub loaded half-wavelength coupled-line is proposed, which has dual-band frequency performance. By using a half-wavelength transmission line to cascade the proposed two stub loaded coupled-line, a dual-wideband BPF with large dual-band central frequency ratio can be designed. As an example, a dual-wideband BPF for 1.228/1.57 GHz GPS and 6.8 GHz RFID applications is designed, fabricated and measured. Equivalent voltage-current analysis method is applied to analyze this dual-band BPF, and the corresponding design rules are given for the filter design.

II. THEORY ANALYSIS

A. ABCD parameters and S parameters

Figure 1 (a) gives the transmission line model of proposed dual-wideband BPF. It consists of two quarter-wavelength open stub loaded half-wavelength coupled-line and one half-wavelength transmission line. In order to analyze this structure, equivalent voltage and current analysis method is used, and the corresponding model is given in Fig. 1 (b). Thus, the *ABCD* parameters of proposed dual-wideband BPF can be given as follows:

Submitted On: June 17, 2014
Accepted On: June 4, 2015

$$\begin{bmatrix} A_F & B_F \\ C_F & D_F \end{bmatrix} = \begin{bmatrix} A_{ci} & B_{ci} \\ C_{ci} & D_{ci} \end{bmatrix} \begin{bmatrix} A_t & B_t \\ C_t & D_t \end{bmatrix} \begin{bmatrix} A_{co} & B_{co} \\ C_{co} & D_{co} \end{bmatrix}, \quad (1)$$

where

$$\begin{bmatrix} A_t & B_t \\ C_t & D_t \end{bmatrix} = \begin{bmatrix} \cos(2\theta) & jZ\sin(2\theta) \\ jY\sin(2\theta) & \cos(2\theta) \end{bmatrix} \quad Y = 1/Z.$$

If even-mode electrical length of coupled-line (θ_e) equaling to odd-mode electrical length of coupled-line (θ_o) are assumed, the following two equations can be obtained from the [9] as follows:

$$\begin{bmatrix} v_1 - v_2 \\ i_1 - i_2 \end{bmatrix} = \begin{bmatrix} \cos(2\theta) & jZ_{co}\sin(2\theta) \\ jY_{co}\sin(2\theta) & \cos(2\theta) \end{bmatrix} \begin{bmatrix} v_4 - v_3 \\ -(i_4 - i_3) \end{bmatrix}, \quad (2a)$$

$$\begin{bmatrix} v_1 + v_2 \\ i_1 + i_2 \end{bmatrix} = \begin{bmatrix} \cos(2\theta) & jZ_{ce}\sin(2\theta) \\ jY_{ce}\sin(2\theta) & \cos(2\theta) \end{bmatrix} \begin{bmatrix} v_4 + v_3 \\ -(i_4 + i_3) \end{bmatrix}, \quad (2b)$$

where

$$Z_{ce} = Z_c\sqrt{(1+k_c)/(1-k_c)} \quad Y_{ce} = 1/Z_{ce},$$

$$Z_{co} = Z_c\sqrt{(1-k_c)/(1+k_c)} \quad Y_{co} = 1/Z_{co}.$$

The coupled-line in Fig. 1 (b) has the boundary condition of $v_3 = -i_3 Z_L = ji_3 Z_s \cot\theta$ and $v_4 = 0$. After substituting these two conditions into the equations (2), the *ABCD* matrix of quarter-wavelength open stub loaded half-wavelength coupled-line can be derived as:

$$\begin{bmatrix} A_{ci} & B_{ci} \\ C_{ci} & D_{ci} \end{bmatrix} = \begin{bmatrix} \dfrac{u_1}{u_5} & -\dfrac{u_3}{u_7} + \dfrac{u_1 u_6}{u_5 u_7} \\ \dfrac{u_2}{u_5} & -\dfrac{u_4}{u_7} + \dfrac{u_2 u_6}{u_5 u_7} \end{bmatrix}, \quad (3a)$$

$$\begin{bmatrix} A_{co} & B_{co} \\ C_{co} & D_{co} \end{bmatrix} = \frac{1}{u_1 u_4 - u_2 u_3} \begin{bmatrix} u_4 u_5 - u_2 u_6 & -u_1 u_6 + u_3 u_5 \\ -u_2 u_7 & -u_1 u_7 \end{bmatrix}, \quad (3b)$$

where

$$u_1 = -j\left[(Z_{ce} + Z_{co})\sin(2\theta)\right]/2,$$

$$u_2 = -\cos(2\theta),$$

$$u_3 = j\left[(Z_{co} - Z_{ce})\sin(2\theta)\right]/2,$$

$$u_4 = \left[(Y_{co} - Y_{ce})Z_s \cot\theta \sin(2\theta)\right]/2,$$

$$u_5 = -j\left[(Z_{co} - Z_{ce})\sin(2\theta)\right]/2,$$

$$u_6 = j\left[2Z_s \cot\theta \cos(2\theta) - (Z_{ce} + Z_{co})\sin(2\theta)\right]/2,$$

$$u_7 = -\frac{2\cos(2\theta) + (Y_{ce} + Y_{co})Z_s \cot\theta \sin(2\theta)}{2}.$$

Since the proposed dual-wideband BPF is symmetrical, its *S*-parameters can be then given by:

$$S_{11} = S_{22} = \frac{A_F + B_F/Z_0 - C_F Z_0 - D_F}{A_F + B_F/Z_0 + C_F Z_0 + D_F}, \quad (4a)$$

$$S_{21} = S_{12} = \frac{2(A_F D_F - B_F C_F)}{A_F + B_F/Z_0 + C_F Z_0 + D_F}. \quad (4b)$$

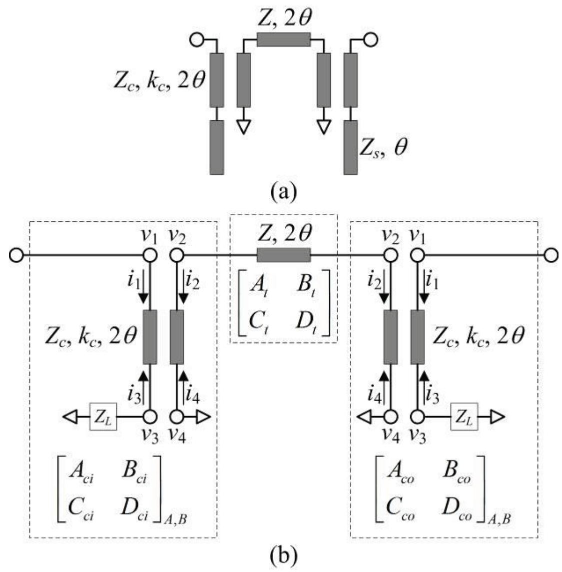

Fig. 1. (a) Transmission line model of proposed dual-wideband BPF, and (b) equivalent voltage and current analysis model.

B. Transmission zeros

The transmission zeros of proposed dual-wideband BPF is dependent on the quarter-wavelength open stub loaded half-wavelength coupled-line and independent on the half-wavelength transmission lines, so that the transmission zeros satisfy:

$$A_{ci,o} D_{ci,o} = B_{ci,o} C_{ci,o}. \quad (5)$$

After simplifying the equations (3), it will be derived that:

$$u_1 u_4 = u_2 u_3. \quad (6)$$

When $\theta = 0$, $\pi/2$ and π at the designing frequency f_0, respectively, it can be verified that the equation (6) is built. Thus, the proposed dual-wideband BPF has fixed transmission zeros at 0, f_0 and $2f_0$, respectively, within the frequency range $[0, 2f_0]$. Substituting u_1~u_6 into the equation (6), it can be gotten that:

$$\tan^2\theta = \left(Z_c\sqrt{1-k_c^2} + 4Z_s\right) \Big/ \left(Z_c\sqrt{1-k_c^2}\right). \quad (7)$$

The proposed dual-wideband BPF has a pair of tunable transmission zeros which are symmetrical along f_0. Its frequency locations are given as follows:

$$f_{z1} = \frac{2f_0}{\pi}\arctan\left(\sqrt{\frac{Z_c\sqrt{1-k_c^2} + 4Z_s}{Z_c\sqrt{1-k_c^2}}}\right), \quad (8a)$$

$$f_{z2} = \frac{2f_0}{\pi}\left(\pi - \arctan\left(\sqrt{\frac{Z_c\sqrt{1-k_c^2} + 4Z_s}{Z_c\sqrt{1-k_c^2}}}\right)\right). \quad (8b)$$

These two transmission zeros have the relationship of $0 < f_{z1} < f_0 < f_{z2} < 2f_0$, and repeat at every frequency range $[2nf_0, 2(n+1)f_0]$, where n is an integer.

C. Design rules

It can be verified that the proposed dual-wideband BPF has a symmetrical frequency response along the design frequency f_0. That is, two passbands of the proposed dual-wideband BPF has an equal value of absolute bandwidth BW. Under the initial designing parameters of Z = 140 Ω and k_c = 0.4, Fig. 2 plots the variation of f_{c2}/f_{c1} and BW/f_0 versus different values of $r_c = Z_c/Z$ and $r_s = Z_s/Z$, where f_{c1} and f_{c2} represents the central frequency of the first and second passband, respectively. It can be seen in Fig. 2 that f_{c2}/f_{c1} increases as r_c increases, but it decreases as r_s increases. It can be also seen in Fig. 2 that BW increases as r_s increases, and as r_c increases, BW increases firstly but then decreases. Figure 3 gives the variation of $|S_{21}|$ and $|S_{11}|$ versus different values of Z and k_c under fixed $r_c = r_s = 1.0$. It can be seen in Fig. 3 (a) that Z has minor effect on $|S_{21}|$ but it can be used to tune the $|S_{11}|$ slightly. It can be seen in Fig. 3 (b) that the BW of two passbands becomes wide as k_c increases.

In summary, in the dual-wideband design process, the designing parameters r_s and r_c can be tuned to achieve the desired frequency position of two passbands. The designing parameter k_c can be used to control the BW of two passbands and the designing parameter Z can be then tuned to acquire a good return loss. In addition, it should be noted that the BW of two passbands cannot be controlled individually due to its symmetrical frequency response.

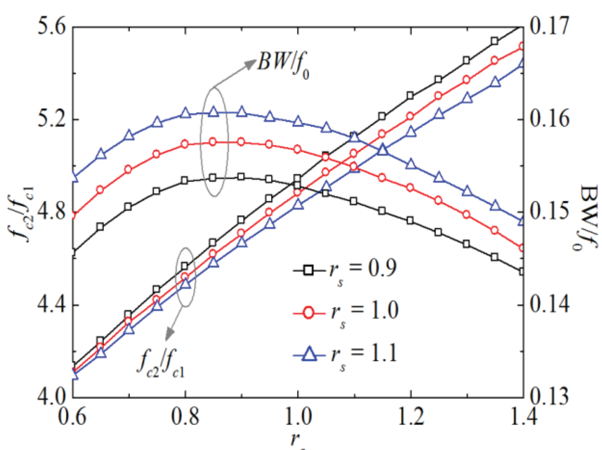

Fig. 2. Variation of f_{c2}/f_{c1} and BW/f_0 versus different values of r_c and r_s.

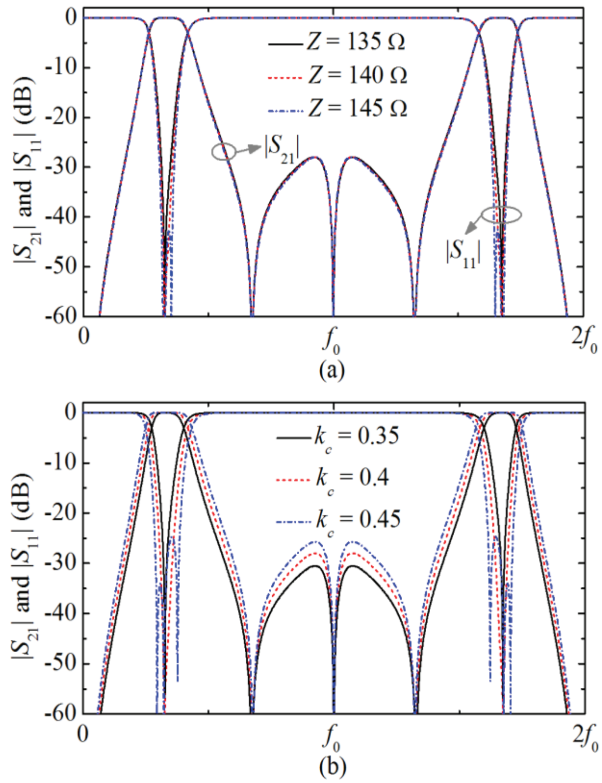

Fig. 3. Variation of $|S_{21}|$ and $|S_{11}|$ versus different values of: (a) Z (k_c = 0.4 fixed), and (b) k_c (Z = 140 Ω fixed).

III. SIMULATION AND MEASUREMENT

According to the above discussion, the initial designing parameters of dual-wideband BPF are pre-selected as Z_c = 147 Ω, k_c = 0.42, Z = 140 Ω and Z_s = 150 Ω, under which the first passband covers 1.228/1.575 GHz and the second passband covers 6.8 GHz. The dual-wideband BPF is designed on the substrate ARlon DiClad 880 (ε_{re} = 2.2, h = 0.508 mm, tanδ = 0.0009). Figure 4 (a) gives the layout of fabricated dual-wideband BPF. In Fig. 4 (a), the half-wavelength microstrip line and the loaded quarter-wavelength stubs are folded, so as to achieve size reduction. The whole structure is optimized by using the full wave EM simulator HFSS to consider the impact of bends, the grounded vias, the impedance discontinuities and the unequal even-/odd-mode phase velocities. The optimized physical dimensions are also labeled in Fig. 4 (a). Figure 4 (b) shows the photograph of fabricated dual-wideband BPF with the circuit size of $0.043\lambda_g \times 0.213\lambda_g$, where λ_g represents the guided wave-length of 50 Ω microstrip line at the central frequency of the first passband.

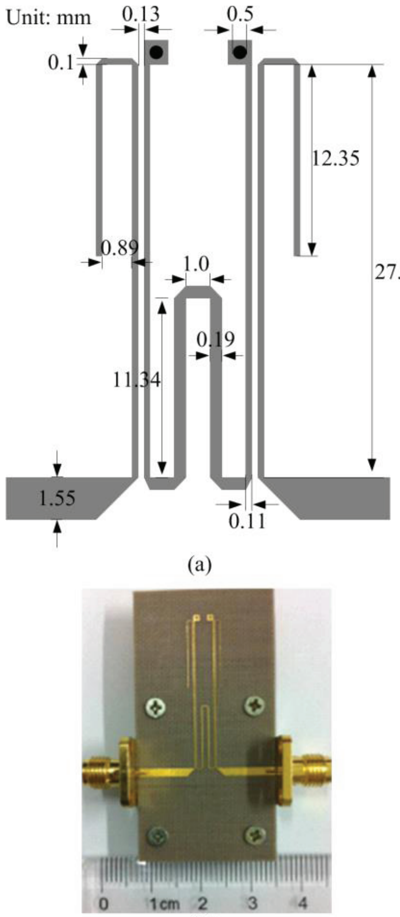

(b)

Fig. 4. (a) Layout, and (b) photograph of fabricated dual-wideband BPF.

The simulated and measured results of fabricated dual-band BPF are plotted in Fig. 5. Good agreement can be observed between the simulation and measurement. There are some discrepancies which are attributed to the fabrication error as well as SMA connectors. The measured central frequencies (CFs) and 3 dB FBW of two passbands are 1.54 GHz / 6.88 GHz and 60%/11.5%, respectively. The measured insertion losses (ILs) at 1.228 GHz, 1.575 GHz and 6.8 GHz are 0.4 dB, 0.4 dB and 0.9 dB, respectively. The return losses of two passbands are better than 26 dB and 15 dB, respectively. The band-to-band isolation is better than 20 dB from 2.5 GHz to 6.1 GHz.

Table 1 gives a performance comparison with some reported coupled-line-type dual-band BPF. In Table 1, CF, FBW and IL represents the central frequency, fractional bandwidth and insertion loss, respectively. After comparison, it obviously shows that the proposed dual-wideband BPF has the merits of low insertion loss, compact circuit size, wide passband, large dual-band central frequency ratio, simple physical topology and quick design procedure.

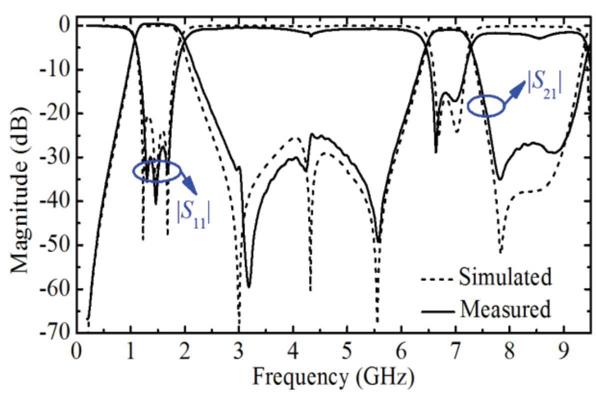

Fig. 5. Simulated and measured results of fabricated dual-wideband BPF.

Table 1: Performance comparison with some reported coupled-line-type dual-band BPFs

	CF (GHz)	3 dB FBW	IL at CF (dB)	Circuit Size (λ_g^2)
Ref. [5]	2.4, 5.2	8%, 3.69%	1.6, 2.5	0.189×0.733
Ref. [6] (Filter B)	2.0, 5.0	12%, 3%	1.0, 3.0	-
Ref. [7] (Filter A)	2.4, 5.8	5.8%, 2.1%	1.59, 2.59	0.312×0.304
Ref. [8] (Filter B)	2.48, 6.63	43.2%, 16.5%	0.33, 0.74	0.12×0.17
This Work	1.54, 6.88	60%, 11.5%	0.4, 0.9	0.043×0.213

IV. CONCLUSION

A dual-wideband BPF covering 1.228/1.57/6.8 GHz for GPS (Link 1 and Link 2) and RFID applications is presented by using proposed quarter-wavelength open stub loaded half-wavelength coupled-line. The fabricated dual-wideband BPF has a compact circuit area of $0.043\lambda_g \times 0.213\lambda_g$. Measured results also show its merits of low insertion loss, good return loss, sharp passband selectivity and good band-to-band isolation. The proposed filter has simple topology and design procedure. All these merits make it attractive in modern dual-wideband communication system.

ACKNOWLEDGMENT

This work was supported in part by the National Natural Science Foundation of China under Grant 61401358, and in part by the Fundamental Research Funds for Central Universities under Grant

3102014JCQ01058 and No. 30920140122005.

REFERENCES

[1] X.-Y. Zhang, J. Shi, J.-X. Chen, and Q. Xue, “Dual-band bandpass filter design using a novel feed scheme,” *IEEE Microw. Wireless Compon. Lett.*, vol. 19, no. 6, pp. 350-352, Jun. 2009.

[2] M. Jiang, L.-M. Chang, and A. Chin, “Design of dual-passband microstrip bandpass filters with multi-spurious suppression,” *IEEE Microw. Wireless Compon. Lett.*, vol. 20, no. 4, pp. 199-201, Apr. 2010.

[3] F. C. Chen, Q. X. Chu, Z. H. Li, and X. H. Wu, “Compact dual-band bandpass filter with controllable bandwidths using stub loaded multiple-mode resonator,” *IET Microw. Antennas Propag.*, vol. 6, no. 10, pp. 1172-1178, Nov. 2012.

[4] J. Xu, W. Wu, and C. Miao, “Compact and sharp skirts microstrip dual-mode dual-band bandpass filter using a single quadruple-mode resonator (QMR),” *IEEE Trans. on Microw. Theory Tech.*, vol. 61, no. 3, pp. 1104-1113, Mar. 2013.

[5] S. Lee and Y. Lee, “A planar dual-band filter based on reduced-length parallel coupled lines,” *IEEE Microw. Wireless Compon. Lett.*, vol. 20, no. 1, pp. 16-18, Jan. 2010.

[6] S. Lee and Y. Lee, “A uniform coupled-line dual-band filter with different bandwidths,” *IEEE Microw. Wireless Compon. Lett.*, vol. 20, no. 10, pp. 545-547, Oct. 2010.

[7] J. Xu, C. Miao, and W. Wu, “A compact and high isolation dual-mode dual-band bandpass filter with tunable transmission zeros,” *J. of Electromagn. Waves and Appl.*, vol. 26, no. 17-18, pp. 2390-2397, Dec. 2012.

[8] J. Xu and W. Wu, “Compact microstrip dual-mode dual-band bandpass filters using stubs loaded coupled line,” *Progress In Electromagnetics Research C*, vol. 41, pp. 137-150, 2013.

[9] I. Z. George and A. K. Johnson, “Coupled transmission line networks in an inhomogeneous dielectric medium,” *IEEE Trans. on Microw. Theory Tech.*, vol. 17, no. 10, pp. 753-759, Oct. 1969.

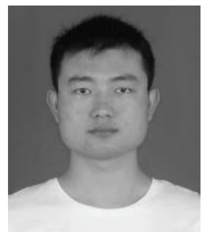

Jin Xu was born in AnHui Province, P.R. China, in 1987. He received the B.Eng. degree in Information Countermeasure Technology and the Ph.D. degree in Information and Communication Engineering from Nanjing University of Science and Technology (NUST), Nanjing, China, in 2009 and 2013, respectively. He is currently an Associate Professor with the School of Electronics and Information, Northwestern Polytechnical University, Xi’an, China. His research interests include UWB technology, MCM technology, microwave passive/active components, microwave and millimeter-wave MMICs developed on SiGe, phased array radar and wireless communication system.

From February 2011 to September 2011, he was an attached Ph.D. student in the Institute of Microelectronics, Singapore. From October 2011 to September 2012, he joined MicroArray Technologies Corporation Limited, Chengdu, P.R. China, where he was an IC R&D Engineer. Since 2011, he has served as a Reviewer for some journals including IEEE Microwave Wireless Component Letters, International Journal of Electronics, PIER and JEMWA.

Study of Various C-Shaped Armatures in Electromagnetic Launcher

M. Sajjad Bayati and Kambiz Amiri

Department of Electrical Engineering
Razi University, Kermanshah, Iran
s.bayati@razi.ac.ir

Abstract **─** The current density distribution on the cross section of the rails is affected by the geometry and dimensions of the rails and armature. This paper analyzed a rectangular railgun that is formed by two parallel rails and an armature with various geometries. Rail thickness (w_r), width (h_r), and separation (s_r) between two rails are equal to 2 cm, 4 cm and 4 cm, respectively. C-shaped armatures have three corners that are named front, back and arm side of armature which rounded step by step. All case studies simulated with the Finite Element Method Three Dimensions (FEM3D). For all steps, the inductance gradient, normal force, current density (J) distribution and maximum values of J are computed. The force between rails and armature named normal force. This force and pressure can be changed the rails and armature form. Friction force is increasing with increasing normal force. Maximum current densities occur at the armature corners and contact section between the rails and armature. These phenomena can produce a hot point that fuse the railgun and must be considered in armature and rail designing. This paper investigates the effect of armature geometry and dimensions on current density distribution, maximum value of current density, inductance gradient and normal force or normal pressure on armature.

Index Terms **─** Current density, FEM, inductance gradient, normal force, railgun.

I. INTRODUCTION

Armature and rails are the two main components of a railgun that are usually made up of materials with higher electrical conductivity. In a simple railgun, the magnetic flux density is generated around rails by passing electric current through them. Magnetic force has two components (normal and axial) which are exerted on armature due to magnetic flux density and the current passed through the armature. The axial force (F_x) is proportional to the inductance gradient (L') and passing current (I) through the rails [1-4]:

$$F_x = \frac{1}{2} L' I^2. \quad (1)$$

The distribution of electric current density over the armature is very high at the contact edges between the armature and rails, and sharp corners of the armature. These points become very hot due to Ohmic losses, hence deformed and after each launch reduce working life of the rails [5-8]. In recent years, significant advances researches have been reported for the railgun. Armature geometry can be assumed simple shape such as cube C and U-shape [9-15]. Passing currents through the up and bottom of the C-shape cause repulsive force between them. This force causes enormous pressure on the inner cross section of rails. This pressure can lead to rail breakage or rail bending too.

To reduce the losses and normal force on armature (contact with rails), we can reduce the amplitude of the input current. But reducing the amplitude of applied current will be decreased the force on the armature.

In Fig. 1 shows a railgun with C-shape armature in 3D and side view of 2D. The objective of this work is to analyze the C-shape armature with and without any rounded in the front, throat and rear side. These structures are simulated with FEM and calculated the inductance gradient, J_{max}, and normal force. These quantities are dependent on various sizes of armature and rounded radiuses. We presented the optimize dimensions for minimum value of the J_{max} and maximum value of the inductance gradient.

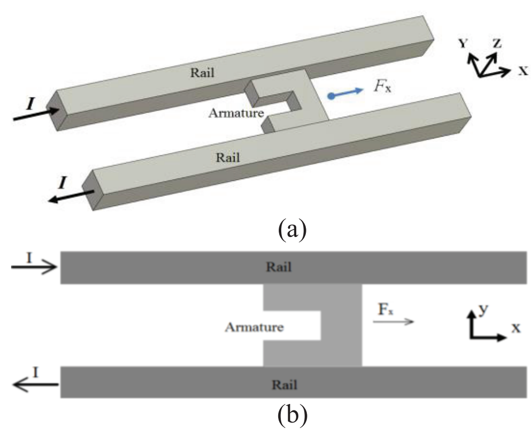

Fig. 1. Structure of railgun: (a) 3D railgun and (b) side view.

Submitted On: October 6, 2014
Accepted On: July 16, 2015

II. PROBLEM STATEMENT

A railgun consist of two parallel rails and a solid armature. Rails and armature are formed a closed current loop. Both rails made of copper and connected to an electrical power supply, and solid armature made of aluminum. The dimensions of the copper rails are as follows; width (h_r), separation (s_r) and thickness (w_r) are 4, 4, and 2 cm, respectively.

A. Railgun structure and parameters

Figure 2 (a) shows the rear view of railgun. The width of armature (h_a) is less than or equal rail's width.

Figure 2 (b) displays the side view of C-shape armature with details of dimensions and applied force.

According to Fig. 2 (b), we design three curvatures at the front, rear and throat of the C-shape armature with R_1, R_2 and R_3 radius, respectively.

In this paper, first C-shape armature without any rounded (Fig. 1), second C-shape armature with rounded in the front, throat and rear side are simulated and analyzed. Inductance gradient, J_{max}, and normal force are calculated for various sizes of X_C, Y_C, R_1, R_2 and R_3. Optimized results according to minimum value of the J_{max} and maximum value of the inductance gradient for various geometries and sizes are presented in the two different tables.

B. Force diagram

The electromagnetic force ($\boldsymbol{F}$) on the armature is depicted in Fig. 3. For the calculation of the electromagnetic force with ANSYS, we assume that the injected current has a constant amplitude.

We used FEM to compute the magnetic force for two and three-dimensional. For 2D, we first calculated the magnetic energy (E_m) than,

$$F = \nabla E_m; \tag{2}$$

and for 3-D simulation,

$$\vec{F} = \int \vec{J} \times \vec{B}\, dv\,, \tag{3}$$

where $\boldsymbol{J}$ and $\boldsymbol{B}$ are current density and magnetic flux density, respectively.

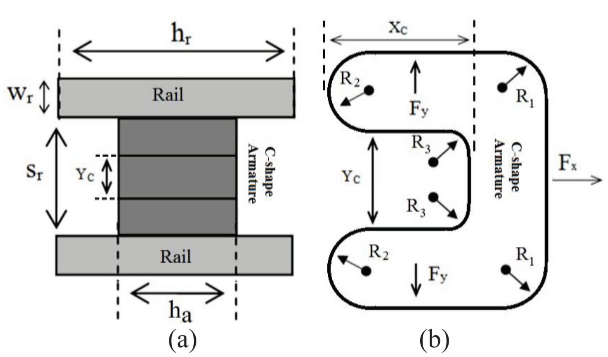

Fig. 2. (a) Rear view of railgun, and (b) side view of C-shape armature.

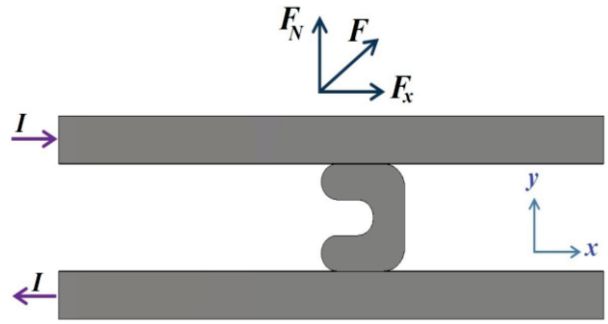

Fig. 3. The electromagnetic force and components.

F has two components, axial force (F_x) and normal force (F_y). The axial force (F_x) is propulsion force that can move the armature along the rails that is shown in Figs. 1-3. The friction force is a function of the normal force that is exerted by the normal force (F_y) and the friction coefficient.

C. Boundary conditions and modeling

Both rails are connected to electrical power supply and the total current flow is the same in two rails, but opposite directions that is displayed in Fig. 1. According to the Fig. 4 (a), the structure is symmetric to *x-z* and *x-y* plans, and only the first quadrant shown in Fig. 4 (b) is modeled.

The *x-y* plan (in 2D view *y* axis) is a symmetrical boundary and replaced by "magnetic wall" or $\boldsymbol{H_t}$=**0**, and the *x-z* plan (in 2D view *z-axis*) is an asymmetrical boundary and can be replaced by "electrical wall" or $\boldsymbol{H_n}$=**0**. We proposed the three models for 3D simulation of the railgun: 1) a half of the rails and armature by using magnetic wall, 2) one rail and a half of the armature by using electric wall, 3) a half of a rail and a quarter of the armature, that are shown in Figs. 5 (a), (b) and (c), respectively. Finally, this paper modeled only the quadrant of total structure (see Fig. 5 (c)). The symmetrical and asymmetrical boundaries are replaced by magnetic and electrical walls, respectively.

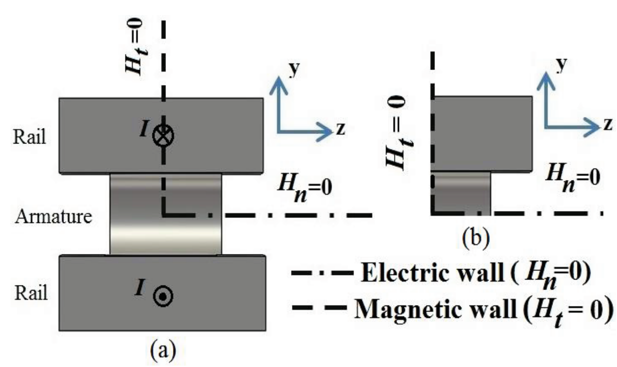

Fig. 4. Boundary conditions in rear view of railgun with C-shape armature.

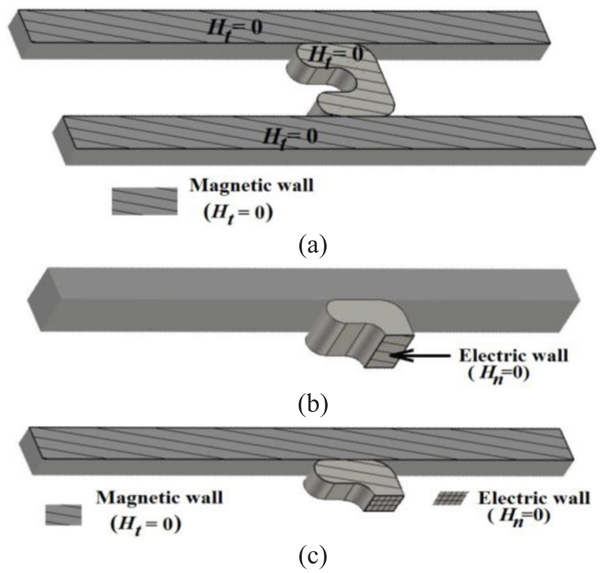

Fig. 5. 3D railgun: (a) half magnetic wall, (b) half electric wall, and (c) a quadrant of 3D railgun using magnetic and electric walls.

III. NUMERICAL RESULTS

In this section, inductance gradient, distribution of the current density and normal force are calculated for with and without rounded in each corner. The optimum structures with different size are obtained by considering two factor maximum value of inductance gradient and minimum value of J_{max}.

A. Inductance gradient and normal force

Table 1 shows the L', J_{max} and F_y for h_a=h_r=4 cm and different values of X_C and Y_C without rounded all the corners [5]. According to this table, the inductance gradient show minor variations of approximately 2%. The normal force variations show an increase of size more than 2.5 times for different values.

For the maximum current density by the way, a maximum increase less than 20% is observed. h_a is reduced to 1.6 cm, and L' obtained 0.5374 and 0.5238 µH/m for X_C=Y_C=2 cm and X_C=Y_C=3 cm, respectively.

L' and F_y are computed for C-shape armature with rounded front side and shown in Table 2. Rounded radius (R_1) equals to 0.50, 1.00, 1.50 and 1.90 cm. This Table illustrated that F_y decreased slightly with increasing R_1. The L' increased with increasing R_1. The rate of variations for L' for X_C=Y_C=3 cm is larger than other sizes. L' and F_y are calculated for C-shape armature with rounded front and arm side and shown in Table 3. Rounded radius for arm side (R_2) equals to 0.30, 0.36, 0.40 and 0.50 cm. Finally, back side is rounded with R_3 radius. R_3 equals to 0.45, 0.90 and 1.35 cm. Table 4 shows L' and F_y for different sizes of all dimensions. According to this table, L' and F_y are increased with increasing R_3. h_a is reduced to 2 cm, and L' obtained 0.5571 µH/m for X_C=Y_C=2 cm, R_1=1.8 cm, R_2=0.44 cm, R_3=1.35cm, which is larger than 0.49467 µH/m for h_a=4 cm. For X_C=Y_C=3 cm, R_1=1.8 cm, R_2=0.2 cm, R_3=1.35 cm, L' is 0.5963 µH/m, which is larger than and 0.54771 µH/m.

Table 1: The inductance gradient, maximum current density and normal force applied to the C-shape armature without rounded for different value of X_C and Y_C

X_C (cm)	Y_C (cm)	L' (µH/m)	J_{max} (10^{12}A/m^2)	F_y (kN)
1	1	0.4804	1.31	132
2		0.4843	1.39	254
3		0.4844	1.55	380
1	2	0.4812	1.32	131
2		0.4852	1.39	241
3		0.4832	1.53	349
1	3	0.4804	1.26	115
2		0.4823	1.27	197
3		0.4772	1.47	276

Table 2: The inductance gradient and normal force applied to the C-shape armature with rounded at front side

	X_C=Y_C=1 cm		X_C=Y_C=2 cm		X_C=Y_C=3 cm	
R_1 (cm)	F_y (kN)	L' (µH/m)	F_y (kN)	L' (µH/m)	F_y (kN)	L' (µH/m)
0.50	129	0.4808	237	0.4870	271	0.4812
1.00	125	0.4817	232	0.4885	268	0.4881
1.50	121	0.4832	226	0.4919	271	0.4969
1.90	117	0.4861	222	0.4962	274	0.5061

Table 3: The inductance gradient and normal force applied to the C-shape armature with rounded at front and arm side

X_C (cm)	Y_C (cm)	R_1 (cm)	R_2 (cm)	F_y (kN)	L' (µH/m)
2.40	2.40	1.60	0.36	225	0.4952
2.40	2.00	1.60	0.30	254	0.4961
2.40	1.80	1.00	0.50	234	0.4876
2.00	2.00	1.00	0.40	197	0.4867
1.60	2.00	1.00	0.30	164	0.4850

Table 4: The inductance gradient and normal force applied to the C-shape armature with rounded at front, back and arm side

	X_C=Y_C=2 cm, R_1=1.8 cm, R_2=0.44 cm		X_C=Y_C=3 cm, R_1=1.8 cm, R_2=0.2 cm	
R_3	F_y (kN)	L' (µH/m)	F_y (kN)	L' (µH/m)
0.45	183	0.49037	263	0.5003
0.90	184	0.49102	267	0.5349
1.35	185	0.49467	274	0.5477

B. Optimization according to L' and maximum value of current density

We want to reduce the maximum value of current density and increase inductance gradient. For both conditions two tables are presented. Table 5 shows the optimum structures according to inductance gradient. The maximum value of L' is 0.53555 µH/m for the C-shape armature without rounded corners. When all corners are rounded, L' increasing to 0.54771 and 0.59625 µH/m for h_a equals to 4 and 2 cm, respectively.

Table 6 shows the minimum value of J_{max}. According to this table, minimum value of J_{max} is 1.09×10^{12} A/m^2 for rounded all three corners.

Table 5: Optimization according to maximum value of the inductance gradient for various geometries (Units: L' (µH/m) and J_{max} (10^{12}A/m^2))

X_C	Y_C	R_1	R_2	R_3	h_a	J_{max}	L'
3	3	1.8	0.44	1.35	2	4.30	0.5962
3	3	1.8	0.44	1.35	4	1.97	0.5477
2.4	2	1.6	0.3	-	4	1.40	0.4961
3	3	1.9	-	-	4	1.39	0.5061
2	2	-	-	-	1.6	2.16	0.5356

Table 6: Optimization according to minimum value of the maximum current density for various geometries (Unit: cm)

X_C	Y_C	R_1	R_2	R_3	h_a	J_{max} (10^{12}A/m^2)	L' (µH/m)
2	2	1.8	0.2	1.35	4	1.09	0.49088
2	2	1.00	0.4	-	4	1.22	0.48674
3	3	0.5	-	-	4	1.25	0.48126
2	2	-	-	-	4	1.39	0.48526
1	3	-	-	-	4	1.26	0.48040

C. Current and normal force distribution on the armature

Due to the skin effect, the current tends to flow on the outer surface on the armature. Figure 6 shows the current density distribution on the quadrant of C-shape armature for $X_C = Y_C = 3$ cm with rounded in all corners. For h_a=4 and 2 cm, these distributions are shown in Figs. 6 (a) and (b), respectively. Velocity skin effect can be by higher current density concentrations at the outer edge of rear armature surface.

With compared between Figs. 6 (a) and (b), can be said the J_{max} increased with decreasing h_a. Figure 7 shows the normal force distribution on the quadrant of C-shape armature for $X_C = Y_C = 3$ cm with rounded in all corners. For h_a=4 and 2 cm, these distributions are shown in Figs. 7 (a) and (b), respectively.

Figure 8 shows the current density distribution on the quadrant of C-shape armature for $X_C = Y_C = 2$ cm with rounded in all corners. For h_a=4 and 2 cm, these distributions are shown in Figs. 8 (a) and (b), respectively. According to this figure, the J_{max} occurs in two places. That is located at the junction of rails and front and back side of armature. The J_{max} at the arm side in Fig. 8 increased than in Fig. 6. With compared between Figs. 8 (a) and (b), can be said the current density is increased with decreasing h_a. Figure 9 shows the normal force distribution on the quadrant of C-shape armature for $X_C = Y_C = 2$ cm with rounded in all corners. For h_a=4 and 2 cm, these distributions are shown in Figs. 9 (a) and (b), respectively.

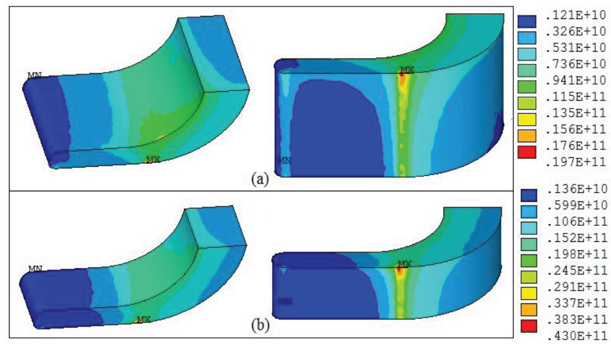

Fig. 6. Current density distribution on the C-shape armature for $X_C = Y_C = 3$ cm: (a) h_a=4 cm and (b) h_a=2 cm.

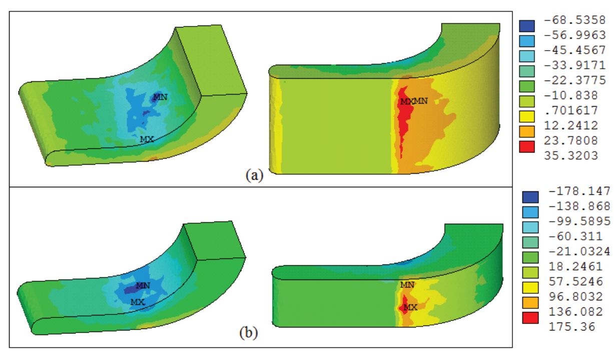

Fig. 7. Normal force distribution on the C-shape armature for $X_C = Y_C = 3$ cm: (a) h_a=4 cm and (b) h_a=2 cm.

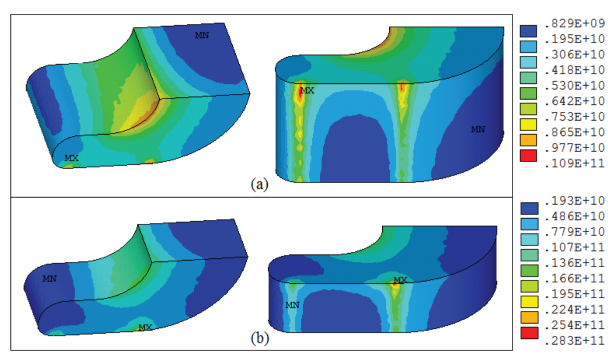

Fig. 8. Current density distribution on the C-shape armature for $X_C = Y_C = 2$ cm: (a) h_a=4 cm and (b) h_a=2 cm.

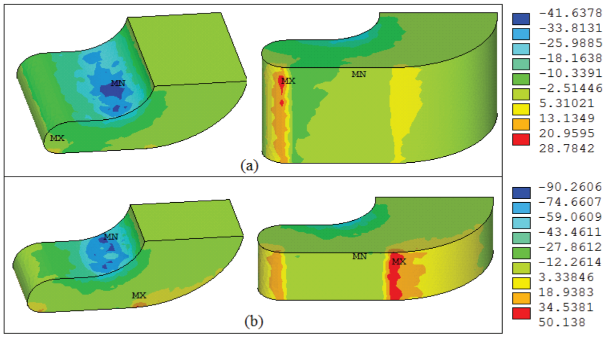

Fig. 9. Normal force distribution on the C-shape armature for X_C=Y_C=2 cm: (a) h_a=4 cm and (b) h_a=2 cm.

IV. CONCLUSION

This paper investigated the effect of C-shape armature geometry on the inductance gradient, normal force and the maximum electrical current density. According to the results of this paper can be said, increasing X_C results in the slightly variations of L', increase the $J_{\max}$ and F_y. Increasing Y_C results in the slightly variations of L' and $J_{\max}$ and decrease the F_y. Variations of the all rounded radius result in slightly on the normal force. Increasing the X_C and Y_C result in the effect of R_1, R_2 and R_3 on L' and $J_{\max}$ and F_y will be more.

REFERENCES

[1] M. S. Bayati, A. Keshtkar, and A. Keshtkar, "Transition study of current distribution and maximum current density in railgun by 3D FEM and IEM," *IEEE Transactions on Plasma Science*, vol. 39, no. 1, pp. 13-17, Jan. 2011.

[2] R. A. Marshall, "Railgun bore geometry round or square?," *IEEE Transactions on Magnetics*, vol. 35, no. 1, pp. 427-431, Jan. 1999.

[3] A. Keshtkar, S. Bayati, and A. Keshtkar, "Derivation of a formula for inductance gradient using IEM," *IEEE Transactions on Magnetics*, vol. 45, no. 1, pp. 305-308, Jan. 2009.

[4] M. S. Bayati and A. Keshtkar, "Study of the current distribution, magnetic field, and L' of rectangular and circular railguns," *IEEE Transactions on Plasma Science*, vol. 45, no. 5, pp. 1376-1381, May 2013.

[5] L. Chen, J. He, Z. Xiao, and Y. Pan, "Three-dimensional numerical simulation of the joule heating of various shapes of armatures in railguns," *IEEE Transactions on Plasma Science*, vol. 39, no. 1, pp. 456-460, Jan. 2011.

[6] J. F. Kerrisk, "Electrical and thermal modelling of railgun," *IEEE Transactions on Magnetics*, vol. MAG-20, no. 1, pp. 339-402, 1984.

[7] H. Vanicek and S. Satapathy, "Thermal characteristics of a laboratory electromagnetic launcher," *IEEE Transactions on Magnetics*, vol. 41, no. 1, pp. 188-193, Jan. 2005.

[8] J. D. Powell and A. E. Zielinski, "Ohmic heating in a double-taper sabot-armature," *IEEE Transactions on Magnetics*, vol. 39, no. 1, pp. 153-157, Jan. 2003.

[9] L. Rip, S. Satapathy, and K-T. Hsieh, "Effect of geometry change on the current density distribution in C-shaped armature," *IEEE Transactions on Magnetics*, vol. 39, no. 1, pp. 72-75, Jan. 2003.

[10] M. S. Bayati, "Projectile geometry," *16th EML Symposium*, China, June 2012.

[11] B-K. Kim and K-T. Hsieh, "Effect of rail/armature geometry on current density distribution and L'," *IEEE Transactions on Magnetics*, vol. 35, no. 1, pp. 413-416, Jan. 1999.

[12] L. Chen, J. He, Z. Xiao, and Y. Pan, "Augmentation of current ramp-down contact pressure in C-shaped armature railguns," *IEEE Transactions on Plasma Science*, vol. 39, no. 1, pp. 48-52, Jan. 2011.

[13] D. C. Haugh and G. M. G. Hainsworth, "Why "C" armature work (and why they don't!)," *IEEE Transactions on Magnetics*, vol. 39, no. 1, pp. 52-55, Jan. 2003.

[14] S. Xia, J. He, L. Chen, Z. Xiao, and J. Li, "Studies on interference fit between armatures and rails in railguns," *IEEE Transactions on Plasma Science*, vol. 39, no. 1, pp. 186-191, Jan. 2011.

[15] Q. Lv, Z. Li, B. Lei, K. Zhao, Q. Zhang, H. Xiang, and S. Xie, "Primary structural design and optimal armature simulation for a practical electromagnetic launcher," *IEEE Transactions on Plasma Science*, vol. 45, no. 5, pp. 1403-1409, May 2013.

Mohammad Sajjad Bayati was born in Sonqor, Kermanshah, Iran, in 1979. He received the B.Sc. degree in Electrical Engineering from the University of Tabriz, in 2002, the M.Sc. in Telecommunication Field and Wave Engineering from the Sahand University of Technology, and the Ph.D. degree in Electrical Engineering from the University of Tabriz in 2011. His M.Sc. dissertation was focused on DF antenna and Ph.D. dissertation was focused on analysis of rail electromagnetic launcher using combined FEM-3D and IEM in time domain.

He is an Assistant Professor with the Department of Electrical Engineering, University of Razi, Kermanshah, Iran. His research interests include electromagnetic, mathematical in electromagnetic, electromagnetic launcher, bio and microstrip antenna.

Kambiz Amiri was born in Kermanshah, Iran, 1981. He received the B.Sc. degree in Electrical Engineering in 2008. He is currently working toward the M.Sc. degree in the Department of Electrical Engineering, Razi University, Kermanshah. His research interests include electromagnetic and antenna design.

Tesla Transformer and its Response with Square Wave and Sinusoidal Excitations

Eduard M. M. Costa

Colegiado de Engenharia Elétrica
Universidade Federal do Vale do São Francisco, Juazeiro, BA 48902-300, Brazil
eduard.montgomery@univasf.edu.br, edmontyc@gmail.com

Abstract **─** This paper analyses the output of Tesla transformer from input defined as square wave and sine wave and its transfer function obtained from its equivalent circuit. The transfer function presented is analyzed in terms of the time, and the output is obtained when applying an input defined as a step and a sine function. When using square wave, the high gain obtained is proved that is due to a sum of responses obtained through positive and negative step that forms the square wave. However, the gain obtained when the excitation is a sine wave is higher than square wave excitation. Thus, in this paper is shown that the Tesla transformer works with sinusoidal excitation too, and present higher gain than square wave excitation, both higher than expected in classical transformer theory (turns ratio). All analysis presented were based in simulating operation using MATLAB® comparing with experimental data.

Index Terms **─** Pulse transformers, resonance, Tesla transformers, transfer function, transformers.

I. INTRODUCTION

Tesla transformer [1,2] is a pulse transformer [3,4] that works at double resonance [5], used to generate high voltages, and so to generates high energy applied to systems as particle accelerators (particle colliders) [6], and others [7]. The theoretical foundation of Tesla transformer defines a double capacitive-inductive circuit, where the primary is excited by a square wave, which resonates with secondary, increasing the output voltage to kilovolts or megavolts.

Several works analyzing the Tesla transformer and the base of the high voltage that is an exception to the rule of the classical transformer theory (turns ratio) [8]. Example is the works of Costa [9-11], which analyzes the effects of induced electromotive force (EMF) at transformers built by planar and ring coils [12], effects of parasitic capacitances [13], going to the resonance with square wave excitation [14]. In these works, a transfer function is obtained, which is based in a specific response, whose result to square wave excitation defines a sum of responses that generates very high gains [1].

In the same way, using experimental results and other analysis of this response, an interesting result about Tesla transformer resonance is found in [15], where the excitation is a sine wave, whose response is higher than the found results of square wave excitation.

New analysis of this system are realized here, which is based in the transfer function of the Tesla transformer, whose parameters are referred to capacitive, inductive and resistive elements, instead of resonance frequencies shown at [1,10-12]. Thus, in this work are presented these results, which are simulated with MATLAB®, as well as experimental, showing that the Tesla transformer presents higher gain when excited with sinusoidal wave, than excited by square wave.

Thus, this paper is presented as follows: in Section II is presented the equivalent circuit and its transfer function formulation. In Section III is shown step response, as well as transient response to sinusoidal excitation. In Section IV are analyzed the responses at steady state for these excitation forms, showing a comparative between gains and, at Section V are presented the conclusions of this work.

II. EQUIVALENT CIRCUIT AND TRANSFER FUNCTION OF TESLA TRANSFORMER

Considering the circuit shown in Fig. 1 (a), that is the equivalent circuit of the Tesla transformer, which is shown based on impedances at Fig. 1 (b), where:

$$\begin{aligned}
&Z_1 = \frac{1}{sC_1} // sL_1 = \frac{sL_1}{1+s^2 L_1 C_1},\\
&Z_2 = sM,\\
&Z_3 = \frac{1}{sC_2} // sL_2 = \frac{sL_2}{1+s^2 L_2 C_2},\\
&Z_{R_1} = R_1,\\
&Z_{R_2} = R_2,
\end{aligned} \tag{1}$$

Submitted On: March 24, 2015
Accepted On: June 22, 2015

then, the transfer function $G(s) = V_0(s)/V_i(s)$ is:

$$G(s) = \frac{V_0(s)}{V_i(s)} = \frac{as}{fs^4 + ds^3 + es^2 + cs + b}, \tag{2}$$

where

$$\begin{aligned} a &= L_1 L_2, \\ b &= (L_1 + L_2 + M) R_1, \\ c &= (L_2 + M) L_1, \\ d &= C_2 L_1 L_2 M, \\ e &= ((C_1 + C_2) L_1 L_2 + (C_1 L_1 + C_2 L_2) M) R_1, \\ f &= C_1 C_2 L_1 L_2 M R_1, \end{aligned} \tag{3}$$

being R_1, R_2 the resistances, L_1, L_2 the inductances, C_1, C_2 the capacitances and M the mutual inductance, with index 1 and 2 being referenced to the primary and secondary, respectively.

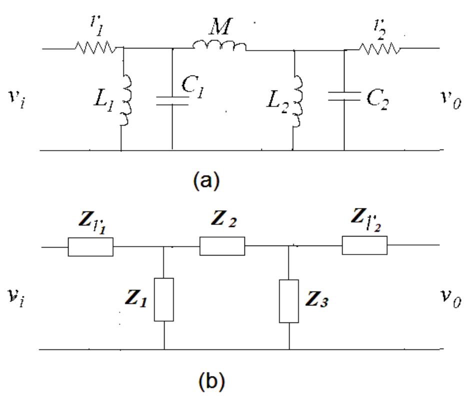

Fig. 1. (a) Equivalent circuit of Tesla transformer, and (b) equivalent circuit based on impedances.

Applying impulse to this transfer function and obtaining the inverse Laplace transform, we found:

$$f_{\uparrow}(t) = a \sum_k \left(k e^{kt} / \left(4fk^3 + 3dk^2 + 2ek + c \right) \right), \tag{4}$$

with k being the roots of the polynomial in w:

$$P(w) = fw^4 + dw^3 + ew^2 + cw + b, \tag{5}$$

with a, b, c, d, e and f defined as shown previously (Eq. (3)).

The impulse response of this function is shown in Fig. 2, where is observed that the transfer function present real and complex conjugate exponential terms (roots of the polynomial $P(w)$), what defines exponential and sinusoidal functions at response.

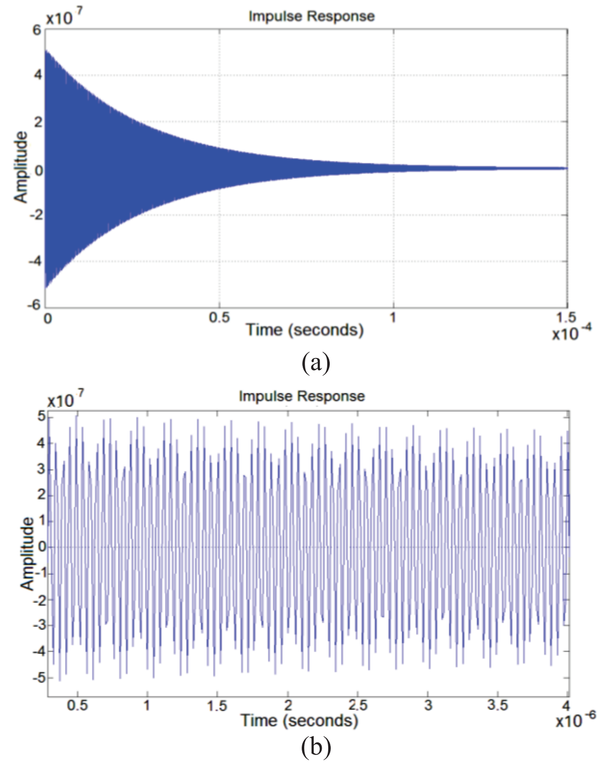

Fig. 2. (a) Impulse response of Tesla transformer, and (b) zoom showing double sinusoidal response.

III. RESPONSES OF TESLA TRANSFORMER TO SQUARE WAVE AND SINUSOIDAL EXCITATIONS

Based on transfer function $G(s)$ (Eq. (2)), applying unitary step ($V_i(s) = 1/s$), the response is:

$$V_0(s) = \frac{as}{fs^4 + ds^3 + es^2 + cs + b} \frac{1}{s}. \tag{6}$$

Making the inverse Laplace transform, then the result found is:

$$f(t) = a \sum_k \left(e^{kt} / \left(4fk^3 + 3dk^2 + 2ek + c \right) \right), \tag{7}$$

with k being the roots of the polynomial in w:

$$P(w) = fw^4 + dw^3 + ew^2 + cw + b, \tag{8}$$

which can be seen at Fig. 3, for the specific case where: $R_1 = 0.5\ \Omega$, $R_2 = 0.89\ \Omega$, $L_1 = 0.433\ \mu H$, $L_2 = 1.85\ \mu H$, $C_1 = 59.5$ pF, $C_2 = 52.5$ pF and $M = 2.801\ \mu H$, as data found in [9-11], referring to planar transformer with 10 turns at primary coil and 20 turns at secondary coil.

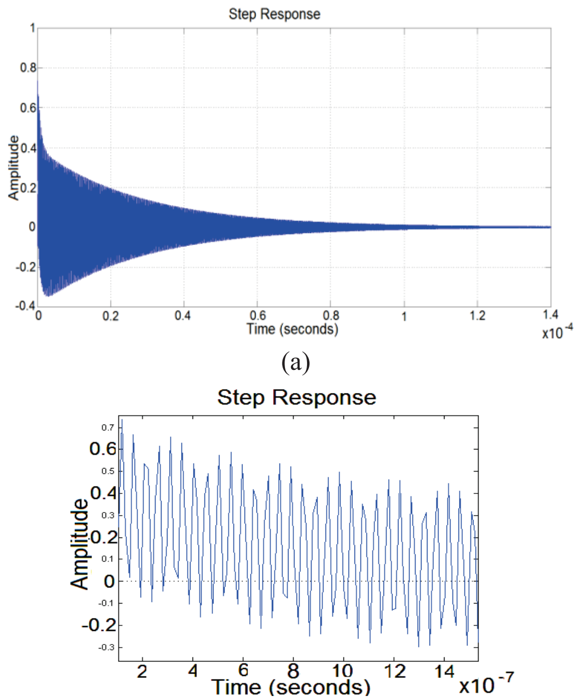

(a)

(b)

Fig. 3. (a) Step response of the Tesla transformer, and (b) zoom showing double sinusoidal oscillation.

Thus, when applied an inverted unitary step (negative sign), the result for this function is only the inverted sign of the function $f(t)$.

By other side, considering the application of sinusoidal excitation to $G(s)$, or:

$$V_0(s)=\frac{as}{fs^4+ds^3+es^2+cs+b}\frac{\omega}{s^2+\omega^2}, \tag{9}$$

and applying the inverse Laplace transform, the result found is:

$$\begin{aligned}
v_0(t)=&\frac{a\omega\left(\left(b-e\omega^2+f\omega^4\right)\cos(\omega t)+\omega\left(c-d\omega^2\right)\sin(\omega t)\right)}{bx+\omega^2y+f^2\omega^8}\\
&-a\omega\left[f^2\omega^4\sum_k\left(\frac{k^3e^{kt}}{q(k)}\right)-e^2\omega^2\sum_k\left(\frac{ke^{kt}}{q(k)}\right)-f^2\omega^6\sum_k\left(\frac{ke^{kt}}{q(k)}\right)\right.\\
&-d^2\omega^4\sum_k\left(\frac{ke^{kt}}{q(k)}\right)-bd\sum_k\left(\frac{k^2e^{kt}}{q(k)}\right)+cd\omega^2\sum_k\left(\frac{ke^{kt}}{q(k)}\right)\\
&+bf\sum_k\left(\frac{k^3e^{kt}}{q(k)}\right)-bf\omega^2\sum_k\left(\frac{ke^{kt}}{q(k)}\right)+2ef\omega^4\sum_k\left(\frac{ke^{kt}}{q(k)}\right)\\
&+bc\sum_k\left(\frac{e^{kt}}{q(k)}\right)-cf\omega^2\sum_k\left(\frac{k^2e^{kt}}{q(k)}\right)-de\omega^2\sum_k\left(\frac{k^2e^{kt}}{q(k)}\right)\\
&\left.-ef\omega^2\sum_k\left(\frac{k^3e^{kt}}{q(k)}\right)-bd\omega^2\sum_k\left(\frac{e^{kt}}{q(k)}\right)+be\sum_k\left(\frac{ke^{kt}}{q(k)}\right)\right]/\\
&\left(bx+\omega^2y+f^2\omega^8\right),
\end{aligned} \tag{10}$$

where $x=b-2e\omega^2+2f\omega^4$ and $y=c^2-(2cd+e^2)\omega^2+(d^2-2ef)\omega^4$ and,

$$q(k)=4fk^3+3dk^2+2ek+c. \tag{11}$$

For this case, using the same parameters previously applied to step excitation example ($R_1=0.5\ \Omega$, $R_2=0.89\ \Omega$, $L_1=0.433\ \mu H$, $L_2=1.85\ \mu H$, $C_1=59.5$ pF, $C_2=52.5$ pF and $M=2.801\ \mu H$), the transient response is shown at Fig. 4, considering an excitation at low frequencies.

This same output can be seen as:

$$V_0(s)=\frac{p(s)}{q(s)}\frac{\omega}{s^2+\omega^2}, \tag{12}$$

where the polynomial $q(s)=fs^4+ds^3+es^2+cs+b$ can be seen as:

$$q(s)=(s+q_1)(s+q_2)\cdots(s+q_4), \tag{13}$$

whose roots are real and complex conjugate, may present all roots distinct, as well as with multiplicity, with known results of the linear systems. In both cases, the steady state response is:

$$v_{0ss}(t)=Y\left|G(j\omega)\right|\sin(\omega t+\varphi), \tag{14}$$

with ϕ being an angle lag and Y the peak at output.

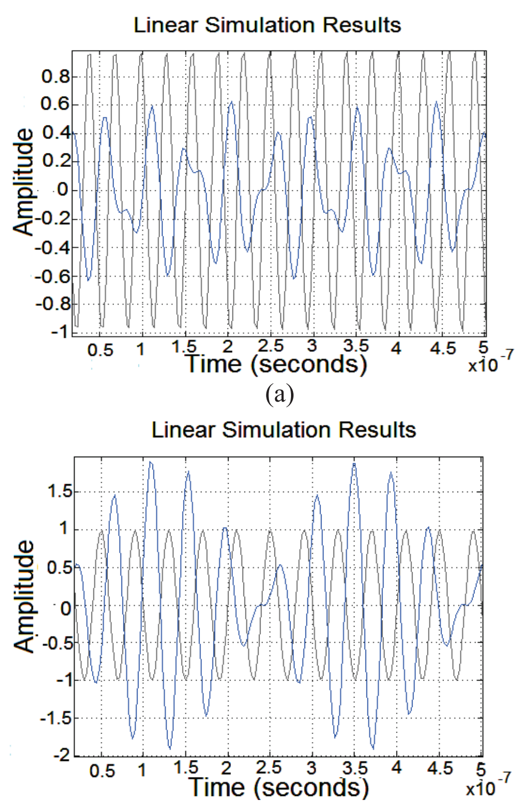

(a)

(b)

Fig. 4. Responses of Tesla transformer at low frequencies to sinusoidal excitation, where all low frequencies occur an overlap of responses as shown in [1].

IV. RESPONSES OF TESLA TRANSFORMER FOR STEADY STATE

Considering steady state, the Tesla transformer shows an output that can present low or high amplitude, depending on the excitation frequency at input. Both in the case of the square wave excitation as the sinusoidal excitation, according to excitation frequency tends to resonance, this gain increases rapidly, reaching high values, which do not follow classical transformer theory (turn ratio).

Considering first the input excitation as a square wave, we have that the step response is given by Eq. (7). Consequently, the excitation with an inverted step (step with negative sign) generates this same response with negative sign. How a square wave can be seen as a sequence of steps up and down, accordingly shown previously, then the response of the Tesla transformer for low frequencies (without resonance) is a series of responses up and down over each rise and fall of the square wave. However, as the square wave frequency increases, these responses overlap, summing up when the responses peak have same sign and subtracting when have inverted signs. These results can be seen at Fig. 5.

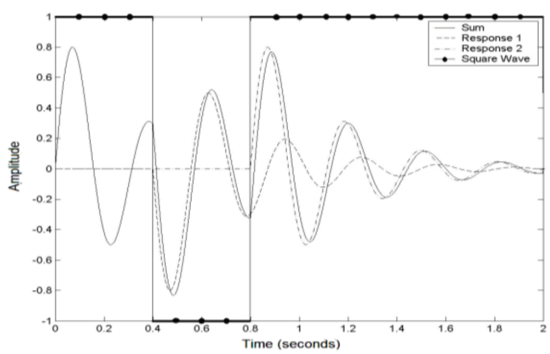

(a)

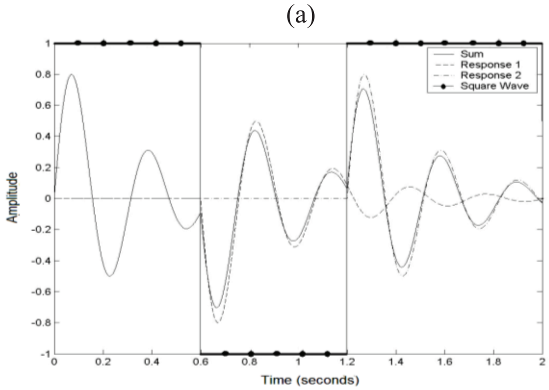

(b)

Fig. 5. Response of Tesla transformers to square wave at rise and fall: (a) sum and (b) subtraction.

When the square wave frequency approaches the frequency of the system response, this sum of responses increases output voltage, as shown at Fig. 6.

Also, when the square wave frequency tends to frequency of the response, the system reaches resonance, giving an output with high gain, defined by:

$$v_0(t) = 2.023\text{x}10^5/\exp(3.361\text{x}10^{10}t) - 5.021\text{x}10^5/\exp(1.26\text{x}10^6t) + 0.29\cos(1.307\text{x}10^8t)/\exp(3.55\text{x}10^4t) + 0.52\sin(1.3075\text{x}10^8t)/\exp(3.55\text{x}10^4t), \quad (15)$$

shown at Fig. 7, that is the result for the specific case to values of inductances, capacitances and resistances found in [9-11] for the case of the planar transformer with 10 turns at primary and 20 turns at secondary, which presents in simulation result the gain $G = v_0/v_i = 465$.

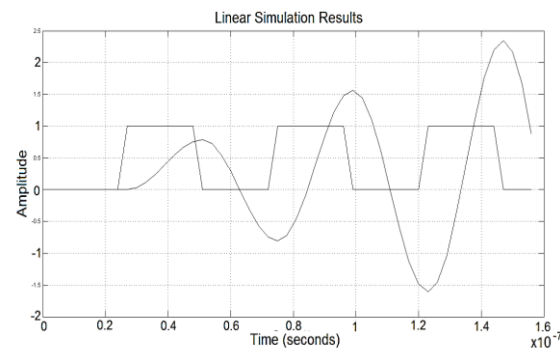

(a)

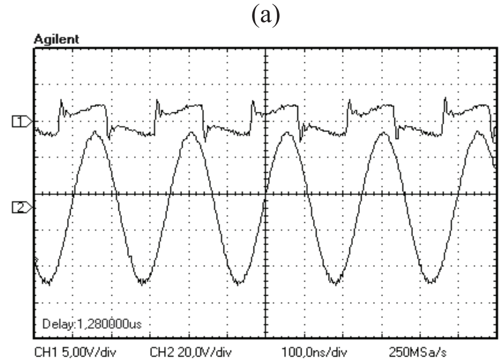

(b)

Fig. 6. Resonance of Tesla coil; frequency of square wave approximately equal to frequency of step response: (a) simulated response for transient response (sum of responses), and (b) experimental result.

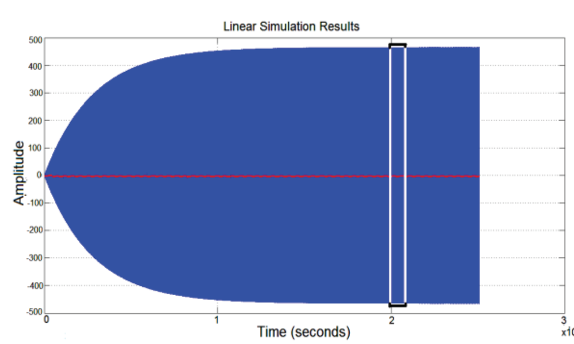

(a)

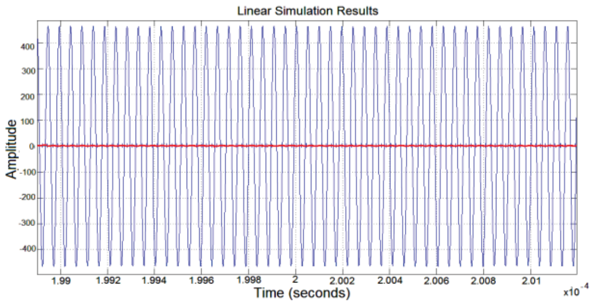

(b)

Fig. 7. Steady state of Tesla transformer excited with square wave in resonance: (a) general response and (b) zoomed.

By other side, considering sinusoidal excitation, on experimental results found in [15], we see that the output at resonance is greater than square wave excitation. Taking the results of the Eq. (9), we have at low frequencies the result shown in Fig. 4. As the sinusoidal excitation frequency increases, approaching to resonance frequency, the system responds with a higher growth than sum of responses of the square wave excitation.

The resonance frequency of Tesla transformer is reached when:

$$\omega = \frac{1}{\sqrt{L_1 C_1}} = \frac{1}{\sqrt{L_2 C_2}}. \tag{16}$$

As this value of ω is a pole of Eq. (9), the system tends to present an output with infinite growth (making $s = j\omega$). In this way, as seen mathematically, the system output rapidly increases, as the case of the shown example of the Eq. (15), what can be seen at Fig. 8, where the gain at steady state is $G = v_0/v_i = 719.1$, since that the input is unitary.

Comparing the gain values obtained with square wave excitation and sinusoidal excitation at their maximum peaks, we find:

$$G_{\sin} / G_{sq} = 719.1 / 465 = 1.546. \tag{17}$$

This result, when compared with experimental results as example shown in Fig. 6, we see that the gain is lesser due to limitations of the used equipment, but does not invalidate the obtained results.

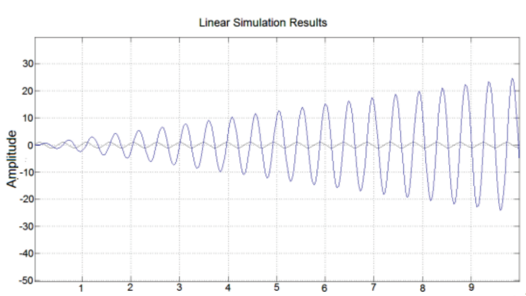

(a)

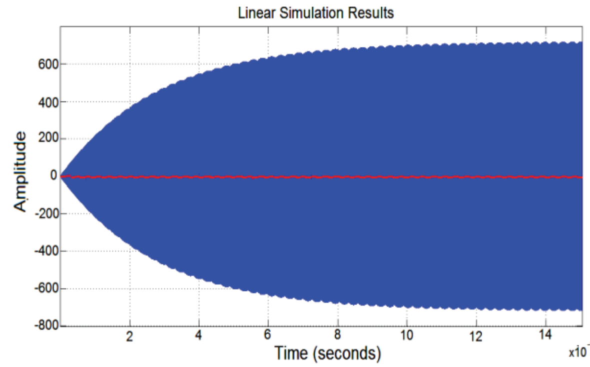

(b)

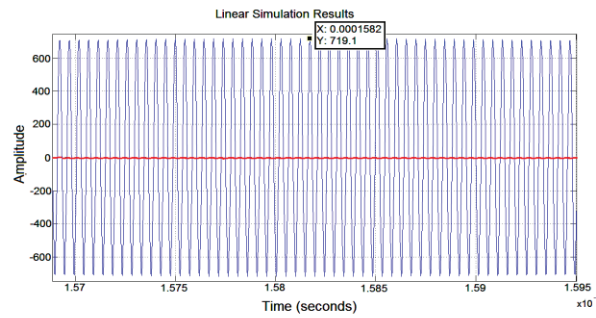

(c)

Fig. 8. Resonant response of Tesla transformer to sinusoidal excitation: (a) transient response, (b) general response, and (c) zoomed response of steady state.

V. CONCLUSION

In this paper was seen the Tesla transformer response at square wave and sinusoidal excitation, where was obtained the transfer function and the responses of these inputs in time domain. It is noted both mathematically as experimentally the effects of high gain due to these inputs, proving that the square wave excitation defines an output, whose response is a sum of step responses (positive and negative), and with sinusoidal excitation, the gain is higher than square wave at steady state. Thus, it is shown that the Tesla transformer operates with sinusoidal excitation and the obtained gains for this case are higher than obtained gains referring to square wave excitation, as shown both simulation as experimental, for the presented specific case, as shown in [15].

REFERENCES

[1] E. M. M. Costa, "Resonance on coils excited by square waves: explaining Tesla transformer," *IEEE Transactions on Magnetics*, vol. 46, no. 5, pp. 1186-1192, May 2010.

[2] P. Ying and R. Jiangjun, "Investigation of very fast transient overvoltage distribution in taper winding of Tesla transformer," *IEEE Transactions on Magnetics*, vol. 42, no. 3, pp. 434-441, Mar. 2006.

[3] H. W. Lord, "Pulse transformers," *IEEE Transactions*

on Magnetics, vol. MAG-7, no. 1, pp. 17-28, Mar. 1971.
[4] P. M. Ranon, “Compact pulsed transformer power conditioning system for generating high voltage, high energy, rapid rise time pulses,” *IEEE Transactions on Magnetics*, vol. 25, no. 1, pp. 480-484, Jan. 1989.
[5] M. Denicolai, “Tesla transformer for experimentation and research,” *Licentiate Thesis*, Helsinki University of Technology, May 2001.
[6] D. K. Dinev, “Design of Tesla transformers used in direct-voltage accelerators,” *Atomic Energy*, vol. 46, no. 3, Mar. 1979.
[7] D. Brown and D. Martin, “Subnanosecond high-voltage pulse generator,” *Rev. Sci. Instrum.*, vol. 58, no. 8, pp. 1523-1529, Aug. 1987.
[8] E. M. M. Costa, “Resonance on transformers excited by square waves and explanation of the high voltage on Tesla transformer,” *Progress in Electromagnetic Research B, PIER B*, vol. 18, pp. 205-224, 2009.
[9] E. M. M. Costa, “A basic analysis about induced EMF of planar coils to ring coils,” *Progress in Electromagnetics Research B, PIER B*, vol. 17, pp. 85-100, Aug. 2009.
[10] E. M. M. Costa, “Responses in transformers built with planar coils inner ring coils excited by square waves,” *Progress in Electromagnetics Research B, PIER B*, vol. 18, pp. 43-58, Sep. 2009.
[11] E. M. M. Costa, “Resonance between planar coils vs ring coils excited by square waves,” *Progress in Electromagnetics Research B, PIER B*, vol. 18, pp. 59-81, Sep. 2009.
[12] E. M. M. Costa, “Planar transformers excited by square waves,” *Progress in Electromagnetics Research, PIER 100*, pp. 55-68, 2010.
[13] E. M. M. Costa, “Parasitic capacitances on planar coils,” *Journal of Electromagnetic Waves and Applications*, vol. 23, pp. 2339-2350, 2009.
[14] E. M. M. Costa, “Effects of induced electromotive force (EMF) in transformers built with planar coils,” *IEEE Latin America*, vol. 9, pp. 649-654, 2011.
[15] E. M. M. Costa, *Resonance Analysis of Induced EMF on Coils, Electromotive Force and Measurement in Several Systems*, InTech Open, Edited by Sadik Kara, pp. 153-174, Rijeka, Croatia, Oct. 2011.

Eduard M. M. Costa was born in Esperança, PB, Brazil, in 1970. He received his M.Sc. and D.Sc. degrees in Electrical Engineering from Universidade Federal da Paraíba, Brazil in 1997 and 2001 respectively. He worked on projects of automation and electromagnetism. He has published several papers and books in the related areas, being their main areas of research.

Costa works in Universidade Federal do Vale do São Francisco (UNIVASF), Juazeiro, BA, Brazil, where he develops researches about electromagnetism, automation, and others. He’s a Member of Brazilian Electromagnetism Society (SBMag) and IEEE.